# APPLICATION OF THE POLYNOMIAL CHAOS EXPANSION TO MULTIPHASE CFD: A STUDY OF RISING BUBBLES AND SLUG FLOW

by

Dustin R. Langewisch

B.S., Mechanical Engineering (2007)
University of Missouri

B.S., Mathematics (2007)
University of Missouri

S.M., Nuclear Science and Engineering (2010)
Massachusetts Institute of Technology

SUBMITTED TO THE DEPARTMENT OF NUCLEAR SCIENCE AND ENGINEERING
IN PARTIAL FULFILLMENT OF THE REQUIREMENTS FOR THE DEGREE OF

DOCTOR OF PHILOSOPHY IN NUCLEAR SCIENCE AND ENGINEERING

at the

MASSACHUSETTS INSTITUTE OF TECHNOLOGY

June 2014





Author ..... Signature redacted
Dustin R. Langewisch
Department of Nuclear Science and Engineering
May 14, 2014

Certified by ..... Signature redacted .....
Jacopo Buongiorno
Associate Professor of Nuclear Science and Engineering, MIT
Thesis Supervisor

Certified by ..... Signature redacted .....
Pierre Lermusiaux
Associate Professor in Ocean Utilization, MIT
Thesis Reader

Accepted by ..... Signature redacted .....
Mujid Kazimi
TEPCO Professor of Nuclear Engineering
Chair, Department Committee on Graduate Studies

**Application of the Polynomial Chaos Expansion to Multiphase CFD: a Study of Rising Bubbles and Slug Flow**

by

Dustin R. Langewisch

Submitted to the Department of Nuclear Science and Engineering
on May 14, 2014, in partial fulfillment of the
requirements for the degree of
Doctor of Philosophy in Nuclear Science and Engineering

## Abstract

Part I of this thesis considers subcooled nucleate boiling on the microscale, focusing on the analysis of heat transfer near the Three-Phase (solid, liquid, and vapor) contact Line (TPL) region. A detailed derivation of one representative TPL model is presented. From this work, it was ultimately concluded that heat transfer in the vicinity of the TPL is rather unimportant in the overall quantification of nucleate boiling heat transfer; despite the extremely high heat fluxes that are attainable, it is limited to a very small region so the net heat transfer from this region is comparatively small. It was further concluded that many of the so-called microlayer heat transfer models appearing in the literature are actually models for TPL heat transfer; these models do not model the experimentally observed microlayer. This portion of the project was terminated early, however, in order to focus on the application of advanced computational uncertainty quantification methods to computational multiphase fluid dynamics (Part II).

Part II discusses advanced uncertainty quantification (UQ) methods for long-running numerical models, namely computational multiphase fluid dynamics (CMFD) simulations. We consider the problem of how to efficiently propagate uncertainties in the model inputs (e.g., fluid properties, such as density, viscosity, etc.) through a computationally demanding model. The challenge is chiefly a matter of economics—the long run-time of these simulations limits the number of samples that one can reasonably obtain (i.e., the number of times the simulation can be run). Chapter 2 introduces the generalized Polynomial Chaos (gPC) expansion, which has shown promise for reducing the computational cost of performing UQ for a large class of problems, including heat transfer and single phase, incompressible flow simulations; example applications are demonstrated in Chapter 2. One of main objectives of this research was to ascertain whether this promise extends to realm of CMFD applications, and this is the topic of Chapters 3 and 4.

Chapter 3 covers the numerical simulation of a single bubble rising in a quiescent liquid bath. The pertinent quantities from these simulations are the terminal velocity of the bubble and terminal bubble shape. The simulations were performed using the open source *Gerris* flow solver. A handful of test cases were performed to validate the simulation results against available experimental data and numerical results from other authors; the results from *Gerris* were found to compare favorably. Following the validation, we considered two uncertainty quantifications problems. In the first problem,

the viscosity of the surrounding liquid is modeled as a uniform random variable and we quantify the resultant uncertainty in the bubbles terminal velocity. The second example is similar, except the bubble's size (diameter) is modeled as a log-normal random variable. In this case, the Hermite expansion is seen to converge almost immediately; a first-order Hermite expansion computed using 3 model evaluations is found to capture the terminal velocity distribution almost exactly. Both examples demonstrate that NISP can be successfully used to efficiently propagate uncertainties through CMFD models. Finally, we describe a simple technique to implement a moving reference frame in *Gerris*.

Chapter 4 presents an extensive study of the numerical simulation of capillary slug flow. We review existing correlations for the thickness of the liquid film surrounding a Taylor bubble and the pressure drop across the bubble. Bretherton's lubrication analysis, which yields analytical predictions for these quantities when inertial effects are negligible and $Ca_b \to 0$, is considered in detail. In addition, a review is provided of film thickness correlations that are applicable for high $Ca_b$ or when inertial effects are non-negligible. An extensive computational study was undertaken with *Gerris* to simulate capillary slug flow under a variety of flow conditions; in total, more than two hundred simulations were carried out. The simulations were found to compare favorably with simulations performed previously by other authors using finite elements. The data from our simulations have been used to develop a new correlation for the film thickness and bubble velocity that is generally applicable. While similar in structure to existing film thickness correlations, the present correlation does not require the bubble velocity to be known *a priori*. We conclude with an application of the gPC expansion to quantify the uncertainty in the pressure drop in a channel in slug flow when the bubble size is described by a probability distribution. It is found that, although the gPC expansion fails to adequately quantify the uncertainty in field quantities (pressure and velocity) near the liquid-vapor interface, it is nevertheless capable of representing the uncertainty in other quantities (e.g., channel pressure drop) that do not depend sensitively on the precise location of the interface.

Thesis Supervisor: Jacopo Buongiorno
Title: Associate Professor of Nuclear Science and Engineering, MIT

Thesis Reader: Pierre Lermusiaux
Title: Associate Professor in Ocean Utilization, MIT

## Acknowledgments

Completion of this thesis would not have been possible without the support and encouragement of countless friends and family and the technical guidance from numerous colleagues. My parents, Randy Langewisch and Tawny Gunter, in particular, have been tremendously encouraging throughout this process.

I am indebted to my advisor, Prof. Jacopo Buongiorno, for his thoughtful input, endless encouragement, and his unwavering patience. I would like to thank my reader, Prof. Pierre Lermusiaux, as well as the rest of my committee, Profs. Grétar Tryggvason and Emilio Baglietto, for their invaluable and insightful feedback. I'd like to thank Dr. Marianne François for mentoring me during my summer at LANL. The first three years of this project were funded through a fellowship from Areva, and I am grateful for their support. I am especially thankful to Alex Guion for taking on the microlayer problem, thus providing me the opportunity to pursue my true interest, uncertainty quantification and stochastic modeling. I am grateful for the assistance of several administrative staff, including Clare Egan, Heather Barry, Peter Brenton, Rachel Morton, and Richard St. Clair. Finally, I owe special thanks to several friends and colleagues who have been instrumental in my completion of this thesis: Despoina Chatzikyriakou, Enrique Lizarraga, Gustavo "What can I do for you, today?" Anjos, Koroush Shirvan, Joe Yurko, Joe Fricano, Matt Reinke, Bao Truong, Stefano Passerini, Tim Lucas, Angela Limoncelli, and many others.

THIS PAGE INTENTIONALLY LEFT BLANK

# Contents

THIS PAGE INTENTIONALLY LEFT BLANK

# List of Figures

# List of Tables

THIS PAGE INTENTIONALLY LEFT BLANK

# Acronyms

| | Meaning |
|---|---|
| BWR | boiling water reactor |
| CFD | computational fluid dynamics |
| CMFD | computational multiphase fluid dynamics |
| FEM | finite element method |
| FTT | Fully-Threaded Tree |
| gPC | generalized polynomial chaos |
| KL | Karhunen–Loève |
| KLE | Karhunen–Loève expansion |
| MCS | Monte Carlo simulation |
| ME-gPC | multi-element gPC |
| MRA | multiresolution analysis |
| NISP | non-intrusive stochastic projection |
| PC | polynomial chaos |
| PCE | polynomial chaos expansion |
| PDE | partial differential equation |
| PWR | pressurized water reactor |
| RMS | root mean square |
| RV | random variable |
| SGM | stochastic Galerkin method |
| SPDE | stochastic partial differential equation |

| | **Meaning** |
|---|---|
| TPL | Three-Phase (apparent) contact Line |
| UQ | uncertainty quantification |
| VoF | Volume-of-Fluid |

# Part I

# Microscale Boiling

THIS PAGE INTENTIONALLY LEFT BLANK

# Chapter 1

# Microscale Boiling

## 1.1 Introduction

This chapter considers subcooled nucleate boiling on a local scale, that is, on the scale of single vapor bubble. To simplify matters, we shall presently restrict our considerations to pool boiling, for which there is no superposed flow field. Under these conditions, we must consider three relevant modes of heat transfer: (*i*) conduction through all phases of the fluid as well as the heater surface; (*ii*) liquid-vapor heat exchange due to phase change, including both condensation and evaporation under subcooled boiling conditions; and (*iii*) convective heat transfer from the wall to the liquid induced by bubble motion (growth), a phenomenon referred to as microconvection [e.g., 17, 118].

The analysis of nucleate boiling is complicated by the need to consider phenomena occurring over multiple, disparate length scales, ranging from the macroscopic (typically on the of order of meters for many engineering problems) down to the nanometric. Hence, the relevant length scales span nearly eight orders of magnitude (from ~10 nm to ~1 m). Even for the present case, where the largest length scale is limited to a single bubble ($l \sim 1$ cm), we must contend with phenomena occurring over spatial scales spanning nearly seven orders of magnitude.

During the initial stages of bubble growth, the bubble expands quite rapidly. This rapid growth is driven by a combination of high internal pressure (due to the small radius of curvature, and hence large overpressure within the bubble) and high evaporation rate (the bubble is sufficiently small that it is completely surrounded by superheated liquid). The expansion is limited by the inertia of the liquid surrounding the bubble, and this stage of growth is termed the inertia-controlled growth regime.

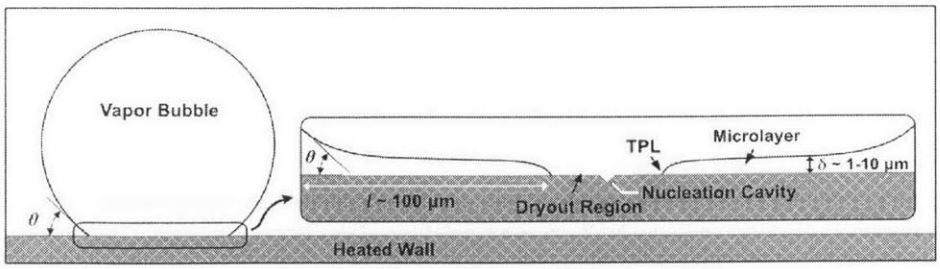


**Figure 1-1:** The microlayer and dryout regions at the base of a bubble growing at a heated wall.

Near the wall, fluid motion is impeded by viscous stresses, and as a consequence, a thin liquid film becomes sandwiched between the bubble and wall. The resulting film is referred to as the microlayer, the existence of which was first confirmed by Cooper and Lloyd [22]. As illustrated in Fig. 1-1, the microlayer initially extends laterally from the root of the bubble (i.e. the location of the nucleation site from which the bubble initiated) up to the macroscopic edge of the bubble. For water at atmospheric pressure, the microlayer can be on the order of hundreds of $\mu$m in length, with a thickness ranging from 1–10 $\mu$m (see Fig. 1-2). Within the microlayer region, high heat fluxes are achievable due to its small thickness, and once established, microlayer evaporation can contribute significantly to bubble growth. Although the importance of microlayer evaporation has been a topic of debate, Kim [69] concluded, based on a literature review, that microlayer evaporation contributes no more than 25% to the overall heat transfer. These conclusions were drawn from a comparison of the approximate mass of vapor generated by microlayer evaporation with the total mass the bubble. On the other hand, Gerardi et al. [39] observed that for steam bubbles microlayer evaporation accounted for most of the bubble growth.

At the boundary between the dryout region and the microlayer (see Fig. 1-1), there is a very short (~1 $\mu$m) transition region, usually referred to as the Three-Phase (apparent) contact Line (TPL), where all three phases (solid, liquid, and vapor) appear to come into contact. The contact between the vapor-liquid interface and the solid is only apparent from a macroscopic perspective; a very thin (~1 nm) film of adsorbed liquid actually separates the vapor from the solid. The adsorbed film is prevented from evaporating by long-range attractive intermolecular forces between the solid and liquid. Nevertheless, due to the exceedingly small thickness of the film in the vicinity of the apparent contact line, heat fluxes far greater than those in the surrounding microlayer are achievable. For this reason, the development of an accurate model for the contact line heat transfer has traditionally been thought a key component to any boiling simulation framework.

Section 1.2 summarizes the most popular models for contact line heat transfer. It is seen that at very high heat fluxes, kinetic effects impose an upper bound on the liquid evaporation rate, thus limiting the maximum achievable heat flux. Consequently, the heat flux near the TPL, while indeed

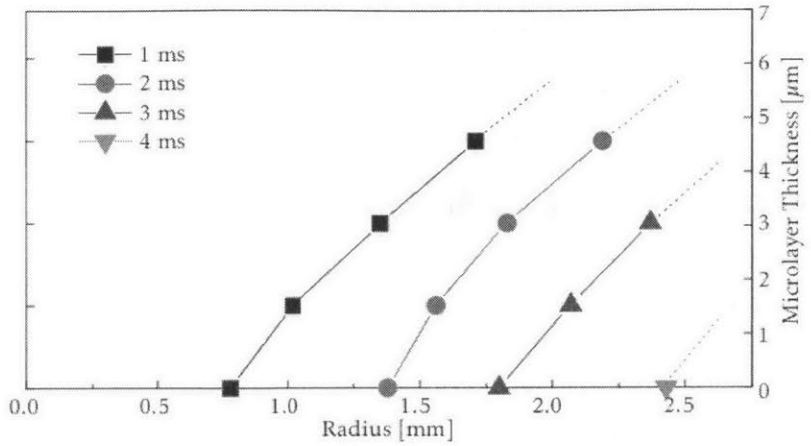


**(a)** Kim and Buongiorno [68, Fig. 12]

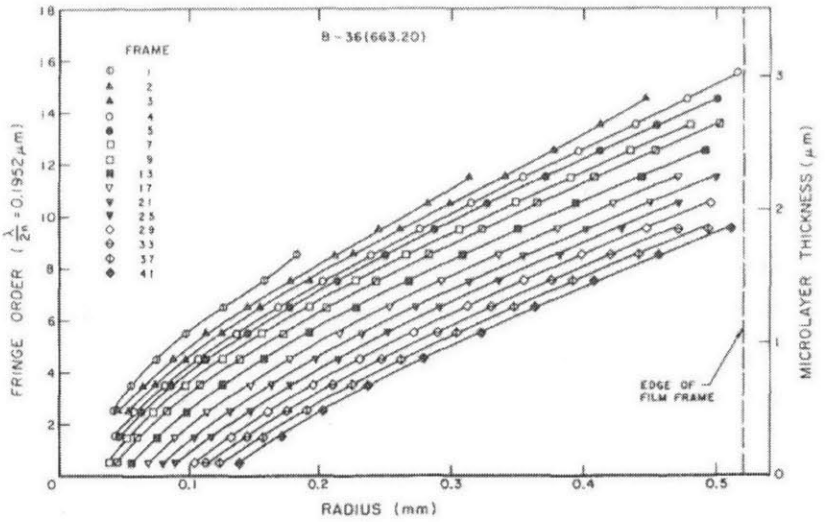


**(b)** Koffman and Plesset [71, Fig. 5]

**Figure 1-2:** Experimentally observed time-evolution of microlayer profiles.

high, is significantly lower than what one might naïvely expect. Moreover, because the TPL is typically only 1–2 $\mu$m in length, its overall contribution to bubble growth is comparatively small [46, 65] in relation to the contribution of the surrounding extended microlayer. Thus, it seems likely that the models described in Sec. 1.2 could be replaced with much simpler and more easily solvable models with minimal loss of accuracy. Finally, it is worth mentioning that many of the so-called "microlayer," "microscale," or "microregion" models that have been previously applied to boiling simulations [e.g., 1, 21, 66, 74, 78, 117] are, in fact, contact line (or TPL) heat transfer models. Despite the rather unfortunate choice of name, these models do not model the boiling microlayer as it is currently understood. The

predicted film thickness profiles are inconsistent with the experimental observations (Fig. 1-2).

## 1.2 Models for contact line heat transfer

Modeling of the flow and heat transfer in the vicinity of the apparent contact line has been an area of active research for several decades now, motivated largely by studies of the heat transfer in microchannels (e.g., microscale heat pipes). Much of the early progress in this area can be credited to Wayner and his colleagues [e.g., 102, 108, 128, 138]. From this work, it was recognized that a capillary meniscus experiences an abrupt transition near the wall where the interface merges smoothly with the adsorbed liquid film. Moosman and Homsy [88] were amongst the first to successfully model this transition region, and the numerous models for the TPL region that have since proliferated can be viewed as extensions of their original model. One of the earliest applications of such a model to the analysis of nucleate boiling was by Stephan and Hammer [121], whose model was based on that developed by Stephan and Busse [122] for modeling heat transfer in grooved heat pipes. Around the same time, Lay and Dhir [78] developed, apparently independently, a nearly identical model to study the heat transfer in vapor stems during fully-developed nucleate boiling; this model has been subsequently used by Dhir and colleagues for several numerical studies of nucleate boiling [1, 91, 92, 117]. More recently, Kern and Stephan [66] extended the earlier model of Stephan and Hammer to be applicable to the study of binary mixtures.

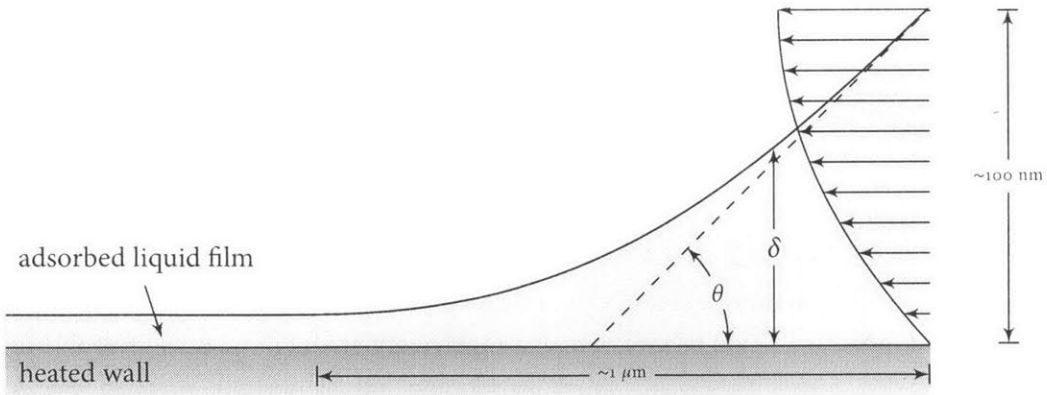


**Figure 1-3:** Schematic of the Three-Phase apparent contact Line (TPL). Note the different length scales in the vertical and horizontal directions.

### 1.2.1 Mass balance

Figure 1-3 provides a schematic of the TPL region, and illustrates that the liquid within the TPL is confined to wedge-shaped domain. Typically, the lateral length scale (order of $1\mu$m or less) is much larger than the maximum film thickness ($\lesssim 100$ nm), so that the slope of this wedge can be considered small. In this case, the Navier-Stokes equations can be reduced via the lubrication approximation [11, §4.8], and a mass balance within the liquid wedge yields,

$$j = \frac{\mathrm{d}}{\mathrm{d}x}\left(\frac{\delta^3}{3\nu_l}\frac{\mathrm{d}P_l}{\mathrm{d}x}\right), \tag{1.1}$$

where $x$ is the spatial coordinate parallel to the wall extending outward from the adsorbed film ($x = 0$), $\delta(x)$ is the film height, $j(x)$ is the mass flux, $P_l(x)$ is the liquid pressure, and $\nu_l$ is the liquid kinematic viscosity. Implicit in (1.1) are the assumptions of no slip at the wall and no shear stress at the liquid-vapor interface. As an additional simplification, we have assumed the flow to be two-dimensional and rectilinear; for an axisymmetric treatment, refer to, e.g., Lay and Dhir [78] and Stephan and Hammer [121]. The assumption of rectilinear flow, however, should be reasonable as the length scale of the TPL is expected to be significantly smaller than the radial location of the apparent contact line (measured from the bubble centerline).

### 1.2.2 Interfacial stress balance

Under most circumstances, the pressure difference $P_v - P_l$ across an interface separating two phases is described by the *Young-Laplace Equation*:

$$P_v - P_l = \sigma\kappa \tag{1.2}$$

where $\sigma$ is the surface tension and the interface curvature $\kappa$ can be expressed in terms of the film heigh $\delta$ as

$$\kappa = \frac{\delta_{xx}}{(1+\delta_x^2)^{3/2}}.$$

For very thin films whose thickness is on the order of nanometers, however, Eq. (1.2) is not directly applicable due to the presence of long-range intermolecular forces between the wall and the liquid. For non-polar liquids, these forces are due mainly to London–van der Waals interactions, whereas for polar liquids, such as water, more complex electrostatic interactions (e.g., electrical double layer formation) must be taken into account [29]. A detailed description of these forces is beyond the current scope; the interested reader is encouraged to consult the reviews by de Gennes [29] and Derjaguin [31], as well as the recent book by Israelachvili [63] for a comprehensive discussion.

Regardless of their particular nature, these forces manifest as an effective additional pressure $\Pi_D$, called the *disjoining pressure*, which gives rise to the so-called *Augmented Young–Laplace Equation* [27, 28, 114],

$$P_v - P_l = \sigma\kappa - \Pi_D. \tag{1.3}$$

Of course, any specific expression for $\Pi_D$ will depend upon the types of intermolecular forces involved. If we assume that London–van der Waals interactions are the dominant contributor, then the disjoining pressure can be expressed as a simple function of the film height (e.g., de Gennes et al. [30, §4], Starov et al. [120, §1.2], and Ajaev [5, §1.7]),

$$\Pi_D = \frac{A_H}{6\pi\delta^3} = \frac{A}{\delta^3}, \tag{1.4}$$

where $A_H = 6\pi A$ is the Hamaker constant and $A$ is called the dispersion coefficient. For a spreading liquid, $A_H < 0$, reflecting the fact that the disjoining pressure acts as a "suction" force that pulls liquid into the film. Strictly speaking, Eq. (1.4) is not applicable for polar liquids, and alternative models have been proposed [e.g., 29, 116]. Nevertheless, Eq. (1.4) seems to provide a reasonable first approximation for the disjoining pressure. Many more details regarding the limitations of this model are given by Truong and Wayner [128].

For modeling phase change, Eq. (1.3) is occasionally augmented with an additional term, called the recoil pressure, that accounts for vapor momentum recoil during evaporation [e.g., 32, 33, 65, 78]. As noted by Christopher and Lu [21], however, the recoil pressure is typically quite small and is negligible in most cases. Consequently, and in the interest of simplifying the presentation, we shall not include this effect in the following.

### 1.2.3 Energy balance

Energy is transferred from the wall to the vapor by a combination of thermal conduction and evaporation. We assume (*i*) that heat is transferred through the liquid solely by conduction; (*ii*) that the temperature distribution in the liquid is linear; and (*iii*) that conduction into the vapor phase is negligible (i.e., all of the heat conducted through the liquid phase contributes to evaporation, and that this energy is transferred to the vapor phase as latent heat). It follows from these assumptions that the heat flux through the liquid is given by

$$q''(x) = h_{fg} j(x) = \frac{k_l (T_w - T_i(x))}{\delta(x)} \tag{1.5}$$

where $k_l$ is the liquid thermal conductivity, $h_{fg}$ is the latent heat, $j(x)$ is the evaporative mass flux, and $T_i(x)$ and $T_w$ are the interface and wall temperatures, respectively (see Fig. 1-4).

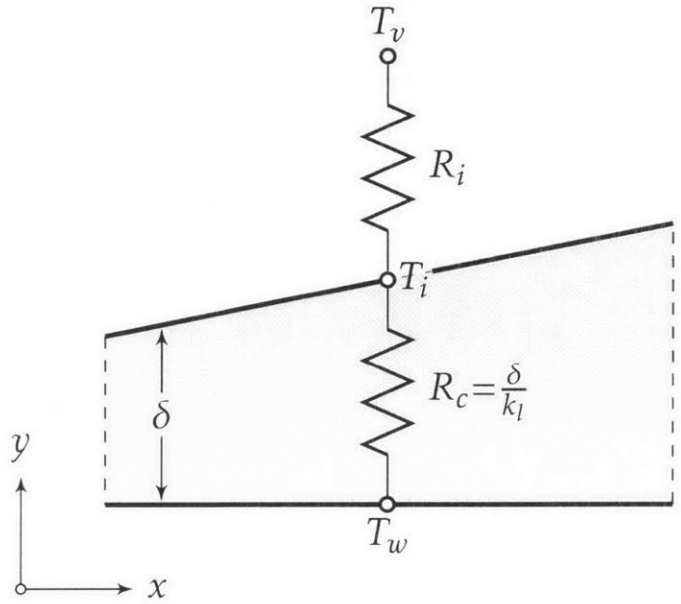


**Figure 1-4:** Thermal resistance diagram for TPL energy balance. $R_c$ denotes conductive resistance and $R_i$ denotes interfacial resistance.

Equation (1.5) is of little use without knowing the interface temperature $T_i(x)$. If we assume $T_i = T_v$, which is often a reasonable, then we should find that for $\delta \sim 1$ nm, Eq. (1.5) predicts heat fluxes greatly exceeding those observed in practice. As it turns out, the assumption $T_i = T_v$ is only applicable at low to moderate heat fluxes, and at higher heat fluxes, kinetic effects place limits on the maximum rate at which mass (hence, heat) can be carried away from the interface. Various models for this "interfacial resistance" are described in detail in Appendix A. One of the simplest and most commonly used models is the Kelvin–Clapeyron Equation (A.14), which we repeat here for convenience:

$$j = a(T_i - T_v) + b(P_l - P_v), \tag{1.6}$$

with the coefficients $a$ and $b$ defined as

$$a \equiv \frac{1}{\sqrt{2\pi R^* T_m}} \left( \frac{2\hat{\sigma}}{2 - \hat{\sigma}} \right) \frac{\rho_v h_{fg}}{T_i} \tag{1.7a}$$

$$b \equiv \frac{1}{\sqrt{2\pi R^* T_m}} \left( \frac{2\hat{\sigma}}{2 - \hat{\sigma}} \right) \frac{\rho_v}{\rho_l} \frac{T_v}{T_i}. \tag{1.7b}$$

Elimination of $T_i(x)$ from Eqs. (1.5) and (1.6) yields

$$j(x) = \frac{a(T_w - T_v) - b(P_v - P_l)}{1 + \left(\frac{ah_{fg}}{k_l}\right)\delta(x)} \tag{1.8}$$

In summary, the TPL film profile and consequent heat transfer are determined as the solutions to Eqs. (1.1), (1.3), and (1.8), which we summarize here:

$$j(x) = \frac{\mathrm{d}}{\mathrm{d}x}\left(\frac{\delta^3}{3\nu_l}\frac{\mathrm{d}P_l}{\mathrm{d}x}\right), \tag{1.9a}$$

$$P_v - P_l(x) = \frac{\sigma\delta_{xx}}{(1+\delta_x^2)^{3/2}} - \frac{A}{\delta^3} \tag{1.9b}$$

$$\left.\begin{aligned} j(x) &= \frac{k_l(T_w - T_i(x))}{h_{fg}\delta(x)} \\ j(x) &= a(T_i(x) - T_v) - b(P_v - P_l(x)) \end{aligned}\right\} \quad j(x) = \frac{a(T_w - T_v) - b(P_v - P_l(x))}{1 + \left(\frac{ah_{fg}}{k_l}\right)\delta(x)} \tag{1.9c}$$

Equations (1.9) comprise a closed system of differential-algebraic equations (DAEs), which can be further manipulated to yield a single $4^{\text{th}}$-order ODE of the form

$$F(\delta, \delta_x, \delta_{xx}, \delta_{xxx}, \delta_{xxxx}) = 0$$

that can be solved for the film thickness $\delta$ when supplemented with appropriate boundary conditions.

### 1.2.4 Scaling analysis and non-dimensionalization

Rather than attempt to solve Eqs. (1.9) as written, it is convenient to first non-dimensionalize the system of equations. Let $\delta_o$ denote the thickness of the adsorbed film. If $\Pi_S$ denotes the pressure difference between the vapor and liquid phases within the adsorbed film, we have from Eq. (1.9b)

$$P_v - P_l = \Pi_S = -\frac{A}{\delta_o^3} \quad \Longrightarrow \quad \delta_o = \left(\frac{|A|}{\Pi_S}\right)^{1/3}, \tag{1.10}$$

where we have dropped the curvature terms because the adsorbed film is flat. Equation (1.10) defines a characteristic length, $\delta_o$, in terms of the as-yet-unspecified characteristic pressure, $\Pi_S$. In addition, let $L_S$ be some characteristic length scale, and define the following dimensionless variables:

$$X \equiv \frac{x}{L_S}, \quad H(X) \equiv \frac{\delta(x)}{\delta_o}, \quad \text{and} \quad \phi(X) \equiv \frac{P_v - P_l(x)}{\Pi_S}.$$

In terms of these variables, Eq. (1.9b) becomes

$$\phi = \left(\frac{\sigma\delta_o}{\Pi_S L_S^2}\right)\frac{H_{XX}}{(1+\lambda^2 H_X^2)^{3/2}} + \frac{1}{H^3}, \tag{1.11}$$

where $\lambda \equiv \frac{\delta_o}{L_S}$ is the ratio of length scales. Setting the dimensionless group on the right-hand side of Eq. (1.11) to unity gives a characteristic length,

$$L_S \equiv \sqrt{\frac{\sigma\delta_o}{\Pi_S}}.$$

Within the adsorbed film, no evaporation occurs ($j = 0$), implying $T_i = T_w$ (*cf.* Eq. (1.5)). It follows from Eq. (1.6) that,

$$P_v - P_l = \frac{a}{b}(T_w - T_v)$$

$$\therefore \quad \Pi_S = \frac{a}{b}\Delta T.$$

Dividing Eq. (1.6) by $a\Delta T = b\Pi_S$ gives

$$\frac{j(x)}{a\Delta T} = \frac{T_i(x) - T_v}{\Delta T} + \frac{P_l(x) - P_v}{\Pi_S},$$

or, equivalently,

$$J(X) = \Theta(X) - \phi(X),$$

where we have defined the dimensionless mass flux and interface temperature as

$$J(X) \equiv \frac{j(x)}{a\Delta T} \quad \text{and} \quad \Theta(X) \equiv \frac{T_i(x) - T_v}{\Delta T}.$$

Using the dimensionless quantities defined above, which we have summarized in Table 1.1,

**Table 1.1:** Definitions of dimensionless quantities and characteristic values

| | | |
|---|---|---|
| Length | $X \equiv \dfrac{x}{L_S}$ | $L_S \equiv \sqrt{\dfrac{\sigma\delta_o}{\Pi_S}}$ |
| Film height | $H(X) \equiv \dfrac{\delta(x)}{\delta_o}$ | $\delta_o \equiv \left(\dfrac{\lvert A\rvert}{\Pi_S}\right)^{1/3}$ |
| Interface temperature | $\Theta(X) \equiv \dfrac{T_i(x) - T_v}{\Delta T}$ | $\Delta T \equiv T_w - T_v$ |
| Pressure jump | $\phi(X) \equiv \dfrac{P_v - P_l(x)}{\Pi_S}$ | $\Pi_S \equiv \dfrac{a}{b}\Delta T$ |
| Mass flux | $J(X) \equiv \dfrac{j(x)}{J_S}$ | $J_S \equiv a\Delta T$ |

Eqs. (1.9) reduce to

$$-\frac{1}{3}\frac{\mathrm{d}}{\mathrm{d}X}\left(H^3\frac{\mathrm{d}\phi}{\mathrm{d}X}\right) = fJ \tag{1.12a}$$

$$\phi = \frac{H_{XX}}{(1+\lambda^2 H_X^2)^{3/2}} + \frac{1}{H^3} \tag{1.12b}$$

$$\left.\begin{aligned} J &= \frac{1-\Theta}{\beta H} \\ J &= \Theta - \phi \end{aligned}\right\} \implies J = \frac{1-\phi}{1+\beta H} \tag{1.12c}$$

where

$$\lambda \equiv \frac{\delta_o}{L_S}, \quad \beta \equiv \frac{\delta_o h_{fg} J_S}{k_l \Delta T}, \quad \text{and} \quad f \equiv \frac{\nu_l L_S^2 J_S}{\delta_o^3 \Pi_S}.$$

The quantity $\beta$ represents the ratio of conductive thermal resistance to the interfacial thermal resistance, i.e.,

$$\beta = \frac{(\delta_o/k_l)}{(\Delta T/h_{fg}J_S)} = \frac{R_c}{R_i},$$

and can therefore be interpreted as a microscale Biot number. Moreover, $f$ provides a measure of the viscous resistance to evaporation (*cf.* Morris [90]); that is, as liquid near the contact line evaporates, additional liquid must be supplied to replenish the film, and $f$ provides a measure of the viscous resistance that this replenishing flow must overcome.

Substituing $J$ from (1.12c) into (1.12a) and rearranging (1.12b) yields a pair of coupled $2^{\text{nd}}$-order ODEs for the dimensionless film thickness and pressure jump,

$$-\frac{1}{3}\frac{\mathrm{d}}{\mathrm{d}X}\left(H^3\frac{\mathrm{d}\phi}{\mathrm{d}X}\right) = f\frac{1-\phi}{1+\beta H}$$

$$H_{XX} = (1+\lambda^2 H_X^2)^{3/2}\left(\phi - \frac{1}{H^3}\right),$$

which can be further reduced to a coupled system of 4 ODEs for $H$, $H_X$, $\phi$, and $\phi_X$. Alternatively, one can eliminate any occurrence of $\phi$ and its derivatives to obtain a single, $4^{\text{th}}$-order ODE in $H$ [e.g., 21, 33, 117, 119, 136].

Regardless the formulation, the choice of appropriate boundary conditions turns out to be non-trivial; the system of equations is very stiff, and solution is highly sensitive to the boundary conditions that one imposes. We take these issues up in the following section.

### 1.2.5 Boundary conditions and solution strategies

As a matter of convenience, let us rearrange the system of equations (1.13) to more standard form,

$$\frac{\mathrm{d}\phi_X}{\mathrm{d}X} = -3\left[\frac{H_X}{H}\phi_X + \frac{f}{H^3}\frac{1-\phi}{1+\beta H}\right]$$

$$\frac{\mathrm{d}H_X}{\mathrm{d}X} = (1+\lambda^2 H_X^2)^{3/2}\left(\phi - \frac{1}{H^3}\right). \tag{1.14a}$$

We seek a solution to (1.14) over a domain $X \in [0, X_\infty]$, where $X = 0$ marks the location where the liquid merges with the adsorbed film, and $X = X_\infty$ marks the end of the TPL transition region, i.e., where the TPL meets the extended microlayer. Assuming $X_\infty$ is specified, Eqs. (1.14) require a total of 4 boundary conditions. Generally, however, $X_\infty$ is not known *a priori* and an additional boundary condition must be imposed. Nevertheless, to simplify the subsequent discussion we shall momentarily assume that $X_\infty$ is given.

Within the adsorbed film, no evaporation occurs, so that $J(0) = 0$. Accordingly (*cf.* (1.12c)),

$$\left.\begin{aligned} 0 = J(0) &= \frac{1-\Theta(0)}{\beta H(0)} \\ 0 = J(0) &= \Theta(0) - \phi(0) \end{aligned}\right\} \Longrightarrow \Theta(0) = \phi(0) = 1.$$

Moreover, $\delta(0) = \delta_o$ so $H(0) = 1$ by construction, and $H_X(0) = H_{XX}(0) = 0$ because the film is flat. From Eq. (1.14a), it is seen that $H_{XX}(0) = 0 \implies \phi(0) = [H(0)]^{-\frac{1}{3}} = 1$.

A seemingly sensible choice for our fourth and final boundary condition would be to impose $H_{XXX}(0) = 0$, or, equivalently, $\phi_X(0) = 0$. The result is the following two equivalent sets of boundary conditions at $X = 0$:

$$H = 1, \quad \frac{dH}{dX} = 0, \quad \frac{d^2H}{dX^2} = 0, \quad \text{and} \quad \frac{d^3H}{dX^3} = 0 \qquad \text{(BC Form 1)}$$

or

$$H = 1, \quad \frac{dH}{dX} = 0, \quad \phi = 1, \quad \text{and} \quad \frac{d\phi}{dX} = 0. \qquad \text{(BC Form 2)}$$

As these four conditions are all applied at $X = 0$, the problem can be formulated as an initial value problem (IVP), and the system can be readily integrated using, e.g., a Runge-Kutta scheme. Unfortunately, such an approach yields only the trivial solution, $H(X) = 1 \; \forall X \in [0, X_\infty]$; this set of initial conditions, which are consistent with the conditions within the adsorbed film, corresponds to a rest point for the system.

To obtain a more meaningful (non-trivial) solution, we can explicitly perturb the solution so that it deviates from the adsorbed film state. This is the approach that has been frequently taken in the literature. For instance, Lay and Dhir [78] impose a nonzero curvature at $X = 0$, Stephan and Hammer [121] impose a nonzero integral heat flow at $X = 0$ (which roughly corresponds to taking $J(0) > 0$ in our formulation), and Wang et al. [136] impose a positive film slope while simultaneously perturbing the initial film thickness ($H(0) = 1 + \epsilon$). While such perturbations are essentially arbitrary, one typically imposes a far-field boundary condition (at $X = X_\infty$) and adjusts the perturbation magnitude so that this condition is satisfied. As an example of such a condition, Stephan and Hammer [121] impose a constant radius of curvature at $X = X_\infty$, and adjust the perturbations at $X = 0$ until this curvature condition is satisfied. In such cases, the problem is no longer an IVP but a boundary value problem (BVP), and the solution strategy just described (iterating on IVPs) is known as a shooting method [see, e.g., 103, §18.1]. For the present problem, however, the shooting IVP is extremely sensitive to the perturbation, which adversely affects convergence of the shooting method. Consequently, it can be extremely difficult to obtain meaningful solutions to Eqs. (1.14), particularly when the perturbations are chosen arbitrarily. We describe later a more consistent manner in which one can choose the perturbations, which partially alleviates this issue.

It was noted above that $X_\infty$ cannot, in general, be specified *a priori*, in which case an additional boundary condition is required. This is typically accomplished by specifying a far-field condition on either the interface slope or curvature, or even by specifying the film height if possible. The imposition of a far-field condition obviates the need to explicitly perturb the solution at $X = 0$, provided, of course, that the far-field condition is not, itself, consistent with the adsorbed film solution; for instance, specification of either $H_X(X_\infty) > 0$ or $H(X_\infty) > 1$ is sufficient to obtain a non-trivial solution, but

specifying $H_{XX}(X_\infty) = 0$ does not suffice since this condition is compatible with a flat film. This observation is significant since the assumption of zero far-field curvature is common, but in itself is insufficient to guarantee a non-trivial result and an additional condition is required. Li and Dhir [83], for example, impose zero far-field curvature in addition to taking $H(X_\infty)$ to be the distance to the nearest grid point to the wall in their macroscopic CFD simulation; the remaining boundary conditions (5 total) are given by $H = 1$ and $H_X = H_{XXX} = 0$ at $X = 0$. The same boundary conditions are used by Son et al. [119], who additionally impose $H_X(X_\infty) = \tan\theta$, where $\theta$ is the apparent contact angle (assumed known) at the end of the TPL region; a total of 6 boundary conditions were needed in this case because the authors treated the dispersion coefficient $A$ as an additional unknown quantity.

Christopher and Lu [21] provide what is arguably the most complete discussion to date on the proper specification of boundary conditions. These authors note that neither Li and Dhir [83] nor Son et al. [119] enforce a zero curvature condition at $X = 0$, and claim that this can significantly affect the computed total heat transfer. The boundary conditions recommended in [21] are

$$H(0) = 1, \quad H_X(0) = H_{XX}(0) = H_{XXX}(0) = 0 \quad \text{and} \quad H_X(X_\infty) = \tan\theta,$$

which requires that the contact angle $\theta$ be known. If one wishes to avoid specifying either $\theta$ or $H(X_\infty)$, then one must perturb the boundary conditions at $X = 0$, as noted earlier. The difficulty with this approach is in choosing which boundary condition(s) to perturb and by how much. Not every perturbation is admissible, and some care is needed to ensure that the perturbed boundary conditions are self-consistent.

One approach to deriving consistent boundary perturbations is to extend the domain over the entire real line ($X \in \mathbb{R}$), and seek solutions $H$ and $\phi$ that asymptotically approach the adsorbed film solution as $X \to -\infty$. Such an approach was taken by DasGupta et al. [28], who obtained the following asymptotic solution for Eqs. (1.14a)

$$\left.\begin{aligned} H &\sim 1 + B_1 \exp\left(\sqrt{3}\gamma X\right) + B_2 \exp\left(\sqrt{3}X\right) \\ \phi &\sim 1 - 3(1-\gamma^2) B_1 \exp\left(\sqrt{3}\gamma X\right) \end{aligned}\right\} \text{ as } X \to -\infty, \tag{1.15}$$

where $\gamma^2 = \frac{f}{1+\beta}$, and $B_1$ and $B_2$ are arbitrary integration constants. A detailed derivation of this result is provided in Appendix B. Note that the solution above is translation-invariant; substituting $X \leftarrow (X - M)$ merely changes the value of the coefficients, $B_1$ and $B_2$. Consequently, taking $M$ to be

suitably large ("computationally infinite"), the limit $X \to -\infty$ can be replace with the limit $X \to 0$, i.e.,

$$\left.\begin{aligned} H &\sim 1 + B_1' \exp(\sqrt{3}\gamma X) + B_2' \exp(\sqrt{3}X) \\ \phi &\sim 1 - 3(1-\gamma^2) B_1' \exp(\sqrt{3}\gamma X) \end{aligned}\right\} \text{ as } X \to 0. \tag{1.16}$$

From (1.16), one readily obtains the following perturbed boundary conditions:

$$\begin{aligned} H(0) &= 1 + B_1' + B_2' & H_X(0) &= \sqrt{3}\gamma B_1' + \sqrt{3} B_2' \\ \phi(0) &= 1 - 3(1-\gamma^2) B_1' & \phi_X(0) &= -3\sqrt{3}\gamma(1-\gamma^2) B_1' \end{aligned} \tag{1.17}$$

The perturbed boundary conditions listed in (1.17) depend only on two degrees of freedom, $B_1'$ and $B_2'$, rather than four, so we have effectively halved the number of "knobs" to turn. Of course, specification of these coefficients is entirely arbitrary. One possible strategy, motivated by the approach of Quach and Ajaev [104], is to set $B_1'$ to some small value (say $B_1' = 10^{-4}$), and choose $B_2'$ so as to satisfy a far-field boundary condition (say $H_{XX}(X_\infty) = 0$); this strategy was used for all subsequent results.

### 1.2.6 Results

We next demonstrate the contact line heat transfer model with some simple text cases. The first considers an evaporating ammonia meniscus subject to a 1 °C superheat. This example is identical to the problem analyzed by Stephan and Busse [122]. Table 1.2 summarizes the relevant fluid properties required for the model; these properties were taken directly from [122]. For this problem, we impose a fixed domain, $X_\infty = 0.5$ $\mu$m. The computed film height and heat flux ($q'' = h_{fg} j$) are shown in Fig. 1-5a, and the results appear to be in good agreement with those of Stephan and Busse (Fig. 1-5b), suggesting we have not made any implementation errors. The maximum heat flux is found to be $q'' = 5260$ W/cm$^2$, compared to 5300 W/cm$^2$ reported in [122].

The results in Fig. 1-5 are characteristic of the heat transfer in the vicinity of the contact line. Moving from right to left ($x \to 0$), the heat flux initially rises steadily as the film becomes thinner in accordance with the conduction equation $q'' = \frac{k_l \Delta T}{\delta}$. Eventually, however, the film grows sufficiently thin that the effect of disjoining pressure starts to dominate, resulting in a rapid suppression of the heat/mass flux. We can gain a better understanding of solution structure by considering the dependence of the dimensionless mass flux $J$ with the film height $H$ illustrated in Fig. 1-6. According

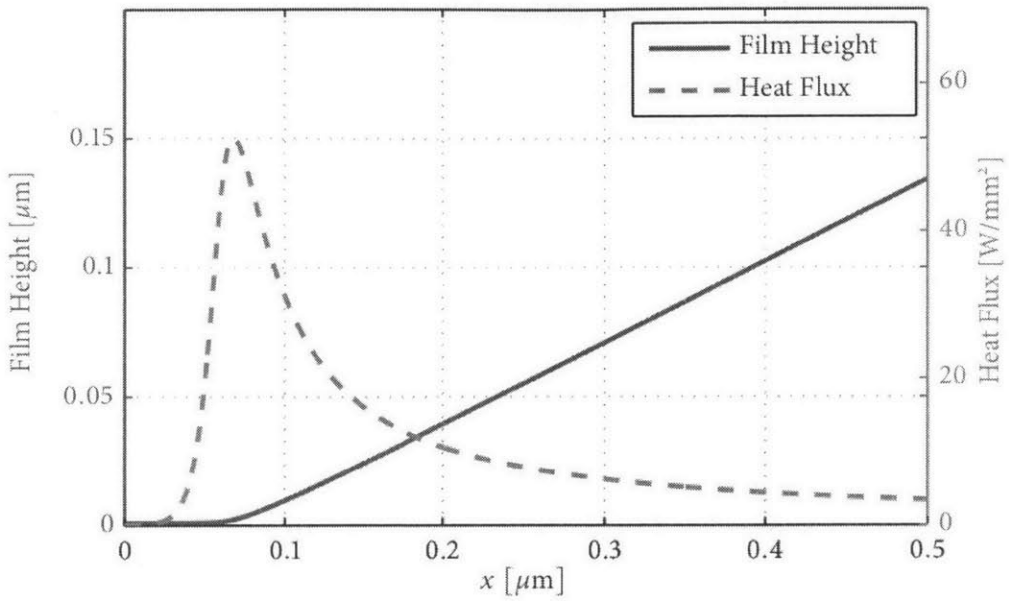


**(a)** Computed heat flux and film thickness for an evaporating ammonia meniscus with $\Delta T = 1\,^{\circ}\mathrm{C}$.

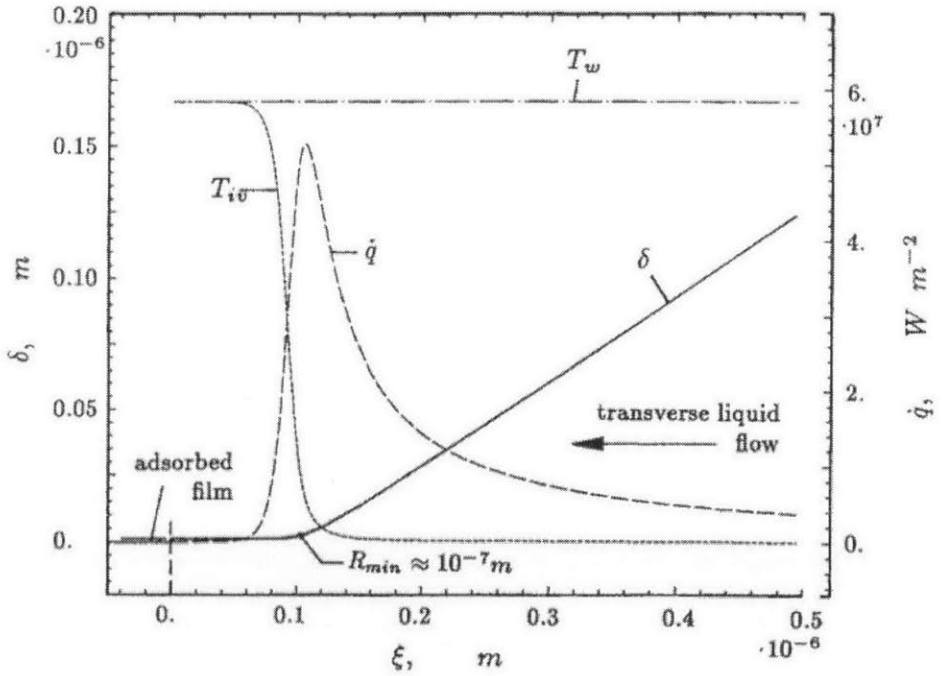


**(b)** Figure 4 from Stephan and Busse [122]

**Figure 1-5:** Comparison of (a) computed heat flux and film thickness with (b) results of Stephan and Busse.

**Table 1.2:** Summary of fluid properties and dimensionless groups for ammonia and water.

| | Ammonia† | | Water | |
|---|---|---|---|---|
| $A$ | $2\times10^{-21}$ | J | $1\times10^{-19}$ | J |
| $\sigma$ | 0.020 | N/m | 0.059 | N/m |
| $T_v$ | 300 | K | 373 | K |
| $h_{fg}$ | 1180.0 | kJ/kg | 2256.5 | kJ/kg |
| $\rho_v$ | 9.0 | kg/m$^3$ | 0.6 | kg/m$^3$ |
| $\rho_l$ | 600 | kg/m$^3$ | 958 | kg/m$^3$ |
| $\nu_l$ | $2.17\times10^{-7}$ | m$^2$/s | $2.94\times10^{-7}$ | m$^2$/s |
| $R^*$ | 488.0 | J/kg-K | 461.5 | J/kg-K |
| $\beta$ | $1.72\times10^{-1}$ | | $3.50\times10^{-2}$ | |
| $f$ | $6.41\times10^{-2}$ | | $3.14\times10^{-4}$ | |

† data from [122]

to (1.12), this dependence is given by

$$J = \frac{1 - K - H^{-3}}{1 + \beta H} \tag{1.18}$$

where

$$K = \frac{H_{XX}}{(1 + \lambda^2 H_X^2)^{3/2}} \tag{1.19}$$

denotes the curvature effects. Letting

$$J_C = \frac{1}{1 + \beta H},$$

denote the mass that would be achieved if only conduction were considered, we can rewrite (1.18) as

$$\frac{J}{J_C} = 1 - K - \frac{1}{H^3}$$

In this form, it is clear that $K$ is a curvature suppression term, while $\frac{1}{H^3}$ is disjoining pressure suppression factor. For $H \gg 1$, $\phi \sim 0$ and $J \sim J_C$. In this regime, effects of disjoining pressure and curvature are negligible; the rate of heat/mass transfer is governed by conduction through the liquid. On the

other hand, as $H \to 1$, assuming negligible curvature,

$$J = J_C \left(1 - \frac{1}{H^3}\right).$$

This effect is clearly illustrated in Fig. 1-6. It turns out that curvature effects are only important in a relatively narrow region, and even then, they are comparatively small, as seen from Fig. 1-7 which plots the curvature suppression factor $K$ defined in (1.19).

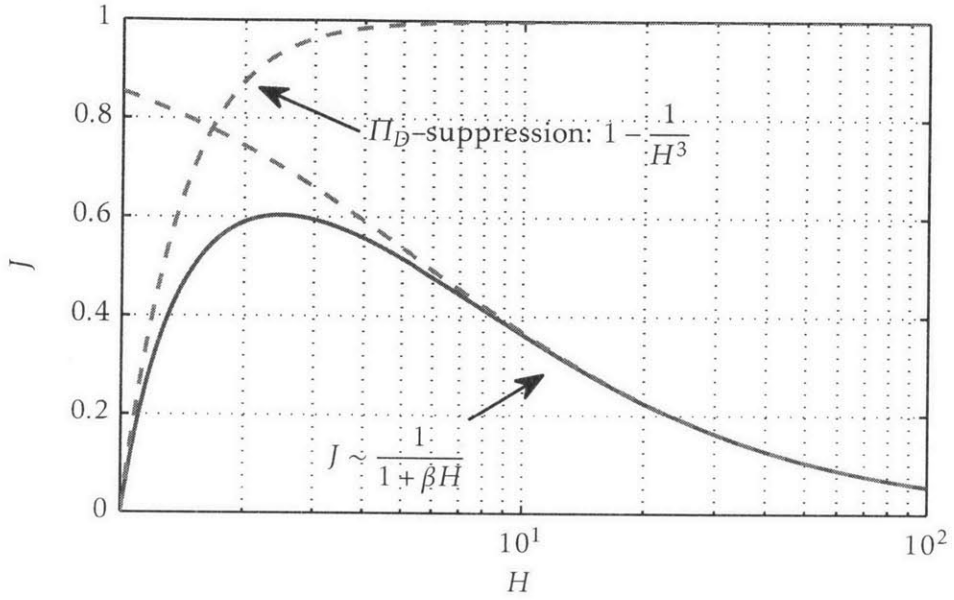


**Figure 1-6:** Dependence of the dimensionless mass flux on film thickness. For $H \gtrsim 7$, the rate of mass transfer is governed by the conduction through the liquid. Disjoining pressure suppression becomes important for $H \approx 1$.

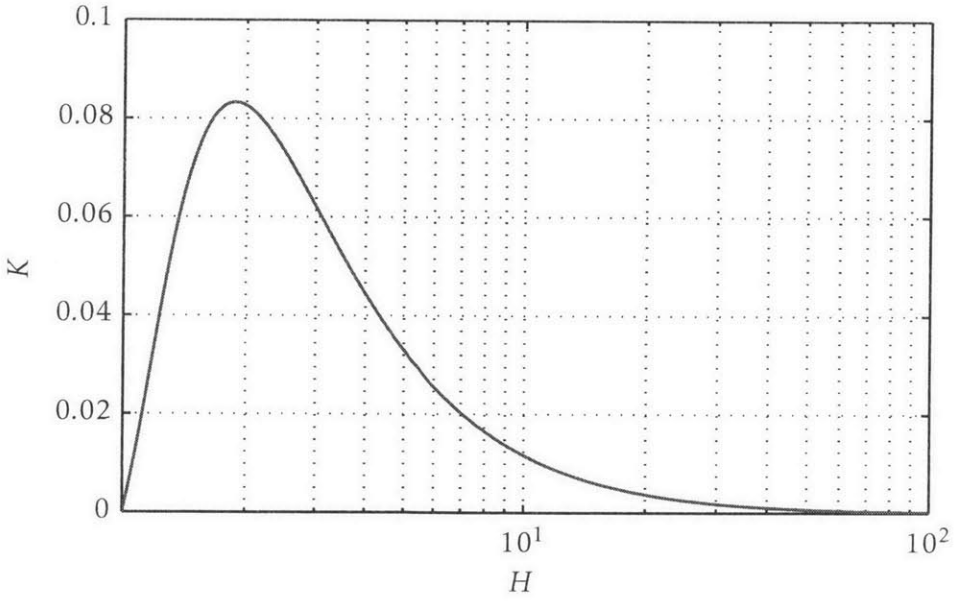


**Figure 1-7:** Contribution of curvature to mass flux suppression. The suppression factor $K$ is defined in Eq. (1.19).

# Part II

# Uncertainty Quantification for Computational Multiphase Fluid Dynamics

THIS PAGE INTENTIONALLY LEFT BLANK

# Chapter 2

# Computational Methods for Uncertainty Quantification

## 2.1 Introduction

The use of numerical simulations as a decision-support tool presently pervades nearly every engineering discipline. As the cost of computational resources continues to drop, engineering design decisions are increasingly being made on the basis of data obtained from computer simulations in lieu of traditional experimental data. In the nuclear power industry, for instance, numerical simulations are essential in performing severe accident analyses as experimental data are frequently unavailable and unobtainable due to cost or safety considerations. Nuclear safety studies are are further complicated by the fact that, in an accident scenario, the state of the plant following an initiating event may not be known with certainty. Depending on the initial conditions provided to the model, different system responses can conceivably be realized, each of which may be classified as either a success or failure. In other words, the uncertainty in the initial conditions to the model induces a corresponding uncertainty in the model output. This problem of propagating uncertainty through a model is representative of one class of problems considered in the study of uncertainty quantification.

Uncertainty quantification (UQ) is an umbrella term referring to any study aimed at the identification, characterization, propagation, analysis, and/or reduction of uncertainties in simulation models [77]. At least three primary sources of uncertainty in numerical simulations can be identified: numerical errors, model discrepancy, and data uncertainty [79, 131]. Each of these sources is

summarized below:

**Numerical Errors:** Numerical errors are defined as any errors introduced by the numerical representation and subsequent solution of a model, and reflect the unfortunate reality that any (numerical) model solved by a computer is necessarily an approximation to some corresponding conceptual (mathematical) model. Such errors are unavoidable owing to the finite memory capacity of computers, which requires that (*i*) all mathematical structures (e.g., functions, vector fields, etc.) be discretely representable in finite terms (*discretization* error) and, at an even lower level, that (*ii*) any numerical quantity be expressible in a finite number of digits (*quantization* error, e.g., round-off).

**Model Discrepancy:** Model discrepancy broadly refers the measured difference between model and reality, and reflects the fact that every (conceptual) model is but an approximate and idealized representation of reality. Such discrepancy may be the result of a poor understanding of the physical phenomena, or perhaps due to the adoption of invalid simplifying assumptions. More detailed descriptions of model discrepancy, as well as a more complete listing of causes, can be found in, e.g., [96, 109]

**Data Uncertainty:** Data uncertainty refers to the uncertainty resulting from one's inability to precisely specify (i.e., with certainty) the problem to be solved. In particular, this includes any uncertainty in inputs to the model, including initial/boundary conditions (e.g., inlet flow velocity, wall temperature, etc.) and model parameters such as material/fluid properties (e.g., density, viscosity, thermal conductivity, etc.).

In the remainder of this thesis, we do not consider numerical error or model discrepancy, focusing instead data uncertainty. From our refined perspective, then, the goal of UQ is to understand and quantify the impact of uncertainties in model data. Whatever the source, an important practical distinction is often drawn between so-called *aleatory* uncertainty and *epistemic* uncertainty—or, to borrow the words of Tony O'Hagan [98], between that which is "unknowable" and that which is "merely unknown to me:"

**Aleatory uncertainty:** From the Latin root *alea*, meaning "die" (as in dice), aleatory uncertainty refers to classical notion of randomness, e.g., the outcome of casting a die or flipping a coin. Such randomness is an inherent property of the model, and is said to be *irreducible* in this context. An alternative term frequently used in reference to aleatory uncertainty is stochastic variability.

**Epistemic uncertainty:** From the Greek root *episteme*, meaning "knowledge," epistemic uncertainty refers to one's degree-of-belief in the truth of a given proposition (e.g., that the sun will rise

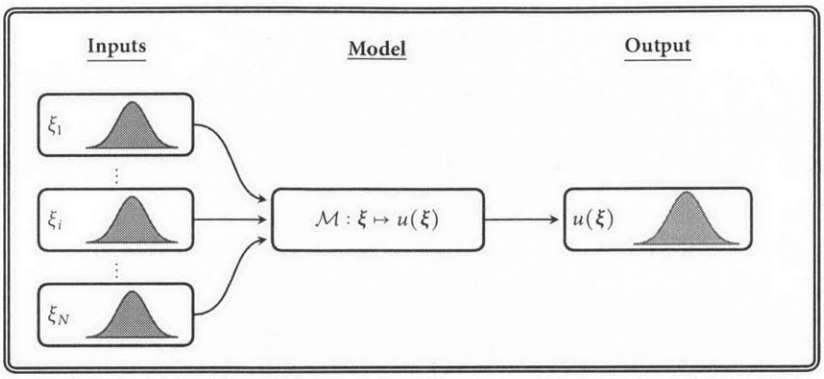


**Figure 2-1:** A generic depiction of the uncertainty propagation problem. The data (input) uncertainties are given as the vector $\boldsymbol{\xi} = (\xi_1, \ldots, \xi_N)$ of random variables. The model is represented abstractly as a mapping $\mathcal{M}: \boldsymbol{\xi} \mapsto u(\boldsymbol{\xi})$.

tomorrow [64, §18.6]). Being the product of one's current state-of-knowledge regarding the world in which he or she lives [8], epistemic uncertainty is *reducible* through the acquisition of more information. Epistemic uncertainty is occasionally referred to as *systematic* uncertainty to distinguish it from the variable (random) nature of aleatory uncertainty.

The final step in characterizing uncertainties is to choose an appropriate mathematical representation. While probability theory is the definitive tool for expressing aleatory uncertainties, whether the same can be said of epistemic uncertainties has been a matter of controversy, particularly amongst adherents to the frequentist interpretation of probability, whose rather restrictive definition of probability is only applicable to infinitely repeatable experiments, having no place for such subjective notions as *knowledge* or *belief*. The result has been the proliferation of various alternative, non-probabilistic representation frameworks, including Dempster-Shafer evidence theory, possibility theory, and fuzzy set theory [52, 54]. We shall not consider such representations here, adopting instead the viewpoint of O'Hagan and Oakley [97] who contend that probability theory (specifically, the Bayesian interpretation) is "uniquely appropriate" for the representation and analysis of *all* uncertainty, epistemic and aleatory alike.

Given the broad scope of uncertainty quantification, as defined above, it should come as no surprise that UQ has found use in a variety of application domains, including design and optimization under uncertainty, risk and reliability assessment, and model validation. A common challenge in all of these applications is the propagation of uncertainty through complex computational models for which a single simulation may require several hours or even days of computing time. A visual depiction of the uncertainty propagation problem is given in Fig. 2-1; in essence, the goal is to push the data uncertainties through the model and subsequently characterize the resulting uncertainty in the

model output, or Quantity of Interest (QoI), denoted $u(\xi)$[†]. Such characterization could involve the calculation of statistical moments or even the estimation of the full probability distribution function for $u$.

Monte Carlo simulation (MCS) has become the *de facto* standard means for performing uncertainty propagation, due to its ease of use and robustness [53]. MCS imposes minimal restrictions on the structural form of input/output mapping, $\xi \mapsto u(\xi)$, and is thus applicable to nearly every problem imaginable. This robustness, however, does not come without cost; MCS converges very slowly. The order of convergence of is $O(N^{-1/2})$, where $N$ is the number of samples (i.e., model evaluations). Consequently, MCS generally requires several thousand (perhaps tens of thousands) evaluations of the model. This poses a prohibitive computational burden in cases for which each simulation requires several hours or days of computing time, as is often the case for multiphase flow simulations. Thus, there exists a clear need for alternative methods capable of performing uncertainty propagation at much lower costs. Recently, UQ methods based on the so-called generalized polynomial chaos (gPC) expansion have garnered considerable attention. These methods seek an approximate representation of the distribution of $u$ in terms of a set of orthogonal basis polynomials. The gPC expansion encodes all of the distributional information of $u$, and once constructed, can be used to efficiently compute any desired statistical quantities from this distribution. Of course, the challenge is to compute this expansion in the first place. For this task, we investigate two approaches—the (intrusive) stochastic Galerkin method and non-intrusive stochastic projection—both of which are discussed in detail in the following sections.

## 2.2 The Karhunen–Loève expansion

A fundamental assumption in the UQ framework just described is that the uncertain inputs to the problem be given as a finite set of random variables (RVs), $\xi = (\xi_1, \ldots, \xi_m)$. It is not uncommon, however, to encounter problems for which one or more inputs is given, not as a random variable, but as a random field. This is almost always the case when considering an uncertain boundary condition or initial condition, but may also arise when considering, e.g., an uncertain thermal conductivity field. In such cases, one must first *parameterize* the random field in terms of a countable set of RVs, $\xi_1, \xi_2, \ldots$, and then *reduce* this set to a finite sub-collection, $\xi_1, \ldots, \xi_m$; in a sense, this process of parameterization is simply the stochastic analog to discretization. An efficient mechanism for performing this task is the Karhunen–Loève (KL) expansion.

In addition, in the following sections, we shall make frequent reference to the space of second-order

[†]Although not explicitly indicated as such, the QoI could be a random field, $u(\mathbf{x}, t; \xi)$.

(finite-variance) RVs on the probability space $(\Theta, \mathcal{F}_\Theta, \mathbb{P})$, which we define as follows:

$$L^2(\Theta,\mathbb{P}) \equiv \left\{ X\colon \Theta \to \mathbb{R} \;\middle|\; \mathbb{E}[X^2(\theta)] \equiv \int_\Theta X^2(\theta)\,\mathrm{d}\mathbb{P}(\theta) < \infty \right\}.$$

Let $\Omega \subset \mathbb{R}^d$ with $d \in \{1,2,3\}$ denote the (spatial) domain of of our problem, and let $\kappa\colon \Omega \times \Theta \to \mathbb{R}$ be a second-order random field (i.e., $\kappa \in L^2(\Omega) \times L^2(\Theta,\mathbb{P})$) with mean $\bar{\kappa}(\mathbf{x}) \equiv \mathbb{E}[\kappa(\mathbf{x};\theta)]$ and covariance kernel $C(\mathbf{x},\mathbf{x}') \equiv \mathrm{cov}\,[\kappa(\mathbf{x};\theta),\kappa(\mathbf{x}';\theta)]$. The Karhunen–Loève expansion of $\kappa(\mathbf{x};\theta)$ is written (e.g., [42, 79, 142])

$$\kappa(\mathbf{x};\theta) = \bar{\kappa}(\mathbf{x}) + \sum_{l=1}^{\infty} \sqrt{\lambda_l}\hat{\kappa}_l(\mathbf{x})\xi_l(\theta), \tag{2.1}$$

where $\lambda_l$ and $\hat{\kappa}_l(\mathbf{x})$ denote, respectively, the ordered (non-increasing) eigenvalues and eigenfunctions of the covariance kernel; i.e., the solutions to the Fredholm equation of the second-kind:

$$\hat{\kappa}_l(\mathbf{x}) = \frac{1}{\lambda_l}\int_\Omega C(\mathbf{x},\mathbf{y})\hat{\kappa}_l(\mathbf{y})\,\mathrm{d}\mathbf{y}, \quad \mathbf{x} \in \Omega. \tag{2.2}$$

The $\xi_l$ in Eq. (2.1) are mutually-uncorrelated, zero-mean RVs with unit variance:

$$\mathbb{E}[\xi_i(\theta)] = 0, \quad \mathbb{E}[\xi_i(\theta)\xi_j(\theta)] = \delta_{ij},$$

and are given by,

$$\xi_l(\theta) = \frac{1}{\sqrt{\lambda_l}}\int_\Omega (\kappa(\mathbf{x};\theta) - \bar{\kappa}(\mathbf{x}))\hat{\kappa}_l(\mathbf{x})\,\mathrm{d}\mathbf{x}. \tag{2.3}$$

Equation (2.1) gives us a countable parameterization of a random field. The next step is to truncate this representation by retaining only the $N_{KL}$ largest (dominant) eigenmodes:

$$\kappa(\mathbf{x};\theta) \approx \bar{\kappa}(\mathbf{x}) + \sum_{l=1}^{N_{KL}} \sqrt{\lambda_l}\hat{\kappa}_l(\mathbf{x})\xi_l(\theta). \tag{2.4}$$

One can show (e.g.., [79, §2.1, 42, §2.3]) that the truncated Karhunen–Loève expansion is *mean square optimal*, meaning that any other finite parameterization of $\kappa(\mathbf{x};\theta)$ in $N_{KL}$ terms will give mean square truncation error at least as large as that of Eq. (2.4). The rate at which the truncation error decays (with increasing $N_{KL}$) depends inversely on the correlation length of the random field, i.e., how fast $C(\mathbf{x},\mathbf{x}+\mathbf{h})$ vanishes as $\|\mathbf{h}\| \to \infty$. The two extreme cases can be summarized as follows [142]:

**Case 1) Fully-correlated:** $C(\mathbf{x},\mathbf{x}') \to 1$

Knowledge of $\kappa(\mathbf{x};\theta)$ at any point $\mathbf{x}$ fully determines $\kappa(\mathbf{x}';\theta)$ at any other point $\mathbf{x}'$. Consequently, $\lambda_l = 0$ for $l > 1$; the random field has only a single degree of freedom.

**Case 2) Vanishing correlation:** $C(\mathbf{x}, \mathbf{x}') \to \delta(\mathbf{x}, \mathbf{x}')$

Knowledge of $\kappa(\mathbf{x}; \theta)$ at any point $\mathbf{x}$ gives no information, whatsoever, about its values at other locations. This is the worst case scenario in which the eigenvalues do not decay ($\lambda_l = 1$ $\forall l$) and no finite expansion can reasonably approximate $\kappa$.

This is yet another manifestation of the (Heisenberg) uncertainty principle.

The Karhunen–Loève expansion says nothing of the distribution of the $\{\xi_l(\theta)\}_{l=1}^{N_{KL}}$ appearing in Eq. (2.4), although their distribution may be inferred from Eq. (2.3). Moreover, while these RVs are guaranteed to be uncorrelated (orthogonal), they will not, in general, be mutually independent RVs. In the special case for which $\kappa(\mathbf{x}; \theta)$ is a Gaussian process, the $\xi_l$ are jointly standard normally distributed, for which uncorrelated implies independent.

### 2.2.1 Demonstration of the Karhunen–Loève expansion

As an illustration of the Karhunen–Loève expansion in action, consider a Gaussian process $\kappa(x; \theta)$ on the unit interval ($x \in [0, 1]$) with constant mean $\bar{\kappa}(x) = 1$ and stationary[‡] exponential covariance kernel,

$$C(x, x') = \sigma_\kappa^2 \exp\left(-\frac{|x - x'|}{L}\right), \tag{2.5}$$

with process variance $\sigma_\kappa^2 = 0.3$ and correlation length $L = 0.3$. The truncated KL expansion (2.4) for $\kappa(x; \theta)$ is then given by

$$\kappa(x; \theta) \approx 1 + \sum_{l=1}^{N_{KL}} \sqrt{\lambda_l}\hat{\kappa}_l(x)\xi_l(\theta),$$

where the $\lambda_l$ and $\hat{\kappa}_l(x)$ satisfy Eq. (2.2). For this particular choice of covariance kernel, Eq. (2.2) admits an analytical solution, the eigenfunctions given by (e.g., [79, p. 22, 142, p. 48][§]):

$$\hat{\kappa}_l(x) = \begin{cases} \dfrac{\cos\left[\omega_l\left(x - \frac{1}{2}\right)\right]}{\sqrt{\frac{1}{2} + \frac{\sin(\omega_l)}{2\omega_l}}} & \text{for } l \text{ odd} \\ \dfrac{\sin\left[\omega_l\left(x - \frac{1}{2}\right)\right]}{\sqrt{\frac{1}{2} - \frac{\sin(\omega_l)}{2\omega_l}}} & \text{for } l \text{ even} \end{cases} \tag{2.6}$$

[‡] A stationary covariance kernel is one such that $C(\mathbf{x}, \mathbf{x}') = \sigma^2\rho(\boldsymbol{\tau})$ where $\boldsymbol{\tau} = \mathbf{x} - \mathbf{x}'$, $\sigma$ is the process variance, and $\rho$ is the correlation function; that is, a stationary covariance kernel is invariant under translations. A random field with constant mean and stationary covariance kernel is said to be *stationary in the wide sense* [3, 20].

[§] The expression given by Le Maître and Knio [79] contains a typographical error; the even and odd eigenfunctions have been swapped.

and the eigenvalues by:

$$\lambda_l = \sigma_\kappa^2 \frac{2L}{1 + L^2\omega_l^2}. \tag{2.7}$$

The coefficients, $\omega_l$, appearing in Eqs. (2.6) and (2.7) are the ordered, positive roots of the characteristic equation:

$$\left[1 - L\omega \tan\left(\tfrac{\omega}{2}\right)\right]\left[L\omega + \tan\left(\tfrac{\omega}{2}\right)\right] = 0. \tag{2.8}$$

Equation (2.8) is solved numerically using, e.g., a bisection method. Figure 2-2a plots the two components of Eq. (2.8) separately, demonstrating that $\omega_l \in [(l-1)\pi,\ l\pi]\ \forall l \in \mathbb{N}$. This domain-partitioning makes solving Eq. (2.8) particularly straightforward while also providing assurance that every root is found in the correct order; every interval $[(l-1)\pi,\ l\pi]$, $l \in \mathbb{N}$, contains exactly one root. Moreover, for $l \gg 1$, $\omega_l \approx (l-1)\pi$, and it follows from Eq. (2.7) that,

$$\lambda_l \approx \sigma_\kappa^2 \frac{2L}{1 + L^2\pi^2(l-1)^2} \sim O(l^{-2}).$$

Figure 2-2b plots the first 100 eigenvalues, and clearly illustrates this asymptotic trend. The first several eigenfunctions are shown in Fig. 2-2c.

Figure 2-3 demonstrates the smoothing effect of truncating the Karhunen–Loève expansion, plotting KL expansions for $N_{KL} = 10$, 20, and 30 for a particular sample of $\kappa(x;\theta)$. Also shown is the "true" sample approximated by taking $N_{KL}$ to be very large ($N_{KL} = 500$ in this case). It is seen that finer scale variability is captured with increasing $N_{KL}$, but most large scale variability is captured with modest $N_{KL}$. Notice, also, that in the limit $N_{KL} \to \infty$, $\kappa(x;\theta)$ appears not to be smooth, exhibiting many small jumps. In fact, $\kappa(x;\theta)$ is not mean square differentiable [105, §4.2], but sample paths (in $x$) are almost surely continuous [3, Example 2.2].

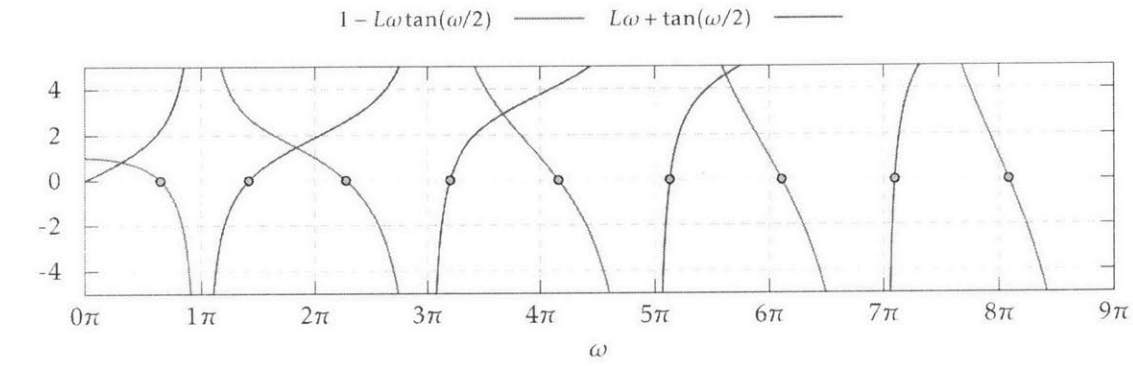


**(a)** Characteristic function and its roots.

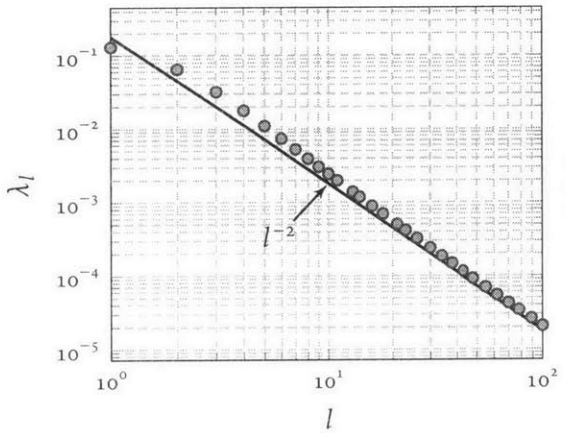


**(b)** Eigenvalues

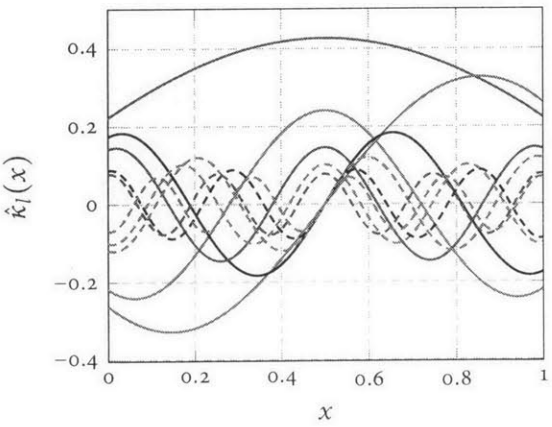


**(c)** Eigenfunctions

**Figure 2-2:** Characteristic roots (a), eigenvalues (b), and eigenfunctions (c) of the exponential covariance kernel

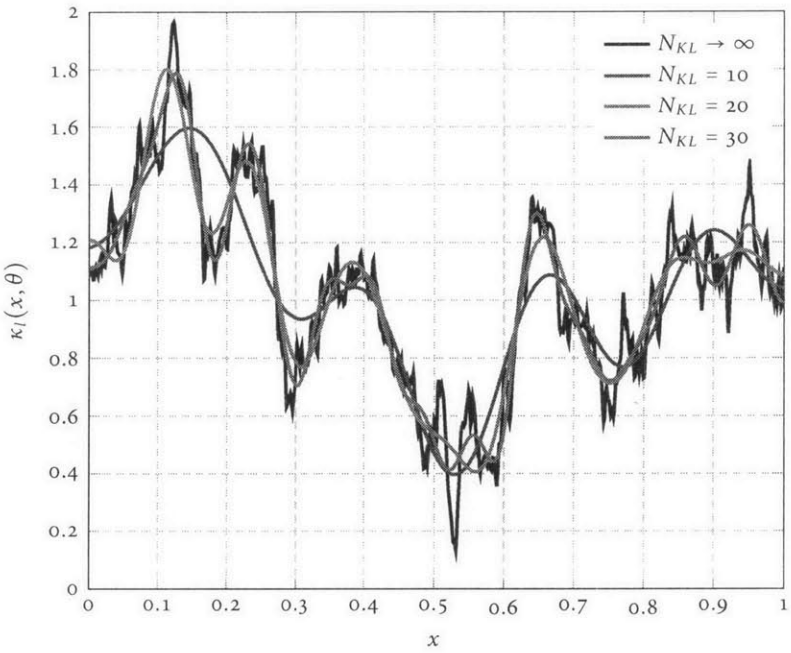


**Figure 2-3:** Comparison of Karhunen–Loève expansions of increasing size ($N_{KL}$) with limiting behavior ($N_{KL} \to \infty$) for a single sample of a Gaussian process with exponential covariance function

## 2.3 The polynomial chaos expansion (PCE)

The polynomial chaos expansion (PCE) is an efficient and convenient tool for representing an arbitrary random variable with finite variance in terms of RVs with known distribution. It is useful to draw the analogy with the familiar Fourier series, which allows one to represent an arbitrary, square-integrable, periodic function as a series of sines and cosines with well-known properties. In the same way, the PCE allows one to express an arbitrary RV as a series of polynomials of RVs with known distribution.

### 2.3.1 The Wiener–Hermite PCE

Let $\{\xi_i(\theta)\}_{i=1}^{\infty}$ be a set of independent standard Gaussian RVs on $(\Theta, \mathcal{F}_\Theta, \mathbb{P})$, and let us introduce the following function(al) spaces:

- $\hat{\Gamma}_p \subset L^2(\Theta, \mathbb{P})$: the space of polynomials in $\{\xi_i\}_{i=1}^{\infty}$ having degree $\leq p$.
- $\tilde{\Gamma}_p \subset \hat{\Gamma}_p$: the orthogonal complement of $\hat{\Gamma}_{p-1}$ in $\hat{\Gamma}_p$; that is,

$$\hat{\Gamma}_p = \tilde{\Gamma}_p \oplus \hat{\Gamma}_{p-1}, \quad \text{with} \quad \tilde{\Gamma}_p \perp \hat{\Gamma}_{p-1}.$$

The space $\tilde{\Gamma}_p$ is called the $p^{\text{th}}$ Homogeneous Chaos [42, 79]. By definition,

$$\hat{\Gamma}_p = \tilde{\Gamma}_p \oplus \hat{\Gamma}_{p-1} = \tilde{\Gamma}_p \oplus (\tilde{\Gamma}_{p-1} \oplus \hat{\Gamma}_{p-2}) = \tilde{\Gamma}_p \oplus \tilde{\Gamma}_{p-1} \oplus \cdots \oplus \tilde{\Gamma}_0$$

$$\therefore \quad \hat{\Gamma}_p = \bigoplus_{i=0}^{p} \tilde{\Gamma}_i,$$

and so,

$$L^2(\Theta, \mathbb{P}) = \lim_{p\to\infty} \hat{\Gamma}_p = \bigoplus_{p=0}^{\infty} \tilde{\Gamma}_p.$$

Consequently, any RV $X \in L^2(\Theta, \mathbb{P})$ can be represented as

$$\begin{aligned} X(\theta) = X_0\Gamma_0 + \sum_{i_1=1}^{\infty} X_{i_1}\Gamma_1(\xi_{i_1}) + \sum_{i_1=1}^{\infty}\sum_{i_2=1}^{i_1} X_{i_1 i_2}\Gamma_2(\xi_{i_1}, \xi_{i_2}) \\ + \sum_{i_1=1}^{\infty}\sum_{i_2=1}^{i_1}\sum_{i_3=1}^{i_2} X_{i_1 i_2 i_3}\Gamma_3(\xi_{i_1}, \xi_{i_2}, \xi_{i_3}) + \cdots \end{aligned} \tag{2.9}$$

where $\Gamma_p \in \tilde{\Gamma}_p$ is the Wiener polynomial chaos (PC) of order $p$ [42, 79, 93]. Through a simple reindexing, Equation (2.9) is usually written more compactly as,

$$X(\theta) = \sum_{k=0}^{\infty} \hat{X}_k \Psi_k(\xi_1, \xi_2, \dots), \tag{2.10}$$

where a one-to-one correspondence exists between the Wiener PC, $\Gamma_m(\xi_{i_1}, \dots, \xi_{i_m})$, in Eq. (2.9) and the functionals, $\Psi_k(\xi_1, \xi_2, \dots)$, in (2.10). By construction, the Wiener PCs satisfy the orthogonality property,

$$\int_\Theta \Psi_i(\xi_1(\theta), \xi_2(\theta), \dots)\Psi_j(\xi_1(\theta), \xi_2(\theta), \dots)\, d\mathbb{P}(\theta) = \mathbb{E}[\Psi_i \Psi_j] = \delta_{ij}\mathbb{E}[\Psi_i^2],$$

from which it follows that the coefficients $\hat{X}_k$ in Eq. (2.10) are given by

$$\hat{X}_k = \frac{\mathbb{E}\big[X(\theta)\Psi_k(\xi_1, \xi_2, \dots)\big]}{\mathbb{E}\big[\Psi_k^2(\xi_1, \xi_2, \dots)\big]}.$$

Furthermore, orthogonality of the Wiener PC (with respect to the Gaussian measure) requires that the $\Psi_k$ (equivalently, $\Gamma_p$) be multivariate Hermite polynomials. For this reason, the expansion given in Eq. (2.10) is often referred to as the Wiener–Hermite PCE to distinguish it from alternative expansions to be discussed below.

### Truncation of the PCE

Notwithstanding the presumed theoretical offerings of the Wiener–Hermite PCE, it is not—at least, not as written in Eq. (2.10)—particularly useful for computational applications due to each $\Psi_k(\xi_1, \xi_2, \dots)$ being an infinite-dimensional polynomial. Consequently, in practice, one considers the (finite) $m$-dimensional PCE,

$$X(\theta) = \sum_{k=0}^{\infty} \hat{X}_k \Psi_k(\boldsymbol{\xi}(\theta)), \quad \boldsymbol{\xi}(\theta) = (\xi_1(\theta), \dots, \xi_m(\theta)) \in \mathbb{R}^m \tag{2.11}$$

for some $m \in \mathbb{N}$. For UQ applications, this restriction is imposed at the outset, following automatically from the finite-dimensional noise assumption (i.e., the assumption that the model depends only a finite set of basic RVs). In other words, this restriction is taken as part of the problem statement, which is to say that, within the scope of the problem statement, Eq. (2.11) is an exact representation of $X(\theta)$. This might be better conveyed by writing $X(\theta) = X(\boldsymbol{\xi}(\theta))$ to explicitly indicate that the uncertainty in $X$ is directly attributable to uncertainty in $\boldsymbol{\xi}$.

The restriction to finite dimension, however, is not sufficient, as we must still contest with an infinite series. So, we are forced to truncate Eq. (2.11) to some order $p \in \mathbb{N}$, and in doing so, we lose the exactness of the expansion and are left with an approximate representation of $X(\theta)$. Returning to the representation given in Eq. (2.9), we find that when restricted to $m$ dimensions and truncated to order $p$, we are left with:

$$\begin{aligned} X(\xi(\theta)) \approx X_0\Gamma_0 + \sum_{i_1=1}^{m} X_{i_1}\Gamma_1(\xi_{i_1}) + \sum_{i_1=1}^{m}\sum_{i_2=1}^{i_1} X_{i_1 i_2}\Gamma_2(\xi_{i_1},\xi_{i_2}) \\ + \cdots + \sum_{i_1=1}^{m}\cdots\sum_{i_p=1}^{i_{p-1}} X_{i_1\ldots i_p}\Gamma_p(\xi_{i_1},\ldots,\xi_{i_p}). \end{aligned} \tag{2.12}$$

A bit of inspection reveals that a total of $\frac{(m+p)!}{m!p!} = \binom{m+p}{m}$ terms appear in Eq. (2.12). Thus, assuming the $\Psi_k$ have been arranged according to increasing polynomial degree, we can write

$$X(\xi(\theta)) \approx \sum_{k=0}^{P} \hat{X}_k \Psi_k(\xi(\theta)), \quad \text{with} \quad P+1 = \binom{m+p}{m},$$

and,

$$\hat{X}_k = \frac{\mathbb{E}[X(\xi)\Psi_k(\xi)]}{\mathbb{E}[\Psi_k^2(\xi)]}.$$

At last, we have something to work with; given a set $\xi(\theta) = (\xi_1(\theta),\ldots,\xi_m(\theta))$ of independent standard Gaussian RVs defined on a probability space, $(\Theta, \mathcal{F}_\Theta, \mathbb{P})$, any $\mathcal{F}$-measurable functional $X : \xi \to \mathbb{R}$ such that $X \in L^2(\Theta,\mathbb{P})$ can be approximated by a series of $m$-dimensional Hermite polynomials in $\xi$ in accordance with Eq. (2.13). This holds even when the distribution of $X$ is unknown (provided $X$ has finite variance). The Wiener–Hermite PCE thus gives us a means to express unknown random variables in terms of known quantities: Hermite polynomials of Gaussian RVs. The obvious question, then, is how many terms (coefficients) must one compute to approximate $X$ to a given level of accuracy? Or, what is the convergence rate ($p$-refinement)? The answer, of course, is that it depends; it depends on how well-behaved is $X(\xi)$, and on the shape of $X(\xi)$ [93]. The closer is $X(\xi)$ to Gaussian, the faster the convergence, with optimal exponential convergence achieved when $X(\xi)$ is distributed according to the same probability law as $\xi$ (i.e., Gaussian) [143]. In fact, if $X \sim \mathcal{N}(\mu,\sigma)$, the Wiener–Hermite PCE of $X(\xi)$ is given by,

$$X(\xi) = \mu\Psi_0(\xi) + \sigma\Psi_1(\xi) = \mu + \sigma\xi.$$

That is, the series terminates after two terms. More generally, when $X(\xi)$ non-Gaussian, the termination of the PCE observed above will not occur.

### Wiener–Hermite PCE of a log-normal RV

To demonstrate this somewhat non-ideal case, consider the log-normally distributed RV $X(\xi) = \exp(\mu + \sigma\xi)$, whose Wiener–Hermite PC expansion $\xi$ is written

$$X(\xi) \approx X^{(P)}(\xi) = \sum_{k=0}^{P} \hat{X}_k \Psi_k(\xi),$$

where

$$\begin{aligned} \hat{X}_k = \frac{\mathbb{E}[X(\xi)\Psi_k(\xi)]}{\mathbb{E}[\Psi_k^2(\xi)]} &= \frac{1}{\sqrt{2\pi}k!} \int_{-\infty}^{\infty} X(\xi)\Psi_k(\xi) \exp\left(-\frac{1}{2}\xi^2\right) \mathrm{d}\xi \\ &= \frac{1}{\sqrt{2\pi}k!} \int_{-\infty}^{\infty} \exp(\mu + \sigma\xi)\Psi_k(\xi) \exp\left(-\frac{1}{2}\xi^2\right) \mathrm{d}\xi \end{aligned} \tag{2.14}$$

For this problem, it is possible to derive analytically an expression for the PCE coefficients. Starting from Eq. (2.14), after a bit of algebra, one obtains

$$\hat{X}_k = \frac{\sigma^k}{k!} \exp\left(\mu + \frac{1}{2}\sigma^2\right).$$

The Wiener–Hermite PCE for a log-normal RV is therefore given by

$$X(\xi) \approx X^{(P)}(\xi) = \exp\left(\mu + \frac{1}{2}\sigma^2\right) \sum_{k=0}^{P} \frac{\sigma^k}{k!} \Psi_k(\xi). \tag{2.15}$$

Figure 2-4a plots the resulting PCE as a function of $\xi$ for increasing order $P$, and illustrates that the polynomial approximants do, in fact, appear to converge to the limiting solution, $\lim_{P\to\infty} X^{(P)} = \exp(\mu + \sigma\xi)$. Figure 2-4b plots the root mean square (RMS) prediction error with increasing $P$, demonstrating the spectral convergence rate of the PCE: RMS Error $\sim O(c^P)$ for some constant $c$. Note that, whereas $X(\xi)$ is almost everywhere nonnegative, i.e., $\mathbb{P}[\{\theta: X(\xi(\theta)) < 0\}] = 0$, $X^{(P)}(\xi)$ can take negative values with nonzero probability, but this probability becomes vanishingly small with increasing $P$. On the other hand, when $X(\xi)$ is markedly non-Gaussian, the convergence rate can be degraded significantly, and this is the motivation for the so-called generalized polynomial chaos (gPC) expansion.

### 2.3.2 The generalized polynomial chaos (gPC) expansion

It was mentioned previously that the convergence of the Wiener–Hermite PCE can be severely deteriorated if $X(\xi)$ is markedly non-Gaussian. For efficiently representing non-Gaussian RVs, Xiu and Karniadakis [143] proposed to extend the Wiener–Hermite PCE by utilizing alternative families of orthogonal polynomials taken from the so-called Askey family of hypergeometric polynomials. The result, which the authors termed the Wiener–Askey PCE, is now known simply as the generalized polynomial chaos (gPC) expansion [144, 145]. The Askey family includes as subsets the the most well-known families of orthogonal polynomials, many of which are orthogonal with respect to various standard probability distributions (see Table 2.1, which summarizes this correspondence).

In the gPC methodology, rather than expand $X$ as a series of Hermite polynomials, which are orthogonal with respect to a Gaussian weight function, one chooses whichever polynomial basis that is orthogonal with respect to the distribution of $X$. This basis is considered the natural basis for representing $X$, and yields the optimal convergence rate of any orthogonal polynomial basis [143].

**Table 2.1:** Correspondence between standard probability distributions and gPC basis polynomials[†]

| Distribution | Polynomial Basis | Support |
|---|---|---|
| Gaussian | Hermite | $(-\infty, \infty)$ |
| Uniform | Legendre | $[a, b]$ |
| Beta | Jacobi | $[a, b]$ |
| Gamma | Laguerre | $[0, \infty)$ |

[†] Adapted from [40]

Of course, there is really no reason to stop there; one could forego the requirement that the basis functions be polynomials altogether and consider more general, orthogonal bases. One glaring weakness of gPC expansions is that, due to their reliance on globally-defined polynomial basis functions, they will suffer from very poor convergence when the RV being approximated exhibits strongly non-polynomial behavior—such as when $X$ depends discontinuously on $\xi$. This has motivated the development of several methods that utilize localized basis functions, one of the earliest being due to Le Maître et al. [80] who used the system of Haar wavelets as a basis, resulting in the Wiener–Haar expansion (see also, [79, §8]). Subsequently, Le Maître et al. [81] extended this method by introducing a multiresolution analysis (MRA) based on the Multiwavelet construction of Alpert [6]. In a similar vein, Wan and Karniadakis [134] introduced the multi-element gPC (ME-gPC), in which the stochastic input domain $\Xi$ is partitioned into a collection of disjoint "elements" with a gPC expansion constructed on the individual elements; through careful selection of the partitions, ME-gPC can adequately cope with discontinuities, and can also be used to represent RVs with arbitrary probability distributions [133,

135].

In any case, the resulting mathematical formulation is unchanged from that of the Wiener–Hermite PCE; that is, we express $X(\theta) = X(\xi(\theta))$ as a series of the form

$$X(\xi) = \sum_{k=0}^{P} \hat{X}_k \Psi_k(\xi), \qquad \hat{X}_k = \frac{\mathbb{E}[X(\xi)\Psi_k(\xi)]}{\mathbb{E}[\Psi_k^2(\xi)]}, \tag{2.16}$$

recognizing that the $\Psi_k$ need not be limited to multivariate Hermite polynomials. In the following, the term "PCE" will be understood to refer to any stochastic expansion of the form (2.16), regardless whether the underlying basis functions are actually polynomials.

It should be noted that the PCE need not be limited to the representation of random variables; the extension to second-order random fields $u: \Omega \times \mathcal{T} \times \Theta \to \mathbb{R}$ is immediately obtained by allowing the PC coefficients to depend on the index $(\mathbf{x}, t) \in \Omega \times \mathcal{T}$. That is, at a given location $\mathbf{x} \in \Omega$ and time $t \in \mathcal{T} \subseteq \mathbb{R}$, the random variable given by the mapping $\theta \mapsto u(\mathbf{x}, t; \theta)$ can be approximated by

$$u(\mathbf{x}, t; \theta) = u(\mathbf{x}, t; \xi(\theta)) \approx \sum_{k=0}^{P} \hat{u}_k(\mathbf{x}, t)\Psi_k(\xi(\theta)), \tag{2.17}$$

where, as before, the PC coefficients (modes) are given by

$$\hat{u}_k(\mathbf{x}, t) = \frac{\mathbb{E}[u(\mathbf{x}, t; \xi)\Psi_k(\xi)]}{\mathbb{E}[\Psi_k^2(\xi)]}. \tag{2.18}$$

In the following, an alternative notation will occasionally prove useful. Expressing the PC basis $\Psi_k(\xi)$ functions as products of univariate polynomials,

$$\Psi_k(\xi) = \psi_{k_1}(\xi_1)\cdots\psi_{k_m}(\xi_m),$$

we can alternatively write this as $\Psi_{\underline{k}}(\xi)$, where $\underline{k} = (k_1, \ldots, k_m)$ is a multi-index. In this notation, Eq. (2.17) can be written

$$u(\mathbf{x}, t; \xi) \approx \sum_{\underline{k} \in \mathcal{K}} \hat{u}_{\underline{k}}(\mathbf{x}, t)\Psi_{\underline{k}}(\xi), \quad \mathcal{K} \equiv \{\underline{k} = (k_1, \ldots, k_m) \mid |\underline{k}| \leq p\}$$

where $|\underline{k}| = \|\underline{k}\|_\infty = \max(k_1, \ldots, k_m)$.

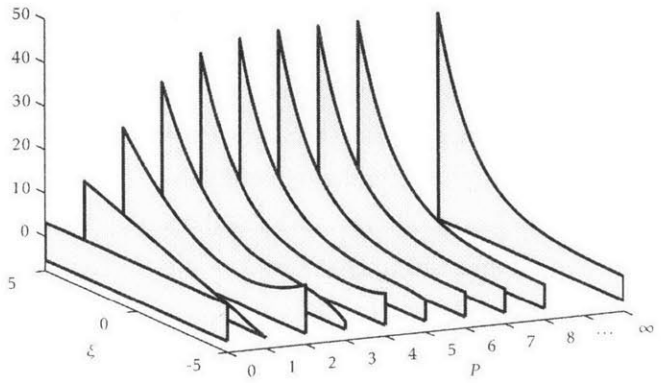


**(a)** Illustrations of successive Wiener–Hermite PC approximations, $\{X^{(0)}, X^{(1)}, \ldots\}$ ($\mu = 1$, $\sigma^2 = 0.3$).

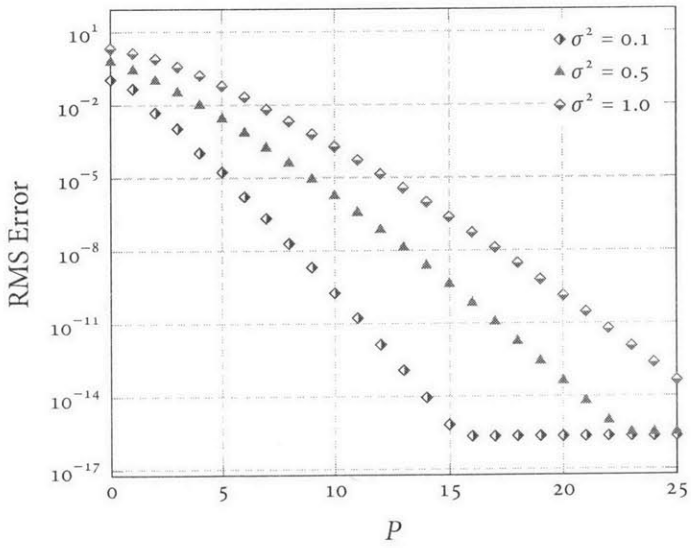


**(b)** RMS convergence for $\sigma^2 = 0.1$, 0.5, and 1.0; in all cases, a (fast) spectral convergence rate is achieved, but the convergence is visibly degraded as $\sigma^2$ is increased.

**Figure 2-4:** Convergence of Wiener–Hermite PCE of a log-normal RV

## 2.4 Uncertainty quantification using gPC expansions

Having introduced various formulations of the generalized polynomial chaos (gPC) expansion in Sec. 2.3, we are ready to proceed to the problem of uncertainty propagation. Given a model $\mathcal{M}: \boldsymbol{\xi} \mapsto u(\mathbf{x}, t; \boldsymbol{\xi})$, where $\boldsymbol{\xi} = (\xi_1, \ldots, \xi_N) \in \Xi$ denotes the set of uncertain inputs, we wish to quantify the resultant output uncertainty; that is, we wish to ascertain the distribution for the mapping $\boldsymbol{\xi} \mapsto u(\mathbf{x}, t; \boldsymbol{\xi})$. Expressing $u(\mathbf{x}, t; \boldsymbol{\xi})$ as a PCE with respect to the input RVs $\boldsymbol{\xi}$, our problem can be formulated as one of computing the PC modes given in Eq. (2.18). Thus, provided we can somehow compute the coefficients, $\hat{u}_k(\mathbf{x}, t)$, we can approximate the full distribution of $u(\mathbf{x}, t; \boldsymbol{\xi})$ via Eq. (2.17).

Methods for estimating the PC coefficients can be broadly classified as being either *intrusive* or *non-intrusive*. In the former, intrusive approach, the original model equations are recast to solve directly for the coefficients $\hat{u}_k$; this is accomplished by implementing a Galerkin projection of the model equations onto the stochastic subspace, $\mathcal{S}^P \equiv \text{span}\{\Psi_k(\boldsymbol{\xi})\}_{k=0}^P$, resulting in what is commonly referred to as the stochastic Galerkin method (SGM) [79]. In the alternative approach, the coefficients are computed numerically using quadrature methods. This method, known as non-intrusive stochastic projection (NISP), requires no modifications be made to the deterministic solver, relying instead on "observations" or "samples" of the solution for specific input configurations. Sections 2.4.1 and 2.4.2 describe the SGM and NISP methodologies, respectively, and present example applications of each.

### 2.4.1 Stochastic Galerkin Method

The stochastic Galerkin method (SGM) is an intrusive approach to quantifying uncertainty; as such, it requires access to the internals of computational model (the box must be opened). The original model equations are reformulated such that the revised model directly computes the set of stochastic modes, $\{\hat{u}_k(\mathbf{x}, t)\}_{k=0}^P$, appearing in the gPC expansion of the solution $u(\mathbf{x}, t)$. This reformulation is accomplished by first expressing all uncertain quantities as gPC expansions and then projecting (via Galerkin projection) the governing equations onto the space $\mathcal{S}^P \equiv \text{span}\{\Psi_k(\boldsymbol{\xi})\}_{k=0}^P$. Suppose that the model is given by

$$\mathcal{A}[u(\mathbf{x}, t; \boldsymbol{\xi}); \boldsymbol{\xi}] = b(\mathbf{x}, t; \boldsymbol{\xi}), \tag{2.19}$$

where $\boldsymbol{\xi}$ is a vector of random inputs to the problem; $\mathcal{A}$ is some (possibly nonlinear) differential operator which, in general, depends on $\boldsymbol{\xi}$; $b$ is a given (source) function; and $u$ is the sought solution. Approximating both $u$ and $b$ in terms of a gPC expansion,

$$u(\mathbf{x}, t; \boldsymbol{\xi}) \approx \sum_{i=0}^{P} \hat{u}_i(\mathbf{x}, t) \Psi_i(\boldsymbol{\xi})$$

and

$$b(\mathbf{x}, t; \xi) \approx \sum_{i=0}^{P} \hat{b}_i(\mathbf{x}, t)\Psi_i(\xi),$$

Equation (2.19) becomes

$$\mathcal{A}\left[\sum_{i=0}^{P} \hat{u}_i(\mathbf{x}, t)\Psi_i(\xi); \xi\right] = \sum_{i=0}^{P} \hat{b}_i(\mathbf{x}, t)\Psi_i(\xi). \tag{2.20}$$

Equation (2.20) is then projected onto the space $\mathcal{S}^P = \text{span}\{\Psi_k(\xi)\}_{k=0}^{P}$. This is accomplished by multiplying Eq. (2.20) by $\Psi_k(\xi)$ and then applying the expectation operator, which gives

$$\mathbb{E}\left[\mathcal{A}\left[\sum_{i=0}^{P} \hat{u}_i(\mathbf{x}, t)\Psi_i(\xi); \xi\right]\Psi_k(\xi)\right] = \hat{b}_k(\mathbf{x}, t)\,\mathbb{E}[\Psi_k^2(\xi)], \qquad k = 0, \ldots, P. \tag{2.21}$$

Note that each of the $P+1$ equations in (2.21) is deterministic; the stochasticity (i.e., the $\xi$-dependence) has been absorbed by taking the expectation. For the sake of clarity, let us assume the operator $\mathcal{A}$ is linear, in which case (2.21) simplifies to

$$\mathbb{E}\left[\sum_{i=0}^{P} \mathcal{A}[\hat{u}_i(\mathbf{x}, t); \xi]\Psi_i\Psi_k\right] = \mathbb{E}[\Psi_k^2]\hat{b}_k(\mathbf{x}, t). \tag{2.22}$$

After expressing $\mathcal{A}$ as a gPC expansion,

$$\mathcal{A}[\hat{u}_i(\mathbf{x}, t); \xi] = \sum_{j=0}^{P} \hat{\mathcal{A}}_j[\hat{u}_i(\mathbf{x}, t)]\Psi_j(\xi),$$

Eq. (2.22) can be written as

$$\sum_{i=0}^{P}\sum_{j=0}^{P} \hat{\mathcal{A}}_j \hat{u}_i(\mathbf{x}, t)\,\mathbb{E}\big[\Psi_i\Psi_j\Psi_k\big] = \mathbb{E}\big[\Psi_k^2\big]\hat{b}_k(\mathbf{x}, t), \qquad k = 0, \ldots, P,$$

or, more succinctly,

$$\sum_{i=0}^{P}\sum_{j=0}^{P} C_{ijk}\hat{\mathcal{A}}_j \hat{u}_i(\mathbf{x}, t) = \hat{b}_k(\mathbf{x}, t), \qquad k = 0, \ldots, P, \tag{2.23}$$

where the *multiplication tensor*, $C_{ijk}$, is defined as

$$C_{ijk} \equiv \frac{\mathbb{E}[\Psi_i\Psi_j\Psi_k]}{\mathbb{E}[\Psi_k^2]}.$$

Although $C_{ijk}$ contains $(P+1)^3$ elements, which could be very large, it is symmetric in the $i$ and $j$ indices so only half as many elements need actually be stored. In fact, $C_{ijk}$ is quite sparse owing to the orthogonality of the PC basis functions, so storage is not generally an issue. Moreover, $C_{ijk}$ is depends only on the basis functions, and not on the specifics of the model under study, and can therefore be precomputed and tabulated prior to running any simulation.

In Eq. (2.23), each $\mathcal{A}_j\hat{u}_i = \hat{b}_k$ represents a deterministic PDE (or system of PDEs), all of which are coupled through the multiplication tensor, $C_{ijk}$. In particular, defining

$$\mathcal{A}_{ki} \equiv \sum_{j=0}^{P} C_{ijk}\hat{\mathcal{A}}_j,$$

we can write Eq. (2.23) in matrix form,

$$\begin{bmatrix} \mathcal{A}_{00} & \cdots & \mathcal{A}_{0P} \\ \vdots & \ddots & \vdots \\ \mathcal{A}_{P0} & \cdots & \mathcal{A}_{PP} \end{bmatrix} \begin{pmatrix} \hat{u}_0 \\ \vdots \\ \hat{u}_P \end{pmatrix} = \begin{pmatrix} \hat{b}_0 \\ \vdots \\ \hat{b}_P \end{pmatrix} \tag{2.24}$$

Furthermore, each $\mathcal{A}_{ki}$ appearing in the above matrix is, itself, an operator that will give rise to a matrix when the problem is spatially discretized. In other words, discretization of Eq. (2.24) yields a block-linear system,

$$\begin{bmatrix} \hat{\mathbf{A}}_{00} & \cdots & \hat{\mathbf{A}}_{0P} \\ \vdots & \ddots & \vdots \\ \hat{\mathbf{A}}_{P0} & \cdots & \hat{\mathbf{A}}_{PP} \end{bmatrix} \begin{pmatrix} \hat{\mathbf{u}}_0 \\ \vdots \\ \hat{\mathbf{u}}_P \end{pmatrix} = \begin{pmatrix} \hat{\mathbf{b}}_0 \\ \vdots \\ \hat{\mathbf{b}}_P \end{pmatrix}. \tag{2.25}$$

The system of equations in Eq. (2.25) need only be solved once for the discretized stochastic modes, $\{\hat{\mathbf{u}}_i\}_{i=0}^{P}$; any subsequent probabilistic information is obtainable from the PCE once these modes have been computed. Consequently, there is no need for repeated runs of the code (i.e., sampling). On the other hand, the system of equations is larger by a factor of $P+1$ than the corresponding deterministic system, which can be problematic when $\dim(\boldsymbol{\xi})$, and therefore $P$, is large. Of course, the additional effort needed to solve Eq. (2.25) is highly dependent on the degree of coupling between the modes, i.e., on how many of the $\hat{\mathbf{A}}_{ki}$ (equivalently, $\mathcal{A}_k i$) are actually nonzero. Figure 2-5 illustrates the block-sparsity pattern for a Wiener–Hermite PCE of the stochastic diffusion operator (see the following example applications) for PC order $p \in \{3,4,5\}$ and stochastic dimension $\dim(\boldsymbol{\xi}) \in \{6,8,10\}$. Terminology aside, it is evident from Fig. 2-5 that the block structure is not necessarily sparse, particularly when $p$ is large. Nevertheless, each $\hat{\mathbf{A}}_{ki}$ generally *is* sparse, so the full system matrix in Eq. (2.25) can perhaps be regarded as sparse—that is, if one considers a dense matrix of sparse matrices to be sparse.

### Examples

We next demonstrate the use of SGM with two example applications, both of which consider different forms of the diffusion equation with an uncertain diffusivity field. The first example considers the 1D steady-state diffusion equation, while the second example considers the 2D transient diffusion equation. Depending on the context, the diffusion equation can have different physical interpretations, e.g.:

| **Heat Equation** | **Mass Diffusion Equation** |
|---|---|
| $u$ = temperature | $u$ = concentration |
| $\kappa$ = thermal conductivity | $\kappa$ = mass diffusivity |
| $F$ = volumetric heat generation rate | $F$ = mass source/sink due to chemical reactions |

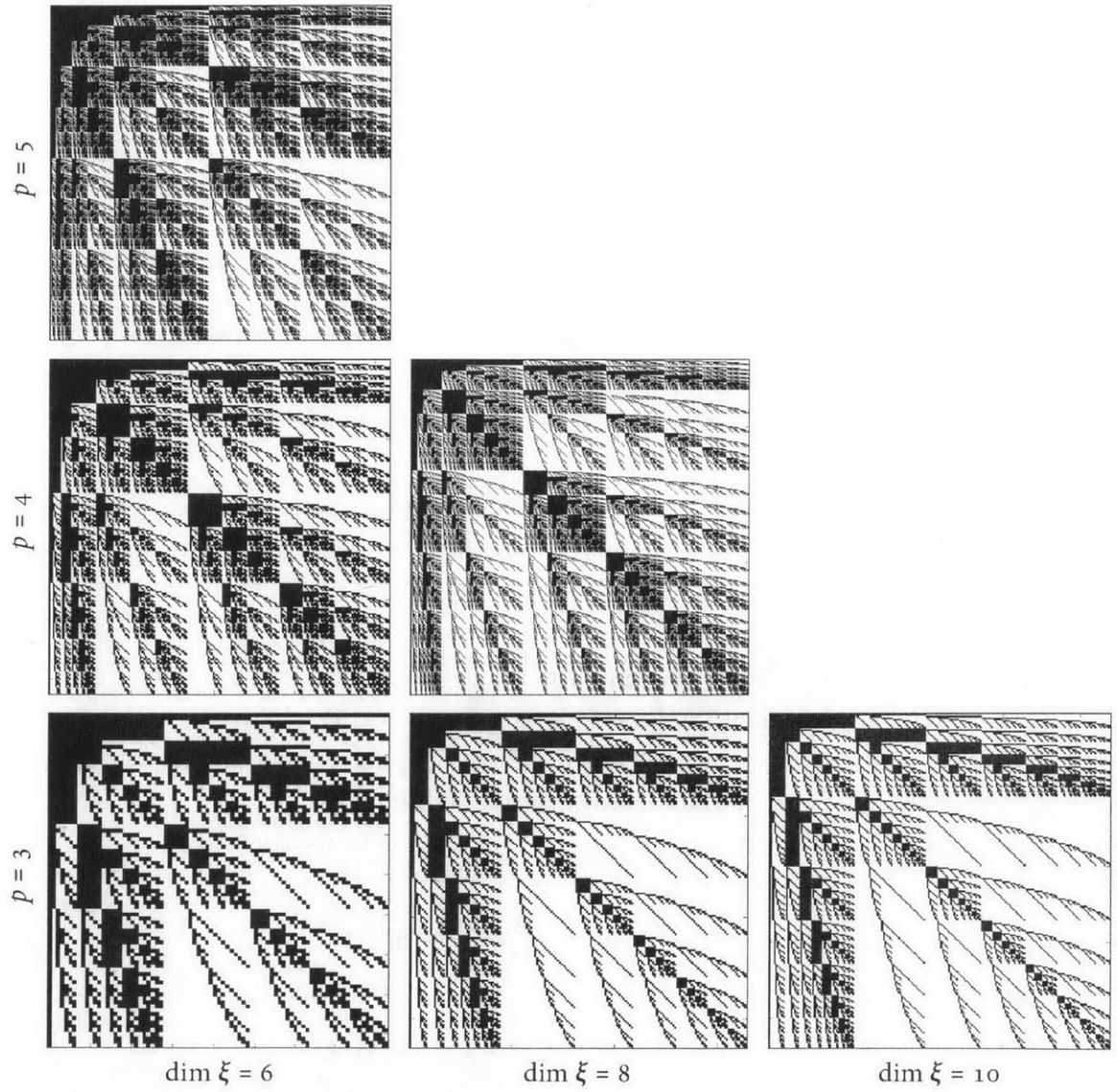


**Figure 2-5:** Block-sparsity structure for a Wiener–Hermite PCE of the stochastic diffusion operator vs. PCE order ($p$) and stochastic dimension. Each point (▪) denotes a matrix corresponding to $\hat{\mathbf{A}}_{ki}$ in Eq. (2.25).

**SGM Example 1: Steady Stochastic Diffusion Equation in 1D**

For our first demonstration, we consider the 1D steady diffusion equation,

$$-\frac{\partial}{\partial x}\left(\kappa(x;\theta)\frac{\partial u}{\partial x}\right) = 5, \quad x \in (0,1),\ \theta \in \Theta$$

with boundary conditions

$$\left.\begin{aligned} \kappa\frac{\partial u}{\partial x} &= 1 \quad \text{at } x = 0 \\ u &= 1 \quad \text{at } x = 1 \end{aligned}\right\}$$

We assume that the diffusivity (or conductivity), $\kappa(x;\theta)$, is a log-normally distributed random field such that $Y(x;\theta) \equiv \ln\kappa(x;\theta)$ is a unit mean Gaussian process with exponential covariance function (*cf.*Eq. (2.5) on page 28); as before in Sec. 2.2, we impose a correlation length $L = 0.3$ and process variance $\sigma_Y^2 = 0.3$.

Given that $\kappa(x;\theta)$ is uncertain, the solution $u = u(x;\theta)$ will likewise be uncertain, and our goal is to quantify this uncertainty, i.e., to determine the probability distribution of $u$. Our plan of attack can be summarized as follows:

1. Parameterize $\kappa(x;\theta)$ in terms of a finite set of random variables $\xi = (\xi_1,\ldots,\xi_m)$ using the Karhunen–Loève expansion. Thus $\kappa(x;\theta) \to \kappa(x;\xi)$ and $u(x;\theta) \to u(x;\xi)$.
2. Given $\xi$, identify the corresponding gPC basis $\{\Psi_k(\xi)\}_{k\in\mathbb{N}_0}$ and choose an appropriate subspace $\mathcal{S}^P = \text{span}\{\Psi_k(\xi)\}_{k=0}^P$ in which to approximate the problem.
3. Use the gPC expansion to express all uncertain quantities in terms of this basis, i.e.,

$$\kappa(x;\xi) \approx \kappa^{(P)}(x;\xi) = \sum_{k=0}^{P} \hat{\kappa}_k(x)\Psi_k(\xi) \tag{2.27}$$

and

$$u(x;\xi) \approx u^{(P)}(x;\xi) = \sum_{k=0}^{P} \hat{u}_k(x)\Psi_k(\xi) \tag{2.28}$$

4. Finally, project the governing equations (2.26) onto the subspace $\text{span}\{\Psi_k(\xi)\}_{k=0}^P$ using a Galerkin projection, and solve the resulting system of equations.

For item 1, since $Y(x;\theta) \equiv \ln\kappa(x;\theta)$ is a Gaussian process with exponential covariance function, so we can use the results from Sec. 2.2, substituting $Y$ for $\kappa$ where appropriate. The $m$-term Karhunen–

Loève expansion for $Y(x;\theta)$ is given by

$$Y(x;\theta) = 1 + \sum_{i=1}^{m} \sqrt{\lambda_i}\tilde{Y}_i(x)\xi_i(\theta), \qquad \xi_i \sim \mathcal{N}(0,1).$$

where the eigenfunctions and eigenvalues are given by Eqs. (2.6) and (2.7), respectively. Defining $\sigma_i(x) \equiv \sqrt{\lambda_i}\tilde{Y}_i(x)$, we thus have the following parameterization:

$$\kappa(x;\boldsymbol{\xi}) = \exp\left(1 + \sum_{i=1}^{m} \sigma_i(x)\xi_i\right), \qquad \xi_i \sim \mathcal{N}(0,1). \tag{2.29}$$

Because $\xi_1, \ldots, \xi_m$ are i.i.d. standard normal, the appropriate gPC basis for our problem is the Wiener–Hermite basis. To express $\kappa(x;\boldsymbol{\xi})$ in terms of this basis, we take note of the similarity between Eq. (2.29) and the expression for log-normal random variable, say

$$X(\xi) = \exp(\mu + \sigma\xi), \qquad \xi \sim \mathcal{N}(0,1)$$

In Sec. 2.3.1, the Wiener–Hermite PCE of a log-normal RV $X(\xi)$ was found to be (*cf.*Eq. (2.15))

$$X(\xi) \approx X^{(P)}(\xi) = \bar{X} \sum_{k=0}^{P} \frac{\sigma^k}{k!} \Psi_k(\xi),$$

where $\bar{X} = \mathbb{E}[X(\xi)] = \exp(\mu + \frac{1}{2}\sigma^2)$. By generalizing the derivation of this expression to multiple dimensions, one obtains

$$\kappa(x;\boldsymbol{\xi}) \approx \kappa^{(p)}(x;\boldsymbol{\xi}) = \bar{\kappa}(x) \sum_{|\underline{k}|\le p} \prod_{i=1}^{m} \left[\frac{\sigma_i^{k_i}(x)}{k_i!}\psi_{k_i}(\xi_i)\right] \tag{2.30}$$

$$= \sum_{|\underline{k}|\le p} \Bigg\{ \underbrace{\left[\bar{\kappa}(x) \prod_{i=1}^{m} \frac{\sigma_i^{k_i}(x)}{k_i!}\right]}_{=\hat{\kappa}_{\underline{k}}(x)} \underbrace{\left[\prod_{i=1}^{m} \psi_{k_i}(\xi_i)\right]}_{=\Psi_{\underline{k}}(\xi)} \Bigg\},$$

where $p$ is the maximum polynomial order in any dimension, and

$$\bar{\kappa}(x) = \exp\left(1 + \frac{1}{2}\sum_{i=1}^{m} \sigma_i^2(x)\right).$$

Equation (2.30) is the multi-index equivalent of Eq. (2.27).

Substituting the PC expansions from Eqs. (2.27) and (2.28) into the governing equations (2.26)

gives

$$\left.\begin{aligned} \sum_{i=0}^{P}\sum_{j=0}^{P} \Psi_i(\xi)\Psi_j(\xi)\left[-\frac{\mathrm{d}}{\mathrm{d}x}\left(\hat{\kappa}_j(x)\frac{\mathrm{d}\hat{u}_i}{\mathrm{d}x}\right)\right] &= 5 \\ \sum_{i=0}^{P}\sum_{j=0}^{P} \Psi_i(\xi)\Psi_j(\xi)\hat{\kappa}_j(x)\frac{\mathrm{d}\hat{u}_i}{\mathrm{d}x} &= 1 \quad \text{at } x = 0 \\ \sum_{i}^{P} \Psi_i(\xi)\hat{u}_i(x) &= 1 \quad \text{at } x = 1 \end{aligned}\right\}$$

Finally, Galerkin projection yields

$$\sum_{i=0}^{P} \mathcal{A}_{ki}\hat{u}_i(x) = 5\,\delta_{k,0}, \quad x \in (0,1)$$

subject to boundary conditions

$$\sum_{i=0}^{P} \mathcal{B}_{ki}\hat{u}_i(0) = \delta_{k,0} \quad \text{and} \quad \hat{u}_k(1) = \delta_{k,0}$$

where

$$\mathcal{A}_{ki} = \sum_{j=0}^{P} C_{ijk}\left[-\frac{\mathrm{d}}{\mathrm{d}x}\left(\hat{\kappa}_j(x)\frac{\mathrm{d}}{\mathrm{d}x}\right)\right] \quad \text{and} \quad \mathcal{B}_{ki} = \sum_{j=0}^{P} C_{ijk}\hat{\kappa}_j(0)\frac{\mathrm{d}}{\mathrm{d}x}$$

This problem was solved using a mixture of MATLAB® and C++. Most of the preprocessing work (e.g., computing $C_{ijk}$) was carried out in C++ and accessed within MATLAB via the MEX interface. The actual solving of the linear system, however, was done in MATLAB using its direct sparse solvers. This approach is adequate for simple 1D problems such as this, but for larger problems iterative solvers are preferred, in which case one would do well to avoid MATLAB as its iterative solvers are quite slow. Spatial discretization was performed using a standard finite-volume scheme ($n_x = 100$ cells). For the parameterization of $\kappa$, the Karhunen–Loève expansion was truncated after $m = 6$ terms; this was done to limit the problem to a reasonable size, but can also be motivated by the fact that the highest order terms in the KL expansion correspond to variations occurring over small length scales (*cf.* Fig. 2-3 on page 31), most of which are smoothed by the diffusion operator and hence have no influence on the solution $u(x;\xi)$.

Figure 2-6a plots the solution obtained with a 4th-order ($p = 4$, $P = 209$) PCE. For comparison, the solution obtained using MCS with $10^4$ samples is shown in Fig. 2-6b. The results are virtually indistinguishable save for some slight differences in the outlier sample (the topmost gray curve in both

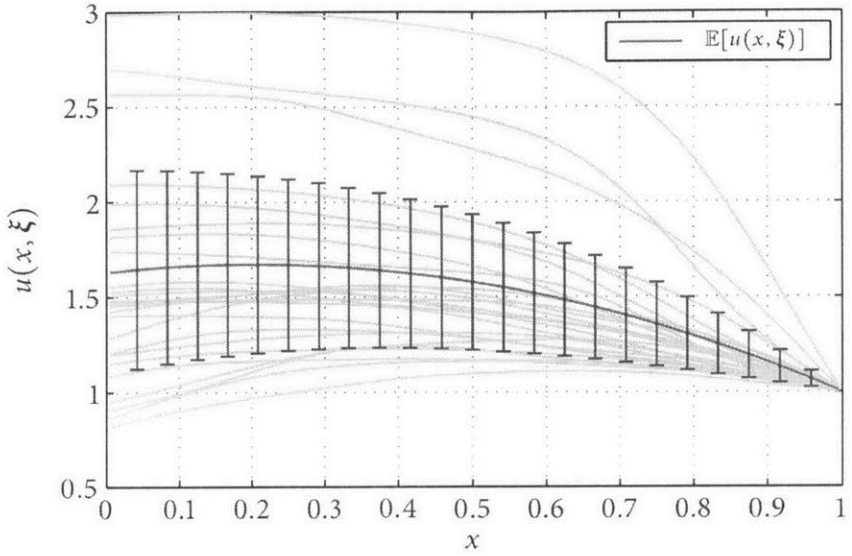


**(a)** Stochastic Galerkin Method ($p = 4$, $P = 209$)

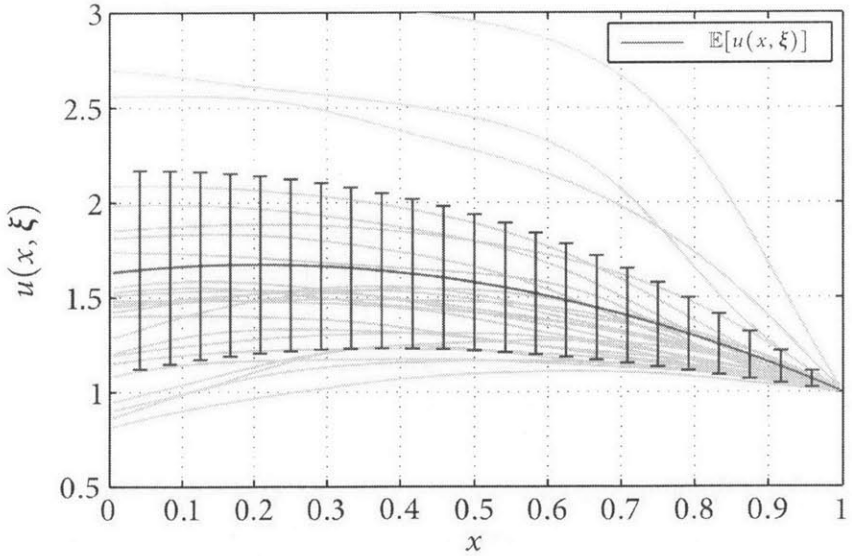


**(b)** Monte Carlo Simulation ($10^4$ samples)

**Figure 2-6:** Comparison of results obtained with (a) the stochastic Galerkin method and (b) Monte Carlo sampling for the 1D stochastic diffusion equation. Error bars (blue) denote ± one standard deviation. The gray curves depict the computed solutions $u$ corresponding to a random sample of $\xi$; the same samples were used for both cases, so any difference between (a) and (b) is indicative of the approximation error incurred by the PC representation.

figures), which is to be expected because the PCE converges most rapidly in the vicinity of the mean, with slower convergence near the tails (*cf.*Fig. 2-4a on page 38). Figure 2-7 illustrates the convergence of the PCE with increasing order $p$; the error metric used is the integrated RMS error, defined as

$$\text{Integrated RMS Error} \equiv \int_0^1 \left\{\mathbb{E}\left[(u^{\text{SGM}} - u^{\text{MCS}})^2\right]\right\}^{1/2} \mathrm{d}x, \tag{2.33}$$

where $u^{\text{SGM}}$ and $u^{\text{MCS}}$ denote the solutions obtained, respectively, from SGM and MCS ($10^4$ samples).

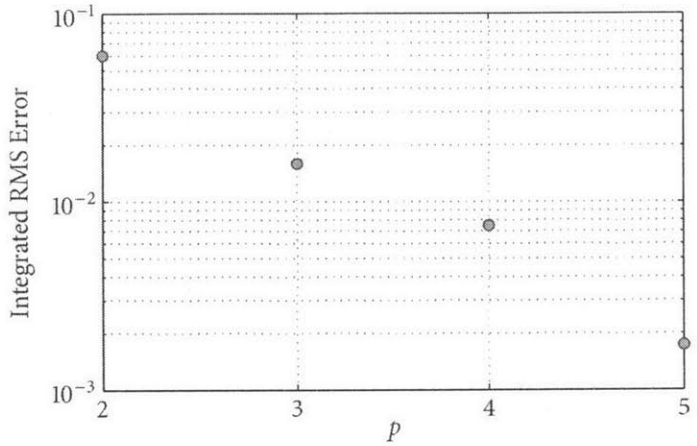


**Figure 2-7:** Convergence of stochastic Galerkin estimate for $u(x;\xi)$ with PC order $p$. The integrated RMS error is defined in Eq. (2.33) and was computing using $10^4$ Monte Carlo samples.

Figure 2-8 compares the expected value, $\mathbb{E}[u(x;\xi)]$, estimated by SGM ($p = 4$) with the deterministic solution, $u(x)$, obtained by replacing $\kappa(x;\theta)$ in Eq. (2.26) with the mean diffusivity, $\bar{\kappa}(x)$. That the two differ may or may not come as a surprise. On the one hand, it is well-known from basic probability that, in general, $\mathbb{E}[f(\xi)] \neq f(\mathbb{E}[\xi])$, where $\xi$ is a RV and $f$ is some function. It is only under special circumstances, namely when $f$ is linear, that $f$ and $\mathbb{E}$ commute ($f \circ \mathbb{E} = \mathbb{E} \circ f$). Now, it is also well-known that the diffusion equation is linear, which could lead one to erroneously assume that the same conclusion—commutativity of the model PDE and $\mathbb{E}$—holds. Figure 2-8 shows this to be false; uncertainty influences the problem nonlinearly, specifically quadratically, through the product of $\kappa$ and $\frac{\partial u}{\partial x}$. Linearity of the governing PDE is necessary but not sufficient for commutativity with $\mathbb{E}$.

As a final note, it should be mentioned that for this particular problem, MCS was actually *faster* than SGM. Each solution of the deterministic system can be obtained in essentially negligible time—approximately 0.4 ms (wall-clock) on my machine—so repeating that $10^4$ times (split across 8 processors) took roughly $t_{\text{MCS}} \approx 0.5$ s. SGM, on the other hand, was slower by a factor of 4: $t_{\text{SGM}} \approx 2$ s. This is largely due to the aforementioned decision to use a direct solver in MATLAB; for this case, the SGM system matrix (Eq. (2.25)) is 210 times larger than the deterministic system matrix, and this does not

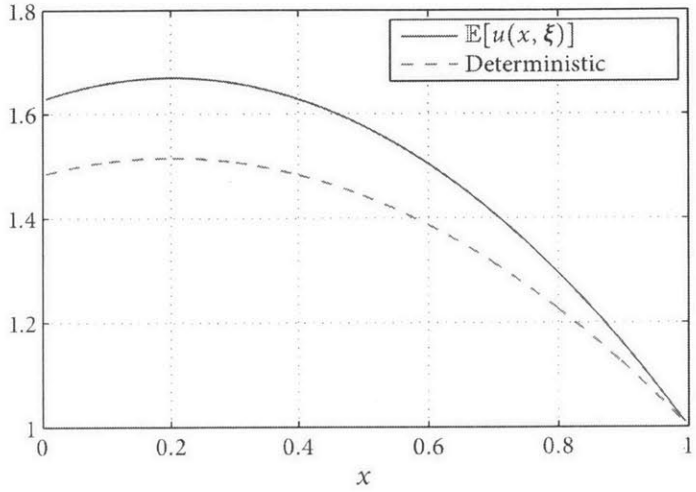


**Figure 2-8:** Comparison of mean, $\mathbb{E}[u(x;\xi)]$, and deterministic solution, $u(x)$, taking $\kappa \leftarrow \bar{\kappa}(x)$.

scale well for direct solvers. Furthermore, nearly 35% of this time was spent simply constructing the block matrix. Clearly, significant performance improvements might be gained by resorting to iterative solvers, specifically matrix-free methods.

### SGM Example 2: Transient Stochastic Diffusion Equation in 2D

Next, we consider the slightly more challenging (computationally) 2D transient diffusion equation on the unit square, $\bar{\Omega} = [0,1]\times[0,1]$:[¶]

$$\left.\begin{aligned} \frac{\partial u}{\partial t} - \nabla\cdot\left[\kappa(\mathbf{x};\theta)\nabla u(\mathbf{x},t;\theta)\right] &= 0, \quad \mathbf{x}\in\Omega \\ u(\mathbf{x},t;\theta) &= 1, \quad \mathbf{x}\in\partial\Omega \end{aligned}\right\} \ \theta\in\Theta \tag{2.34}$$

Once again, we assume $\kappa(\mathbf{x};\theta)$ is uncertain, but rather than starting from an assumed distribution and using the Karhunen–Loève expansion (KLE) to parameterize $\kappa$, we work backwards starting from an assumed parameterization (written as a KLE):

$$\kappa(\mathbf{x};\theta) = \kappa(\mathbf{x};\boldsymbol{\xi}) = 0.2 + \sum_{i=1}^{m}\sqrt{\lambda_i}\tilde{\kappa}_i(\mathbf{x})\xi_i, \tag{2.35}$$

[¶] $\bar{\Omega} = \Omega\cup\partial\Omega$ denotes the closure of $\Omega$

where $\xi_i$ are i.i.d. uniformly distributed in $[0, 1]$, and $\lambda_i$ and $\tilde{\kappa}_i(\mathbf{x})$ are the eigenvalues and eigenfunctions of the 2D exponential covariance kernel,

$$C(\mathbf{x}, \mathbf{x}') = 0.01 \exp\left(|x - x'| + |y - y'|\right).$$

Initially, we take $u = 0$ uniformly. Because we have not considered any source terms in Eq. (2.34), the steady-state ($t \to \infty$) solution is simply $u = 1$ almost surely $\forall \mathbf{x} \in \bar{\Omega}$. The system thus undergoes a transition from one deterministic state ($u = 0$ at $t = 0$) to another ($u = 1$ as $t \to \infty$), but the everything in between is uncertain.

Proceeding as before, we first identify the appropriate gPC basis. Since the $\xi_i$ are uniformly distributed, Table 2.1 (page 36) recommends the Legendre PC basis. In terms of the Legendre basis, Eq. (2.35) can be written

$$\kappa(\mathbf{x}; \xi) = 0.2\Psi_0(\xi) + \sum_{i=1}^{m} \sqrt{\lambda_i}\tilde{\kappa}_i(\mathbf{x})\Psi_i(\xi),$$

which implies taking

$$\hat{\kappa}_i(\mathbf{x}) = \begin{cases} 0.2 & i = 0 \\ \sqrt{\lambda_i}\tilde{\kappa}_i(\mathbf{x}) & 1 \le i \le m \\ 0 & m < i \le P \end{cases}$$

After projecting Eq. (2.34), we are left with

$$\frac{\partial \hat{u}_k}{\partial t} + \sum_{i=0}^{P}\sum_{j=0}^{m} C_{ijk}\hat{\mathcal{A}}_j\hat{u}_i(\mathbf{x}, t) = 0, \quad \mathbf{x} \in \Omega, \ t > 0, \tag{2.36}$$

where $\hat{\mathcal{A}}_i = \nabla \cdot [\hat{\kappa}_i(\mathbf{x})\nabla]$. Initial and boundary conditions are given by $\hat{u}_i(\mathbf{x}, 0) = 0$ and $\hat{u}_i\,|_{\mathbf{x}\in\partial\Omega} = \delta_{i0}$, respectively.

This problem was solved using the Stokhos package from the Trilinos library [56–58]. Trilinos is an extensive collection of C++ libraries for parallel numerical computing. The Stokhos package, in particular, provides an assortment of classes and utilities for intrusive stochastic Galerkin UQ methods. In other words, Stokhos was designed specifically for problems of this sort. Unfortunately, there is no official documentation for Stokhos, and the example codes provided with the package are rather difficult to decipher without having first mastered roughly half a dozen or so other Trilinos packages. Ultimately, however, despite investing a considerable amount of time attempting to gain such a mastery, this route was eventually abandoned, having concluded that Stokhos was simply too difficult to use. In fairness, Stokhos appeals to rather niche market, and there is likely little demand

currently for increased user-friendliness.

Equation (2.36) was discretized using the Crank-Nicholson method. The solution at each time step was obtained using the GMRES method provided by the AztecOO [55] library of Trilinos. Preconditioning consisted of a multilevel symmetric Gauss–Seidel smoother from the ML package [38] with a direct solve on the coarsest level; for the latter, the serial KLU algorithm provided with the Amesos [110–112] package was used. The mean and variance of the solution $u(\mathbf{x}, t; \xi)$ at various times are illustrated in Fig. 2-9. The mean behaves as expected, and is not particularly interesting. On the other hand, the variance starts from zero (initial condition is certain), rises to a peak in the middle of the domain (the furthest point from any boundary), and then decays back to zero (end state is certain). Moreover, it appears almost as if variance is being "injected" from the boundaries. Strictly speaking, this is not the case since variance of $u$ vanishes at the boundaries for all $t$. The apparent injection of variance is a consequence of the fact that the rate of diffusion (or heat transfer) from the boundaries is uncertain.

### 2.4.2 Non-Intrusive Stochastic Projection Method

Similarly to the stochastic Galerkin method, the departure point for NISP is to parameterize the uncertain model inputs via a finite set $\xi = (\xi_1, \ldots, \xi_m)$ of independent RVs, which is then followed by the selection of an appropriate gPC basis $\{\Psi_k(\xi)\}_{k=0}^{P}$ with which to approximate the model output[‖], $u(\xi) \approx u^{(P)}(\xi) = \sum_{k=0}^{P} \hat{u}_k \Psi_k(\xi)$. The final, pivotal step is to compute the expansion coefficients, $\hat{u}_k$, and it is in this step that NISP and SGM part ways; whereas SGM reformulates the model to yield $\hat{u}_k$ directly, NISP seeks to compute these coefficients numerically, relying only on observations (Le Maître and Knio [79] refer to these "observations" as *deterministic model resolutions*), $\{u^{(i)}\}_{i=1}^{N}$, obtained from the deterministic model for specific input configurations, $\{\xi^{(i)}\}_{i=1}^{N}$. Specifically, NISP seeks to estimate the expectation of functionals, $F[u(\xi)] = u(\xi)\Psi_k(\xi)$, via numerical quadrature methods, e.g.,

$$\begin{aligned} \mathbb{E}\big[u(\xi)\Psi_k(\xi)\big] &= \int_{\Xi} u(\xi)\Psi_k(\xi)\rho(\xi)\,\mathrm{d}\xi \\ &\approx \sum_{i=1}^{N} u\big(\xi^{(i)}\big)\Psi_k\big(\xi^{(i)}\big)\rho\big(\xi^{(i)}\big)w^{(i)} \end{aligned} \tag{2.37}$$

where $\rho(\xi) = \prod_{i=1}^{m} \rho_i(\xi_i)$ is the probability density of $\xi$. NISP thus allows one to consider the model as a black-box, and in this regard is similar to Monte Carlo simulation. Consequently, one can take advantage of preexisting (legacy) codes for deterministic models, which can be used without modifi-

[‖] In this section, to simplify notation we write $u(\xi)$ rather than $u(\mathbf{x}, t, \xi)$, understanding that $u(\xi)$ could, in fact, be a random field. By virtue of its non-intrusive nature, NISP makes no distinction between vectors, fields, and vector fields, all of which are regarded simply as sets of scalar quantities.

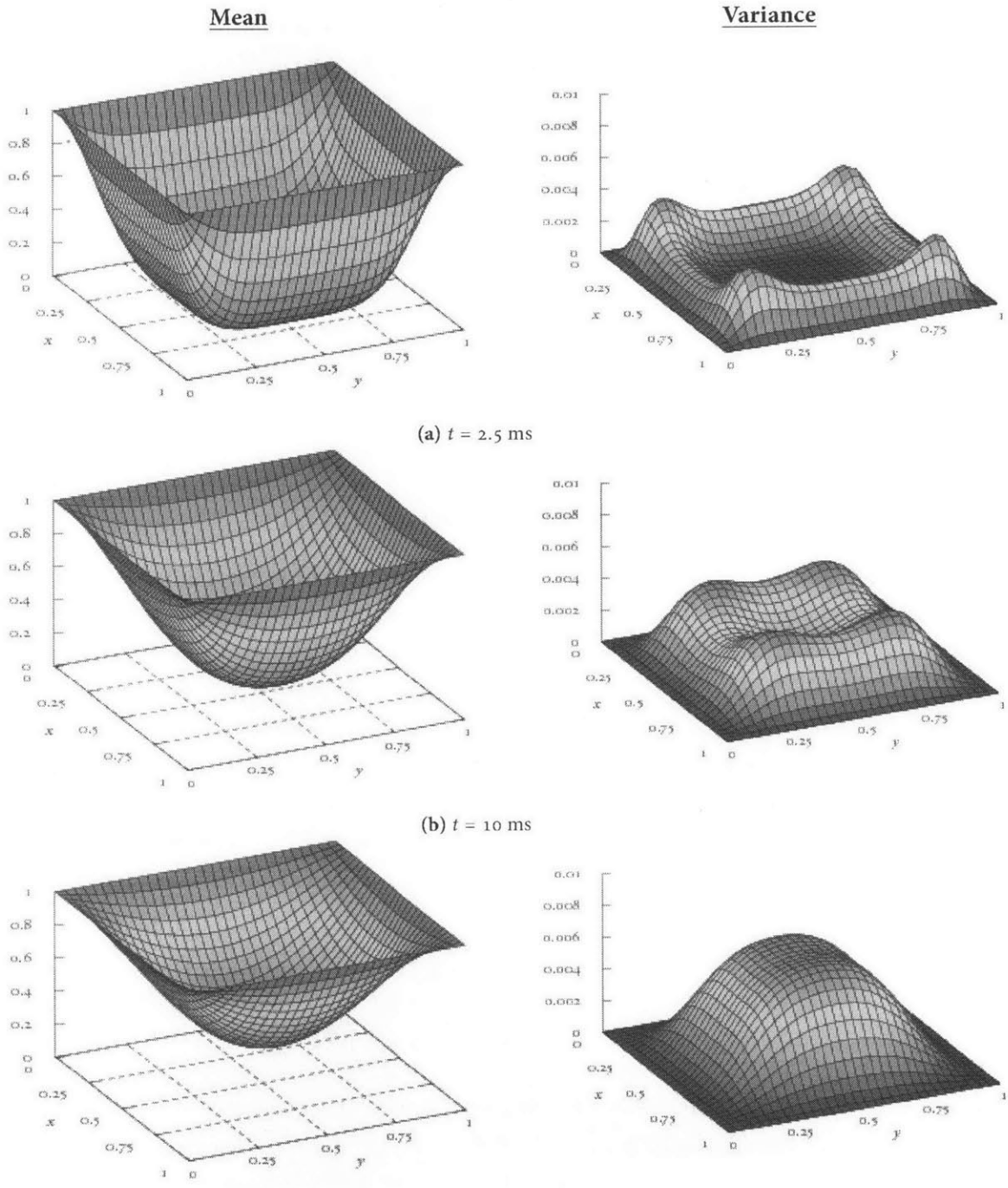


(a) $t = 2.5$ ms

(b) $t = 10$ ms

(c) $t = 15$ ms

**Figure 2-9:** Time-evolution of the mean and variance of $u(\mathbf{x}, t; \boldsymbol{\xi})$.

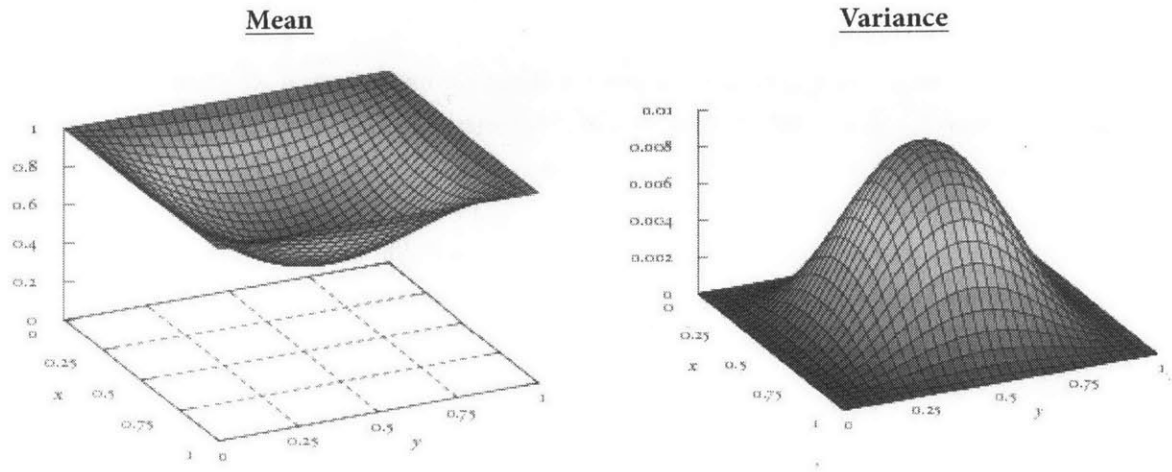


(d) $t = 20$ ms

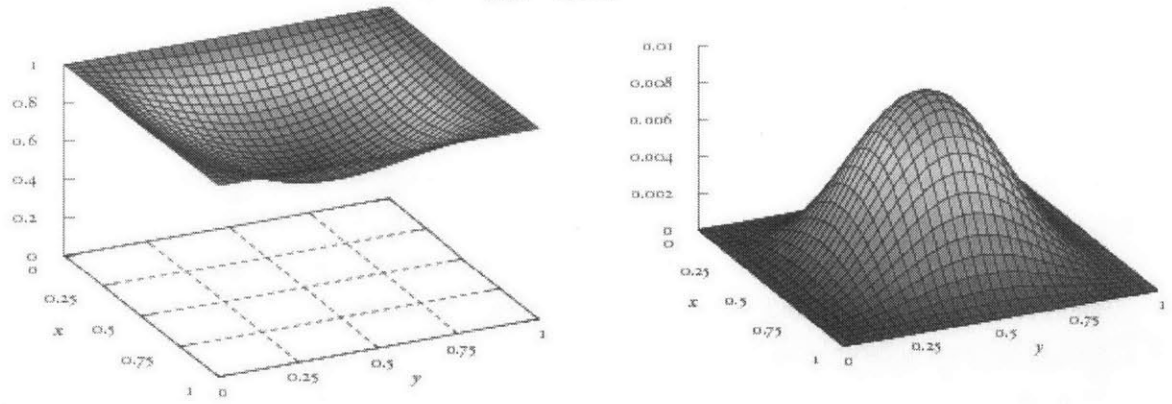

(e) $t = 25$ ms

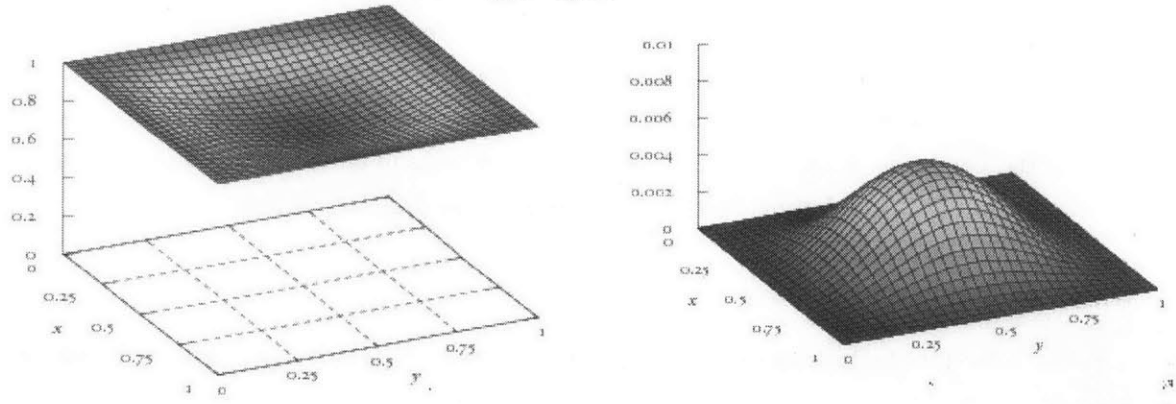

(f) $t = 30$ ms

**Figure 2-9 (cont.):** Time-evolution of the mean and variance of $u(\mathbf{x}, t; \xi)$.

cation. This has obvious advantages for problems with complex physics, for which the development of new codes might be impractical.

The obvious issue, then, is how to choose the input configurations at which the model is to be evaluated. Because each evaluation of the model is potentially costly, possibly requiring several hours or even days of computing time, we require $N$ to be as small as possible. Monte Carlo simulation is a possibility, but that effectively defeats the point of using a PC representation in the first place. Stated differently, the assumption that a gPC representation is suitable for given problem (i.e., that gPC even works) presupposes a certain degree of regularity (smoothness) in the solution, regularity that is not taken into account by MCS thereby leading to sub-optimal ($O(N^{-1/2})$) convergence [41]. An alternative approach, which can be vastly more efficient than MCS for low-to-moderate dimensional problems ($N \ll 100$), is to use deterministic (structured grid) quadrature methods; compared to MCS, which requires model evaluations for a set of randomly selected input configurations, deterministic quadratures achieve higher efficiency by using carefully chosen input configurations that better exploit the assumed smoothness of the integrand. For the computation of PC expansion coefficients, Clenshaw–Curtis and Gauss quadratures are especially attractive due to their ability to exactly integrate polynomials of a given order. The Gauss quadratures hold the added appeal that their weight functions generally correspond (up to a constant scaling factor) to common probability distributions. Consequently, for these quadratures the $\rho(\xi^{(i)})$ term in Eq. (2.37) is absorbed by the weighting factor, $w^{(i)}$. The practical significance of this is seen by the fact that, even if $u(\xi)\Psi_k(\xi)$ happens to be a polynomial, and is therefore exactly integrable with Gaussian quadrature, the product $u(\xi)\Psi_k(\xi)\rho(\xi)$ will most likely *not* be a polynomial.

The difficulty with deterministic quadrature rules comes when attempting to extend them to multiple dimensions. Traditionally, this is achieved through a tensor-product construction. For fixed $N$, the accuracy of such methods is found to diminish exponentially ($\sim N^m$) with increasing dimension. This *curse of dimensionality* can be regarded as the Achilles' heel of these methods [75]. In other words, to maintain a given level of accuracy, the number of quadrature points must increase exponentially with $m$. An alternative construction that seeks to tame this explosive growth is the so-called sparse-grid quadrature, first proposed by Smolyak (e.g., [14, 59, 95]).

### Tensor-product quadrature

Consider a family of 1D quadrature rules $\mathcal{Q}^\ell$ indexed by $\ell \in \mathbb{N}$, which represents the "level" of the quadrature rule. The level $\ell$ is just an abstract indicator of the accuracy (e.g. polynomial precision) of the quadrature rule, such that $\mathcal{Q}^{\ell+1}$ is more accurate than $\mathcal{Q}^\ell$. For a given level, let $\mathfrak{p}(\ell)$ denote the *polynomial precision* of the quadrature rule (the maximal degree polynomial that is integrated exactly), and let $o(\ell)$ denote the *order* (i.e. the number of quadrature points). For some function

$f(\xi)$, let $\mathcal{I}f(\xi)$ denote its integral, i.e.

$$\mathcal{I}f \equiv \int_{\Xi} f(\xi)\rho(\xi)\,\mathrm{d}\xi.$$

In 1D, we approximate $\mathcal{I}f$ by

$$\mathcal{I}f \approx \mathcal{Q}^{\ell}f = \sum_{i=1}^{o(\ell)} w^{(i)} f\big(\xi^{(i)}\big),$$

and in 2D,

$$\mathcal{I}f \approx \mathcal{Q}^{(\ell_1,\ell_2)}f = \sum_{i_1=1}^{o_1(\ell_1)} \sum_{i_2=1}^{o_2(\ell_2)} w^{(i_1)} w^{(i_2)} f\big(\xi_1^{(i_1)}, \xi_2^{(i_2)}\big) = \big(\mathcal{Q}^{l_1} \otimes \mathcal{Q}^{l_2}\big) f.$$

In general, letting $\underline{\ell} = (\ell_1, \ldots, \ell_m)$,

$$\mathcal{I}f \approx \mathcal{Q}^{\underline{\ell}}f = \big(\mathcal{Q}^{l_1} \otimes \cdots \otimes \mathcal{Q}^{l_m}\big) f(\xi)$$

The number of quadrature points (i.e. the number of required model evaluations) is given by

$$o(\ell) = \prod_{i=1}^{m} o_i(\ell_i).$$

If $o_i(\ell_i) = M$, $\forall i = \in \{1, \ldots, m\}$, then $o(\ell) = M^m$.

The exponential growth of quadrature points results the fact that tensor-produce quadratures constructed in this manner are, in some sense, overkill—they exhibit wasted precision. Suppose, for example, that we wish to integrate a function of the form

$$\alpha + \beta\xi_1 + \gamma\xi_2 \tag{2.38}$$

Let $\mathcal{Q}^1$ and $\mathcal{Q}^2$ be 1D quadrature rules of orders 1 and 2, respectively, that integrate exactly constant and linear expressions. Then $\mathcal{Q}^2$ is sufficient to integrate either $\alpha + \beta\xi_1$ or $\alpha + \gamma\xi_2$. The 2D tensor product formula, $\mathcal{Q}^{(2,2)} = \mathcal{Q}^2 \otimes \mathcal{Q}^2$ requires 4 evaluations, and exactly integrates functions of the form

$$\alpha + \beta\xi_1 + \gamma\xi_2 + \kappa\xi_1\xi_2.$$

Yet, the polynomial precision of the method is still is 1; it cannot exceed the maximum precision in any dimension. Integration of the product term, $\xi_1\xi_2$, does not contribute to the precision of the method, and is therefore regarded as wasted effort. As an alternative, we could consider a quadrature

rule of the form

$$\mathcal{Q}^{(2,1)} + \mathcal{Q}^{(1,2)} - \mathcal{Q}^{(1,1)} = (\mathcal{Q}^2 \otimes \mathcal{Q}^1) + (\mathcal{Q}^1 \otimes \mathcal{Q}^2) - (\mathcal{Q}^1 \otimes \mathcal{Q}^1).$$

It is readily verified that this scheme exactly integrates the expression in Eq. (2.38). In the worst case, this scheme requires 5 model evaluations: two from each of $\mathcal{Q}^{(2,1)}$ and $\mathcal{Q}^{(1,2)}$, and one from $\mathcal{Q}^{(1,1)}$. If, however, the quadrature rules are nested, then this requires only 3 model evaluations due to repetition of quadrature points. Smolyak proposed a general procedure for extending this idea to arbitrary dimensions, and for arbitrary level. The resulting quadratures are referred to as sparse-grid quadratures.

### Sparse-Grid Quadrature

Again, consider a family of 1D quadrature rules $\mathcal{Q}^\ell$. We can express any quadrature rule $\mathcal{Q}^\ell$ as a telescoping sum,

$$\mathcal{Q}^\ell = \sum_{k=1}^{\ell} \left(\mathcal{Q}^k - \mathcal{Q}^{k-1}\right) = \sum_{k=1}^{\ell} \Delta^k, \quad \text{where} \quad \Delta^k \equiv \mathcal{Q}^k - \mathcal{Q}^{k-1}, \quad \mathcal{Q}^0 \equiv 0. \tag{2.39}$$

With the decomposition given by (2.39), we can write the $m$-dimensional tensor-product quadrature rule as

$$\mathcal{Q}^{\underline{\ell}} = \mathcal{Q}^{\ell_1} \otimes \cdots \otimes \mathcal{Q}^{\ell_m} = \left(\sum_{k_1=1}^{\ell_1} \Delta^{k_1}\right) \otimes \cdots \otimes \left(\sum_{k_m=1}^{\ell_m} \Delta^{k_m}\right). \tag{2.40}$$

For the special case in which the 1D quadrature rules are all of the same level, $L = \ell_1 = \cdots = \ell_m$, we can write (2.40) more succinctly as

$$\mathcal{Q}^{\underline{\ell}} = \sum_{\|\underline{k}\|_\infty \leq L} \left(\Delta^{k_1} \otimes \cdots \otimes \Delta^{k_m}\right). \tag{2.41}$$

The rule expressed by (2.41) is called the *max-order* tensor-product quadrature, so-named because it integrates exactly any polynomial whose maximal order $\mathfrak{p}(\ell_i)$ in any dimension $i \in \{1, \ldots, m\}$ does not exceed $L$.

Notice that alternative quadrature rules can be formed by choosing an alternate summation constraint in (2.41). In particular, the Smolyak sparse grid construction is obtained by replacing the

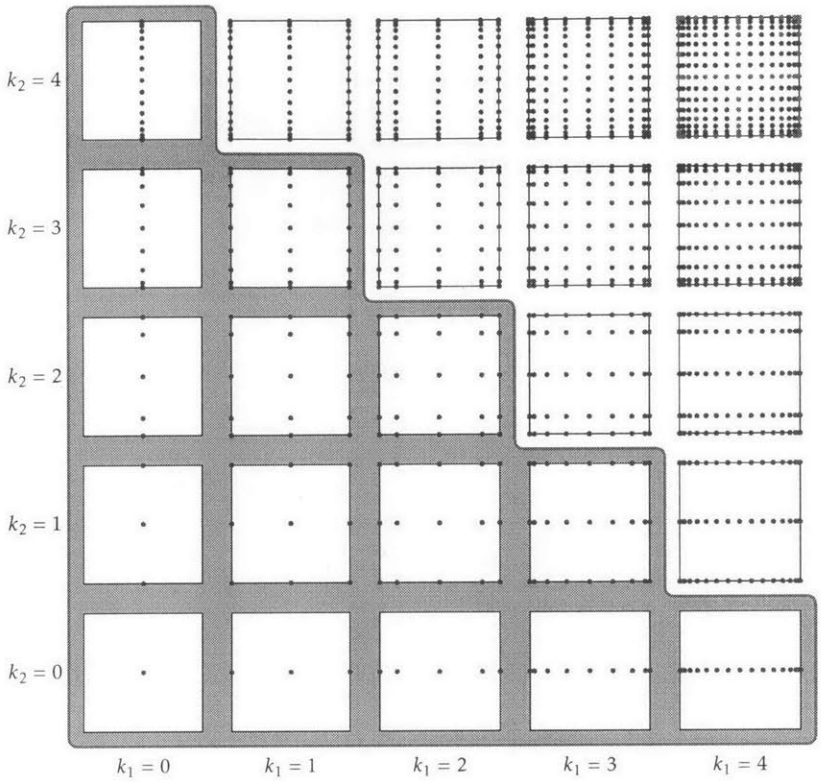


**Figure 2-10:** Smolyak construction of a two-dimensional Clenshaw-Curtis sparse grid quadrature.

$\infty$-norm in (2.41) with the 1-norm, $\|\underline{k}\|_1 \equiv |\underline{k}|$:

$$\mathcal{Q}^{\underline{\ell}} = \sum_{|\underline{k}| \leq L} \left( \Delta^{k_1} \otimes \cdots \otimes \Delta^{k_N} \right) = \sum_{L-N+1 \leq |\underline{k}| \leq L} c_{\underline{k}} \, (\mathcal{Q}^{k_1} \otimes \cdots \otimes \mathcal{Q}^{k_N}),$$

where

$$c_{\underline{k}} \equiv (-1)^{L-|\underline{k}|} \binom{N-1}{L-|\underline{k}|}$$

is called the *combining coefficient*. In general, a sparse-grid construction can be written as

$$\mathcal{Q}^{\underline{\ell}} = \sum_{\underline{k} \in \mathcal{K}} \left( \Delta^{k_1} \otimes \cdots \otimes \Delta^{k_N} \right).$$

where $\mathcal{K}$ is some set of admissible multi-indices. Figure 2-10 provides a pictorial demonstration of the Smolyak construction in 2D for nested Clenshaw–Curtis quadratures. Finally, Table 2.2 compares the number of quadrature points required by tensor-product and sparse grid quadratures for varying dimension ($m$) and polynomial degree. The results are tabulated for Gauss–Hermite rules. It is seen

that for $m \geq 3$, the sparse grids are considerably smaller than the corresponding tensor-product grids, with the difference becoming more pronounced with increasing dimension. For $m = 2$, the tensor-product quadrature performs as well or better than the sparse grids. This is due to the fact that the Gauss–Hermite quadratures are not nested.

**Table 2.2:** Comparison of the number of quadrature points required by (a) Tensor-Product and (b) Smolyak Sparse Grid quadratures for Gauss–Hermite rules.

**(a)** Tensor-Product Quadrature

| Dimension (dim $\xi$) \ Polynomial Degree | 2 | 3 | 4 | 5 | 6 |
|---|---|---|---|---|---|
| 2 | 9 | 16 | 25 | 36 | 49 |
| 3 | 27 | 64 | 125 | 216 | 343 |
| 4 | 81 | 256 | 625 | 1296 | 2401 |
| 5 | 243 | 1024 | 3125 | 7776 | 16807 |
| 6 | 729 | 4096 | 15625 | 46656 | 117649 |
| 7 | 2187 | 16384 | 78125 | 279936 | 823543 |
| 8 | 6561 | 65536 | 390625 | 1679616 | 5764801 |

**(b)** Smolyak Sparse Grid Quadrature

| Dimension (dim $\xi$) \ Polynomial Degree | 2 | 3 | 4 | 5 | 6 |
|---|---|---|---|---|---|
| 2 | 9 | **17** | **33** | **45** | **81** |
| 3 | 19 | 39 | 87 | 153 | 273 |
| 4 | 33 | 81 | 193 | 409 | 777 |
| 5 | 51 | 151 | 391 | 933 | 1973 |
| 6 | 73 | 257 | 737 | 1925 | 4509 |
| 7 | 99 | 407 | 1303 | 3697 | 9465 |
| 8 | 129 | 609 | 2177 | 6705 | 18577 |

### NISP Example 1: Steady Stochastic Diffusion Equation in 1D

As a demonstration of the method, we repeat the 1D steady diffusion equation example from Sec. 2.4.1. The deterministic model was implemented in Python. The sparse grids were generated externally using a customized version of the `VPISparseGrid` library buried deep in the internals** of the DAKOTA program [4]. Figure 2-11 compares the solution variance estimated via NISP for gPC order $p \in \{4, \ldots, 7\}$ with the cost-equivalent MCS, which is simply a Monte Carlo simulation using the

**Specifically, `<DAKOTA_ROOT>/packages/pecos/packages/VPISparseGrid/src/`

same number of samples as quadrature points required by NISP. The MCS simulations were repeated 500 to give a rough assessment of the amount of variability in their predictions; the error bars in the figure depict ± one standard deviation based on these simulations. Figure 2-12 compares the NISP-estimates of the variance for $p = \{2, \ldots, 8\}$, demonstrating that variance estimate has effectively converged for $p \geq 3$ ($N = 257$). In contrast, the MCS estimates exhibit appreciable variability even for $N \approx 10^4$. Finally, Fig. 2-13 compares the computed mean and variance using both NISP and SGM; the results are indistinguishable for this problem.

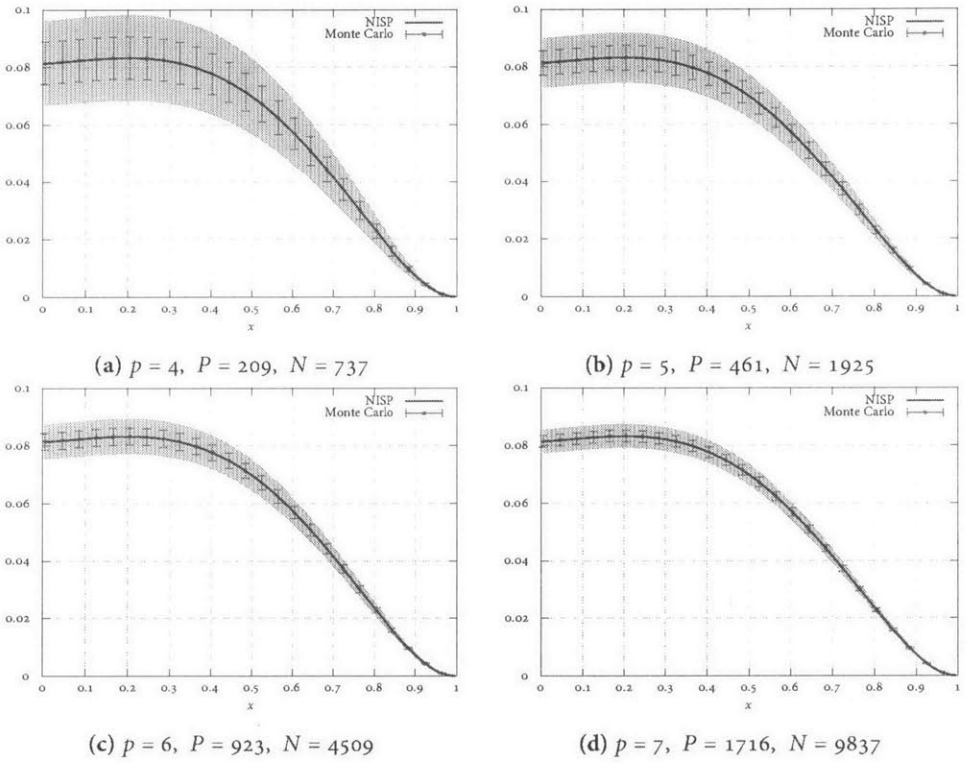


(a) $p = 4$, $P = 209$, $N = 737$

(b) $p = 5$, $P = 461$, $N = 1925$

(c) $p = 6$, $P = 923$, $N = 4509$

(d) $p = 7$, $P = 1716$, $N = 9837$

**Figure 2-11:** Comparative performance of NISP and cost-equivalent Monte Carlo simulation for estimating the solution variance. MCS data obtained using the same number $N$ of samples required by NISP. MCS error bars depict ± one standard deviation based on 500 simulations. For all cases, $\dim(\boldsymbol{\xi}) = 6$. $p$ is the polynomial degree of the gPC, and $P + 1$ is total number of terms in the gPC expansion.

### NISP Example 2: 2D laminar channel flow

Our final example considers 2D single-phase, laminar channel flow. The flow was simulated using the open source *Gerris* flow solver, which is described more fully in Chapter 3; a detailed description of the algorithms implemented in the code can be found in [100, 101]. The flow domain is a $6 \times 1$ rectangular channel with a uniform inlet velocity ($x = 0$) of $u = 1$, an outlet boundary ($p = 0$, $\frac{\partial v}{\partial x} = 0$)

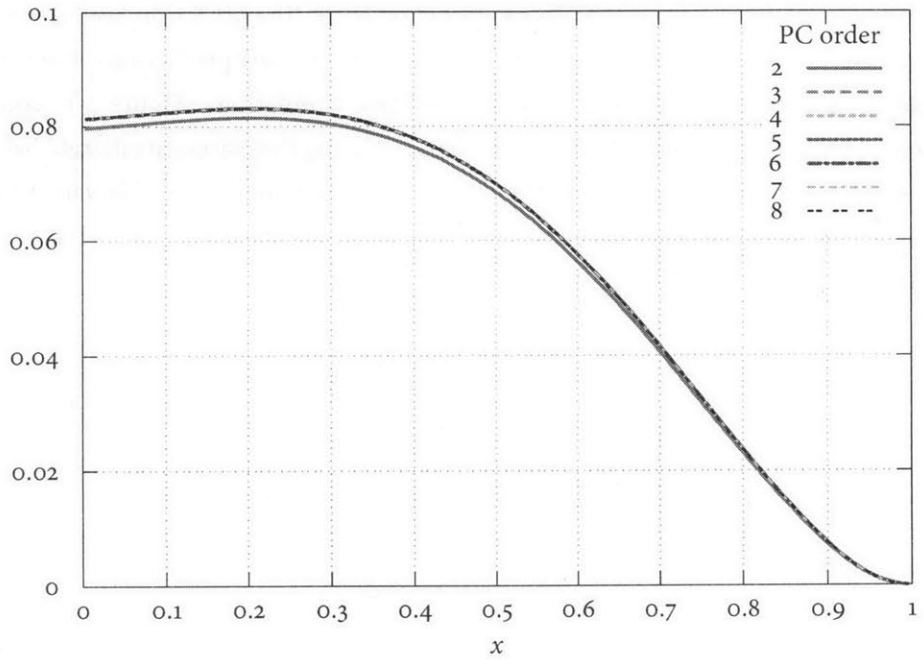


**Figure 2-12:** Convergence of variance estimate obtained via NISP.

at $x = 6$, and non-slip boundaries at $y = 0$ and $y = 1$ (see Fig. 2-14).

Before attempting the stochastic problem, a simple verification case was run to ensure that everything was set up properly with *Gerris*, For this, a kinematic viscosity $\nu = 0.02$, corresponding to a Reynolds number $\mathrm{Re} = 50$, was selected. A 384×64 grid was used with a uniform mesh spacing $h = \frac{1}{64}$. Figure 2-15a plots the computed outlet velocity, $u(y)$, and compares the result against the analytical solution, $u(y) = 6y(y-1)$. The results are seen to agree very well. In addition, Fig. 2-15b plots the computed centerline ($y = 0.5$) pressure. Away from the inlet ($x \gtrsim 2$), the pressure gradient agrees with the analytically expected result, $-\frac{\mathrm{d}p}{\mathrm{d}x} = \frac{12}{\mathrm{Re}} = 0.24$.

Next, we consider the stochastic problem. We assume the kinematic viscosity is normally distributed with mean $\bar{\nu} = 0.0246$ (i.e., $\mathbb{E}[\mathrm{Re}] = 40.65$) and standard deviation $0.2\bar{\nu}$, i.e.,

$$\nu \sim \mathcal{N}(\bar{\nu}, 0.2\bar{\nu}). \tag{2.42}$$

For these conditions, the problem is identical to that described in Le Maître and Knio [79, §6], who used the intrusive stochastic Galerkin method. According to Eq. (2.42), we write $\nu = \nu(\xi) = \bar{\nu} + 0.2\bar{\nu}\xi$,

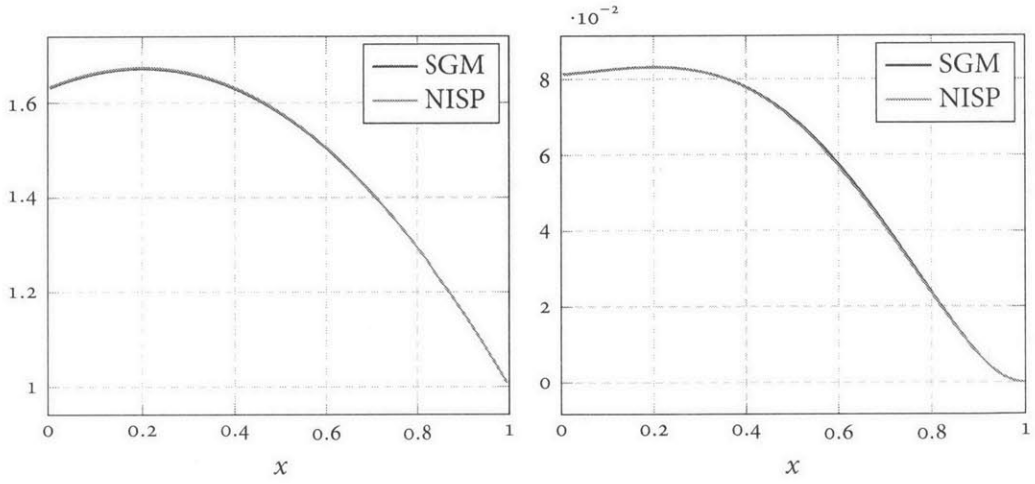


**(a)** Mean

**(b)** Variance

**Figure 2-13:** Comparison of (a) mean and (b) variance estimates using NISP and SGM.

where $\xi \sim \mathcal{N}(0, 1)$. Next, we expand the velocity and pressure fields as Hermite gPC expansions in $\xi$:

$$\mathbf{u}(\mathbf{x}, t, \xi) = \sum_{k=0}^{p} \hat{\mathbf{u}}_k(\mathbf{x}, t)\, \Psi_k(\xi)$$

$$p(\mathbf{x}, t, \xi) = \sum_{k=0}^{p} \hat{p}_k(\mathbf{x}, t).\, \Psi_k(\xi)$$

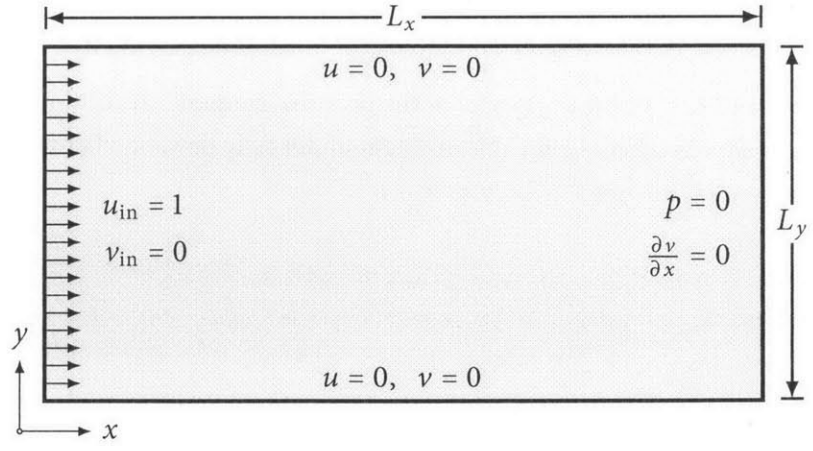


**Figure 2-14:** Schematic of the channel flow problem: $L_x = 6$ and $L_y = 1$.

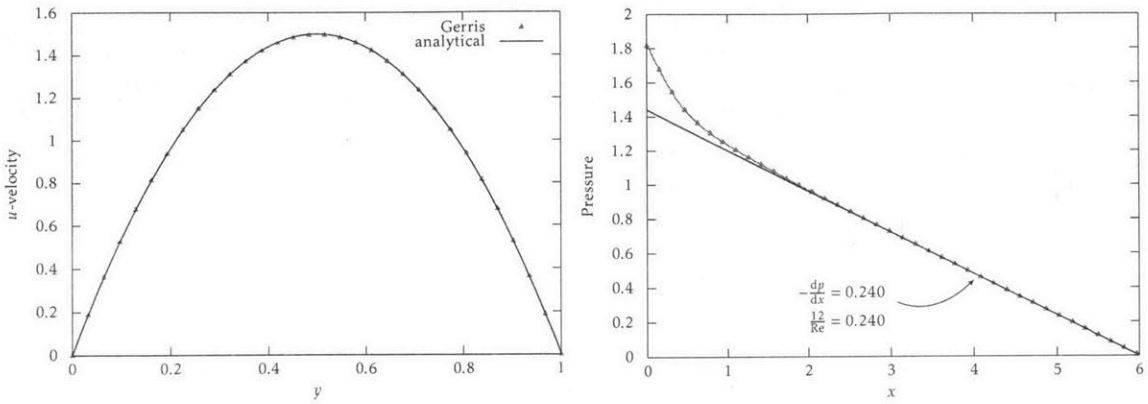


**(a)** Comparison of computed outlet velocity with analytical solution.

**(b)** Centerline pressure drop.

**Figure 2-15:** Results from deterministic channel flow simulation.

For this problem, we have taken $p = 5$. Assuming $\mathbf{u}$ is an order 5 polynomial in $\xi$, the maximum order of the products, $\mathbf{u}\Psi_k$, is 10, which requires a 6-point Gauss–Hermite quadrature; in other words, we must run the code a total of 6 times at different values of $\xi$ corresponding to the Gauss–Hermite quadrature nodes. When finished, the data are combined to compute the stochastic modes, $\hat{\mathbf{u}}_k(\mathbf{x}, t)$ and $\hat{p}_k(\mathbf{x}, t)$. Figure 2-16a illustrates contours for the mean and standard deviation of the steady-state $u$-component of the velocity field. The standard deviation reaches a maximum at the centerline just past the inlet, and then steadily decays. For $x > 3$, the standard deviation is essentially zero. This corresponds to the fact that for fully developed flow, the velocity is independent of viscosity; thus, $\mathbf{u}(\mathbf{x}, t, \xi)$ is independent of $\xi$, and the velocity is not uncertain. Figure 2-16b plots the ratio,

$$\frac{\partial \hat{p}_1/\partial x}{\partial \hat{p}_0/\partial x},$$

of the zeroth- and first-order PC modes of the pressure gradient. According to Le Maître and Knio [79], this ratio should equal 0.2 for this problem under fully developed flow conditions. Indeed the pressure gradient ratio approaches 0.2 as $x \to 6$.

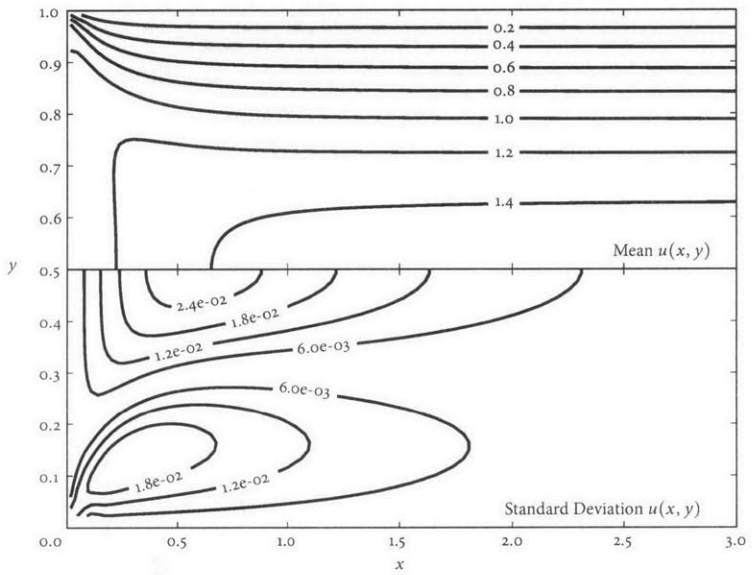


**(a)** Contours of mean (top) and standard deviation (bottom) of stream-wise velocity component, $u(x, y)$

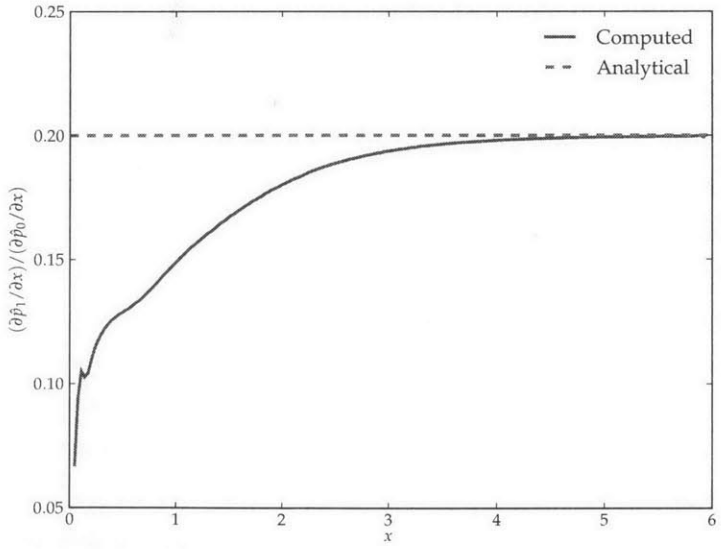


**(b)** Ratio of computed $0^{th}$- and $1^{st}$-order PC modes of the pressure gradient compared to the analytical value (0.2) for fully-developed flow.

**Figure 2-16:** Results from stochastic channel flow simulation.

## 2.5 Challenges in gPC methods and outlook for CMFD

The preceding examples have demonstrated the immense power of gPC-based UQ methods—both the intrusive (SGM) and non-intrusive (NISP) flavors. But the gPC expansion is not a silver bullet and is subject to some limitations that are particularly limiting for CMFD applications. In Sec. 2.3.2 we noted in passing that the gPC expansion can suffer from poor convergence when used to approximate RVs that are strongly non-polynomial in $\xi$, such as when the output exhibits a sharp/discontinuous dependence on $\xi$. Approximation of such a discontinuous (or nearly discontinuous) function with a polynomial basis will obviously require a high-order expansion, which adds to the computational cost. Even worse, any finite polynomial expansion will suffer from Gibbs/Runge phenomena, as illustrated in Fig. 2-17. Thus, whenever the quantity of interest varies discontinuously in the inputs, then the convergence rate of the gPC expansion is expected to be severely degraded. This is a significant limitation in the context of multiphase flow simulations since fluid properties (density and viscosity) and pressure vary discontinuously in space and time, and these spatio-temporal discontinuities lead to discontinuities in parameter space. More advanced methods utilizing localized basis functions, such as wavelets [80] or the multi-element gPC expansion [134], can occasionally be used to successfully handle discontinuities. These methods work best when the discontinuity in $\xi$-space is fixed in time, in which case one it is possible to identify an appropriate basis to approximate the function on either side of the discontinuity. If, however, this discontinuity is evolving in time as part of the solution (as it will for nearly every multiphase flow simulation), then the situation is far more complex. The problem is essentially the same as that of tracking a fluid interface, except in this case the "interface" is not a 2D surface (or 1D curve), but is a $(\dim \xi - 1)$-dimensional hypersurface.

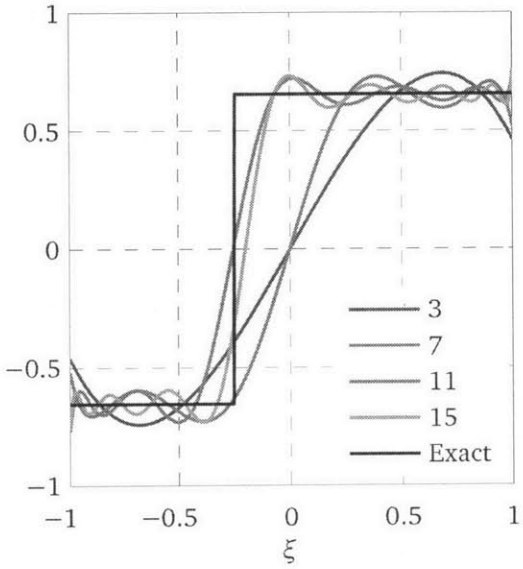


**Figure 2-17:** Illustration of gPC expansion subject to Gibbs/Runge phenomena

As discussed by Najm [94], another limitation of gPC expansions is met when dealing with problems involving long time horizons. The essential problem is that the gPC basis that is optimal at time $t_1$ need not be optimal for subsequent times, and in fact might be downright unacceptable for $t_2 \gg t_1$. One solution is to periodically recompute a new set of basis functions and project the solution onto this new basis, leading to the so-called time-dependent gPC expansion [40]. Even more

advanced approaches make use of continuously evolving, dynamic bases [113].

For multiphase flow simulations, the long time horizon problem is perhaps a less severe limitation than the discontinuity problem, but it could still prove significant. Nevertheless, it is possible with NISP (but not SGM) to circumvent these issues by focusing only on well-behaved observables that depend smoothly on the inputs, such as RMS velocity profiles or energy spectra in turbulent flow [94]. This is possible with NISP due to its non-intrusive nature, which makes it possible to selectively disregard badly behaved quantities that would otherwise defeat the gPC expansion. For the intrusive SGM, this is not possible since all dependent variables must be expressible in terms of the gPC expansion, regardless whether those quantities are actually of any interest to the analyst. For this reason, in the following chapters we shall only consider applications of NISP to computational multiphase fluid dynamics simulations. We shall focus primarily on observables that do not depend on the specific location of the liquid-vapor interface, such as the velocity of a bubble (Ch. 3) or the pressure drop across a Taylor bubble in slug flow (Ch. 4), thereby avoiding the complications introduced by the presence of discontinuities in the fluid properties.

THIS PAGE INTENTIONALLY LEFT BLANK

# Chapter 3

# Computational Study of Bubbles Rising in a Quiescent Liquid

## 3.1 Introduction

This chapter presents our first attempted application of the uncertainty quantification techniques described in Chapter 2 to multiphase flow simulations. The case that we consider is the relatively problem of simulating a 2D axisymmetric bubble rising in a quiescent liquid bath. The motivation for this study was largely to serve as a warm-up exercise in preparation for the study of capillary slug flow considered in Chapter 4, and to gain familiarity with the *Gerris* [100, 101] flow solver, which is briefly described in Section 3.2. The rising bubble problem, which is the focus of this chapter, is described in Section 3.3, and the results of our validation exercises and convergence studies are summarized in Section 3.4. The UQ techniques of Chapter 2 are applied to the rising bubble simulations in Section 3.5. Two examples are considered; in the first example, the Galilei number (which serves the role of a viscous diffusion coefficient) is assumed to be a uniformly distributed random variable, and we estimate the resulting uncertainty in the bubble's terminal velocity using the Legendre-PC expansion. The second example models the bubble's size (diameter) as an uncertain quantity (log-normally distributed) and we estimate the resultant probability distribution of the bubble's velocity as a function of time using the Hermite-PC expansion. This second example is interesting in that it demonstrates the extremely fast convergence rates achievable with the gPC expansion if the chosen basis (Hermite polynomials) happens to be the optimal basis for representing the uncertainty in the observable

(bubble velocity).

Finally, we conclude this chapter by describing in Section 3.6 how one can implement a moving reference frame model in *Gerris*. This will be a crucial feature of our slug flow simulations discussed in Chapter 4. The reason for deferring this discussion to the end of this chapter is due to an unfortunate timing of events—it was not realized how to accomplish this until after this rising bubble study had already been completed. On the other hand, the reason for including this discussion in the present chapter at all is because we will use the rising bubble example to demonstrate that the implementation works as expected.

## 3.2 The *Gerris* flow solver

*Gerris* is a free (as in beer and speech) and open-source computational fluid dynamics (CFD) code for incompressible, single- and multi-phase flow simulations. *Gerris* implements an adaptive quad/octree mesh based on the Fully-Threaded Tree (FTT) algorithm of Khokhlov [67]. This is a particularly attractive feature for multiphase flow simulations, as it allows for extremely high resolution near the liquid-vapor interface with a much coarser mesh in the surrounding fluid where such high resolution is unnecessary. *Gerris* is written in C and is fully parallelizable using domain decomposition.

*Gerris* uses a fractional step projection method coupled with a multilevel Poisson solver for the pressure equation that takes advantage of the hierarchical structure of the quad/octree mesh. Alternatively, *Gerris* can be linked to the Hypre library [37], providing access to Hypre's algebraic multigrid solvers. Solid boundaries are handled using an embedded surface representation, i.e. the so-called immersed boundary method. For multiphase flow simulations, *Gerris* implements a geometric Volume-of-Fluid (VoF) method. A height function-based curvature calculation algorithm is implemented for the accurate estimation of surface tension forces.* A more detailed discussion of the *Gerris* code, including implementation details, discretization schemes and solvers implemented by *Gerris* are given in [100, 101]. The cited references also contain the results from several verification and convergence studies, and *Gerris* input files for these tests and many more are freely available online.† Moreover, an adaptation of the rising bubble problem considered herein (and written by myself) can be obtained from the *Gerris* website.‡

Because the source code is freely available, *Gerris* is an ideal tool for academic research. It is possible, in principle, to extend the code in whatever way a particular problem demands. But this is not necessarily a straightforward task; the source code for *Gerris* is rather complex. On the other hand,

*The height function curvature algorithm is currently only implemented in 2D. For 3D simulations, a less accurate, but still adequate, curvature estimation algorithm is available.

†`http://gerris.dalembert.upmc.fr/gerris/tests/tests/index.html`

‡`http://gerris.dalembert.upmc.fr/gerris/examples/examples/bubble.html`

*Gerris* was designed with flexibility in mind, and it is frequently unnecessary to modify the source code directly. The functionality of *Gerris* can be controlled by user-defined events (or `GfsEvents`, in *Gerris*-speak). During each timestep, *Gerris* reads through the list of user-defined events and executes whichever events have been scheduled for that particular timestep. Examples of such events include initialization of arbitrary variables, controlling/updating boundary conditions, and even executing arbitrary C code that is written in the input file and compiled on-the-fly. We will see in Section 3.6 how to exploit this feature to simulate a moving reference frame that can follow a moving bubble while maintaining the time-accuracy of the simulation. In short, the possibilities are endless, and this was one of the motivations for choosing *Gerris* in this project (although, at the time of making that decision, the extent of this flexibility was not fully realized).

## 3.3 Problem description

Consider the fluid domain illustrated in Fig. 3-1 consisting of an initially spherical bubble with diameter $D$ submerged within a fluid cylinder of length $L$ and radius $W$. The bubble has density $\rho_v$ and dynamic viscosity $\mu_v$, whereas the surrounding fluid has density $\rho_l$ and dynamic viscosity $\mu_l$. We choose the bubble diameter as our length scale, and thus introduce the dimensionless coordinates, $x = x^*/D$ and $r = r^*/D$. We use the gravitational velocity scale, $U_c = \sqrt{gD}$, and similarly introduce the dimensionless velocity, $\mathbf{u} = \mathbf{u}^*/U_c$. This choice of length and velocity scales yields a characteristic time scale, $t_c = D/U_c = \sqrt{D/g}$. Density and viscosity are scaled relative to the density $\rho_l$ and viscosity $\mu_l$ of the liquid phase. In particular, if $H = H(\mathbf{x}, t)$ denotes the phase marker function satisfying $H = 1$ in the bubble and $H = 0$ in the surrounding liquid (*cf.* Fig. 3-1), then the density can be written

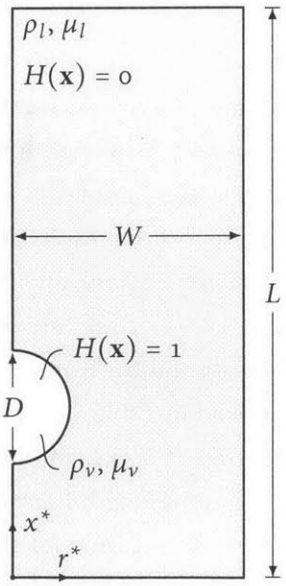


**Figure 3-1:** Illustration of the axisymmetric rising bubble problem.

$$\rho(\mathbf{x}, t) = \rho(H(\mathbf{x}, t)) = 1 + H(\mathbf{x}, t)\left(\frac{\rho_v}{\rho_l} - 1\right). \qquad (3.1)$$

The viscosity is taken to be the harmonic mean of the viscosities of the individual phases, which can yield better approximations of the velocity gradients near the interface compared to the arithmetic

average [129]. Thus, the viscosity can be written as

$$\mu(\mathbf{x},t) = \mu(H(\mathbf{x},t)) = \left[1 + H(\mathbf{x},t)\left(\frac{\mu_l}{\mu_v} - 1\right)\right]^{-1} \tag{3.2}$$

With these definitions, the dimensionless Navier-Stokes equations are given by

$$\frac{D\mathbf{u}}{Dt} = \frac{1}{\rho}\left\{-\nabla p + \frac{1}{\mathrm{Ga}}\nabla\cdot\left[\mu(\nabla\mathbf{u} + \nabla\mathbf{u}^{\mathsf{T}})\right] + \frac{1}{\mathrm{Bo}}\kappa\hat{\mathbf{n}}\delta_S\right\} + \hat{\mathbf{g}}, \tag{3.3}$$

where $\hat{\mathbf{g}}$ is the unit vector parallel to the gravitational acceleration vector ($\mathbf{g} = g\hat{\mathbf{g}}$), $\hat{\mathbf{n}}$ is the unit normal vector to the interface, $\kappa = -\nabla\cdot\hat{\mathbf{n}}$ is the mean curvature of the interface, $\delta_S$ is the surface delta function, and Bo and Ga denote, respectively, the Bond (a.k.a. Eötvös) number and the Galilei number, defined as

$$\mathrm{Bo} \equiv \frac{\rho_l g D^2}{\sigma} \qquad \text{(Bond/Eötvös number)}$$

$$\mathrm{Ga} \equiv \frac{\rho_l g^{\frac{1}{2}} D^{\frac{3}{2}}}{\mu_l} \qquad \text{(Galilei number)}$$

It is clear from Eq. (3.3) that Ga controls the amount of viscous diffusion in our problem and Bo controls the effective surface tension.

The numerical simulation of rising bubbles has been studied extensively by Hua and Lou [61], who report the results of severals test cases under a variety of Bond and Galilei numbers,[§] of which we consider six. Specifically, we consider cases A1–A3 and B1–B3 from Hua and Lou [61], summarized in Table 3.1. The nominal domain size was $6D\times 18D$ (i.e., $W = 6D$ and $L = 3W$ in Fig. 3-1), but the length $L$ was adjusted as needed to allow sufficient time for the bubble to reach terminal velocity. Hua and Lou [61] found boundary effects to be negligible for $W \gtrsim 4D$, and consequently chose $W = 4D$; we have opted to use a slightly larger domain for our simulations. Mesh adaptivity was employed using the vorticity, volume fraction, and curvature as refinement criteria.

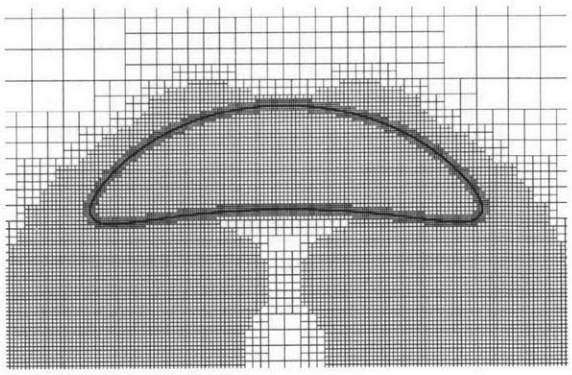

**Figure 3-2:** Representative mesh for the rising bubble simulations illustrating adaptive mesh refinement.

[§]Instead of the Galilei number, Hua and Lou refer to a modified Reynolds number, $\mathrm{Re}^*$, which is identical to the Galilei number defined above. In subsequent work, Hua et al. [62] refer to the same quantity as the Archimedes number, Ar.

In other words, the mesh was refined within the bubble as well as in regions of high vorticity and interface curvature; see Fig. 3-2 for a representative illustration of the resulting mesh when the bubble reached its terminal velocity. Note, in particular, the fine resolution around the bubble interface as well as the higher refinement in the regions of high vorticity in the bubble's wake.

**Table 3.1:** Summary of rising bubble simulations with *Gerris* (see also Fig. 3-4). The left half of the table describes the inputs for the test cases from Hua and Lou [61]. The right half of the table compares the predicted terminal Reynolds number with the simulations of Hua & Lou [61] and experimental data of Bhaga & Weber [12]. %-error for simulations (compared to experimental data) listed in parentheses.

| | | | | | Terminal Reynolds number ($Re_\infty$) | | | | |
|---|---|---|---|---|---|---|---|---|---|
| Case | Bo | Ga | $\rho_l/\rho_v$ | $\mu_l/\mu_v$ | Bhaga & Weber | Hua & Lou | | *Gerris* | |
| A1 | 8.67 | 0.970 | 1000 | 100 | 0.078 | 0.071 | (9.63%) | 0.083 | (6.31%) |
| A2 | 17.70 | 1.671 | 1000 | 100 | 0.232 | 0.211 | (9.05%) | 0.252 | (8.69%) |
| A3 | 32.20 | 79.88 | 1000 | 100 | 55.3 | 52.96 | (4.23%) | 54.00 | (2.34%) |
| B1 | 116.0 | 6.546 | 1000 | 100 | 2.47 | 2.32 | (6.18%) | 2.42 | (1.85%) |
| B2 | 116.0 | 8.747 | 1000 | 100 | 3.57 | 3.62 | (1.45%) | 3.75 | (5.04%) |
| B3 | 116.0 | 13.95 | 1000 | 100 | 7.16 | 7.00 | (2.19%) | 7.12 | (0.56%) |

## 3.4 Results and discussion

Table 3.1 lists the computed terminal Reynolds numbers ($Re_\infty$) for each of the six simulations. Also listed are the corresponding results from Hua and Lou [61] and the experimentally measured values of Bhaga and Weber [12]. Figure 3-4 presents a comparison of the terminal interface shapes predicted with *Gerris* with the results of Hua and Lou [61] and the observations of Bhaga and Weber [12]. The agreement with the simulations is quite good, and the predicted shapes are in reasonable agreement with the observations. In addition, Figure 3-4 illustrates time-traces of the bubble's velocity for each case, also plotting the results from Hua and Lou [61] and Bhaga and Weber [12] for comparison. For Cases A1 and A2, the analytical solution of Hadamard and Rybczynski (see, e.g., [11]) is also plotted for comparison. The Hadamard–Rybczynski solution is applicable only for spherical bubbles in an infinite (unbounded) domain, and is given by

$$\frac{U}{U_c} = \frac{\mathrm{Ga}}{18}\left(1 - \frac{\rho_v}{\rho_l}\right)\left[\frac{1 + \frac{\mu_l}{\mu_v}}{1 + \frac{2}{3}\frac{\mu_l}{\mu_v}}\right] \tag{3.4}$$

Analytical solutions exist also for the terminal velocity of spherical bubbles in finite domains (see, e.g., Haberman and Sayre [48]), but these results are applicable for no-slip wall boundaries. In any case,

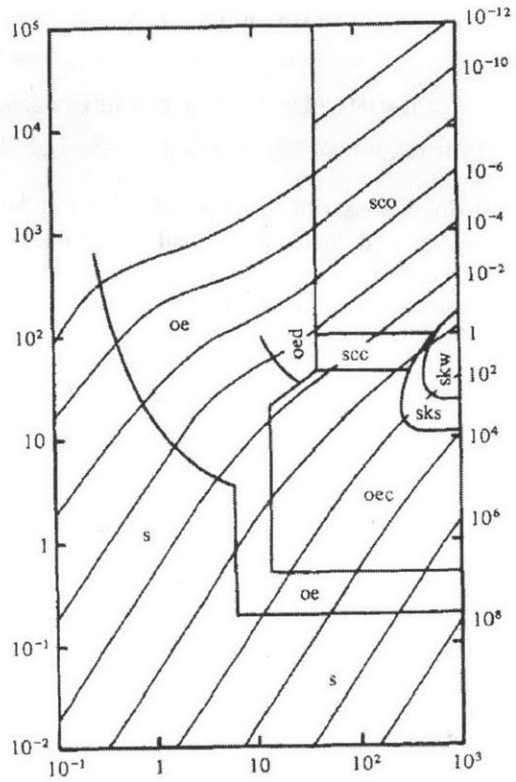


**Figure 3-3:** Bubble shape map (from Whalley [141]).

our computed solutions, where applicable, agree very well with the infinite-domain solution (3.4). For case A3, the bubble's velocity was significantly higher than either case A1 or A2. Moreover, the bubble took longer to reach its terminal velocity, and consequently, the domain length had to be extended to $L = 48D$. In this case, also, the bubble shape was seen to resemble that of a spherical cap, for which the terminal velocity can be approximated by [141]:

$$\frac{U}{U_c} = 0.71\left[1 - \frac{\rho_v}{\rho_l}\right]^{\frac{1}{2}} \approx 0.71. \tag{3.5}$$

This spherical cap approximation has also been plotted in Fig. 3-4 for case A3, and is seen to closely approximate the computed terminal velocity. Note, however, that according to the flow map in Fig. 3-3, this particular case would fall somewhere between ellipsoidal and spherical cap. In all cases, the *Gerris* results are found to agree reasonably well with the existing data, particularly for the B-series tests (high-Bo).

To further validate the results from Gerris, convergences studies for cases A1 and B1 were carried

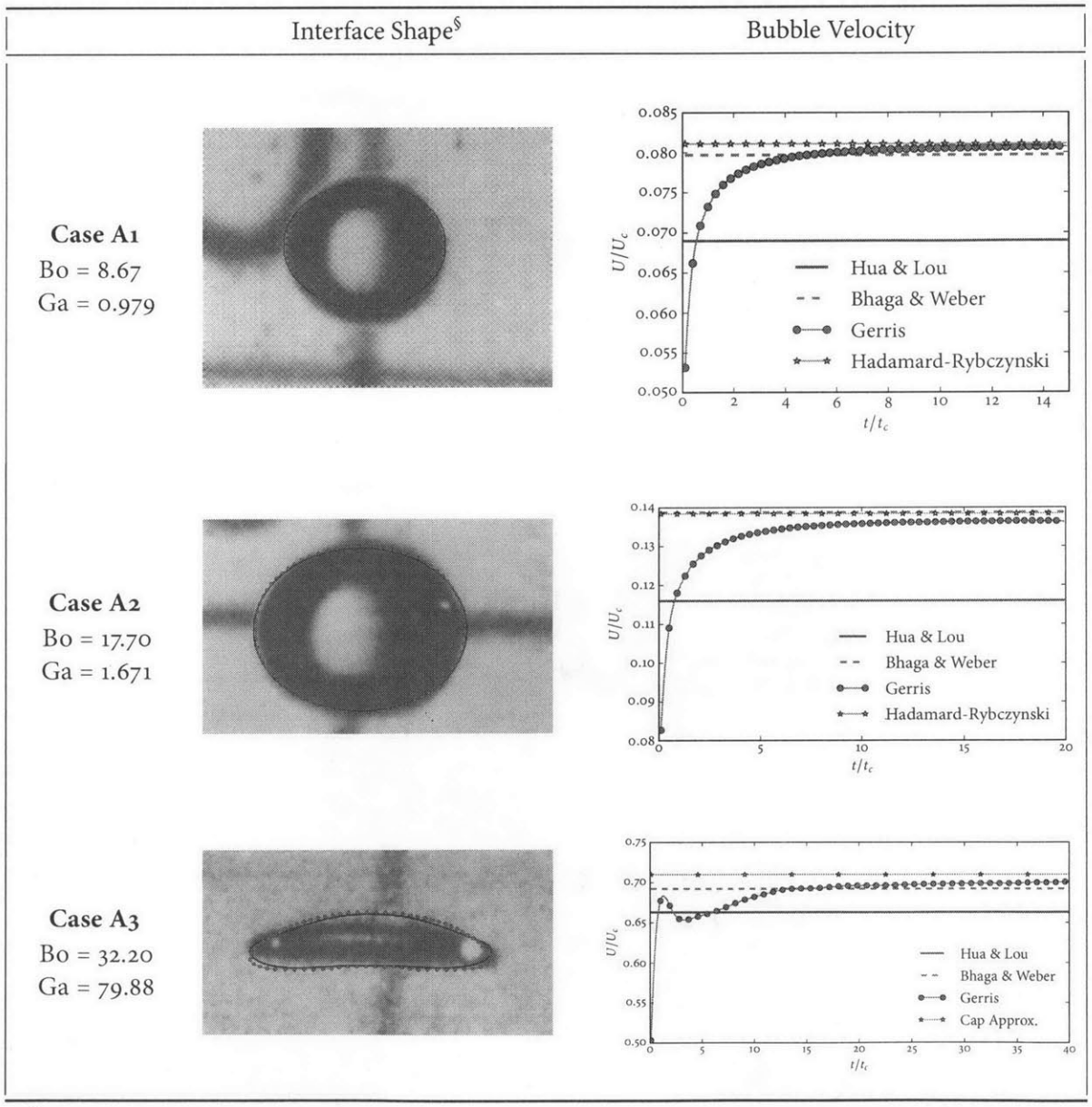


**Figure 3-4:** Comparison of terminal bubble shape and velocity with front tracking simulations of Hua & Lou [61] and experimental observations of Bhaga & Weber [12].

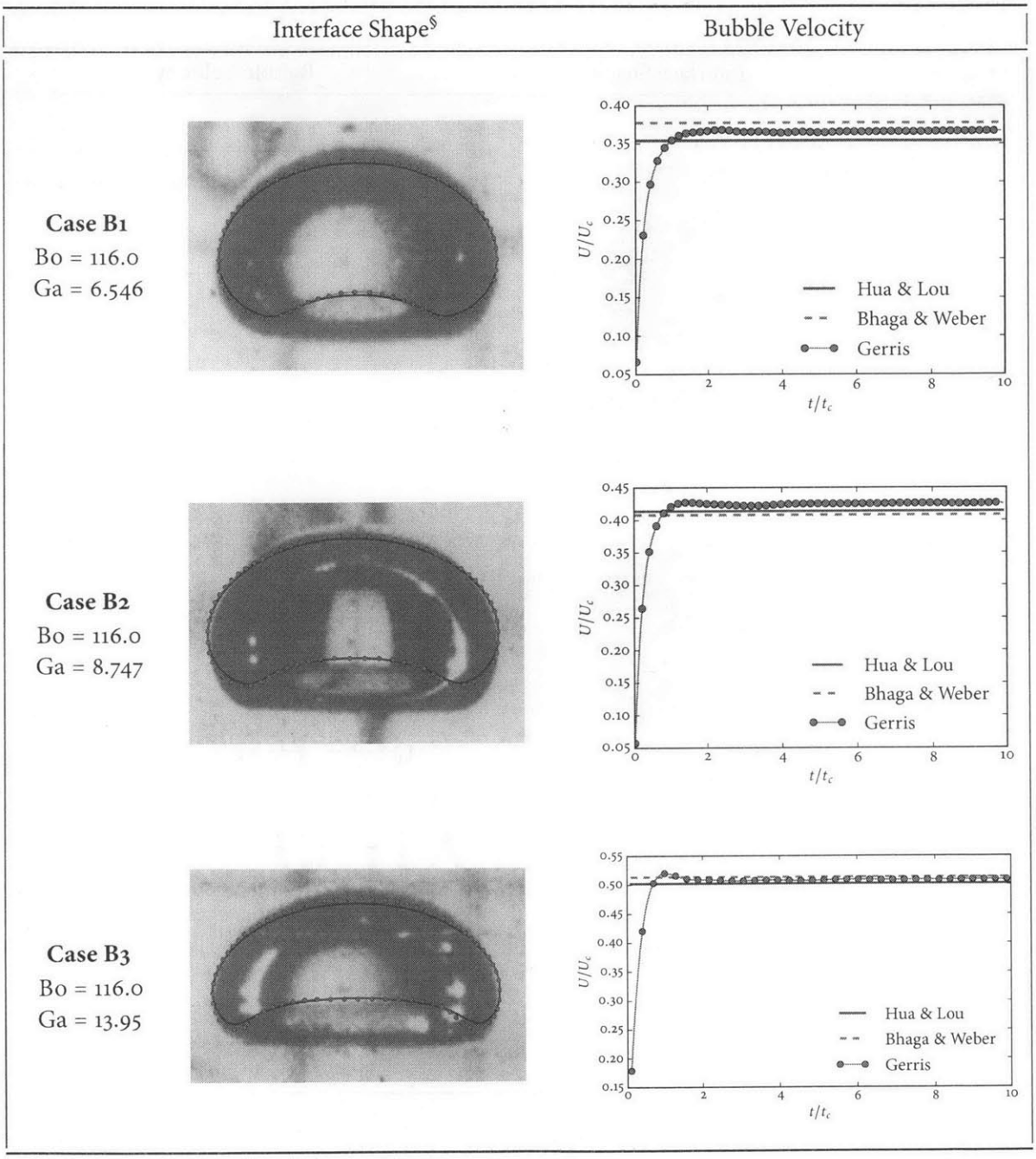


**Figure 3-4 (cont.):** Comparison of terminal bubble shape and velocity with front tracking simulations of Hua & Lou [61] and experimental observations of Bhaga & Weber [12].

out. As discussed previously, *Gerris* uses a quad-tree data structure to handle mesh generation and refinement. The grid resolution is set by specifying a refinement level, $\ell$, that determines the depth of the tree. $\ell = 0$ implies no refinement—the entire box is treated as a single cell of width $W$. $\ell = 1$ means one level of refinement—the box is split into four cells (in 2D, or eight cells in 3D), each of width $W/2$. In general, for a given refinement level, $\ell$, the mesh spacing is given by $h = W2^{-\ell}$. In our first convergence study (case A1), the simulation was performed on a sequence of 5 grids with "background" refinement levels $\ell = 3, 4, 5, 6$, and 7. In the vicinity of the bubble interface, however, additional refinement was enabled; for a given background refinement level $\ell$, the refinement level at the interface was taken as $\ell' = \ell + 3$. Figure 3-5a plots the location of the bubble's centroid as well as the bubble's velocity as computed on each of the five grids, and Fig. 3-5b illustrates the roughly second-order convergence rate in the terminal velocity estimate. Note that the large scatter seen in the velocity plot (Fig. 3-5a) is due to the way in which the bubble's velocity was computed, i.e., by computing the time-derivative of the instantaneous centroid location using a finite difference scheme. When the mesh is very coarse, the estimate of the centroid location experiences slight perturbations as the grid is dynamically refined and coarsened, and these perturbations are amplified in the computation of the bubble's velocity. As discussed later when describing the moving-frame implementation, a more robust estimation of the velocity can be obtained by computing the volume-averaged velocity within the bubble,

$$U_b(t) = \frac{\int \mathbf{u}(\mathbf{x}, t) H(\mathbf{x}, t)\, \mathrm{d}\mathbf{x}}{\int H(\mathbf{x}, t)\, \mathrm{d}\mathbf{x}}. \tag{3.6}$$

Our second convergence study considered case B3. From the previous results, it was observed that terminal velocity for the B-series of tests was insensitive to the domain width due to the relatively high Galilei number (compared to case A1 and A2). Consequently, to cut costs, the domain was downsized by a factor of two from $W = 6D$ to $W = 3D$. This modification had no noticeable effect on the computed terminal velocity, but it means that the refinement levels now correspond to different mesh spacings compared to the previous convergence study. In particular, the highest refinement level $\ell = 6$ for this case gives the same mesh spacing, $h = W2^{-\ell}$ as the $\ell = 7$ case for the previous study. The results are summarized in Fig. 3-6, and are seen to be similar to those illustrated in Fig. 3-5.

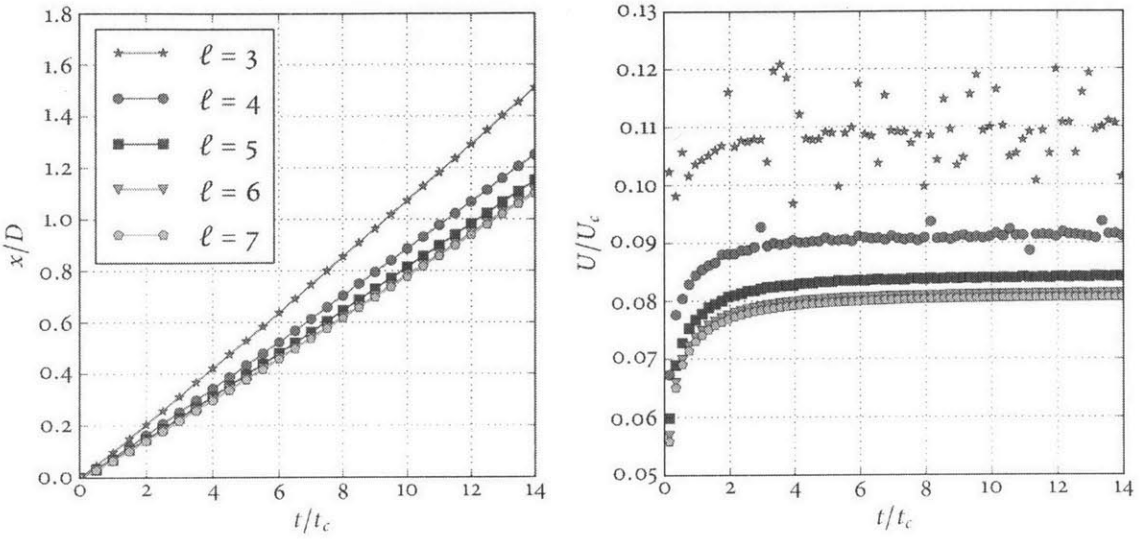


**(a)** Bubble location and velocity under mesh refinement

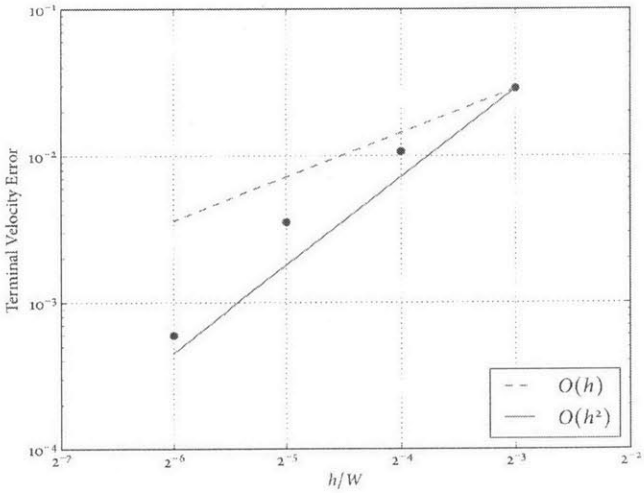


**(b)** Terminal velocity error under mesh refinement. The "true" terminal velocity was taken to be that computed for $\ell = 7$.

**Figure 3-5:** Convergence study for case A1.

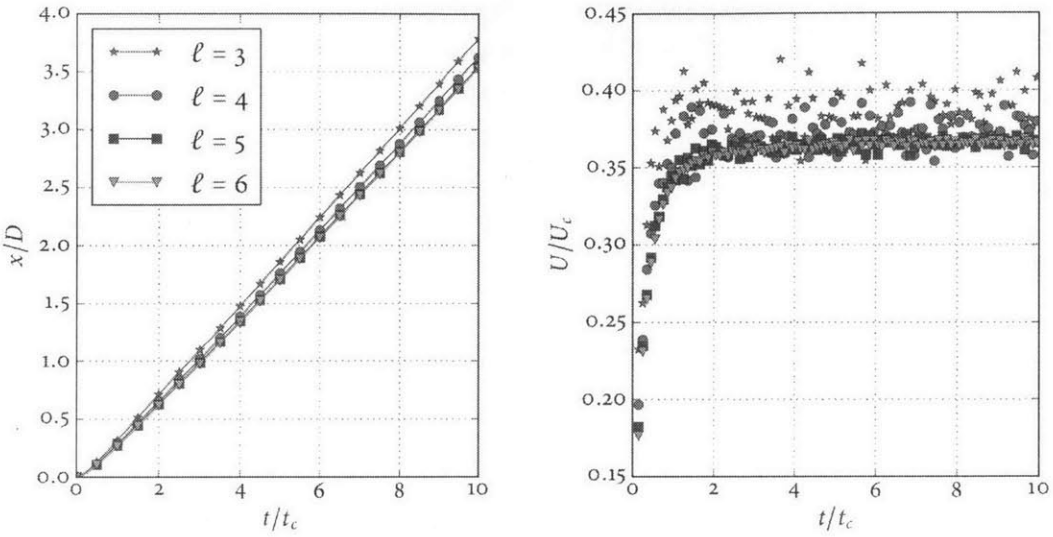


**(a)** Bubble location and velocity under mesh refinement

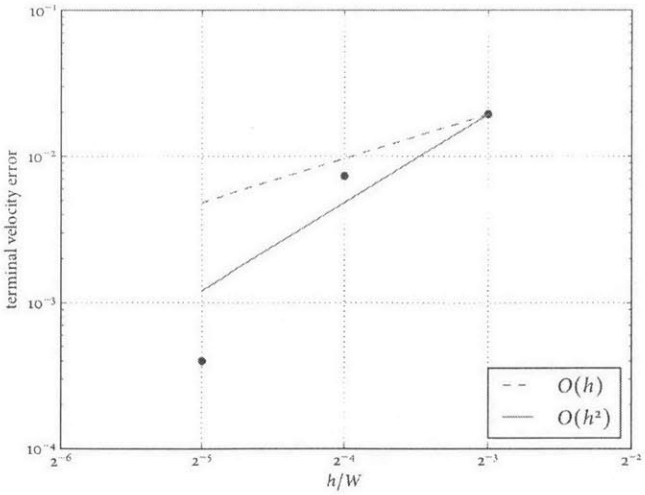


**(b)** Terminal velocity error under mesh refinement. The "true" terminal velocity was taken to be that computed for $\ell = 6$.

**Figure 3-6:** Convergence study for case B1.

## 3.5 The stochastic bubble rise problem

We now consider the effect of assigning uncertainties (probability distributions) to the inputs of our simulation. As our intention is to demonstrate the application of the gPC expansion to multiphase flow simulations, and to show that it is still possible to obtain useful results despite the noted shortcomings of the gPC expansion, the problems that we consider are fairly simple, each involving only a single random input. Of course, the methodology could be applied to more complex problems involving more random inputs, but computational cost (the number of necessary evaluations) will increase accordingly; strategies to minimize the requisite number of simulations (e.g., sparse grid quadratures) were discussed at length in Chapter 2.

### Case 1

Our first example derives from the B-series cases described above. We fix Bo = 116, $\rho_l/\rho_v$ = 1000, and $\mu_l/\mu_v$ = 100, but suppose the Galilei number is uncertain. Physically, this corresponds to an uncertainty ascribed to the viscosity of the liquid since $\rho_l$, $g$, and $D$ are effectively fixed by the Bond number (which is not uncertain in this example). We take Ga to be uniformly distributed between 1 and 50, i.e., Ga $\sim \mathcal{U}[1, 50]$. This is not necessarily reflective of any physically meaningful uncertainty distribution; it was merely selected as being a sufficiently large distribution that some noticeable variation would be observable in the simulations. Our quantity of interest (QoI) is the bubble's terminal velocity, $U_b$.

To model the uncertainty in Ga, we introduce an auxiliary variable $\xi \sim \mathcal{U}[-1, 1]$, and write $\mathrm{Ga}(\xi) = \frac{51}{2} + \frac{49}{2}\xi$. We thus seek to estimate the unknown resultant distribution of $U_b(\xi) \sim ?$, which we can do using the gPC expansion. Specifically, since our independent variable $\xi$ is uniformly distributed, the natural basis to choose is the Legendre polynomials. Let us suppose $U_b(\xi)$ can be adequately represented using an $7^{\text{th}}$-order Legendre-PC expansion; then

$$U_b(\xi) \approx \sum_{k=0}^{7} \hat{U}_k \Psi_k(\xi), \tag{3.7}$$

where

$$\hat{U}_k = \frac{\mathbb{E}[U_b(\xi)\Psi_k(\xi)]}{\mathbb{E}[\Psi_k^2(\xi)]} = \frac{\int_{-1}^{1} U_b(\xi)\Psi_k(\xi)\frac{1}{2}\mathrm{d}\xi}{\int_{-1}^{1} \Psi_k^2(\xi)\frac{1}{2}\mathrm{d}\xi}. \tag{3.8}$$

To compute the coefficients in (3.8) we use a 9-point Gauss–Legendre quadrature, for a maximum polynomial precision of 16; this quadrature will thus compute exactly the coefficients, $\{\hat{U}_k\}_{k=0}^{7}$, in the unlikely event that $U_b(\xi)$ happens to be a polynomial of order 8 or less, but will, in general, only

**Table 3.2:** Summary of quadrature points and model evaluations for stochastic rising bubble problem (case 1) and the computed Legendre-PC expansion coefficients for the terminal velocity.

| $i$ | $\xi_i$ | $w_i$ | $\mathrm{Ga}(\xi_i)$ | $U_b(\xi_i)$ | $k$ | $\mathbb{E}[\Psi_k^2]$ | $\hat{U}_k$ |
|---|---|---|---|---|---|---|---|
| 0 | −0.968160 | 0.040637 | 1.780 | 0.136 | 0 | 1.000 | $5.260 \times 10^{-1}$ |
| 1 | −0.836031 | 0.090324 | 5.017 | 0.316 | 1 | 0.333 | $1.645 \times 10^{-1}$ |
| 2 | −0.613371 | 0.130306 | 10.472 | 0.466 | 2 | 0.200 | $-1.295 \times 10^{-1}$ |
| 3 | −0.324253 | 0.156174 | 17.556 | 0.540 | 3 | 0.143 | $8.098 \times 10^{-2}$ |
| 4 | 0.000000 | 0.165120 | 25.500 | 0.575 | 4 | 0.111 | $-4.527 \times 10^{-2}$ |
| 5 | 0.324253 | 0.156174 | 33.444 | 0.596 | 5 | 0.091 | $2.172 \times 10^{-2}$ |
| 6 | 0.613371 | 0.130306 | 40.528 | 0.605 | 6 | 0.077 | $-5.435 \times 10^{-3}$ |
| 7 | 0.836031 | 0.090324 | 45.983 | 0.609 | 7 | 0.067 | $9.022 \times 10^{-4}$ |
| 8 | 0.968160 | 0.040637 | 49.220 | 0.612 | | | |

approximate these coefficients. The coefficients are thus approximated as

$$\hat{U}_k \approx A_k^{-1} \sum_{i=0}^{8} U_b(\xi_i) \Psi_k(\xi_i) w_i,$$

where the normalization factors, $A_k^{-1} = \mathbb{E}[\Psi_k^2(\xi)]$, can be computed exactly *a priori*. The Gauss–Legendre quadrature nodes and weights are listed in Table 3.2. Also listed are the corresponding computed values for the terminal velocity, $U_b(\xi_i)$, as well as the Legendre-PC expansion coefficients $\hat{U}_k$.

After computing the coefficients, $\{\hat{U}_k\}_{k=0}^{7}$, we can readily evaluate the mean and variance of the terminal velocity using the orthogonality properties of the gPC expansion:

$$\mathbb{E}[U_b] \approx \hat{U}_0 = 0.526$$

$$\operatorname{var} U_b \approx \sum_{k=1}^{7} \hat{U}_k^2 \, \mathbb{E}[\Psi_k^2] = 0.0136.$$

Moreover, it is a simple matter to perform Monte Carlo sampling using the Legendre-PC expansion from Eq. (3.7) as a surrogate for *Gerris* to obtain an estimate for the probability density function of the terminal velocity.

Figure 3-7 shows snapshots of the interface shape taken at 1 second intervals for each of the 9 simulations. It is seen that for $\mathrm{Ga} \gtrsim 30$, all the simulations yield nearly identically shaped (dimpled ellipsoidal caps) bubbled that, consequently, have nearly identical terminal velocities $U_b \approx 0.6$. Physically, once the liquid viscosity is sufficiently small (equivalently, Ga sufficiently large), further reduction of the viscosity has no significant influence on the terminal velocity; at this point, the

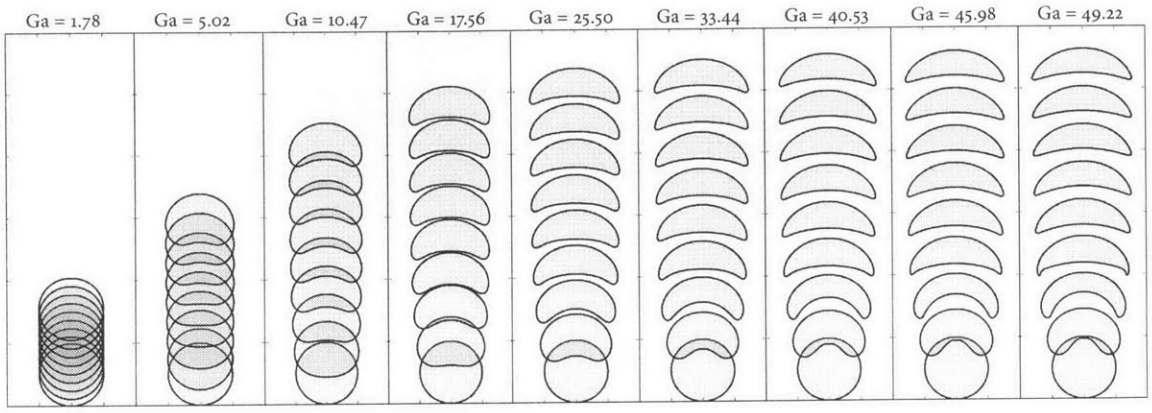


**Figure 3-7:** Snapshots of interface position taken at one second intervals for each of the 9 quadrature samples for the stochastic rising bubble problem: Bo = 116, $\rho_l/\rho_v$ = 1000, $\mu_l/\mu_v$ = 100, and Ga $\sim \mathcal{U}[1, 50]$.

terminal velocity is determined by form drag as opposed to viscous stresses. As a result, we expect the probability distribution of the terminal velocity to be heavily skewed, with most of the probability density being concentrated about $U_b$ = 0.6. This is, indeed, the case, as seen from Fig. (3.7), which plots which plots the time-dependent velocity for each case (left) as well as the estimated probabilty density of $U_b$ (right).

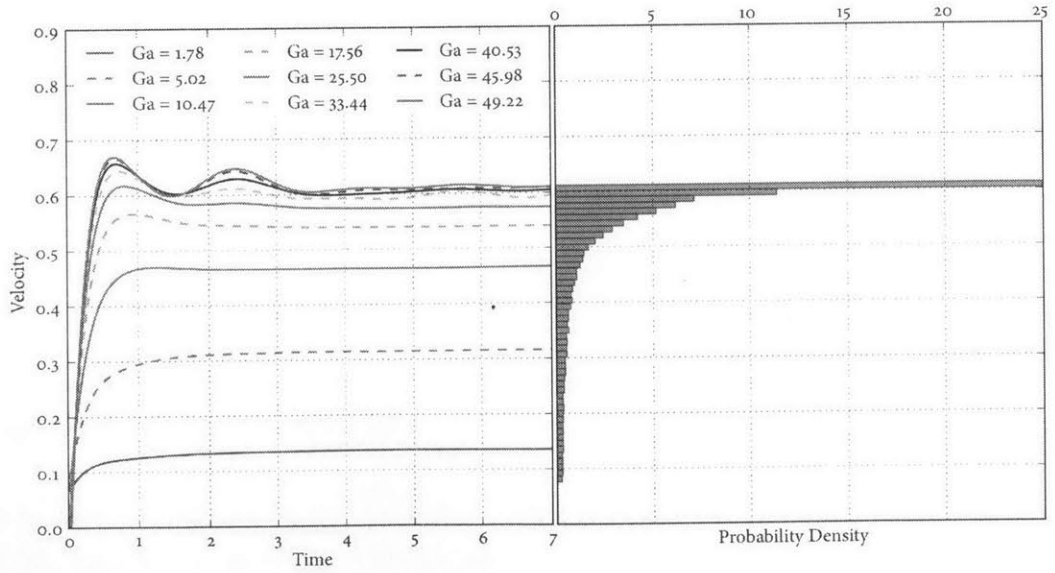


**Figure 3-8:** Bubble rise velocity (left) and probability density (right) for the stochastic rising bubble problem: Bo = 116, $\rho_l/\rho_v$ = 1000, $\mu_l/\mu_v$ = 100, and Ga $\sim \mathcal{U}[1, 50]$.

### Case 2

Our second example addresses the following question: for a given probability distribution of possible bubble sizes (diameters), what is the resulting uncertainty in the bubble velocity as a function of time, $t$? We assume that the bubble diameter is log-normally distributed, i.e.,

$$D(\xi) = D_0 \exp(0.15\xi), \quad \xi \sim \mathcal{N}(0,1),$$

where we have taken $D_0 = 1$. The quantity of interest is the time-dependent bubble velocity, $U_b(t;\xi)$. Since $\xi \sim \mathcal{N}(0,1)$ is Gaussian, its natural basis is the Hermite polynomials. Hence, we seek an approximation of $U_b(t;\xi)$ in terms of the Hermite basis:

$$U_b(t;\xi) \approx \sum_{k=0}^{P} \hat{U}_k(t)\Psi_k(\xi),$$

where $\Psi_k$ denotes the $k$-th Hermite polynomial. Similarly to the previous example, the stochastic modes are computed as

$$\hat{U}_k(t) = \frac{\mathbb{E}[U_b(t;\xi)\Psi_k(\xi)]}{\mathbb{E}[\Psi_k^2(\xi)]},$$

where, now,

$$\mathbb{E}[U_b(t;\xi)\Psi_k(\xi)] = \int_{-\infty}^{\infty} U_b(t;\xi)\Psi_k(\xi)\left[\frac{1}{\sqrt{2\pi}}\exp\left(-\frac{\xi^2}{2}\right)\right] d\xi$$

$$\approx \sum_i U_b(t;\xi_i)\Psi_k(\xi_i)w_i$$

We can write the Galilei and Bond numbers as follows:

$$\mathrm{Ga} = \mathrm{Mo}^{-1}\left(\frac{D}{D_0}\right)^{\frac{3}{2}}, \qquad \mathrm{Bo} = \mathrm{Mo}^{-1}\left(\frac{D}{D_0}\right)^{2},$$

where

$$\mathrm{Mo} \equiv \frac{g\mu_l^4}{\rho_l\sigma^3} \qquad \text{(Morton number)}$$

is the *Morton number*. To complete the specification of the problem, we take $\mathrm{Mo} = 0.1$.

Figure 3-9 illustrates the time-dependent velocity for each of 9 simulations corresponding to a 9-point Gauss–Hermite quadrature. Also plotted is the time-dependent probability density estimated from a $7^{\text{th}}$-order Hermite-PC expansion. Interestingly, for this choice of parameters, it is seen that the bubble's velocity is very nearly Gaussian after a short, initial transient. Consequently, the Hermite-PC

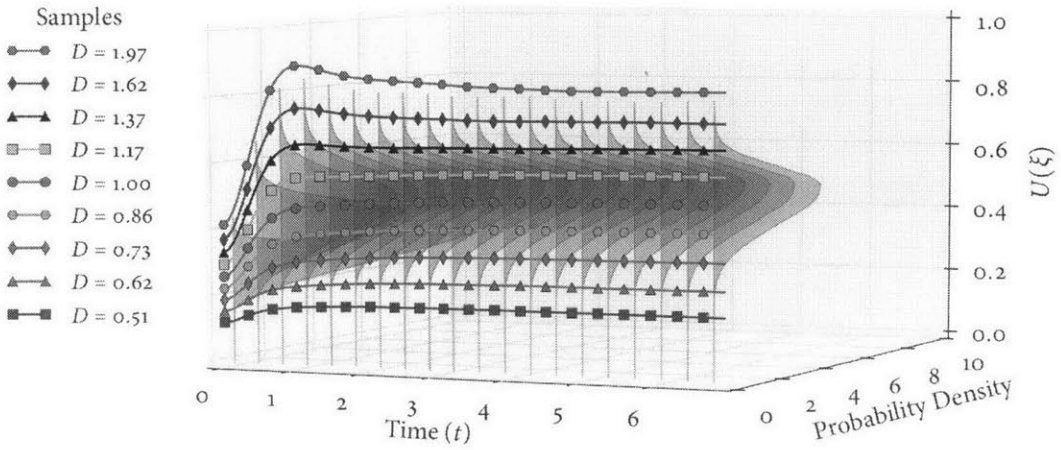


**Figure 3-9:** Time-evolution of the probability density of the bubble's velocity.

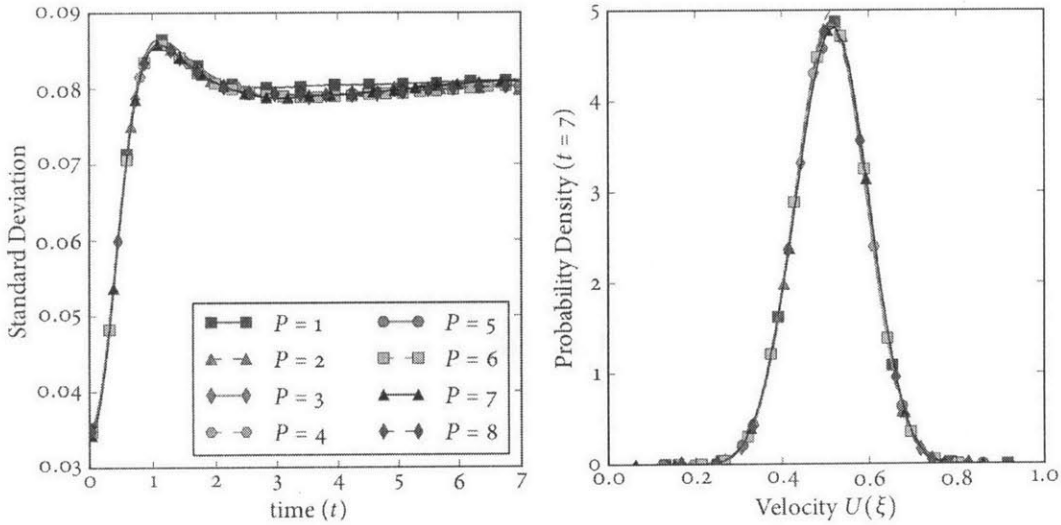


**Figure 3-10:** Standard deviation of bubble velocity (left) and probability density of bubble velocity at $t = 7$ (right).

basis turns out to be the optimal basis in which to represent the bubble's velocity, and converges quite rapidly. If $U_b$ were truly Gaussian, we would expect the Hermite-PC expansion to converge after two terms ($P = 1$). To test this, we repeated the simulations to construct Hermite-PC expansions ranging from $P = 1$ to $P = 8$. The results are shown in Fig. 3-10. Indeed, we see essentially no change in the estimated standard deviation with increasing $P$. We also see no change in the probability density at $t = 7$. In other words, for this problem, we require only a first-order expansion to fully express the uncertainty in $U_b$, which we could have computed with only two simulations. This demonstrates the extreme rapidity with which the gPC expansion can converge if one happens to choose to the

optimal basis. Unfortunately, in general, there is no way to know *a priori* what that optimal basis is. Nevertheless, even if the choice of basis is sub-optimal, the gPC expansion may still converge quite rapidly, requiring only a dozen or so simulations.

## 3.6 Moving reference frame

Shortly after completion of the previous studies, it was realized how to exploit *Gerris*'s event system to implement a moving reference frame that can track a bubble. Of course, it is trivial to implement a reference frame that translates at a constant velocity, say $U_{\text{trans}}$. This situation is illustrated in Fig. 3-11. Compared to the control volume illustrated in Fig. 3-1, the only change is that the top and bottom boundaries are now inflow and outflow boundaries, respectively, and since the liquid surrounding the bubble is initially at rest relative to a stationary frame, the flow enters our moving domain with a uniform velocity $U_{\text{trans}}$. Relative to this moving frame, the bubble's velocity will be $U_b - U_{\text{trans}}$. At the very least, then, if we know approximately the bubble's terminal velocity, we can choose $U_{\text{trans}} \approx U_b$ and thus prevent the bubble from moving too far during the course of the simulation. But we can do even better. Listing 3.1 provides a snippet of "*Gerris*-script" the demonstrates the basic implementation of our moving reference frame. For brevity, only the essential elements have been listed; it is not a complete setup script. The basic strategy can be summarized as follows:

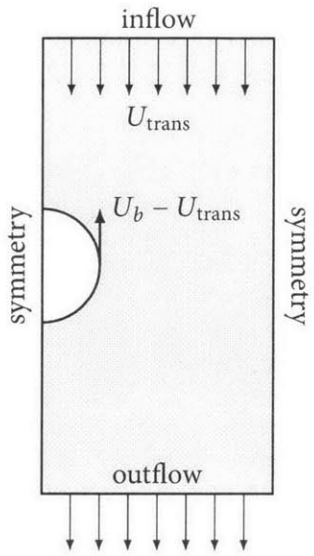


**Figure 3-11:** Control volume moving with velocity $U_{\text{trans}}$ containing a bubble moving with velocity $U_b$ relative to a stationary frame.

1. Evaluate the relative volume-averaged bubble velocity from Eq. (3.6) using the predefined `GfsSpatialSum` event, which performs spatial integration (summation) over the entire domain. The result is labeled `dv_bub` in Listing 3.1.

2. Estimate the acceleration of the reference frame, `a_frame`, using the current relative bubble velocity, and use this to augment the gravity source term.

3. Update the absolute translational velocity, `Utrans`, and use this value to impose the updated inflow velocity.

Listing 3.1: *Gerris* code snippet demonstrating the moving reference frame

```
2 1 GfsAxi GfsBox GfsGEdge {} {

    ## Declare T as our VOF tracer
    VariableTracerVOFHeight T

    ## compute bubble volume
    SpatialSum { istep = 1 } bubble_volume T

    ## compute relative bubble velocity
    SpatialSum { istep = 1 } dv_bub (U*T/bubble_volume)

    ## This is executed only at the start of simulation
    GfsInit {} {
        ## Utrans holds the translational velocity of the domain relative
        ## to a fixed coordinate system. This is needed to impose the inflow
        ## boundary condition
        Utrans  = 0.0
        ## a_frame stores the domain acceleration. This is needed to
        ## augment the gravity source term
        a_frame = 0.0
    }
    ## This is executed every subsequent timestep
    GfsInit {istart=1 istep=1} {
        ## update acceleration. dt is a predefined variable. Its value
        ## is the current timestep size.
        a_frame = dv_bub/dt
        ## increment translational velocity
        Utrans = Utrans + dv_bub
    }
    ## Augmented gravity source term
    GfsSource U -1.0-a_frame
}
## Boundary conditions have access to any variables defined in the main
## script above. In particular, we can make use of the currently computed
## value of Utrans to set the inflow velocity
GfsBox {
    bottom = GfsBoundary          ## r = 0: default symmetry boundary
    left = GfsBoundaryOutflow     ## x = 0
}
GfsBox {
    bottom = GfsBoundary          ## r = 0: default symmetry boundary
    right = GfsBoundaryInflowConstant -Utrans
}
1 2 right
```

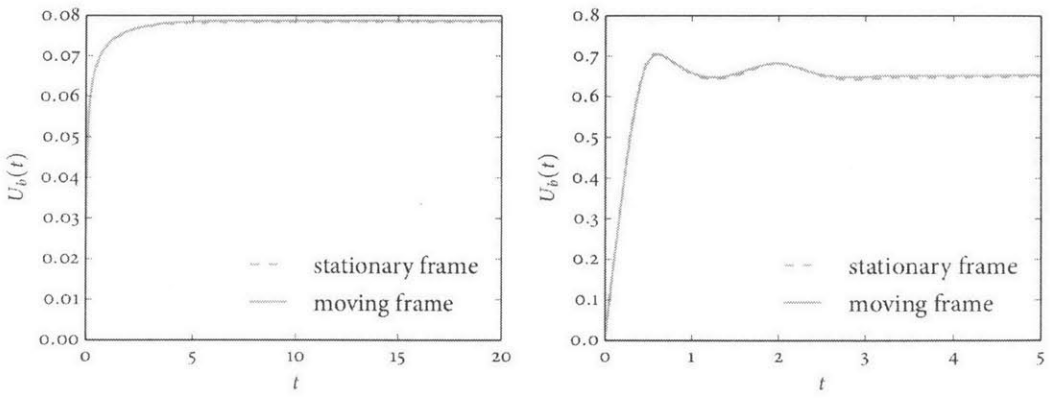


**(a)** Ga = 1, Bo = 5, $Re_\infty$ = 0.079 **(b)** Ga = 80, Bo = 40, $Re_\infty$ = 54.72

**Figure 3-12:** Comparison of time-dependent bubble velocity computed with stationary and moving reference frames.

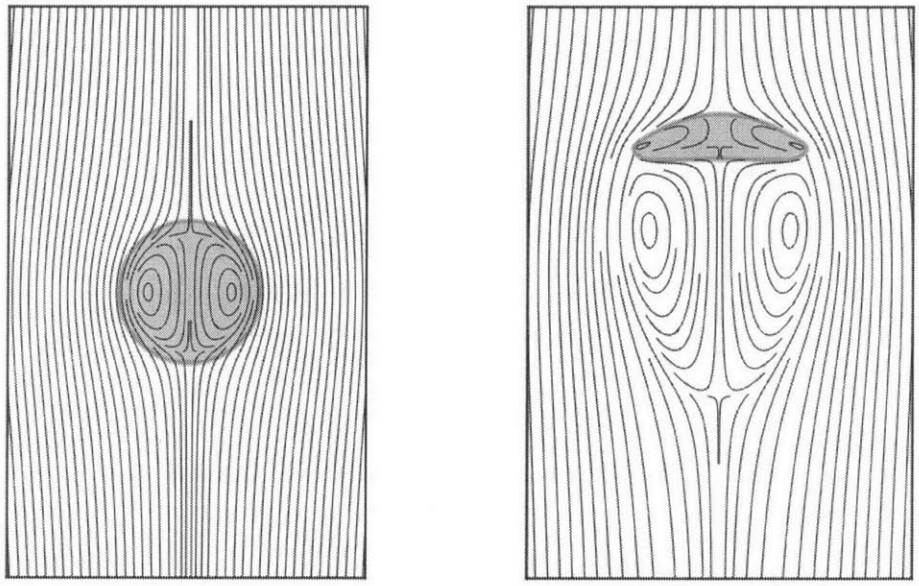

**(c)** Ga = 1, Bo = 5, $Re_\infty$ = 0.079 **(d)** Ga = 80, Bo = 40, $Re_\infty$ = 54.72

**Figure 3-13:** Illustration of terminal bubble shapes and streamlines relative to moving coordinate system.

Figure 3-12 compares the time-dependent bubble velocity computed relative to a stationary frame to that computed with the new moving frame implementation. For both of the cases illustrated, the difference between the stationary and moving frame implementations is nearly imperceptible. This is somewhat surprising considering the simplicity of our implementation. The terminal bubble shapes and streamlines for both cases are illustrated in Fig. 3-13.

A slightly more challenging case is shown in Fig. 3-14, illustrating the comparison for Ga = 200 and Bo = 10. For this particular case, the bubble does not reach a steady terminal velocity. Rather, the bubble experiences a series of shape oscillations and the velocity oscillations seen in Fig. 3-14 grow in amplitude until the bubble ultimately gets locked into a periodic vortex shedding cycle. The oscillatory behavior for this case was noted by Cano-Lozano et al. [16], but they did not provide any description of the behavior beyond that since they were investigating the steady terminal bubble shapes. Figure 3-15 plots the bubble's velocity over a single cycle and illustrates the vorticity being shed from the bubble. While the study of such phenomena is beyond the scope of this work, it is an interesting example of the sorts of phenomena that can be studied using the moving frame implementation described above.

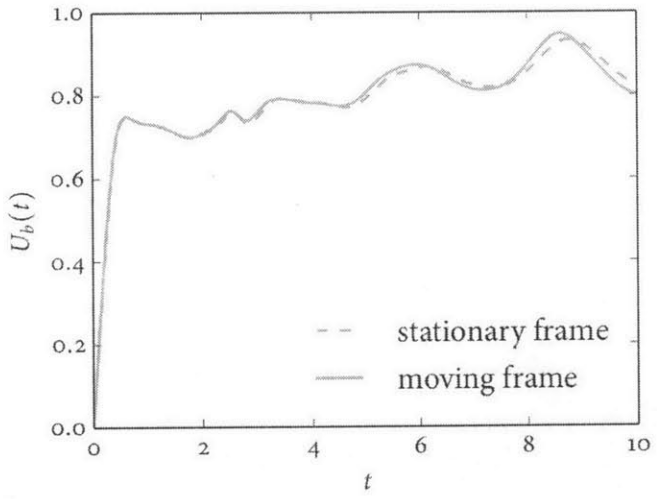


**Figure 3-14:** Comparison of time-dependent bubble velocity computed with moving and stationary reference frames: Ga = 200, Bo = 10

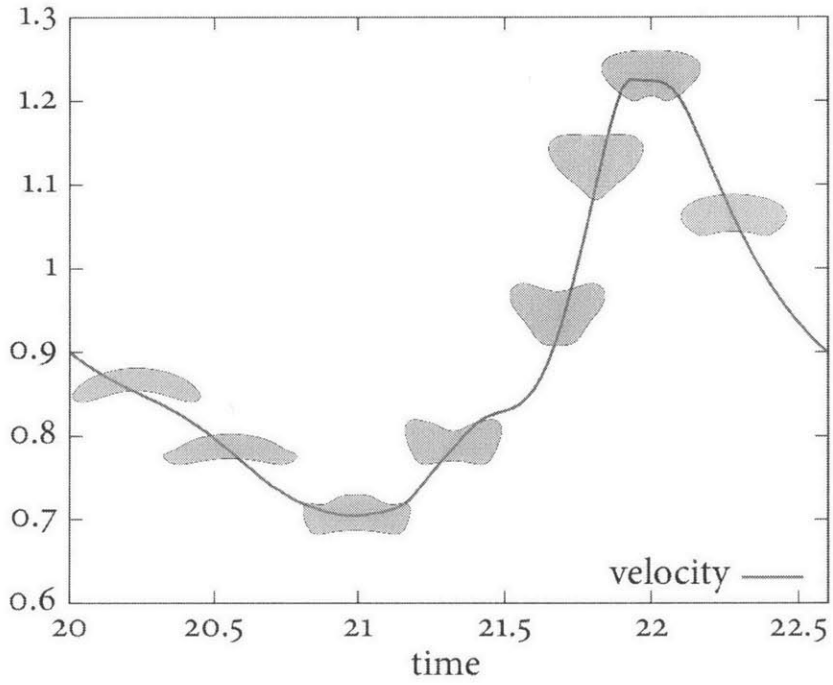


(a) Evolution of the shape and velocity of a bubble during a single vortex shedding cycle.

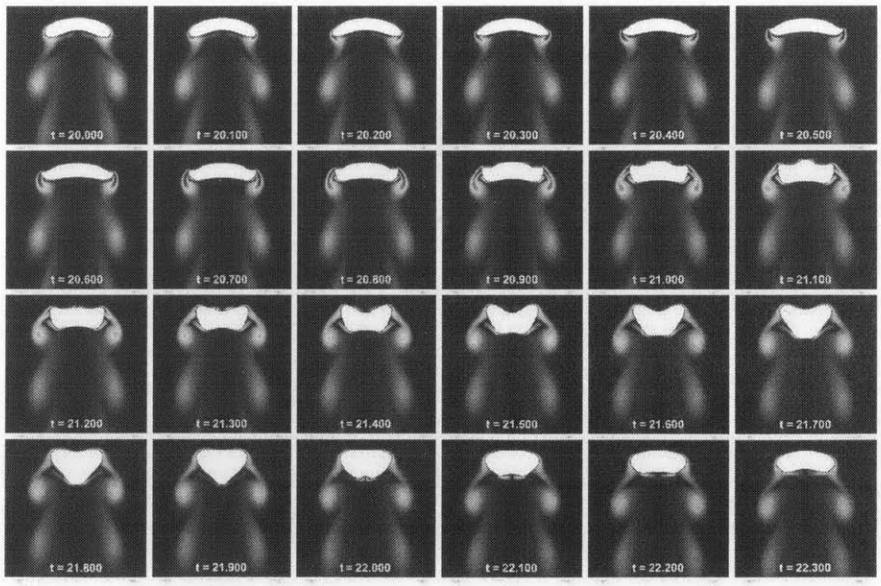


(b) Vortex shedding

**Figure 3-15:** Illustration of vortex shedding cycle for Ga = 200 and Bo = 10.

THIS PAGE INTENTIONALLY LEFT BLANK

# Chapter 4

# Computational Study of Capillary Slug Flow

## 4.1 Introduction

Capillary slug flow (a.k.a. Taylor flow, plug flow, bubble train flow, or segmented flow) refers to a multiphase flow regime characterized by the regular, periodic flow of large, elongated (capsule-shaped) bubbles/droplets that nearly fill the channel cross-section, being separated from the channel wall by a thin liquid film. These droplets, or *Taylor bubbles* as they are called in the case of a dispersed gas phase, typically have lengths several times the channel diameter, and are separated from one another by intermittent regions of liquid, called *slugs*.

Slug flow is a prominent flow regime for numerous industrial applications, including oil recovery [34], oil and gas production, and handling and transport of cryogenic fluids [35]. In nuclear power plants, slug flow is present in boiling water reactor (BWR) fuel assemblies as well as in the steam generators or pressurized water reactors (PWRs). Additionally, capillary slug flow has been exploited to enhance various chemical processes, such as microfiltration devices [25], chemical microprocessing (lab-on-a-chip) [47], and multiphase monolith reactors [34, 72, 126, 127, 132], due in part to its favorable mass transfer characteristics—flow recirculation in the liquid slugs promotes radial mixing, while the thin liquid film surrounding the bubbles inhibits inter-slug axial mixing. Such systems typically involve Taylor flow through an array of parallel channels, so the potential for flow instabilities is present [73, 132]. Understanding how the presence of Taylor bubbles affects the pressure drop in a

channel is crucial to establishing stability criteria for these systems to prevent flow oscillations. Slug flow also exhibits favorable heat and mass transfer characteristics. The thin liquid film surrounding the bubbles allows for high rates of heat and mass transfer between the bubble and the channel wall [50, 60, 73, 85, 86]. In such applications, the film thickness is a critical parameter for accurately predicting slug flow heat and mass transfer rates [49].

Depending on the particular application, various flow parameters are of interest to designers, including the film thickness, wetting/void fraction (or *liquid holdup*, as it is more commonly called in the oil and gas industry), bubble velocity, and pressure drop. As we show, many quantities, such as the film thickness, bubble velocity, and wetting/void fractions are interrelated, so computing any one of these quantities yields immediately the others [123]. These quantities are discussed more thoroughly in the following sections. Other quantities, such as bubble frequency, bubble length, and slug length, are primarily determined by the specific geometry and flow conditions at the inlet (e.g., the manner in which the gas is injected). Because these quantities are specific to a particular system, we shall not consider them here; or, rather, we shall only consider such quantities as (possibly uncertain) inputs to our problem, and make no attempt to model them.

In the following sections, we review the existing theory of capillary slug flow and review available correlations to predict the film thickness and pressure drop across a Taylor bubble. One of the objectives of this work is to validate the use of *Gerris* for slug flow simulations using the moving reference frame implementation described in Section 3.6. Section 4.4 discusses the results of our simulations using *Gerris*, and compares these results with the numerical and experimental data of other researchers. In total, more than 200 simulations were performed for nearly 150 different combinations of Reynolds and capillary numbers. Existing correlations for the film thickness require knowledge of the bubble's velocity, $U_b$, which is not always known *a priori*. Consequently, in Section 4.4.1, we propose a correlation that relates the bubble's velocity to the average liquid velocity $\bar{U}$ in the slug.

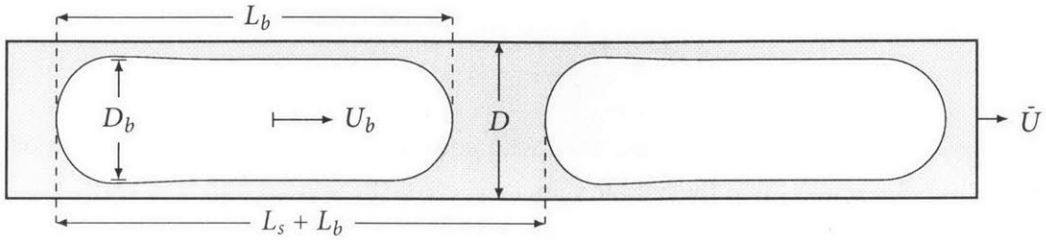


**Figure 4-1:** Slug flow schematic

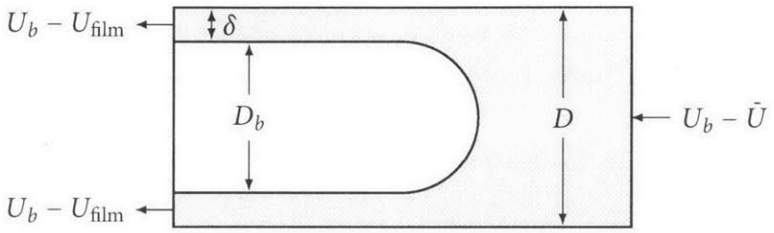


**Figure 4-2:** Mass conservation control volume (CV) around the nose of a Taylor bubble. $\bar{U}$ denotes the mean liquid velocity in the slug, $U_{\text{film}}$ the mean liquid velocity in the film, and $U_b$ the bubble velocity. As illustrated, the CV is translating with a velocity $U_b$ so that the bubble is stationary in this reference frame.

## 4.2 Background and theory

Let us begin by establishing some notation. Figure 4-1 illustrates a typical capillary slug flow configuration consisting of a series of bubbles of diameter $D_b$ and length $L_b$ traveling through a capillary of diameter $D$ with velocity $U_b$. The film thickness is denoted by $\delta = D - D_b$ (*cf.* Fig. 4-2). The bubbles are separated by a liquid slug of length $L_s$. $\bar{U}$ denotes the average liquid velocity in the slugs. We let $\rho_l$ and $\mu_l$ ($\rho_v$ and $\mu_v$) denote the density and dynamic viscosity of the liquid (vapor) phase. Other relevant quantities are the *void fraction* in the Taylor bubble region,

$$\alpha \equiv \frac{\pi D_b^2/4}{\pi D^2/4} = \left(\frac{D_b}{D}\right)^2 = \left(1 - 2\frac{\delta}{D}\right)^2, \tag{4.1}$$

and its complement, the *wetting fraction*, $W \equiv 1 - \alpha$.

Consider the control volume illustrated Fig. 4-2, which is moving with the bubble at a velocity $U_b$. The quantity $U_{\text{film}}$ in Fig. 4-2 is the liquid velocity in the film. It follows from mass conservation that

$$(\bar{U} - U_b)\frac{\pi D^2}{4} = (U_b - U_{\text{film}})\left(\frac{\pi D^2}{4} - \frac{\pi D_b^2}{4}\right) \iff \frac{U_b - \bar{U}}{U_b - U_{\text{film}}} = 1 - \left(\frac{D_b}{D}\right)^2 = W \tag{4.2}$$

If $U_{\text{film}} = 0$, Eq. (4.2) simplifies to

$$\frac{U_b - \bar{U}}{U_b} = W. \tag{4.3}$$

Notice that $W \geq 0$, so Eq. (4.3) implies $U_b \geq \bar{U}$, with equality only if $D_b = D$; that is, the presence of a *static* liquid film implies that the bubble velocity exceeds the average liquid velocity, a fact that was evidently first pointed out by Fairbrother and Stubbs [36] in 1935. Furthermore, the thicker the film, the faster the bubble travels. The quantity on the left-hand side of Eq. (4.3) is referred to as the *relative excess velocity*, and is denoted by $m$. Equation (4.3) therefore establishes the identity of $m$ and $W$ provided $U_{\text{film}} = 0$, and consequently these terms often appear interchangeably in the literature. Thus, $\alpha$, $m$, $W$, and $\delta/D$ are all related according to the following expression:

$$\alpha = 1 - m = 1 - W = \left(1 - 2\frac{\delta}{D}\right)^2.$$

Sufficient conditions for the liquid film to be static ($U_{\text{film}} = 0$) are summarized as follows:

1. horizontal flow (no gravity draining)
2. the bubble is sufficiently long that a uniform (constant thickness) film is established
3. $\mu_v \ll \mu_l$

The first two conditions imply that the pressure in the film is constant, while the third condition, which is typically satisfied for gas–liquid slug flow, implies that the shear stress at the interface between the bubble and the film is effectively zero. In the absence of a pressure gradient and shear stress to drive the flow, the film will be stagnant.

Taylor [125] hypothesized three possible streamline patterns in the liquid slug ahead of the bubble in a frame of reference in which the bubble is stationary. These patterns are illustrated in Fig. 4-3. Note that, for $m = 0.5$, it follows from the definition of the relative excess velocity that $U_b = 2\bar{U}$, which is equal to the maximum (centerline) velocity in fully-developed Hagen-Poiseuille flow. In other words, for $m > 0.5$, the bubble travels faster than the maximum liquid velocity; this condition is referred to as *bypass flow* since all of the liquid simply bypasses the bubble as it travels through the channel (i.e., there is no recirculation in the liquid slug ahead of the bubble). The first two patterns ((*a*) and (*b*) in Fig. 4-3) were experimentally confirmed by Goldsmith and Mason [45] and Cox [24], but neither author found evidence to support the existence of the third pattern (*c*) in Fig. 4-3; in fact, to date, this flow pattern has never been observed in experiments [7, 127]. It was, however, observed in the numerical simulations of Giavedoni and Saita [43] for $0.605 < \text{Ca}_b < 0.690$; Angeli and Gavriilidis [7] have suggested that this small range of $\text{Ca}_b$ is likely the reason that this flow pattern has evaded experimental observation.

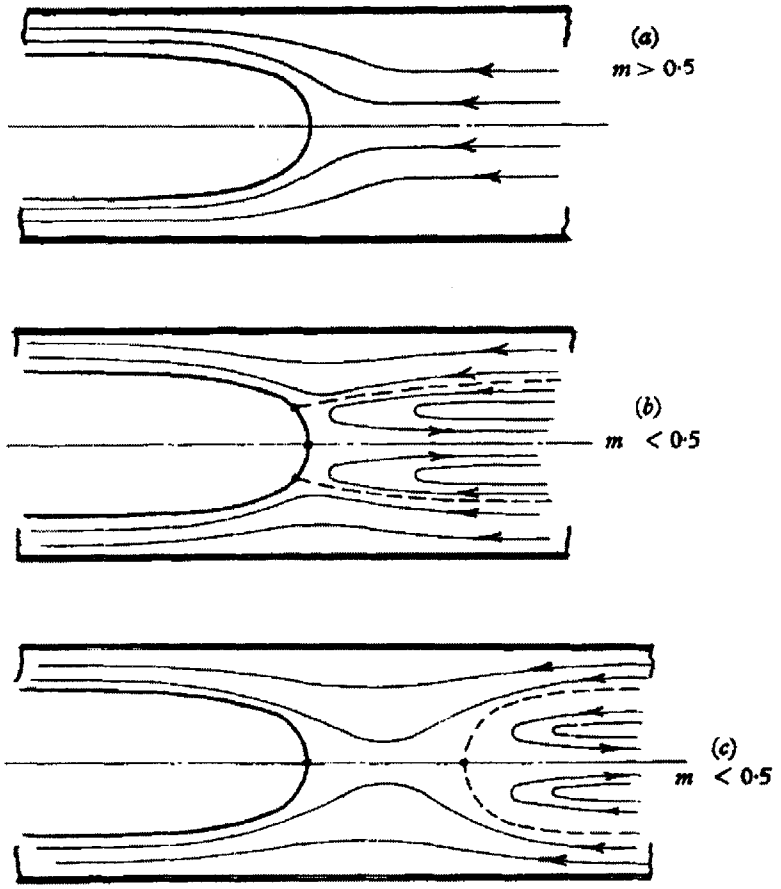


**Figure 4-3:** Streamline patterns hypothesized by Taylor [125]

A defining feature of capillary slug flow is that gravitational forces are typically negligible in comparison to other forces—viscous, inertial, and capillary—at least in the case of horizontal channels (see condition 1 above) considered here. The film thickness, bubble velocity, and pressure drop will thus be functions of the following dimensionless groups:

$$\mathrm{Ca}_b \equiv \frac{\mu_l U_b}{\sigma} = \frac{\text{viscous forces}}{\text{capillary forces}} \qquad \text{(Capillary number)}$$

$$\mathrm{Re}_b \equiv \frac{\rho_l U_b D}{\mu_l} = \frac{\text{inertial forces}}{\text{viscous forces}} \qquad \text{(Reynolds number)}$$

$$\mathrm{We}_b \equiv \frac{\rho_l U_b^2 D}{\sigma} = \frac{\text{inertial forces}}{\text{capillary forces}}, \qquad \text{(Weber number)}$$

which express the relative magnitudes of these forces. Note that $We_b = Re_b Ca_b$, so one of these numbers is actually redundant. Additionally, the flow could depend on the properties of the vapor phase, but for gas–liquid slug flow, this dependence is typically very weak since $\rho_v \ll \rho_l$ and $\mu_v \ll \mu_l$.

Capillary slug flow can be classified as either *visco-capillary* or *visco-inertial*, depending whether inertial forces are significant [10]. In the visco-capillary regime, which corresponds to low velocities, inertial forces are insignificant and the flow is dependent on a single parameter—the capillary number, $Ca_b$. In this regime, analytical and semi-analytical results from lubrication theory can be used to provide satisfactory expressions for the film thickness, bubble velocity, and the capillary pressure drop. When inertial forces are non-negligible (visco-inertial regime), however, the situation is less favorable to analysis due to the nonlinearity introduced by the intertial (advection) terms.* In this case, one must appeal to correlations developed from experimental and numerical data.

### 4.2.1 Visco-capillary regime

#### Film thickness models

For low velocities, inertial forces in the fluid can be neglected, so the only relevant dimensionless group is the capillary number, $Ca_b$. In this so-called *visco-capillary* regime [10], the high pressure in the bubble resulting from surface tension forces will tend to cause the bubble to expand radially (and contract axially) to fill the entire capillary, thereby reducing the film thickness. At the same time, viscous forces in the liquid will favor a thicker film—in a reference frame that moves with the bubble (*cf.* Fig. 4-2), viscous shear stresses at the wall will tend to drag liquid into the film between the bubble and the wall. We therefore anticipate

$$\text{larger } Ca_b \implies \text{larger } \delta \implies \text{larger } m,$$

and vice versa. Indeed, from their experiments, Fairbrother and Stubbs [36] deduced that

$$m = 1.0\, Ca_b^{\frac{1}{2}}. \tag{4.4}$$

This result was found to give satisfactory agreement over the entire range of their experiments (up to $Ca_b < 0.014$). Nearly a quarter century later, Taylor [125] extended the range of validity of Eq. (4.4) up to $Ca_b < 0.09$, but noted that Eq. (4.4) significantly overestimates $m$ for larger $Ca_b$. Taylor experimented with highly viscous fluids, reaching capillary numbers as large as 1.9, and observed that $m$ appeared to be approaching an asymptotic value of approximately 0.55. Figure 4-4 compares the

*Even for the visco-capillary regime, where the inertial terms are negligible and Navier–Stokes equation reduces to the linear Stokes equation, the problem is still nonlinear in the film thickness.

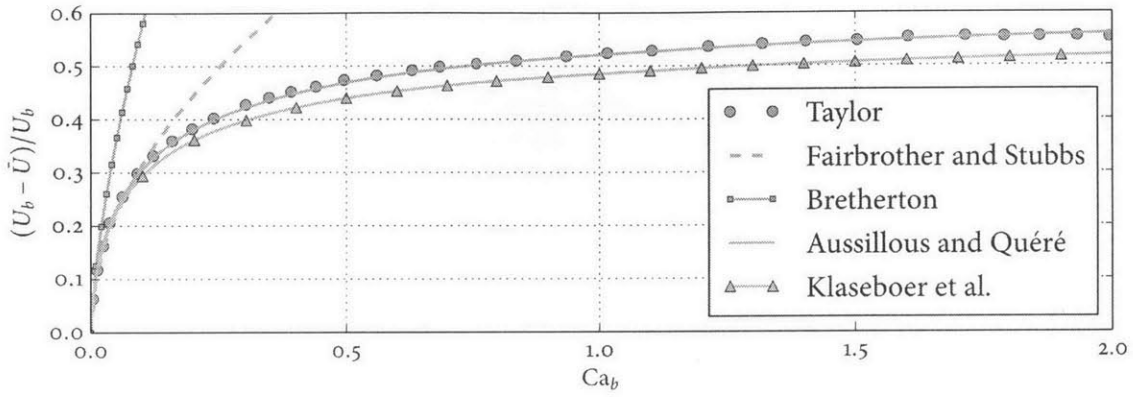


**Figure 4-4:** Comparison of correlations for the relative excess velocity with Taylor's data.

data obtained by Taylor with Fairbrother and Stubbs's correlation, and illustrates clearly the deviation from Eq. (4.4) for large $Ca_b$. Cox [23] subsequently estimated the asymptotic limit to be $m = 0.60$.

In his pioneering work, Bretherton [13] provided the first theoretical treatment of slug flow, using lubrication theory to model the liquid flow in the so-called dynamic meniscus, or transition region, separating the thin liquid film from the bulk fluid (see Fig. 4-5). By additionally imposing a curvature matching condition between the dynamic and static menisci, Bretherton deduced that the film thickness should be proportional to $Ca_b^{\frac{2}{3}}$ in the limit of vanishing $Ca_b$, that is

$$\frac{\delta}{D} \sim Ca_b^{\frac{2}{3}}, \quad \text{for} \quad Ca_b \to 0 \qquad \text{(Bretherton's scaling law)}$$

The details of Bretherton's analysis can be found in Appendix C. Here, we present a derivation of this result using simple scaling arguments; similar scaling arguments have been used to motivate more recent relations for the film thickness that are applicable over a wider range of $Ca_b$ [10, 49].

Consider the bubble illustrated in Fig. 4-5, where $R$ is the channel radius, $\delta$ is the film thickness, and $\ell$ is the (unknown) length of the dynamic mensicus (or transition region). We suppose $\delta \ll R$ so that the bubble radius $R_b \approx R$. Assuming negligible fluid inertia ($Re \approx 0$), the liquid flow in the transition region is governed by the Stokes equations,

$$\frac{\partial P}{\partial x} = \mu \frac{\partial^2 u}{\partial y^2} \tag{4.5}$$

An order of magnitude estimate for the viscous stresses and pressure gradient within the transition

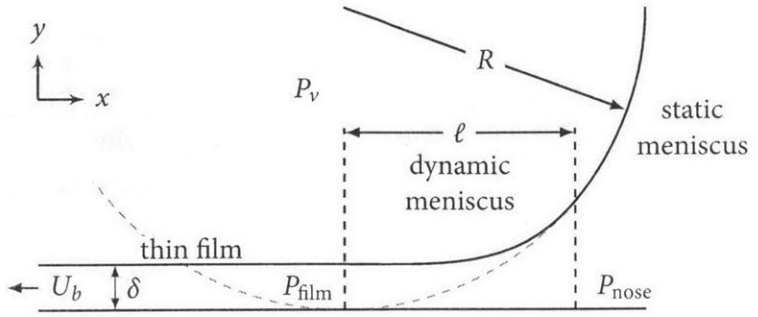


**Figure 4-5:** Illustration of the transition region (dynamic meniscus) near the nose of a Taylor bubble. Note: the thickness of the film has been exaggerated for clarity.

region are given, respectively, by

$$\mu \frac{\partial^2 u}{\partial y^2} \sim \mu \frac{(-U_b)}{\delta^2} \tag{4.6}$$

and

$$\frac{\partial P}{\partial x} \sim \frac{P_l - P_{\text{film}}}{\ell}, \tag{4.7}$$

where $P_{\text{nose}}$ is the pressure in the bulk liquid ahead of the bubble, and $P_{\text{film}}$ is the liquid pressure in the film, as illustrated in Fig. 4-5. These pressures can be related to the pressure $P_v$ of the vapor phase via the Young–Laplace equation,

$$P_v - P_l = \frac{2\sigma}{R} \tag{4.8a}$$

$$P_v - P_{\text{film}} = \frac{\sigma}{R} \tag{4.8b}$$

Substituting Eqs. (4.8) into Eq. (4.7) gives

$$\frac{\partial P}{\partial x} \sim \frac{P_l - P_{\text{film}}}{\ell} = -\frac{1}{\ell}\frac{\sigma}{R}. \tag{4.9}$$

Combining Eqs. (4.5), (4.6), and (4.9) gives

$$\mu \frac{U_b}{\delta^2} \sim \frac{1}{\ell}\frac{\sigma}{R} \iff \frac{\delta^2}{\ell R} \sim \text{Ca}_b. \tag{4.10}$$

In this result, both $\delta$ and $\ell$ are unknown. Elimination of one of these quantities obviously requires another condition, namely the curvature matching condition—we require that the curvature of the

dynamic meniscus match that of the static mensicus at the point where the two menisci meet,

$$\frac{\delta}{\ell^2} \sim \frac{1}{R} \tag{4.11}$$

Finally, eliminating $\ell$ from Eqs. (4.10) and (4.11) yields the desired result (after substituting $D$ for $R$),

$$\frac{\delta}{D} \sim \mathrm{Ca}_b^{\frac{2}{3}}$$

Through a more formal analysis (*cf.* Appendix C), Bretherton was able to deduce the following relation in the limit $\mathrm{Ca}_b \to 0$:

$$\frac{\delta}{D} = \frac{1}{2} 0.643 \, (3\mathrm{Ca}_b)^{\frac{2}{3}}, \tag{4.12}$$

From this result, one readily obtains the relative excess velocity,

$$m = W = 1 - \left(1 - 2\frac{\delta}{D}\right)^2 \approx 4\frac{\delta}{D} = 1.29 \, (3\mathrm{Ca}_b)^{\frac{2}{3}} \tag{4.13}$$

which is plotted in Fig. 4-4 alongside Taylor's experimental data and the correlation of Fairbrother and Stubbs (4.4). From Fig. 4-4, it is apparent that Eq. (4.13) holds only for very small $\mathrm{Ca}_b$. Bretherton [13] found good agreement (less than 10% error) between Eq. (4.13) and experiments for $\mathrm{Ca}_b < 10^{-2}$. Curiously, however, Bretherton observed that the theoretical predictions compared worse with experiments at the smallest $\mathrm{Ca}_b$, which is inconsistent with the fact that his theory was expected to hold in the limit $\mathrm{Ca}_b \to 0$; Eq. (4.12) was found to systematically underpredict the measured film thickness for $\mathrm{Ca}_b < 10^{-4}$. Ratulowski and Chang [107] subsequently demonstrated that the discrepancy could be explained by the Marangoni effect. Surfactant contaminants in the fluid will tend to accumulate at the liquid-gas interface. At low $\mathrm{Ca}_b$, when flow recirculation is present, the surfactants will be swept away from the stagnation ring near the nose of the bubble, as illustrated in Fig. 4-6. The resulting concentration gradient will result in a surface tension gradient that, in turn, will induce a shear stress along the interface that opposes the local flow. This effect is sometimes referred to as Marangoni *hardening* since the interface will tend to behave more like a solid (no slip) boundary. As demonstrated by Ratulowski and Chang [107], Marangoni hardening increases the film thickness by a factor of $4^{\frac{2}{3}}$ compared to Eq. (4.12).

For moderate to large $\mathrm{Ca}_b$, the film thickness is no longer negligible in comparison to the channel radius, which suggests one explanation for why Bretherton's scaling law breaks down for $\mathrm{Ca}_b \gtrsim 10^{-3}$. For these conditions, the radius of curvature of the bubble is more appropriately approximated by

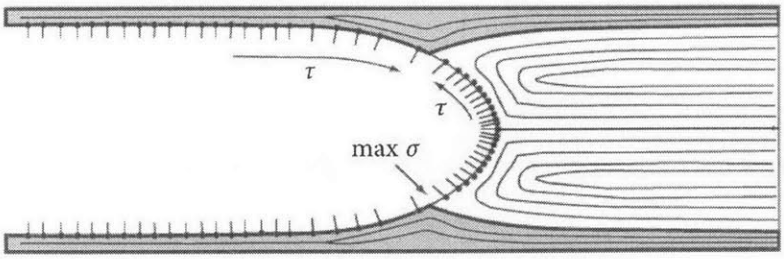


**Figure 4-6:** Illustration of the Marangoni effect and interfacial hardening (from Kreutzer et al. [72]). The surface tension $\sigma$ is largest near the stagnation ring, where the concentration of surfactants is lowest. The surface tension gradients result in shear stresses $\tau$ that oppose the local fluid motion, causing the interface to behave like a no-slip, solid boundary.

$R - \delta$. Substituting $R - \delta$ for $R$ in Eqs. (4.10) and (4.11) and solving for $\delta$ yields [10]

$$\frac{\delta}{D} \sim \frac{\mathrm{Ca}_b^{\frac{2}{3}}}{1 + \mathrm{Ca}_b^{\frac{2}{3}}}.$$

Aussillous and Quéré [10] combined the above result with Bretherton's solution (4.12) and proposed a correlation of the form

$$\frac{\delta}{D} = \frac{1}{2} \cdot \frac{0.643\,(3\mathrm{Ca}_b)^{\frac{2}{3}}}{1 + A \cdot 0.643\,(3\mathrm{Ca}_b)^{\frac{2}{3}}}. \tag{4.14}$$

By fitting this expression to Taylor's data [125], Aussillous and Quéré determined that $A = 2.5$, resulting in the following semi-empirical expression:

$$\frac{\delta}{D} = \frac{1}{2} \cdot \frac{0.643\,(3\mathrm{Ca}_b)^{\frac{2}{3}}}{1 + 1.61(3\mathrm{Ca}_b)^{\frac{2}{3}}} = \frac{0.670\,\mathrm{Ca}_b^{\frac{2}{3}}}{1 + 3.35\mathrm{Ca}_b^{\frac{2}{3}}}, \tag{4.15}$$

which the authors refer to as *Taylor's law*. From Eq. (4.15), one can compute the relative excess velocity, which has been plotted in Fig. 4-4 alongside Taylor's data. While the agreement is seen to be quite remarkable considering that their correlation contained only a single free parameter, Aussillous and Quéré note that this could be entirely coincidental. Very recently, however, Klaseboer et al. [70] extended Bretherton's argument to higher $\mathrm{Ca}_b$ and obtained a result equivalent to Eq. (4.14), thus giving Eq. (4.15) a more rigorous backing. But their theory predicts $A = 2.79$, which is seen to significantly underpredict the film thickness, as seen in Fig. 4-4. Klaseboer et al. [70] note that it is possible to perform the numerical integration in such a way that the value $A = 2.5$ is obtained, but there is little theoretical justification to support this modification beyond the fact that it just so happens to work.

**Capillary pressure drop models**

In the visco-capillary regime, the pressure drop, $\Delta P_b$, across the bubble is likewise a function of only the capillary number, $Ca_b$. Since the liquid in the film is static, the pressure drop across the majority of the bubble will be zero (or at least negligibly small). The total pressure drop across the bubble is therefore independent of bubble length, and is determined solely by the pressure drop at the front and rear caps of the bubble. This, in turn, can be related to the change in curvature between the front and back of the bubble. If the bubble were symmetric, the pressure drop across the bubble would be zero, but this would imply that the bubble is not moving since there is nothing pushing it forward. No, that the bubble *is* moving implies there *must* be a pressure drop across the bubble, implying further that the radius of curvature at the rear of the bubble is greater than that at the front of the bubble; this results in the bubble having a slightly swollen posterior, or "junk in the trunk."

From his analysis, Bretherton [13] found the pressure drop across a Taylor bubble to be given by

$$\Delta P_b = 4.52\,(3\mathrm{Ca}_b)^{\frac{2}{3}}\frac{\sigma}{R} = 9.4\mathrm{Ca}_b^{\frac{2}{3}}\frac{\sigma}{R}. \tag{4.16}$$

Note that many authors [e.g., 2, 7, 9, 72, 73, 132] mistakenly present Bretherton's expression for the pressure drop as

$$\Delta P_b = 3.58(3\mathrm{Ca}_b)^{\frac{2}{3}}\frac{\sigma}{R} = 7.45\,\mathrm{Ca}_b^{\frac{2}{3}}\frac{\sigma}{R}. \tag{4.17}$$

This confusion seemingly originates from Bretherton's statement in the abstract of his article that Eq. (4.17) gives the pressure drop across a bubble. Yet, from the main text of his article (specifically, the first paragraph of pg. 172), it is clear that Eq. (4.17) accounts only for the pressure drop across the front meniscus; in the subsequent paragraph he gives the pressure drop across the rear meniscus, and lists the total pressure drop as Eq. (4.16). Ratulowski and Chang [106] found Eq. (4.16) to over-predict the pressure drop for $\mathrm{Ca}_b > 10^{-3}$. They introduced an empirical correction factor that is reportedly valid for $\mathrm{Ca}_b < 10^{-1}$, resulting in the following correlation:

$$\frac{\Delta P_b}{\sigma/R} = 4.52\,(3\mathrm{Ca}_b)^{\frac{2}{3}} - 12.6\mathrm{Ca}_b^{0.95}. \tag{4.18}$$

As will be seen in the following sections, our simulations suggest that this correlation holds for $\mathrm{Ca}_b < 10^{-2}$, rather than the originally reported limit of $\mathrm{Ca}_b < 10^{-1}$.

### 4.2.2 Visco-inertial regime

Inertial effects in capillary slug flow have been considered only much more recently. One of the earliest studies to consider the effect of inertia was by Edvinsson and Irandoust [34], who modeled Taylor flow

in a cylindrical capillary using finite elements. They observed a slight increase in the film thickness with increasing Re = $\rho_l \tilde{U} D/\mu_l$, but noted that at higher Re, a uniform film was not present. Edvinsson and Irandoust also observed that the amplitude of the undulations at the tail of the bubble increased with increasing Re, while their wavelength decreased. They did not consider the effect of finite Re on the pressure drop across the bubble.

Giavedoni and Saita [43] used the finite element method to study finite-$Re_b$ flow around the front of the bubble. They observed slight, but non-monotonic dependence of the film thickness on $Re_b$. At higher $Re_b$, the film thickness was found to increase slightly with increasing $Re_b$, consistent with the observations of Edvinsson and Irandoust. At lower $Re_b$, however, the opposite trend was observed; the film thickness was seen to decrease to a minimum value with increasing $Re_b$. In a follow-up study, Giavedoni and Saita [44] analysed the effect of inertia on the shape of the rear meniscus, again using FEM. They observed the same trend as Edvinsson and Irandoust; increasing $Re_b$ resulted in larger amplitude undulations with smaller wavelength.

Heil [51] studied the influence of inertia on the flow around a 2D (non-axisymmetric) air finger propagating through a viscous fluid using FEM. He confirmed the findings of Giavedoni and Saita [43] that inertia has a relatively small effect on the asymptotic film thickness, but concluded that inertial forces can drastically affect the pressure distribution near the bubble's tip and can also increase the pressure drop through the front transition region. Heil [51] noted that at finite $Re_b$, the flow recirculation near the nose of the bubble can result in strong centrifugal pressure gradients that reduce the radius of curvature of the bubble tip, and that the effect is most significant for small $Ca_b$ when recirculation is strongest. In addition, increasing $Re_b$ increased the length of the transition region (the length between the bubble tip and the uniform film increased); this is consistent with the observations of Edvinsson and Irandoust [34] who found that, for bubbles of finite length, a uniform film was not established at high Re.

More recently, Kreutzer et al. [73] used the commercial FEM/CFD code, FIDAP, to study effects of inertia on film thickness and pressure drop in Taylor flow. The author's obtained similar results as reported Heil [51], but their study was not limited to front of the bubble. In particular, Kreutzer et al. noted that the pressure drop across the channel increased with increasing Re and decreasing Ca, and that inertial effects were most significant for higher Ca.

None of the aforementioned authors offered any revised correlations for the film thickness when inertial effects are significant, having concluded only that the effect was relatively minor. A first step in this direction was by Aussillous and Quéré [10], who used a scaling argument to deduce the influence of finite-$We_b$ on the film thickness. In doing so, they were able to explain the "inertial thickening" effect noted above, but they nevertheless stopped short of actually proposing a correlation for the film thickness. We present a variation of their scaling argument below.

Consider again the bubble shown in Fig. 4-5. Assuming steady flow with possibly non-negligible inertial effects, the $x$-component of the Navier–Stokes equations in the liquid can be written

$$-\mu \frac{\partial^2 u}{\partial y^2} = -\frac{\partial P}{\partial x} - \rho u \frac{\partial u}{\partial x} \tag{4.19}$$

As before, the first two terms can be approximated as

$$-\mu \frac{\partial^2 u}{\partial y^2} \sim \frac{\mu U_b}{\delta^2} \tag{4.20a}$$

and

$$-\frac{\partial P}{\partial x} \sim \frac{P_{\text{film}} - P_l}{\ell} \sim \frac{1}{\ell} \frac{\sigma}{R-\delta}. \tag{4.20b}$$

For the inertial terms, we have

$$\rho u \frac{\partial u}{\partial x} \sim \frac{\rho(-U_b)^2}{\ell} = \frac{\rho U_b^2}{\ell} \tag{4.20c}$$

Substituting Eqs. (4.20) into Eq. (4.19) yields

$$\frac{\mu U_b}{\delta^2} \sim \frac{1}{\ell} \frac{\sigma}{R-\delta} - \frac{\rho U_b^2}{\ell}. \tag{4.21}$$

By defining the *modified Weber number* as

$$\text{We}_b' \equiv \frac{\rho U_b^2 (R-\delta)}{\sigma},$$

equation (4.21) can be written as

$$\text{Ca}_b \sim (1 - \text{We}_b') \left(\frac{\delta}{R-\delta}\right)\left(\frac{\delta}{\ell}\right). \tag{4.22}$$

The length scale, $\ell$, of the transition region is once again obtained by matching the curvature of the dynamic meniscus with that of the static meniscus [10, 49],

$$\frac{\delta}{\ell^2} \sim \frac{1}{R-\delta} \iff \frac{\delta}{\ell} \sim \sqrt{\frac{\delta}{R-\delta}} \tag{4.23}$$

Combining Eqs. (4.23) and (4.22) gives

$$\frac{\delta}{R} \sim \frac{\mathrm{Ca}_b^{\frac{2}{3}}}{\mathrm{Ca}_b^{\frac{2}{3}} + (1 - \mathrm{We}_b')^{\frac{2}{3}}} \tag{4.24}$$

Equation (4.24) differs slightly from the result originally presented by Aussillous and Quéré [10], which was

$$\frac{\delta}{R} \sim \frac{\mathrm{Ca}_b^{\frac{2}{3}}}{\mathrm{Ca}_b^{\frac{2}{3}} + 1 - \mathrm{We}_b'}. \tag{4.25}$$

It is seen that Eqs. (4.24) and (4.25) differ only in the exponent of the inertial terms, and for $0 < \mathrm{We}_b' \ll 1$, they are, in fact, equivalent.† Both expressions predict an increase in film thickness with increasing $\mathrm{We}_b'$, and thus account for the so-called *inertial thickening* that is observed for $\mathrm{Re}_b \gtrsim 10^2$. The above analysis leading to Eq. (4.24) closely follows that of Han and Shikazono [49], who do not comment on the difference between these two expressions. In either case, the conclusions of Aussillous and Quéré [10] are unaffected since both Eqs. (4.24) and (4.25) predict an increase in film thickness with increasing $\mathrm{We}_b'$, which was what the authors sought to demonstrate.

Han and Shikazono [49] have taken this a step further. They note that the $\mathrm{We}_b'$ term in (4.24) accounts for inertial thickening of the film, but fails to account for the initial thinning of the film for non-zero $\mathrm{Re}_b$. As observed by Heil [51] and Edvinsson and Irandoust [34], the bubble nose becomes more slender, and the corresponding curvature increases with increasing $\mathrm{Re}_b$. Thus, Han and Shikazono [49] proposed to modify the curvature with an expression of the form:

$$\kappa = \frac{1 + f(\mathrm{Re}_b, \mathrm{Ca}_b)}{R - \delta}$$

With this modification, Eq. (4.21) becomes

$$\frac{\mu U_b}{\delta^2} \sim \frac{\sigma}{\ell}\left[\frac{1 + f(\mathrm{Re}_b, \mathrm{Ca}_b)}{R - \delta}\right] - \frac{\rho U_b^2}{\ell},$$

which can be rewritten as

$$\mathrm{Ca}_b \sim \left[1 + f(\mathrm{Re}_b, \mathrm{Ca}_b) - \mathrm{We}_b'\right]\left(\frac{\delta}{\ell}\right)\left(\frac{\delta}{R - \delta}\right).$$

†Equivalent up to a multiplicative factor on $\mathrm{We}_b'$, which is irrelevant to the scaling analysis since it would ultimately be replaced by a fitting coefficient anyway.

Now, the matching condition becomes

$$\frac{\delta}{\ell^2} \sim \frac{1 + f(\mathrm{Re}_b, \mathrm{Ca}_b)}{R - \delta} \implies \frac{\delta}{\ell} \sim \left(\frac{\delta}{R - \delta}\right)^{\frac{1}{2}} \sqrt{1 + f(\mathrm{Re}_b, \mathrm{Ca}_b)}$$

Solving for the film thickness gives

$$\frac{\delta}{R} \sim \frac{\mathrm{Ca}_b^{\frac{2}{3}}}{\mathrm{Ca}_b^{\frac{2}{3}} + (1 + f(\mathrm{Re}_b, \mathrm{Ca}_b))\left[1 - \frac{\mathrm{We}_b'}{1 + f(\mathrm{Re}_b, \mathrm{Ca}_b)}\right]^{\frac{2}{3}}}$$

Han and Shikazono [49] go on to approximate this result as

$$\frac{\delta}{R} \sim \frac{\mathrm{Ca}_b^{\frac{2}{3}}}{1 + \mathrm{Ca}_b^{\frac{2}{3}} + f(\mathrm{Re}_b, \mathrm{Ca}_b) - g(\mathrm{We}_b)}$$

where $\mathrm{We}_b'$ has been replaced with $\mathrm{We}_b$, which is not dependent on $\delta$. By fitting this expression to experimental data, they obtain the following correlation:

$$\frac{\delta}{D} = \frac{0.670\mathrm{Ca}_b^{\frac{2}{3}}}{1 + 3.13\mathrm{Ca}_b^{\frac{2}{3}} + 0.504\mathrm{Ca}_b^{0.672}\mathrm{Re}_b^{0.589} - 0.352\mathrm{We}_b^{0.629}}. \tag{4.26}$$

Han and Shikazono report that Eq. 4.26 is accurate to within ±15% of their experimental data.

Equation (4.26) is currently the most complete correlation for the film thickness, and is evidently the only existing correlation that attempts to account for inertial effects. Note, however, that Eq. (4.26) does not reduce exactly to Eq. (4.15) when $\mathrm{Re}_b = 0$ due to the factor 3.35 being replaced with 3.13. An inconveninet feature of Eq. (4.26), and indeed all of the film thickness correlations considered above, is that they relate the film thickness to the bubble velocity, $U_b$, which might not be known in practice; given the film thickness, it is a straightforward matter to determine the bubble velocity, but the bubble velocity must first be known to estimate the film thickness using the above correlations. In Section 4.4.1, we use the results of our simulations to develop an alternate correlation that the relates the film thickness to the mean velocity $\bar{U}$ rather than the bubble velocity $U_b$; this is more convenient for our purposes since $U_b$ is not imposed by our simulations, but $\bar{U}$ is.

Finally, we note that literature review presented above is far from complete, covering only the most important results that will be referred to in the following sections when we present the results of our computational study. More extensive reviews are given by Angeli and Gavriilidis [7], covering additional topics such as slug flow in non-circular capillaries. Additionally, Talimi et al. [124] give a thorough review of numerical studies of Taylor flow; their review covers heat transfer simulations,

slug flow in non-circular channels, and bubble/slug formation in mixing junctions.

## 4.3 Computational framework

For this work, we have completed a fairly extensive computational study of slug flow in circular capillaries using the *Gerris* flow solver with the moving-frame implementation described in Section 3.6. The computational domain is a cylindrical capillary of radius $R$ and length $L$, as shown schematically in Fig. 4-7. Unless indicated otherwise, the domain length was given by $L = 35R$. This length was chosen to be sufficiently long that the fully developed, Hagen–Poiseuille velocity profile could reasonably be imposed at the ends of the domain [73]; note that in the moving domain, neither boundary is a pure inflow or outflow boundary, and explicitly imposing a Dirichlet condition on the velocity was found to give the best results. The bubble was initialized as a cylindrical tube with spherical caps. The initial radius was taken to be $R_b = 0.85R$, and the initial length was $L_b = 12R_b$, unless specified otherwise. For the simulations, all quantities were non-dimensional; all lengths were normalized with respect to $R$, and all velocities were scaled with the average velocity, $\bar{U}$. Thus, the appropriate velocity profile applied to the left and right boundaries is given by

$$u(r) = 2\left(1 - r^2\right) - U_b$$

where $U_b = U_b^*/\bar{U}$ is the relative, instantaneous bubble velocity; note that we are changing notation slightly from the previous sections where $U_b$ was used to denote the absolute (unscaled) bubble velocity—this quantity is here denoted by $U_b^*$. Treatment of the fluid properties (density and viscosity) is the same as described in Section 3.3; i.e., density and viscosity are scaled relative to the density $\rho_l$ and viscosity $\mu_l$ of the liquid phase, and are given by Eqs. (3.1) and (3.2), respectively.

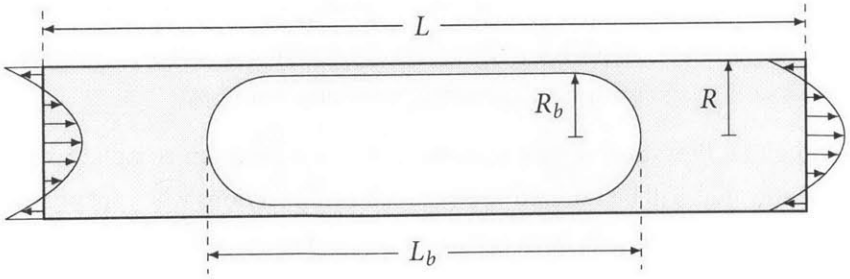


**Figure 4-7:** Schematic representation of the computational domain used for slug flow simulations.

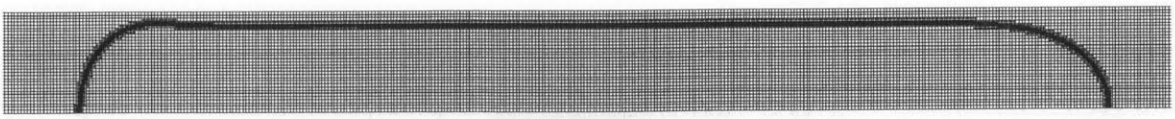

**Figure 4-8:** Typical computational mesh used for slug flow simulations. Shown is the mesh for Ca = 0.05.

For the majority of our simulations, the inertial pressure scale was used, i.e.

$$p = \frac{p^*}{\rho \bar{U}^2},$$

where $p^*$ denotes the dimensional pressure. With this scaling, the relevant governing equations can be written as

$$\frac{D\mathbf{u}}{Dt} = \frac{1}{\rho}\left[-\nabla p + \left(\frac{2}{\mathrm{Re}}\right)\nabla\cdot(2\mu\mathbf{D}) + \left(\frac{2}{\mathrm{We}}\right)\kappa\delta_S\hat{\mathbf{n}}\right], \tag{4.27}$$

where[‡]

$$\mathrm{Re} \equiv \frac{\rho_l \bar{U} D}{\mu_l} = 2\frac{\rho_l \bar{U} R}{\mu_l} \quad \text{and} \quad \mathrm{We} \equiv \mathrm{Re}\,\mathrm{Ca} = 2\frac{\rho_l \bar{U}^2 R}{\sigma}$$

should not be confused with $\mathrm{Re}_b$ and $\mathrm{We}_b$. An exception to this scaling was for the Re = 0 simulations, in which case the viscous pressure scale was used,

$$p = \frac{p^*}{(\mu \bar{U}/R)}.$$

and the relevant governing equations are written

$$\rho\frac{\mathrm{Re}}{2}\frac{D\mathbf{u}}{Dt} = 0 = -\nabla p + \nabla\cdot(2\mu\mathbf{D}) + \left(\frac{1}{\mathrm{Ca}}\right)\kappa\delta_S\hat{\mathbf{n}}.$$

In any case, it is seen that the simulations depend on four dimensionless groups: Ca, Re (or We = Re Ca), $\rho_v/\rho_l$, and $\mu_v/\mu_l$. In this work, we have primarily considered variations in Re and Ca, fixing $\rho_v/\rho_l = 10^{-3}$ and $\mu_v/\mu_l = 10^{-2}$, although a few cases were considered with differing density and viscosity ratios.

Figure 4-8 illustrates a typical mesh used for the slug flow simulations. The base mesh consisted of a uniform grid with mesh spacing $h = 2^{-5} = 0.03125$, which gave a nominal grid composed of 35,840 cells. An additional 2 levels of refinement were added around the interface, so that the actual grid was composed of roughly 46,000 cells. For some of the low-Ca simulations, additional refinement was added to resolve the thin film, as seen in Fig. 4-9.

[‡]The Reynolds number has been defined using the channel diameter $D$ as the length scale, whereas the channel radius $R$ is the more natural length scale for setting up the simulations. This explains the spurious factors of 2 in Eq. (4.27).

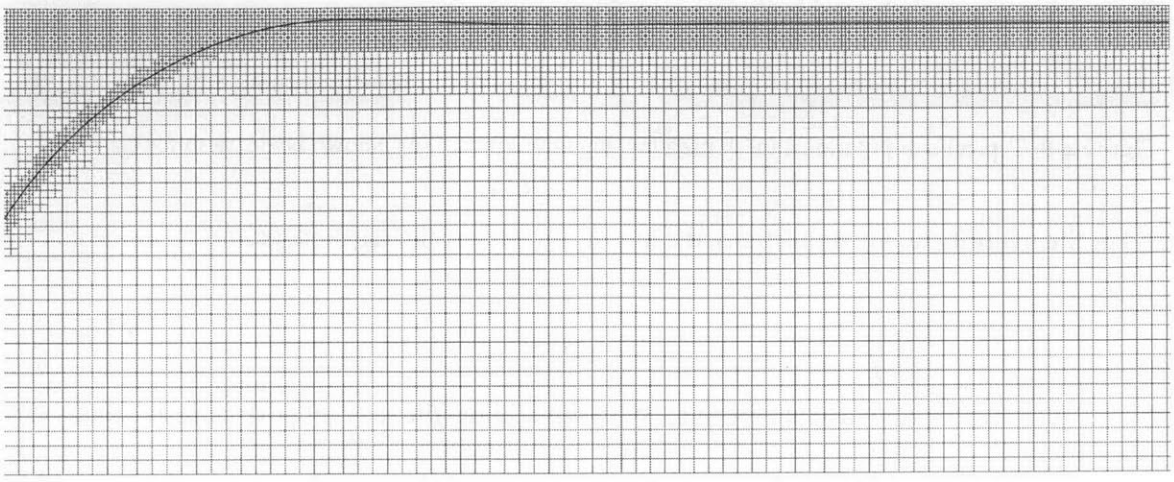

**Figure 4-9:** Computational mesh with film refinement. Shown is the mesh for Ca = 0.005.

## 4.4 Results and validation

Slug flow simulations were performed for nearly 150 different combinations of Re and Ca, with $\mathrm{Ca} \in [0.001, 2]$ and $\mathrm{Re} \in [0, 1000]$. In this section, we present the main results of these simulations and compare these results with available data from the literature. The computed film thickness and bubble velocity for a subset of these simulations are listed in Table 4.1. Note that with increasing Ca, the maximum Re for which a steady solution was achieved was found to decrease, and for $\mathrm{Ca} = \mathcal{O}(1)$, the bubble breakup was observed for Re much larger than 10.

### 4.4.1 Film thickness

Figure 4-10 plots the computed film thickness vs. $\mathrm{Ca}_b$ for various values of Re. For low Re, the results are seen to agree well with Taylor's law (4.15). Figure 4-11 plots the computed film thickness vs. $\mathrm{Re}_b$ for various values of Ca. As anticipated, we observe an initial thinning of the film with increasing $\mathrm{Re}_b$, followed by a steady thickening of the film for increasing $\mathrm{Re}_b$ beyond $\mathrm{Re}_b \gtrsim 200$. Some of these cases have been replotted in Fig. 4-12, which also plots the film thickness data from Kreutzer et al. [73]. Note that only two of the cases, namely Ca = 0.010 and Ca = 0.040, have a direct correspondence between both data sets. Both of these cases agree reasonably well. Finally, Fig. 4-13 plots the computed film thickness against the corresponding film thickness predicted by Han and Shikazono's correlation (4.26). All of the data fall within ±15% of the predicted values, which is the reported accuracy range of the correlation [49]. The mean relative error between the predicted and computed film thickness is 1.9%, with a standard deviation of 5.28%, while the maximum relative error is 10.8%.

As noted previously, an inconvenient feature of Han and Shikazono's correlation is that it requires

**Table 4.1:** Summary of velocity and film thickness data. All data are for $\rho_l/\rho_v = 1000$ and $\mu_l/\mu_v = 100$.

| Ca | Re | $U_b/\bar{U}$ | $\delta/D$ |
|---|---|---|---|
| 0.001 | 0 | 1.025709 | 0.006184 |
| | 100 | 1.025905 | 0.006236 |
| | 160 | 1.026136 | 0.006292 |
| | 200 | 1.026303 | 0.006332 |
| | 400 | 1.027104 | 0.006526 |
| | 600 | 1.027874 | 0.006712 |
| | 800 | 1.028594 | 0.006887 |
| | 1000 | 1.029262 | 0.007050 |
| 0.005 | 0 | 1.077116 | 0.018153 |
| | 100 | 1.078577 | 0.018462 |
| | 160 | 1.079078 | 0.018564 |
| | 200 | 1.079484 | 0.018645 |
| | 300 | 1.080654 | 0.018875 |
| | 400 | 1.082020 | 0.019159 |
| | 600 | 1.085299 | 0.020034 |
| | 1000 | 1.093582 | 0.022278 |
| 0.010 | 0 | 1.123563 | 0.028247 |
| | 2 | 1.123233 | 0.028179 |
| | 10 | 1.117247 | 0.026969 |
| | 20 | 1.117114 | 0.026964 |
| | 60 | 1.116801 | 0.026951 |
| | 100 | 1.120216 | 0.027540 |
| | 140 | 1.117896 | 0.027070 |
| | 200 | 1.120917 | 0.027575 |
| | 240 | 1.121835 | 0.027733 |
| | 300 | 1.123312 | 0.028092 |
| | 340 | 1.124488 | 0.028489 |
| | 400 | 1.126691 | 0.029259 |
| | 500 | 1.131090 | 0.030576 |
| | 600 | 1.135715 | 0.031284 |
| | 700 | 1.140679 | 0.031817 |
| | 800 | 1.144700 | 0.033209 |
| 0.025 | 2 | 1.223857 | 0.048076 |
| | 5 | 1.222877 | 0.047900 |
| | 10 | 1.221154 | 0.047589 |
| | 20 | 1.218341 | 0.047080 |
| | 40 | 1.213315 | 0.046190 |
| | 60 | 1.210066 | 0.045541 |
| | 80 | 1.208005 | 0.045062 |
| | 100 | 1.207091 | 0.044817 |
| | 140 | 1.207275 | 0.045077 |
| | 180 | 1.209214 | 0.045864 |
| | 200 | 1.210369 | 0.046085 |
| | 240 | 1.213498 | 0.046380 |
| | 300 | 1.220082 | 0.048622 |
| | 360 | 1.226921 | 0.051823 |
| 0.040 | 2 | 1.306983 | 0.062757 |
| | 20 | 1.292883 | 0.060373 |
| | 60 | 1.275609 | 0.057383 |
| | 100 | 1.269886 | 0.056384 |
| | 200 | 1.275664 | 0.057501 |
| | 300 | 1.292173 | 0.061160 |
| 0.050 | 0 | 1.358022 | 0.071233 |
| | 2 | 1.353530 | 0.070417 |
| | 4 | 1.350522 | 0.069954 |
| | 6 | 1.348412 | 0.069630 |
| | 8 | 1.345904 | 0.069239 |
| | 10 | 1.342990 | 0.068778 |
| | 20 | 1.332415 | 0.067067 |
| | 40 | 1.318125 | 0.064645 |
| | 60 | 1.309970 | 0.063300 |
| | 80 | 1.304874 | 0.062542 |
| | 100 | 1.302996 | 0.062291 |
| | 120 | 1.303249 | 0.062455 |
| | 140 | 1.304586 | 0.063032 |
| | 160 | 1.306540 | 0.063755 |
| | 180 | 1.309192 | 0.064570 |
| | 200 | 1.312375 | 0.065691 |
| | 220 | 1.316563 | 0.067153 |
| | 240 | 1.320017 | 0.068400 |
| 0.075 | 0 | 1.462587 | 0.086946 |
| | 2 | 1.455044 | 0.085848 |
| | 20 | 1.417032 | 0.080290 |
| | 40 | 1.393461 | 0.076753 |
| | 60 | 1.382140 | 0.075098 |
| | 80 | 1.376150 | 0.074332 |
| | 100 | 1.375105 | 0.074487 |
| | 120 | 1.375691 | 0.075038 |
| 0.100 | 0 | 1.551358 | 0.099164 |
| | 2 | 1.538411 | 0.097439 |
| | 4 | 1.531067 | 0.096451 |
| | 10 | 1.509510 | 0.093507 |
| | 20 | 1.483523 | 0.089952 |
| | 40 | 1.453358 | 0.085683 |
| | 60 | 1.440021 | 0.083948 |
| | 80 | 1.434403 | 0.083478 |
| | 100 | 1.432850 | 0.083819 |
| | 140 | 1.437208 | 0.086305 |
| | 160 | 1.441622 | 0.088213 |
| | 180 | 1.445675 | 0.090242 |
| | 200 | 1.451229 | 0.092542 |
| | 220 | 1.457668 | 0.095145 |
| | 240 | 1.463650 | 0.097690 |
| | 300 | 1.482868 | 0.105845 |
| 0.150 | 0 | 1.687671 | 0.115973 |
| | 2 | 1.671506 | 0.114128 |
| | 10 | 1.624087 | 0.108396 |
| | 20 | 1.585868 | 0.103628 |
| | 60 | 1.531462 | 0.097120 |
| | 100 | 1.523413 | 0.097960 |
| | 240 | 1.556700 | 0.115718 |
| 0.250 | 0 | 1.881680 | 0.136940 |
| | 2 | 1.851720 | 0.133885 |
| | 20 | 1.726494 | 0.120627 |
| | 40 | 1.678265 | 0.115823 |
| | 100 | 1.646483 | 0.118262 |
| | 200 | 1.661419 | 0.134046 |
| 0.375 | 0 | 2.029754 | 0.150990 |
| | 2 | 1.993754 | 0.147653 |
| | 10 | 1.901014 | 0.138846 |
| | 20 | 1.841227 | 0.132780 |
| | 40 | 1.784454 | 0.126914 |
| | 60 | 1.761051 | 0.124710 |
| | 80 | 1.749769 | 0.124213 |
| | 100 | 1.744459 | 0.124753 |
| 0.500 | 2 | 2.084894 | 0.155784 |
| | 10 | 1.981792 | 0.146553 |
| | 20 | 1.918280 | 0.140499 |
| | 40 | 1.856472 | 0.134528 |
| | 60 | 1.829942 | 0.132284 |
| | 80 | 1.815937 | 0.131864 |
| | 100 | 1.808398 | 0.132458 |
| 0.750 | 0 | 2.271161 | 0.170884 |
| | 2 | 2.204268 | 0.165462 |
| | 10 | 2.096972 | 0.156644 |
| | 20 | 2.020302 | 0.150286 |
| | 40 | 1.950633 | 0.145148 |
| | 50 | 1.932258 | 0.144560 |
| | 60 | 1.918401 | 0.144593 |
| 0.900 | 0 | 2.318754 | 0.174501 |
| | 2 | 2.243707 | 0.168620 |
| | 10 | 2.131266 | 0.159885 |
| | 20 | 2.059834 | 0.153769 |
| 1.500 | 0 | 2.390106 | 0.179579 |
| | 2 | 2.337629 | 0.175805 |
| | 10 | 2.208941 | 0.166164 |
| 2.000 | 0 | 2.399687 | 0.180171 |
| | 2 | 2.347216 | 0.176372 |
| | 10 | 2.227203 | 0.167232 |

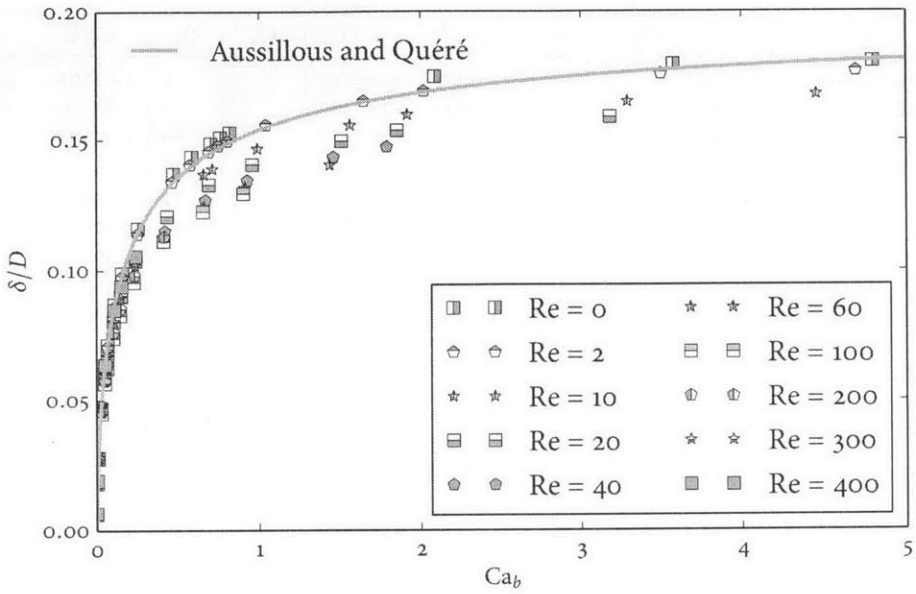


**Figure 4-10:** Film thickness vs. $Ca_b$ for various Reynolds numbers. Also illustrated is the low-Re correlation of Aussillous and Quéré.

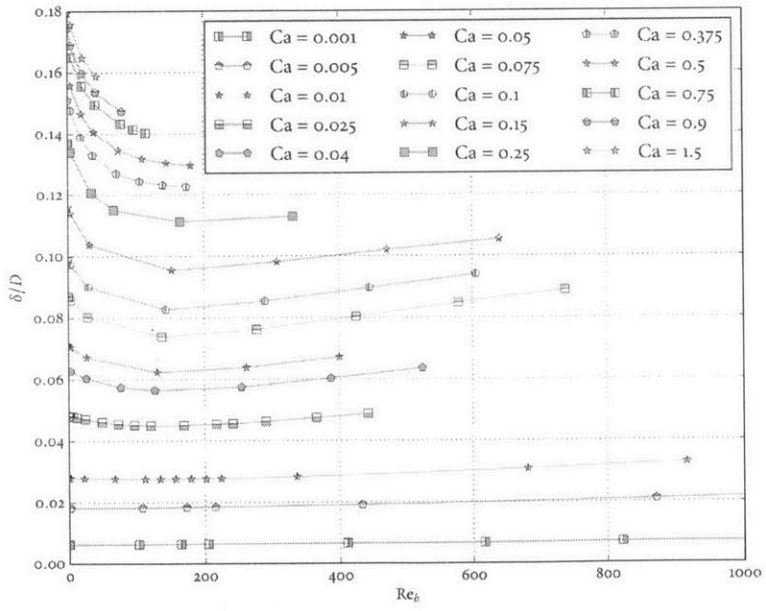


**Figure 4-11:** Effect of varying $Re_b$ on the computed film thickness for various capillary numbers.

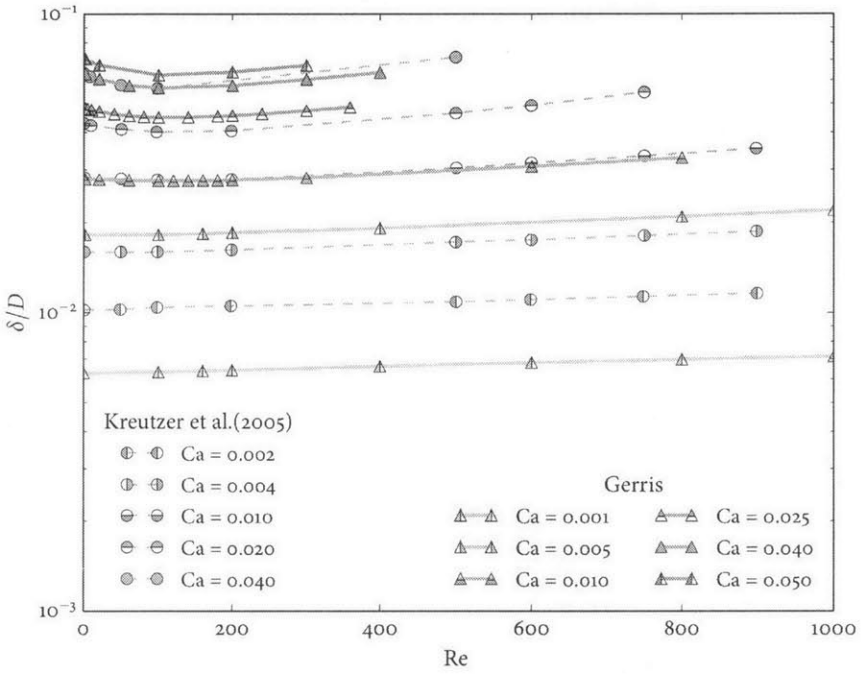


**Figure 4-12:** Comparison of computed film thickness vs. Re with simulation data of Kreutzer et al. [73].

the bubble velocity to be known in order to predict the film thickness. For our simulations, and perhaps in most applications, we do not know the bubble's velocity *a priori*. Rather, we know only the flow rate through the capillary, or in our case, the average liquid velocity $\bar{U}$. On the other hand, if we knew the film thickness as a function of Re and Ca, it is a relatively simple matter to compute the bubble velocity. Assuming fully-developed annular flow in the uniform liquid film, and fully-developed Poiseuille flow in the bubble, the bubble velocity is found to be

$$\frac{U_b}{\bar{U}} = \frac{\alpha + 2\gamma(1-\alpha)}{1-(1-\gamma)(1-\alpha^2)} \tag{4.28}$$

where $\gamma = \mu_v/\mu_l$ is the viscosity ratio and $\alpha$ is the bubble void fraction defined in Eq. (4.1). In the limit $\gamma \to 0$ (no shear at the bubble interface), Eq. (4.28) reduces to

$$\frac{U_b}{\bar{U}} = \frac{1}{\alpha} = \left(1 - 2\frac{\delta}{D}\right)^{-2} \tag{4.29}$$

which is consistent with (4.3). In this limit, the liquid in the film is stagnant. For our simulations, $\gamma = 0.01$, so (4.29) gives a good approximation of the bubble velocity.

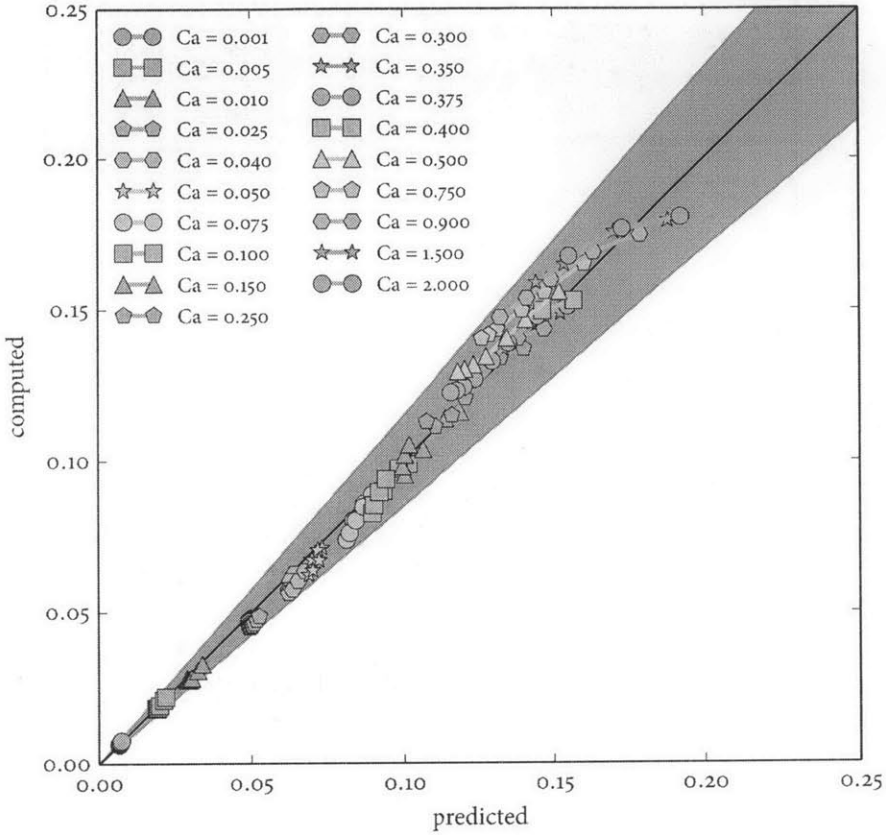


**Figure 4-13:** Comparison of computed film thickness with predictions from Han and Shikazono's correlation (4.26). The shaded region denotes ±15%, which was the accuracy reported in [49]. The mean relative error between the predicted and computed film thickness is 1.9%, with a standard deviation of 5.28%, while the maximum relative error is 10.8%.

We suppose $\delta = \delta(\mathrm{Ca}, \mathrm{Re})$ can expressed in the following form:

$$\frac{\delta}{D} = \frac{0.670\mathrm{Ca}^{\frac{2}{3}}}{1 + [1 + \Phi(\mathrm{Re})]C \cdot \mathrm{Ca}^{c}}. \tag{4.30}$$

Equation (4.30) is similar in form to the correlation of Aussillous and Quéré [10] (4.15), the key difference being the use of Ca instead of $\mathrm{Ca}_b$ as well as the inclusion of inertial effects through the $\Phi(\mathrm{Re})$ term. This expression is motivated by the observation that as $\mathrm{Ca}_b \to 0$, $U_b \to \bar{U}$, and thus $\mathrm{Ca} \to \mathrm{Ca}_b$. Hence, we have retained the factor 0.670 in the numerator of (4.30) to maintain consistency with Bretherton's asymptotic result in the limit $\mathrm{Ca}_b \to 0$. The inertial factor, $\Phi(\mathrm{Re})$, is motivated

by considering Klaseboer et al.'s recent extension of Bretherton's analysis. Using the notation of Appendix C, their analysis predicts the film thickness to be given by

$$\frac{\delta}{R} = \frac{\alpha^+(3\mathrm{Ca}_b)^{\frac{2}{3}}}{1+\kappa^+\alpha^+(3\mathrm{Ca}_b)^{\frac{2}{3}}},$$

where $\alpha^+ = 0.643$ as determined by Bretherton. On the other hand, the $\kappa^+$ factor relates to the curvature at bubble's nose. As pointed out by Han and Shikazono [49], inertial effects will tend to alter this nose curvature, so we might anticipate $\kappa^+$ to exhibit a dependence on Re, which we have incorporated into our model through the $\Phi(\mathrm{Re})$ term. Combining Eqs. (4.30) and (4.29) yields the corresponding correlation for the bubble velocity:

$$\frac{U_b}{\bar{U}} = \left\{1 + \frac{1.34\mathrm{Ca}^{\frac{2}{3}}}{1+\left[1+\Phi(\mathrm{Re})\right]\,C\cdot\mathrm{Ca}^c - 1.34\mathrm{Ca}^{\frac{2}{3}}}\right\}^2. \tag{4.31}$$

Equation (4.31) is the expression that has been fit to our computed data, rather than Eq. (4.30). The reason for doing it this was is that the bubble velocity is an unambiguous quantity that is easily computed from our simulations, whereas the film thickness is more difficult to extract; in many cases, the film will only be very nearly uniform since we are simulating finite-length bubbles, so the computed film thickness can vary slightly depending on the particular axial location at which the measurement was made.

To determine an appropriate expression for $\Phi(\mathrm{Re})$, we started with the imposition that $\Phi(0) = 0$, so that for $\mathrm{Re} = 0$, Eq. (4.31) reduces to

$$\frac{U_b}{\bar{U}} = \left\{1 + \frac{1.34\mathrm{Ca}^{\frac{2}{3}}}{1+C\cdot\mathrm{Ca}^c - 1.34\mathrm{Ca}^{\frac{2}{3}}}\right\}^2.$$

This result was then fit to our $\mathrm{Re} = 0$ data to yield values for the coefficients $C$ and $c$. Given these coefficients, we then proceeded to step through each $\mathrm{Re} > 0$ and compute the value of $\Phi(\mathrm{Re})$ for which Eq. (4.31) was satisfied, and then fit this result to an expression of the form:

$$\Phi(\mathrm{Re}) = \left[\frac{A}{\mathrm{Re}^a} + B\cdot\mathrm{Re}^b\right]^{-1}.$$

The fitting coefficents are summarized below:

| | |
|---|---|
| $A = 3.205\times10^{1}$ | $a = 0.593$ |
| $B = 4.564\times10^{-5}$ | $b = 1.909$ |
| $C = 2.860$ | $c = 0.764$ |

Figure 4-14 plots computed bubble velocity vs. Ca and Re together with predictions of correlation (4.31), and demonstrates that our proposed correlation is able to adequately capture the dominant trends in the observed variation of $U_b$ with Re and Ca. Figure 4-15 plots the predicted bubble velocity using Eq. (4.31) against the computed values. The agreement is seen to be quite good; the mean relative error is 0.15%, with standard deviation 0.81%, and the maximum relative error is 2.54%. This is perhaps unsurprising considering that the correlation was specifically fit to this data. Figures 4-16 and 4-17 present the same comparisons using the film thickness predictions instead of the bubble velocity. Once again, the agreement is very good, albeit slightly worse than for the velocity predictions. The mean relative error is 0.76%, with standard deviation 2.97%; both of these values are lower than the corresponding values obtained from Han and Shikazono's correlation. On the other hand, the maximum relative error is 15.25%, which is about 50% larger than the maximum relative error obtained from Han and Shikazono's correlation, but is on par with the reported accuracy of their correlation.

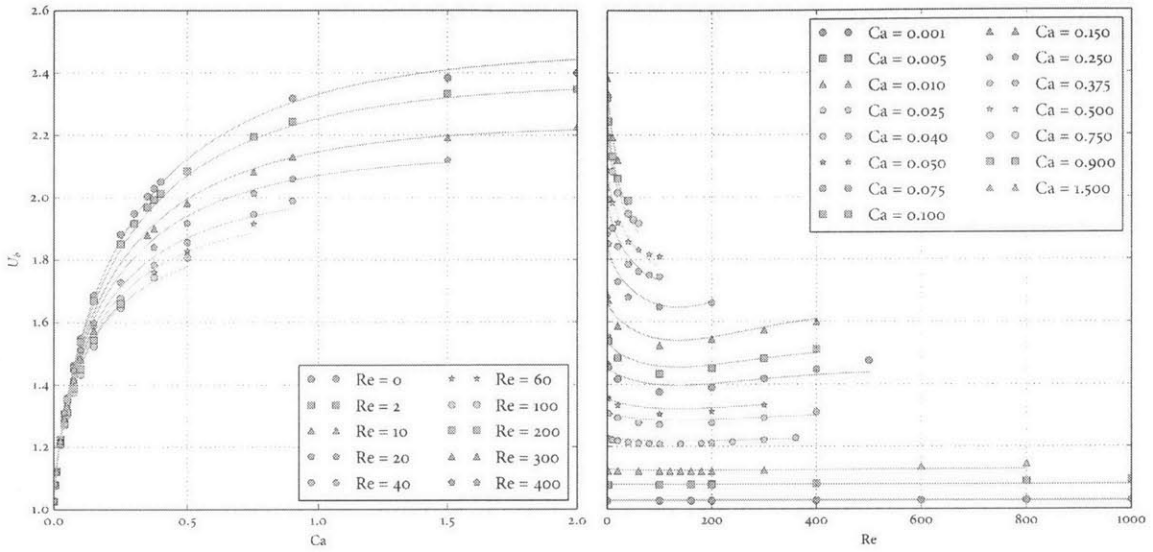


**Figure 4-14:** Bubble velocity vs. Ca (left) and Re (right) and comparison with predictions obtained from correlation (4.31)

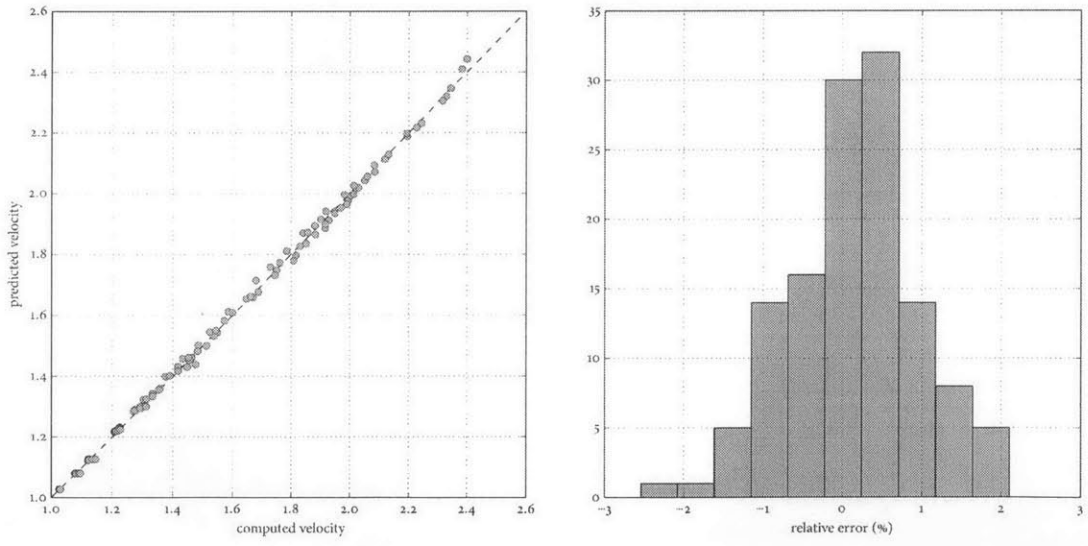


**Figure 4-15:** Comparison of computed bubble velocity with predictions of Eq. (4.31) (left) and histogram of relative prediction error (right). The mean relative error is 0.15%, with standard devaition 0.81%, and the maximum relative error is 2.54%.

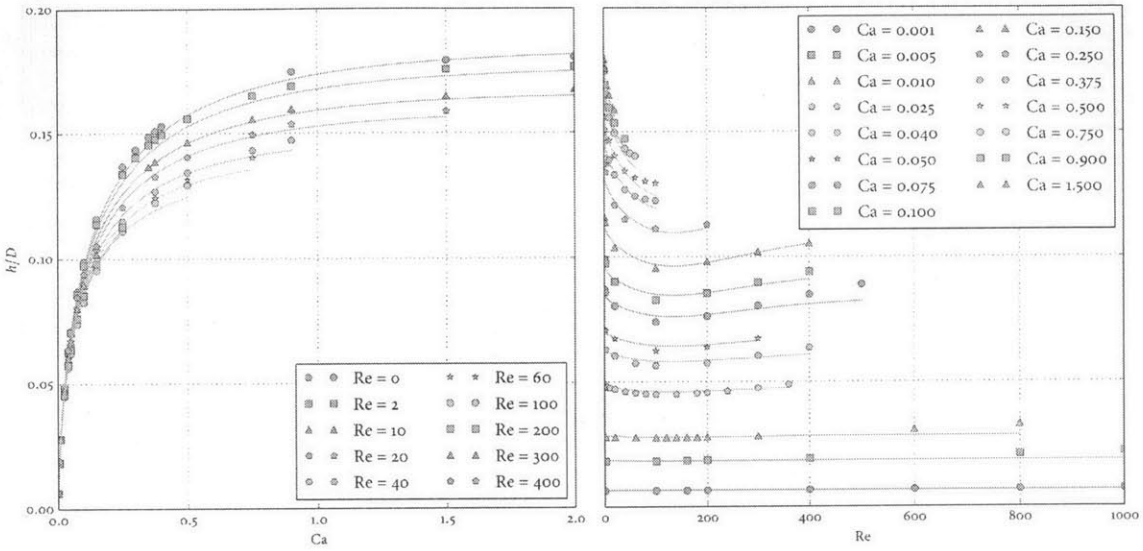


**Figure 4-16:** Film thickness vs. Ca (left) and Re (right) and comparison with predictions obtained from correlation (4.30)

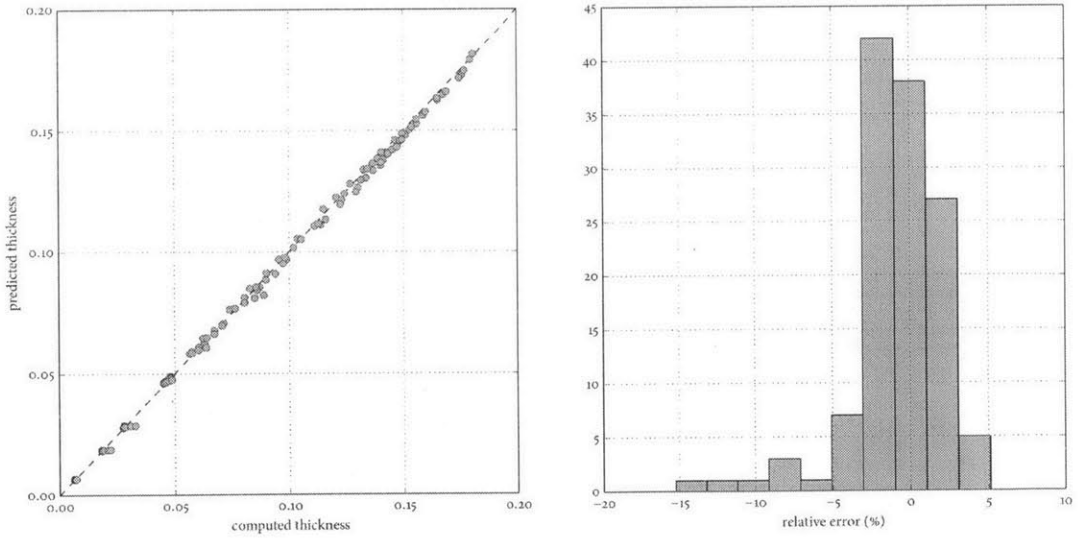


**Figure 4-17:** Comparison of computed film thickness with predictions of Eq. (4.30) (left) and histogram of relative prediction error (right). The mean relative error is 0.76%, with standard deviation 2.97%, and the maximum relative error is 15.25%.

### 4.4.2 Interface shapes

Figures 4-18 and 4-19 illustrate the effect of increasing the Reynolds number on the steady-state (terminal) shape of the rear meniscus. At low Ca (Fig. 4-18), the undulations at the rear of the bubble are seen to grow in amplitude with increasing Re, while simultaneously decreasing in wavelength. This is consistent with the observations of Giavedoni and Saita [44]; in their simulations, however, $Ca_b = CaU_b$ and $Re_b = ReU_b$ are the independent variables, which makes direct comparison with their results difficult. At higher Ca (Fig. 4-19), a similar effect is observed, but at the highest values of Re, the rear interface becomes concave. This, too, is consistent with the observations of Giavedoni and Saita [44]. As Re was increased further, transient oscillations were observed in the tail, resulting in the curvature periodically switching from concave to convex and back again. For these simulations, no steady bubble velocity was ever achieved, and these simulations were not considered further. For $Ca \gtrsim 0.5$, a jet of liquid was observed to penetrate through the bubble's tail at sufficiently high Re; this jet continued to propagate forward, through the bubble, until eventually breaking through the front. As the objective of this study was not to study bubble breakup, these cases were also removed from further consideration.

### 4.4.3 Capillary pressure drop across a bubble

Figure 4-20 plots the capillary pressure drop across the bubble as a function of $Ca_b$ for the low-Re simulations (Re = 0 and Re = 2). For comparison, the theoretical prediction by Bretherton (4.16), and the correlation by Ratulowski and Chang (4.18) are also shown. As expected, Bretherton's prediction significantly overestimates the pressure drop for $Ca_b > 10^{-3}$. Our results agree quite well with Ratulowski and Chang's correlation for $Ca_b \lesssim 10^{-2}$. Curiously, in what is perhaps a bizarre coincidence, our results compare remarkably well to Bretherton's correlation reduced by a factor of 2 for $Ca_b > 10^{-2}$; this is seen by the dashed line in Fig. 4-20. The author is neither aware of any previous observation of this fact nor able to provide any explanation for why this result should agree so well with the data.

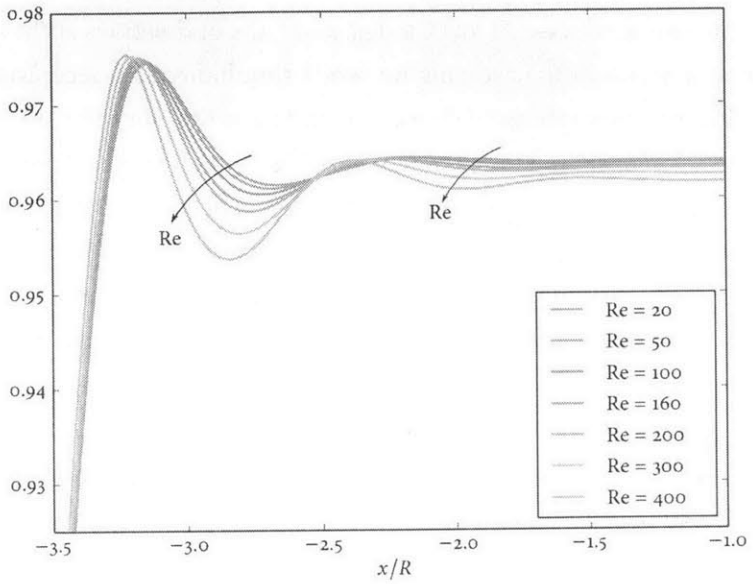


**(a)** Ca = 0.005

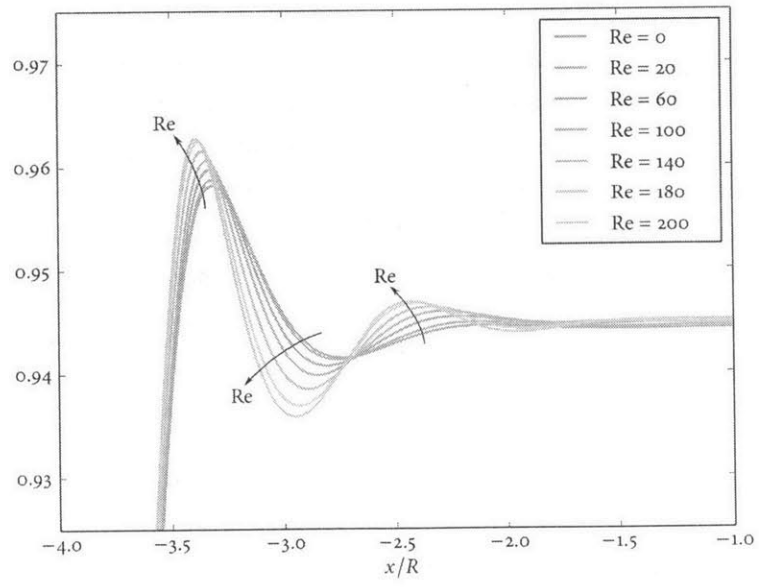


**(b)** Ca = 0.010

**Figure 4-18:** Effect of increasing Re on the rear meniscus for (a) Ca = 0.005 and (b) Ca = 0.010.

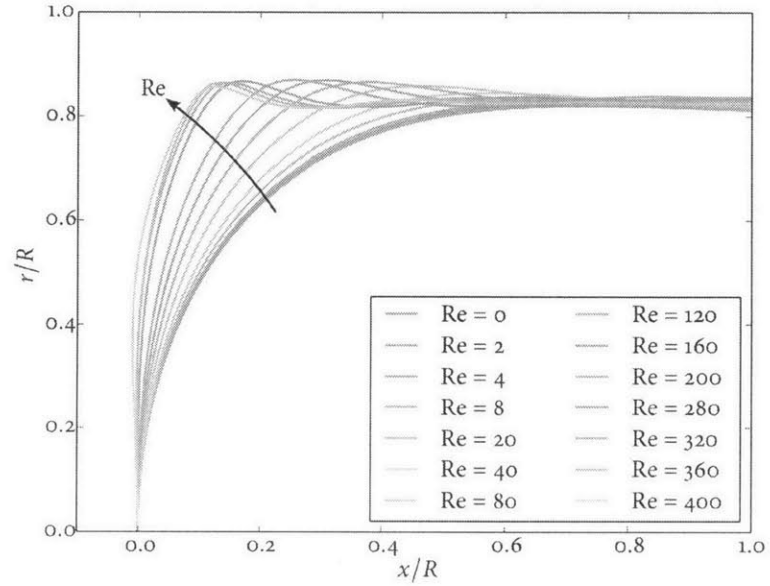


**(a)** Ca = 0.100

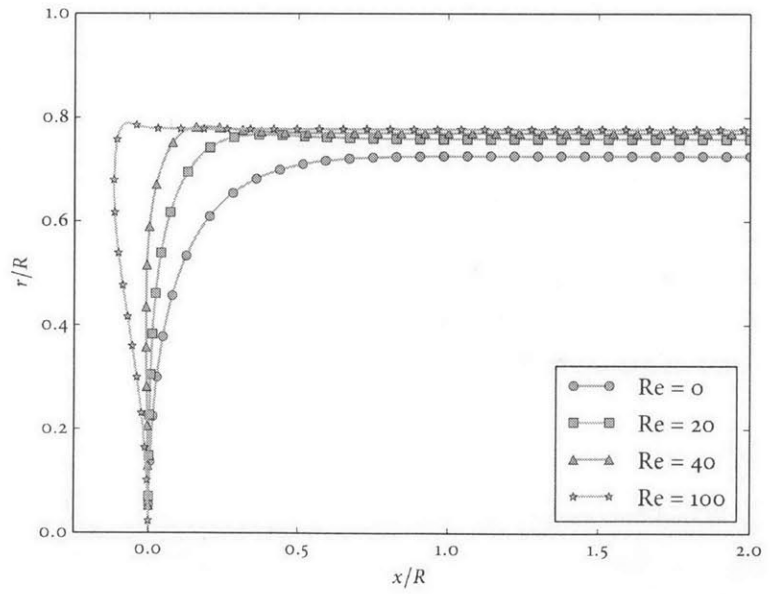


**(b)** Ca = 0.250

**Figure 4-19:** Effect of increasing Re on the rear meniscus for (a) Ca = 0.100 and (b) Ca = 0.250.

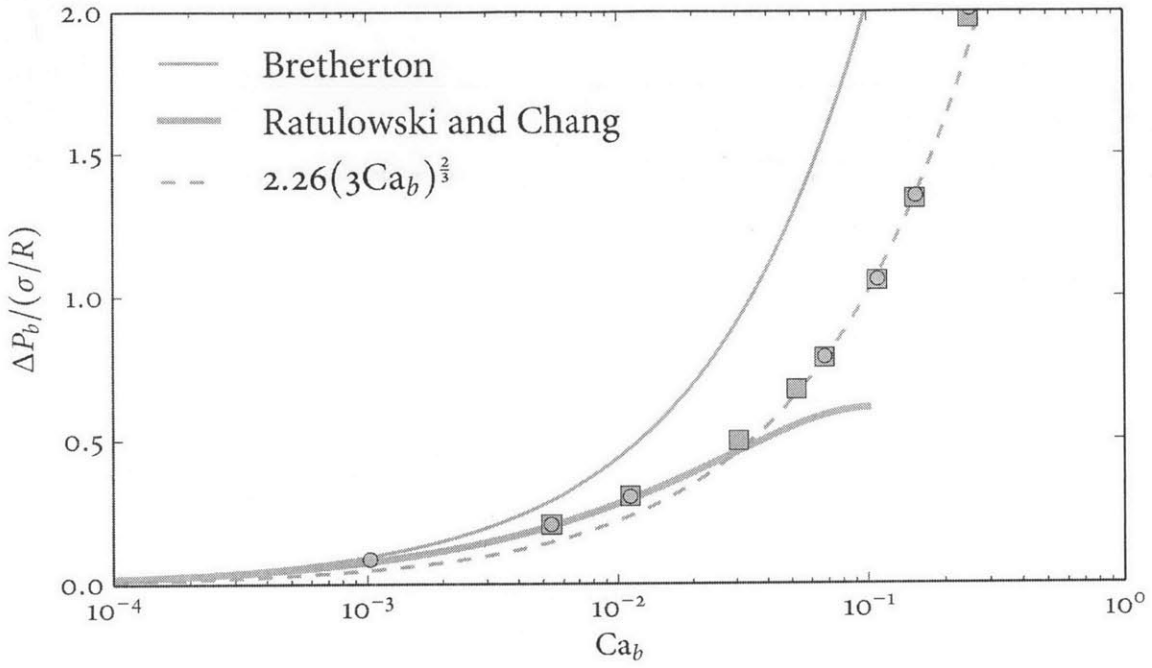


**Figure 4-20:** Comparison of computed pressure drop with Bretherton's theory [13] and the correlation of Ratulowski and Chang [106] for Re = 0 (circles) and Re = 2 (squares). The dashed line corresponds to Bretherton's correlation reduced by a factor of 2.

## 4.5 Uncertainty quantification applications

Having gained some confidence in *Gerris*'s ability to accurately simulate slug flow, we can proceed with the gPC expansion applications. For our first test, we suppose the capillary number is log-normally distributed,

$$\ln \mathrm{Ca} \sim \mathcal{N}(-4, 1),$$

and fix Re = 100. The probability density function for Ca is illustrated in Fig. 4-21. We wish to compute the resultant uncertainty in the excess velocity, $m$, given this distribution for Ca. This choice of distribution suggests the use of the Hermite-PC expansion to represent $m$. Rather than use *Gerris* to evaluate $m$ at quadrature nodes, we instead use our newly-developed

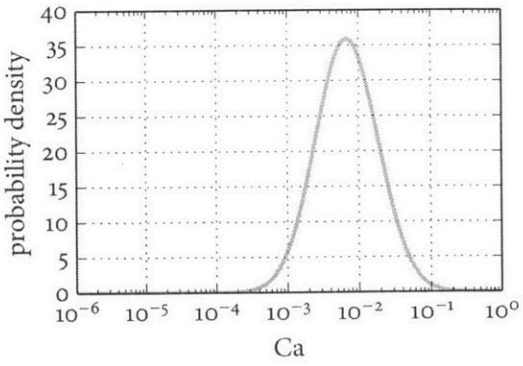


**Figure 4-21:** Probability density for Ca.

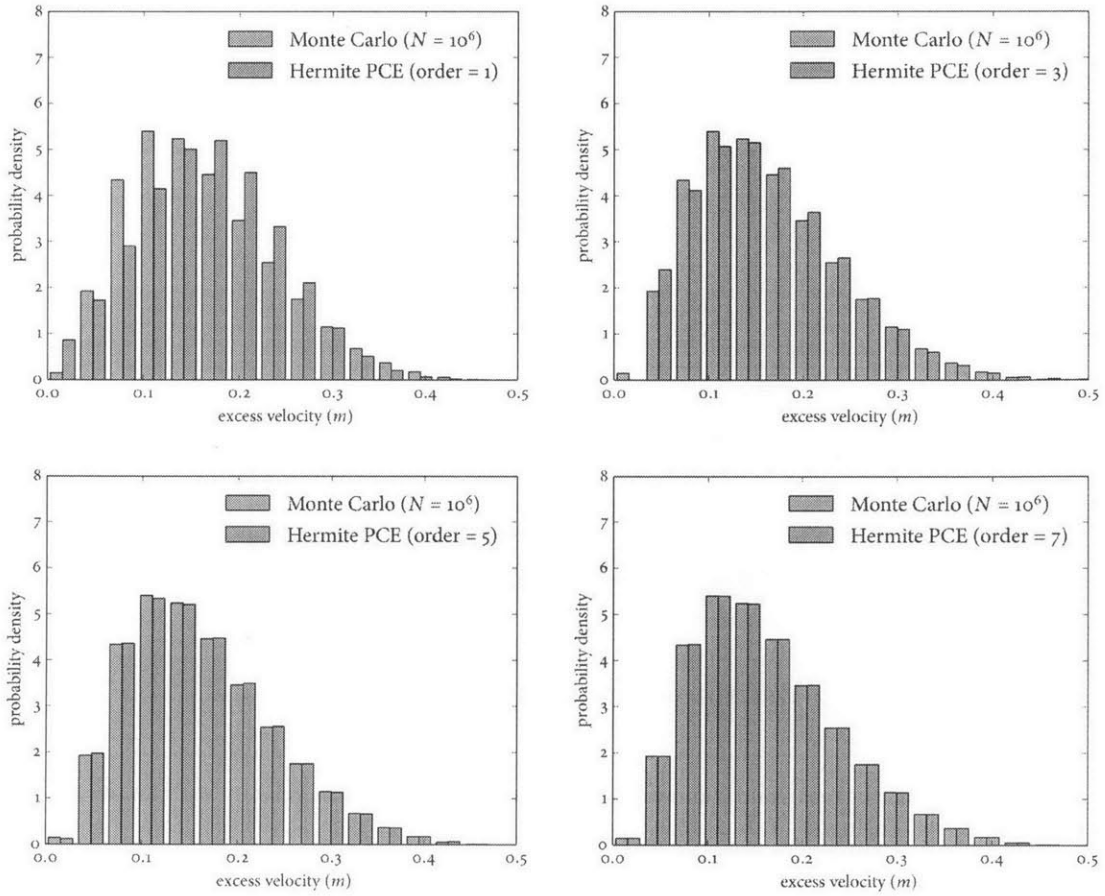


**Figure 4-22:** Comparison of estimated probability density of excess velocity $m$ for Hermite-PC expansions of order 1, 3, 5, and 7.

correlation for the bubble velocity given in Eq. (4.31); that is, for this test, Eq. (4.31) is our model, serving as a surrogate for *Gerris*. Because this surrogate can be cheaply evaluated, we can readily perform Monte Carlo simulation to verify our calculations using the Hermite-PC expansion. Figure 4-22 illustrates the estimated p.d.f. for $m$ using Hermite-PC expansions of order 1, 3, 5, and 7. As expected, the first-order expansion performs poorly, but the convergence is rapid with increasing order, and the seventh-order expansion yields a distribution that is nearly indistinguishable from the Monte Carlo results. A better sense of the rapid convergence can be obtained from Fig. 4-23, which plots the relative error of the mean and standard deviation estimates of $m$ for Hermite-PC expansions up to order 50. After order 10, the mean has converged to within machine precision, and the standard deviation is similarly converged after order 25.

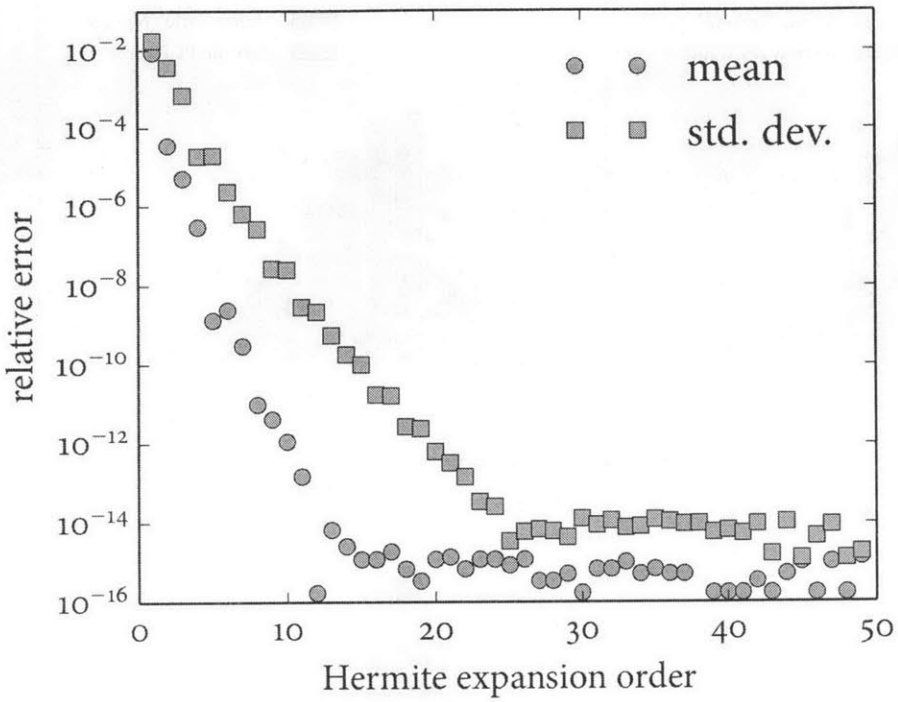


**Figure 4-23:** Convergence of mean and standard deviation estimates for excess velocity with increasing gPC expansion order: Re = 100, $\ln \mathrm{Ca} \sim \mathcal{N}(-4, 1)$.

### 4.5.1 Modeling slug flow with an uncertain bubble size

In practical applications of slug flow, the Taylor bubbles need not be of a uniform size; rather, there will be a distribution of bubble sizes, and this distribution might be described by probability density function. Of course, the exact nature of the bubble size distribution will be problem-specific as it will be a function of the flow conditions at the mixing junction where the two phases are combined (i.e., the location(s) where the bubbles are injected into the capillary).

For our final application of the gPC method to multiphase flow simulations, we shall demonstrate how one might utilize the gPC expansion to develop probabilistic models for slug flow applications when the bubble sizes are described by a probability distribution. For the purposes of this demonstration, we take Ca = 0.050 and assume the bubble volume is uniformly distributed such that

$$\left(\frac{D_{\mathrm{eq}}^*}{D}\right)^3 \sim \mathcal{U}\left[\frac{3}{8}, \frac{9}{4}\right] \tag{4.32}$$

where $D^*_{\text{eq}}$ denotes the equivalent diameter of the bubble, i.e.,

$$D^*_{\text{eq}} = \left(\frac{6V^*_b}{\pi}\right)^{\frac{1}{3}},$$

where $V^*_b$ is the (dimensional) bubble volume. For the distribution given in Eq. (4.32), roughly one-third of the bubbles will have an equivalent diameter smaller than the channel diameter, and are therefore *not* Taylor bubbles. This distribution was chosen to give more interesting variation in the output, and to illustrate the differences in behavior between Taylor bubbles and small, nearly spherical bubbles. We consider three different Reynolds numbers: Re = 1, Re = 10, and Re = 100.

Let $L^*$ denote the dimensional channel length, and $L^*_b$ denote the dimensional bubble length (*cf.* Fig. 4-1). We let $L^*_s = L^* - L^*_b$ denote the dimensional slug length. The corresponding dimensionless quantities are given by $L = L^*/D$, $L_b = L^*_b/D$, and $L_s = L^*_s/D$. Following Kreutzer et al. [73] and Walsh et al. [132], we decompose the total pressure drop into the sum of two parts: the pressure drop $\Delta P^*_{\text{slug}}$ within the liquid slug and $\Delta P^*_{\text{bub}}$, which accounts for the overall effect of the presence of the bubble:

$$\Delta P^*_{\text{tot}} = \Delta P^*_{\text{slug}} + \Delta P^*_{\text{bub}}. \tag{4.33}$$

Assuming fully-developed, laminar flow within the slug (i.e., Hagen–Poiseuille flow), we can write the pressure drop in the slug as

$$\Delta P^*_{\text{slug}} = \frac{64}{\text{Re}}\left(\frac{1}{2}\rho\bar{U}^2\right)\frac{L^*_s}{D} = 32L_s\left(\frac{\mu\bar{U}}{D}\right).$$

Thus, in terms of the viscous pressure scaling,

$$\Delta P = \frac{\Delta P^*}{\mu\bar{U}/D},$$

equation (4.33) can be written as

$$\Delta P_{\text{tot}} = 32L_s + \Delta P_{\text{bub}}.$$

As noted previously, for sufficiently long bubbles, the pressure drop is independent of the bubble's length. This is because the liquid in the film is stagnant, and consequently there are no viscous losses in this region; the pressure drop across the bubble is due solely to losses at the nose and tail. Thus, for our computational experiment, we should anticipate a saturation effect wherein the pressure drop increases with bubble volume until $(D^*_{\text{eq}}/D)^3 > 1$, at which point the pressure drop across the bubble becomes nearly constant. This is, indeed, the observed behavior, as seen in Fig. 4-24a. We have run 13 simulations (corresponding to a 13-point Gauss–Legendre quadrature) for Re = 1, Re = 10, and

**Table 4.2:** Summary of capillary pressure drop data and statistics. See Fig. 4-24 for illustration.

| | $(D^*_{eq}/D)^3$ | $\Delta P_{bub} = \Delta P_{tot} - 32L_s$ | | | $\Delta P_{tot}$ | | |
|---|---|---|---|---|---|---|---|
| | | Re = 1 | Re = 10 | Re = 100 | Re = 1 | Re = 10 | Re = 100 |
| $\xi_0$ | 0.389828 | 19.676 | 19.872 | 21.695 | 316.152 | 316.717 | 321.035 |
| $\xi_1$ | 0.452252 | 21.089 | 21.184 | 24.280 | 316.291 | 316.777 | 322.359 |
| $\xi_2$ | 0.561021 | 22.702 | 23.434 | 30.395 | 315.685 | 316.894 | 325.801 |
| $\xi_3$ | 0.710297 | 26.683 | 27.974 | 39.497 | 316.396 | 318.042 | 330.085 |
| $\xi_4$ | 0.892038 | 30.943 | 32.119 | 47.156 | 315.673 | 316.977 | 330.683 |
| $\xi_5$ | 1.096445 | 32.891 | 34.052 | 47.987 | 311.342 | 312.549 | 325.124 |
| $\xi_6$ | 1.312500 | 32.182 | 33.667 | 47.803 | 304.105 | 305.753 | 320.282 |
| $\xi_7$ | 1.528555 | 31.824 | 33.684 | 49.317 | 297.494 | 299.646 | 315.249 |
| $\xi_8$ | 1.732962 | 32.279 | 33.949 | 49.245 | 292.105 | 294.115 | 309.716 |
| $\xi_9$ | 1.914703 | 32.048 | 33.888 | 49.407 | 286.623 | 288.805 | 304.832 |
| $\xi_{10}$ | 2.063979 | 32.461 | 34.171 | 49.756 | 282.710 | 284.823 | 300.962 |
| $\xi_{11}$ | 2.172748 | 32.404 | 34.366 | 49.694 | 279.488 | 281.924 | 297.896 |
| $\xi_{12}$ | 2.235172 | 32.510 | 34.092 | 49.814 | 277.801 | 279.801 | 296.303 |
| | **mean:** | 30.215 | 31.605 | 44.923 | 302.126 | 303.800 | 317.376 |
| | **std. dev.:** | 3.759 | 4.154 | 7.704 | 13.011 | 12.597 | 10.613 |

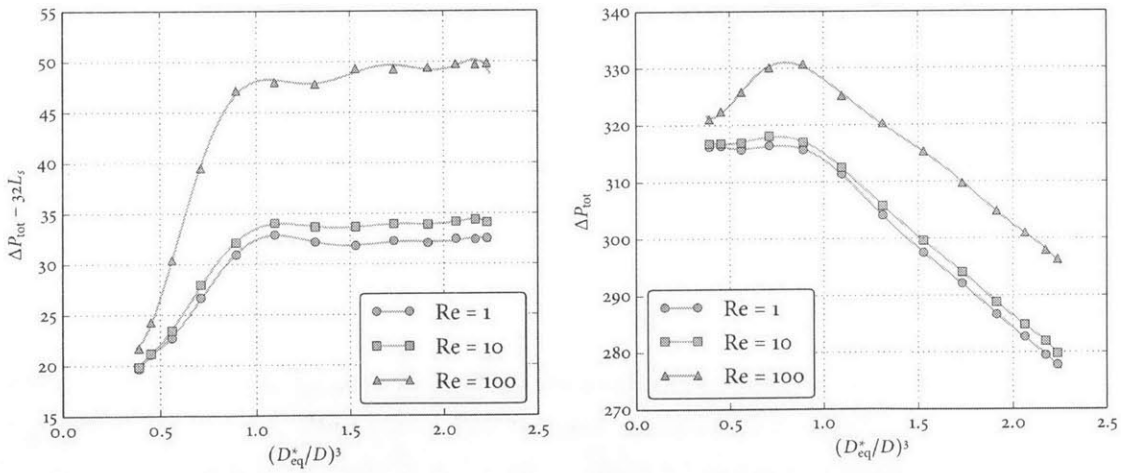


(a) (b)

**Figure 4-24:** Pressure drop vs. bubble volume for Re = 1, Re = 10, and Re = 100; Markers depict values computed at quadrature nodes (*cf.* Table 4.2 for listing of data). Solid lines depict Legendre-PC expansion.

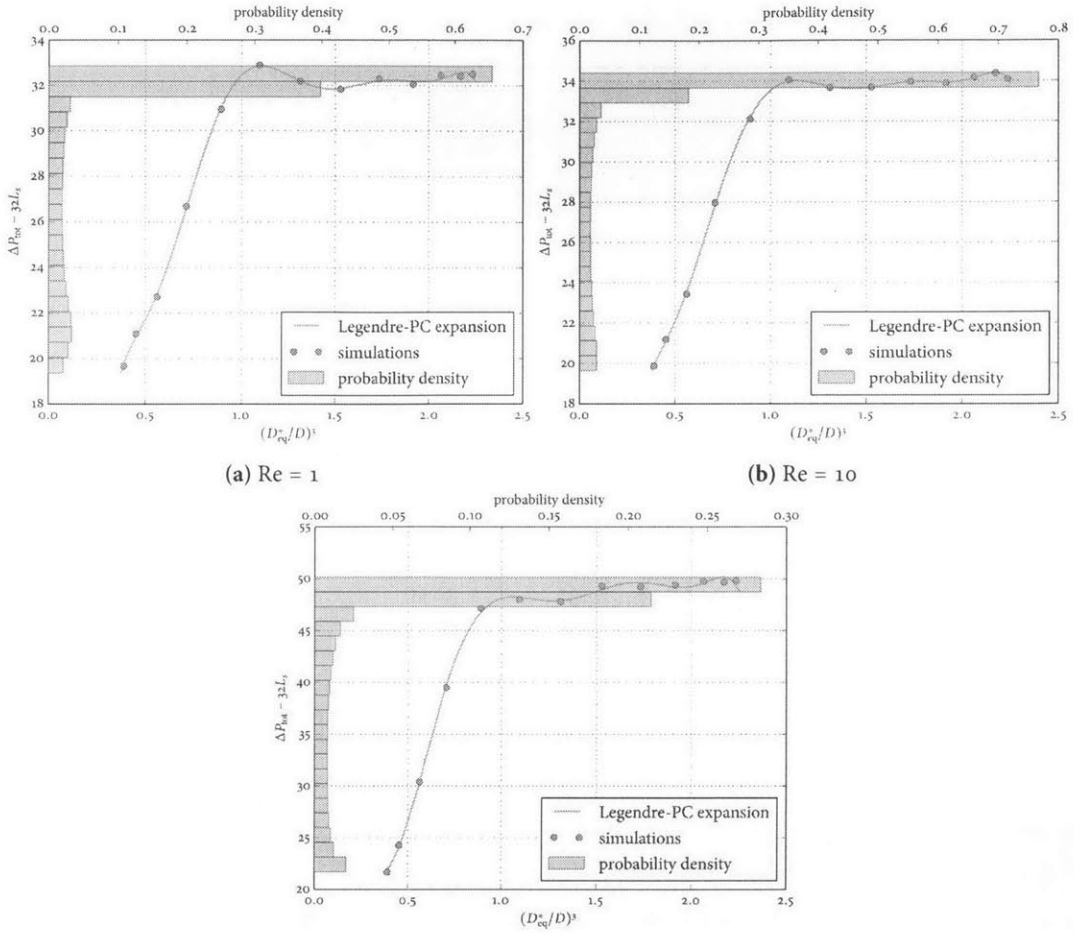


**(a)** Re = 1

**(b)** Re = 10

**(c)** Re = 100

**Figure 4-25:** Comparison of probability distribution of pressure drop across bubble for (a) Re = 1, (b) Re = 10, and (c) Re = 100.

Re = 100. The computed bubble pressure drop for each simulation is listed in Table 4.2, and the results are plotted in Fig. 4-24a. Also plotted in Fig. 4-24a are the $8^{\text{th}}$-order Legendre-PC expansions that were constructed from the 13 observations. In Fig. 4-25, these Legendre-PC expansions have been used to estimate the probability distribution of the bubble pressure drop. We, of course, see that the distribution is highly peaked near the constant $\Delta P_{\text{bub}}$. Notice also that the pressure drop across the bubble increases with increasing Re.

Figure 4-24b plots the computed total pressure drop, $\Delta P_{\text{tot}}$ vs. the bubble volume together with the Legendre-PC expansion for Re = 1, Re = 10, and Re = 100. Since our simulations were all run on a fixed-length domain ($L = 10$), an increase in the bubble's volume corresponds to a decrease in the slug length, and therefore a reduced overall pressure drop. The estimated mean and standard

**Table 4.3:** Summary of bubble velocity data. See Fig. 4-26 for illustration.

| | $(D^*_{eq}/D)^3$ | $U_b/\bar{U}$ | | |
|---|---|---|---|---|
| | | Re = 1 | Re = 10 | Re = 100 |
| $\xi_0$ | 0.389828 | 1.7054 | 1.6777 | 1.4999 |
| $\xi_1$ | 0.452252 | 1.6267 | 1.5992 | 1.4123 |
| $\xi_2$ | 0.561021 | 1.5129 | 1.4795 | 1.3062 |
| $\xi_3$ | 0.710297 | 1.3934 | 1.3656 | 1.2536 |
| $\xi_4$ | 0.892038 | 1.3407 | 1.3246 | 1.2777 |
| $\xi_5$ | 1.096445 | 1.3459 | 1.3361 | 1.3313 |
| $\xi_6$ | 1.312500 | 1.3570 | 1.3474 | 1.2978 |
| $\xi_7$ | 1.528555 | 1.3584 | 1.3469 | 1.3072 |
| $\xi_8$ | 1.732962 | 1.3570 | 1.3451 | 1.3057 |
| $\xi_9$ | 1.914703 | 1.3564 | 1.3454 | 1.3046 |
| $\xi_{10}$ | 2.063979 | 1.3567 | 1.3454 | 1.3057 |
| $\xi_{11}$ | 2.172748 | 1.3570 | 1.3450 | 1.3056 |
| $\xi_{12}$ | 2.235172 | 1.3568 | 1.3459 | 1.3053 |
| | **mean:** | 1.3877 | 1.3721 | 1.3091 |
| | **std. dev.:** | 0.0819 | 0.0763 | 0.0404 |

deviation of $\Delta P_{bub}$ and $\Delta P_{tot}$ are listed in Table 4.2.

Table 4.3 summarizes the bubble velocity for each of the quadrature samples and lists the estimated mean and standardard deviation, again computed using an $8^{th}$-order Legendre-PC expansion. Figure 4-26 gives a graphical illustration of the same data. It is seen that bubble's velocity is insenstive to the bubble's size provided $(D^*_{eq}/D)^3 \gtrsim 1.25$, or, equivalently, $D_{eq} \gtrsim 1.07D$; consequently, the probability density is concentrated about this limiting velocity. Smaller bubbles travel at faster speeds, which makes sense because these bubbles are located in the central region of the channel where the liquid velocity is highest.

Figures 4-27–4-29 plot the mean pressure along the channel wall and the mean shear stress for Re = 1, 10, and 100. Also plotted are error bars corresponding to ± one standard deviation. The pressure has been normalized such that $P_w(2) = 0$. Consequently, the standard deviation of the pressure is seen to be zero in the right-most portion of the plot, where the bubble has no influence on the flow. Moving from right to left, the departure point from Hagen–Poiseuille flow is clearly dependent on the size of the bubble, so the uncertainty builds rapidly in the region near the nose of the bubble and continues to increase slightly in the film. Once past the tail of the bubble, there are no more sources for uncertainty, so the standard deviation is constant in this region. The behavior of the shear stress distribution is similar, except the flow away from the bubble on either end is deterministic

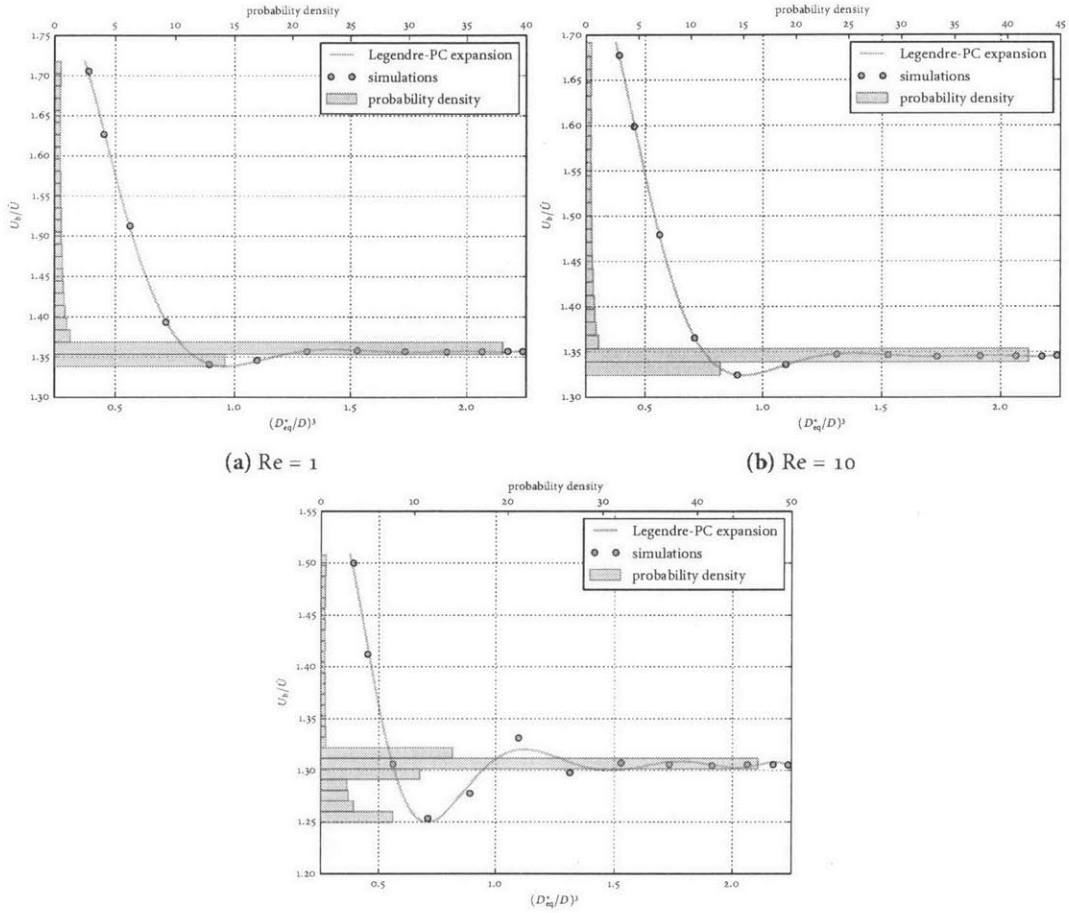


(a) Re = 1

(b) Re = 10

(c) Re = 100

**Figure 4-26:** Comparison of probability distribution of bubble velocity for (a) Re = 1, (b) Re = 10, and (c) Re = 100.

(fully-developed, and uninfluenced by the presence of the bubble), so the standard deviation vanishes for $|x| \gtrsim 1.75$. For the Re = 100 case illustrated in Fig. 4-29, we observe significant oscillations in the standard deviation estimate for both $P_w$ and $\tau_w$ in the film region surrounding the bubble; this tell-tale sign of the Gibbs/Runge phenomena suggests that the gPC expansion has not converged, and a higher order expansion would be necessary to resolve the uncertainty in both quantities in this region. On the other hand, the lack of any such oscillatory behavior away from the bubble suggests that, in this region, the gPC expansion has converged. Consequently, the computed uncertainty in the total pressure drop across the channel is expected to be a reliable estimate even though the method fails to adequately represent the uncertainty in the film region, where both the pressure and shear stress strongly influenced by the location of the interface. To test this claim, we have rerun the Re = 100 case

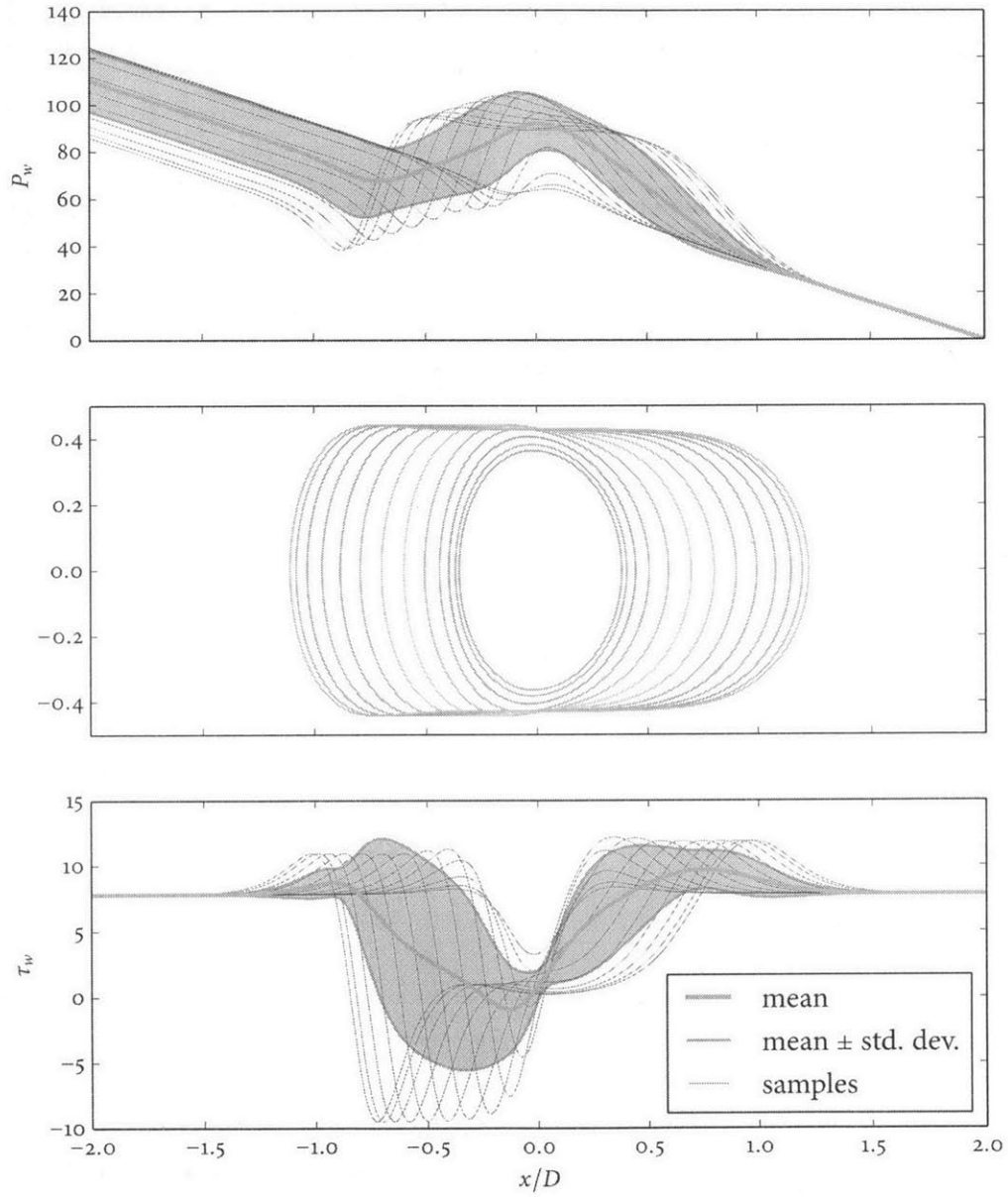


**Figure 4-27:** Pressure (top) and shear stress (bottom) measured at the wall for Re = 1. The interfaces for each of the 13 simulations have been plotted in the middle to assist interpretation of the results. The shaded region in the top and bottom plots corresponds to the mean ± one standard deviation.

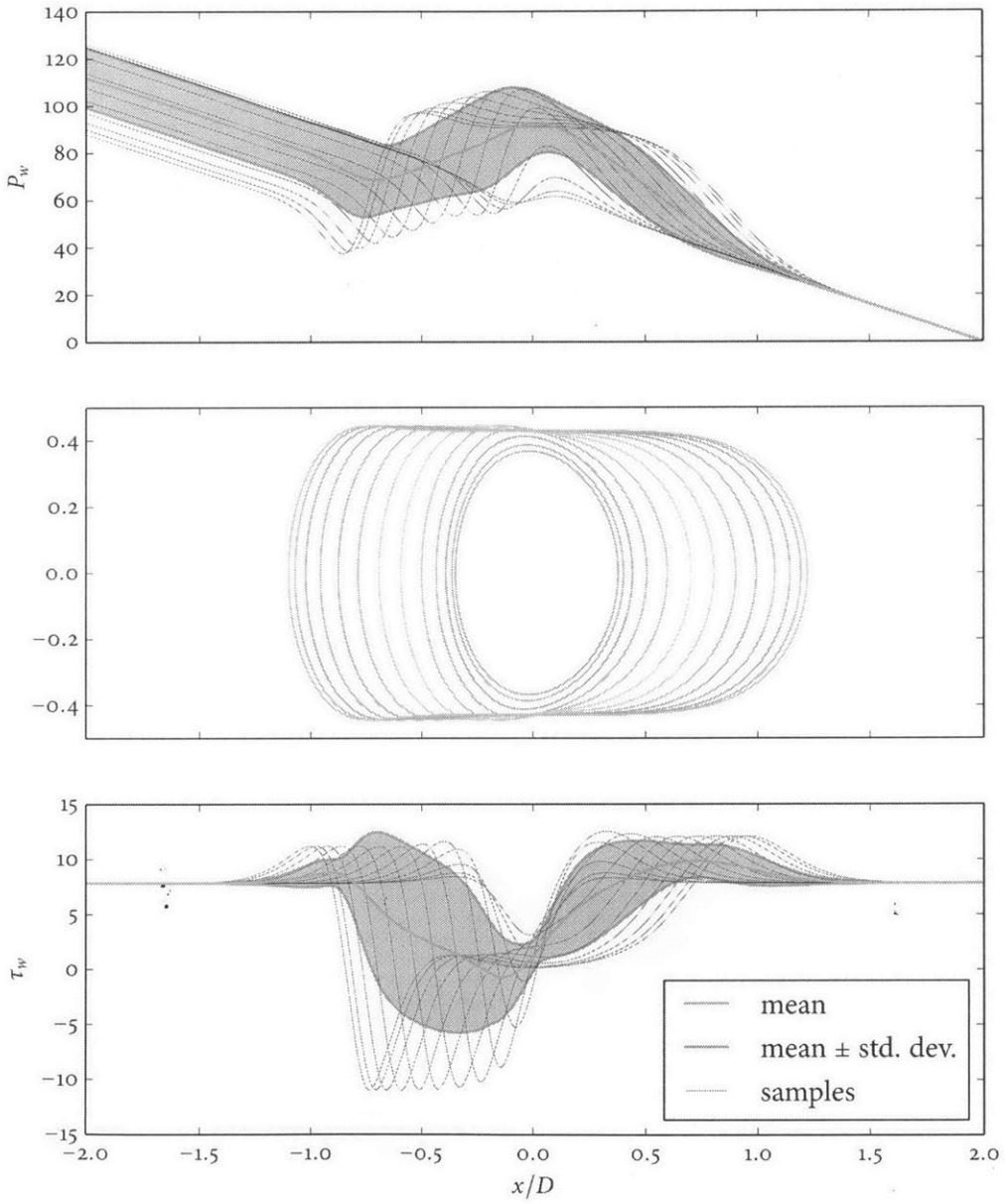


**Figure 4-28:** Pressure (top) and shear stress (bottom) measured at the wall for Re = 10. The interfaces for each of the 13 simulations have been plotted in the middle to assist interpretation of the results. The shaded region in the top and bottom plots corresponds to the mean ± one standard deviation.

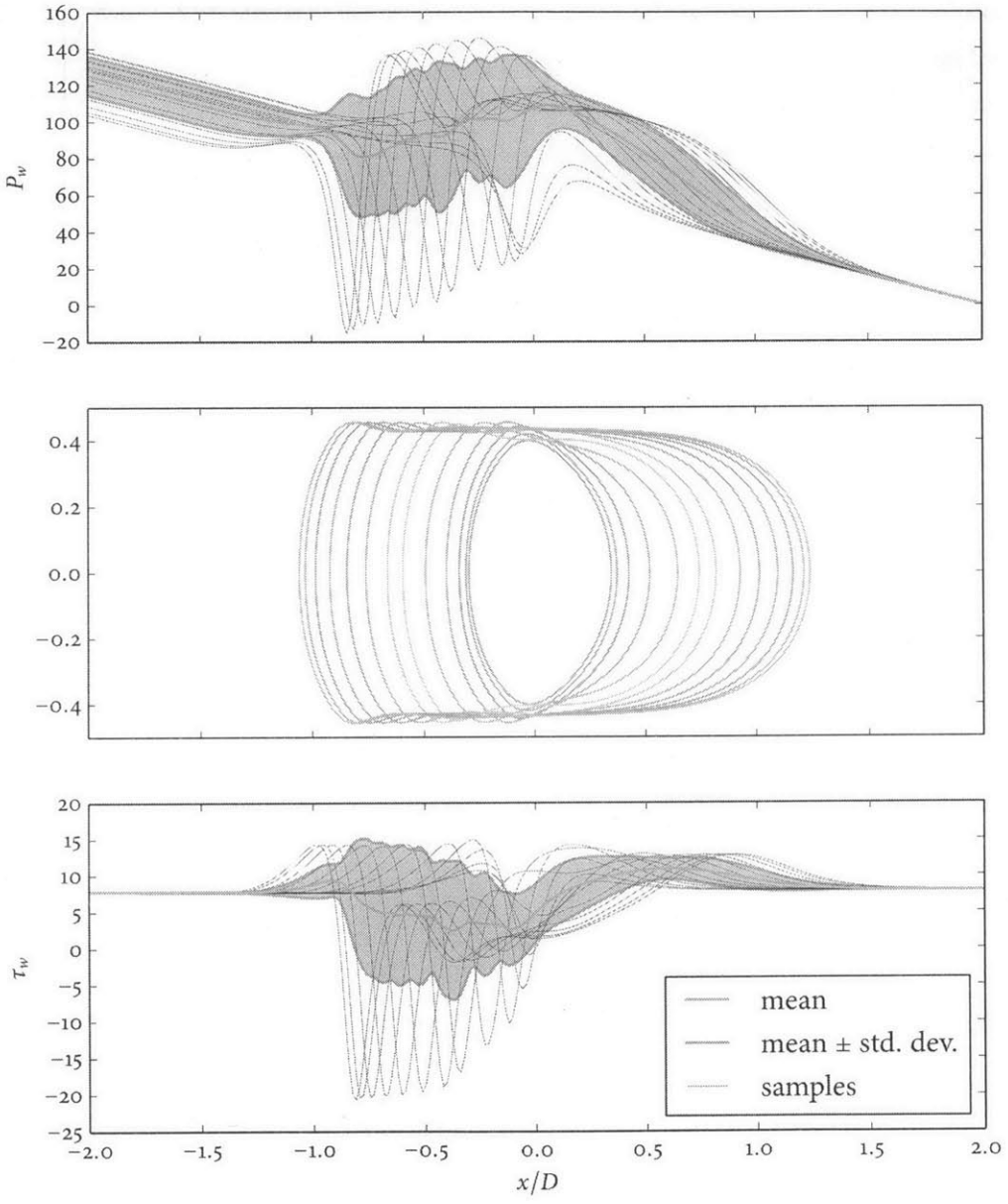


**Figure 4-29:** Pressure (top) and shear stress (bottom) measured at the wall for Re = 100. The interfaces for each of the 13 simulations have been plotted in the middle to assist interpretation of the results. The shaded region in the top and bottom plots corresponds to the mean ± one standard deviation.

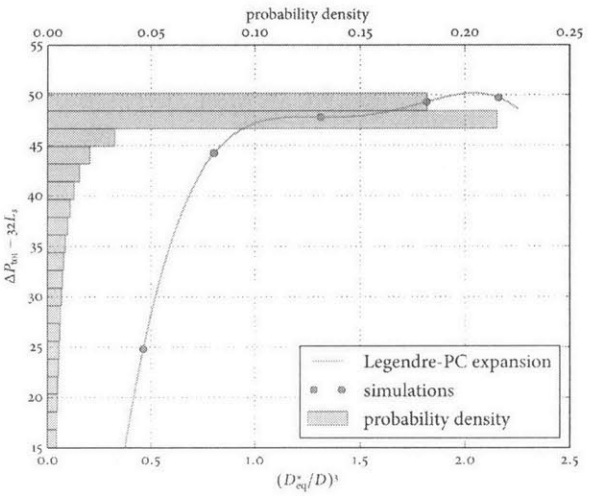


**Figure 4-30:** Probability distribution of pressure drop across bubble using $4^{th}$-order Legendre-PC expansion for Re = 100.

using a 5-point quadrature to construct a $4^{th}$-order Legendre-PC expansion. Figure 4-30 illustrates the resulting probability distribution for the bubble pressure drop, and agrees well with the higher-order expansion results illustrated in Fig 4-25c. In fact, for the $4^{th}$-order expansion, we compute the mean to be 44.83 and the standard deviation to be 7.594, compared to 44.923 and 7.704 listed in Table 4.2. Figure 4-31 is the counterpart to Fig. 4-29, and demonstrates even more severe oscillations, yet the computed uncertainty in the bubble pressure drop (which is a smooth observable) is nearly the same in both cases.

Figures 4-32, 4-33, and 4-34 illustrate the mean and standard deviation of the $u$- and $v$-velocity components for Re = 1, 10, and 100, respectively. As for the pressure, in all cases the standard deviation is zero ahead of and behind the bubble, where the velocity approaches its fully-developed profile and is not influenced by the bubble's presence. In all cases, we observe significant spatial oscillations in the mean and standard deviation of the radial velocity component, $v$. While $v(r, x, \xi)$ is technically continuous across the interface, it will vary significantly depending on the location of the interface (i.e., $v$ exhibits a steep variation in $\xi$). On the other hand, the axial velocity $u(r, x, \xi)$ is much better behaved.[§]

[§]Note that $u(r, x, \xi)$ is the velocity relative to the bubble's velocity, which is likewise a function of $\xi$. Thus, the absolute axial velocity is given by $u(r, x, \xi) + U_b(\xi)$.

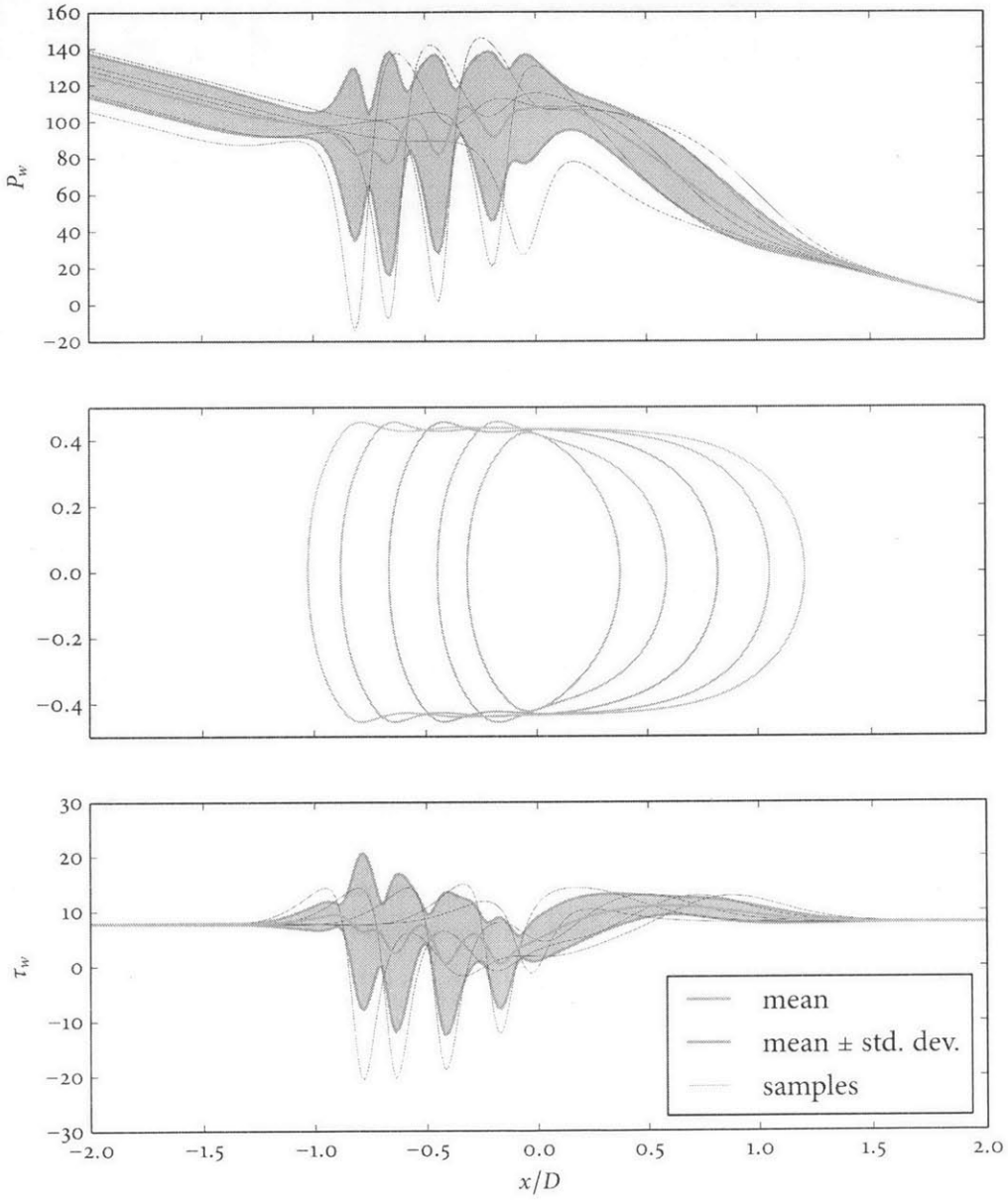


**Figure 4-31:** Pressure (top) and shear stress (bottom) measured at the wall for Re = 100 using $4^{\text{th}}$-order gPC expansion illustrating signficant Gibbs/Runge oscillations near interface.

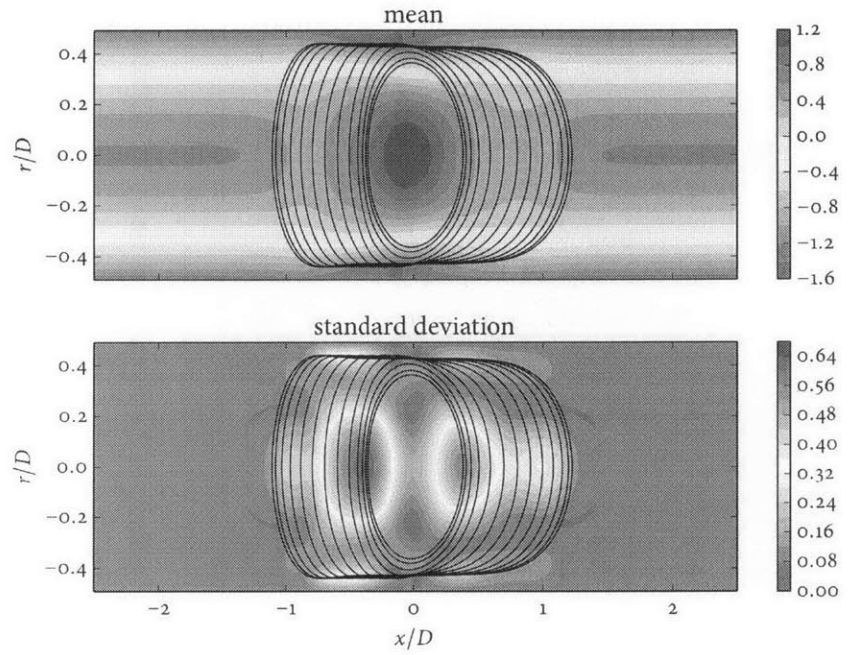


**(a)** $u(r, x; \xi)$

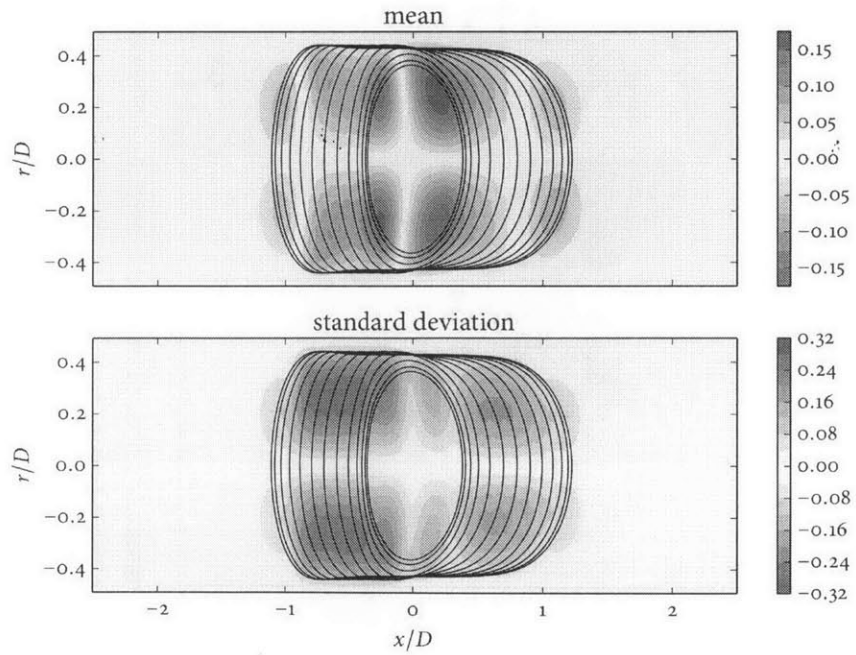


**(b)** $v(r, x; \xi)$

**Figure 4-32:** Mean and standard deviation of axial (a) and radial (b) components of velocity field for Ca = 0.050 and Re = 1.

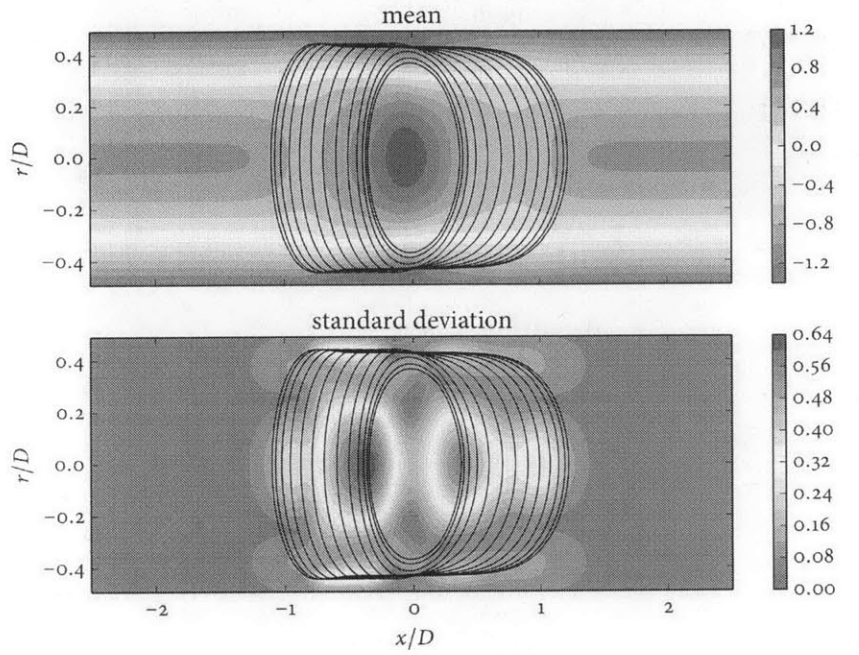


**(a)** $u(r, x; \xi)$

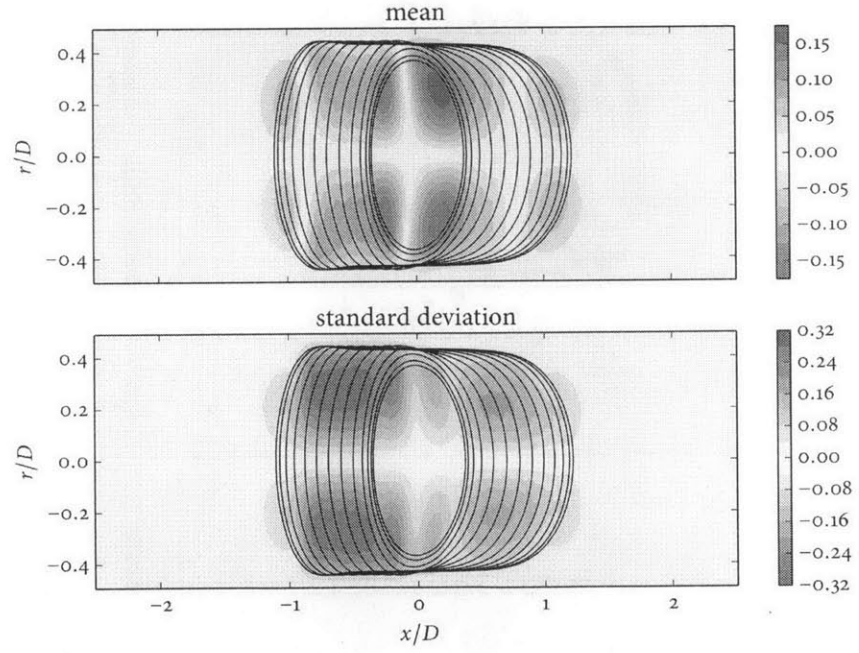


**(b)** $v(r, x; \xi)$

**Figure 4-33:** Mean and standard deviation of axial (a) and radial (b) components of velocity field for Ca = 0.050 and Re = 10.

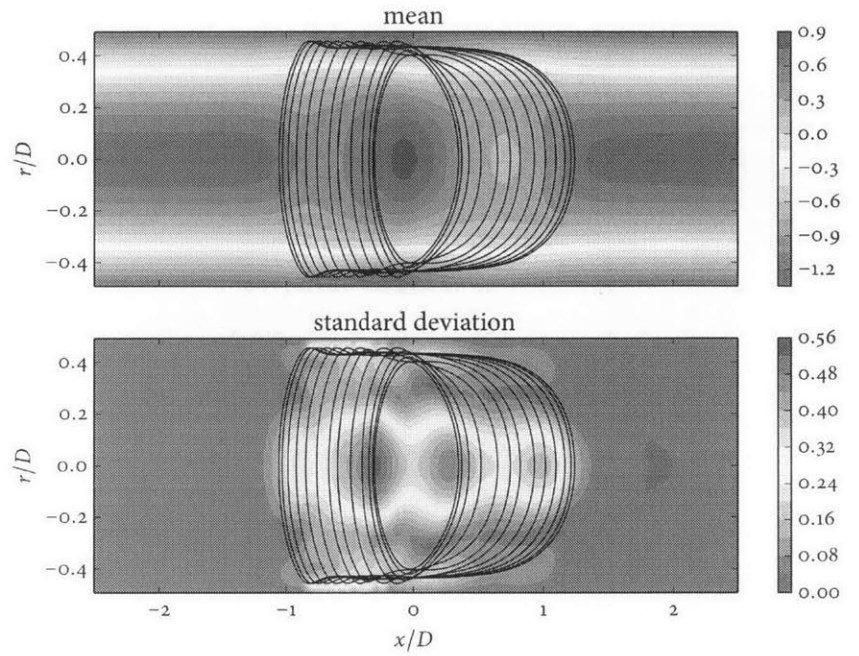


**(a)** $u(r, x; \xi)$

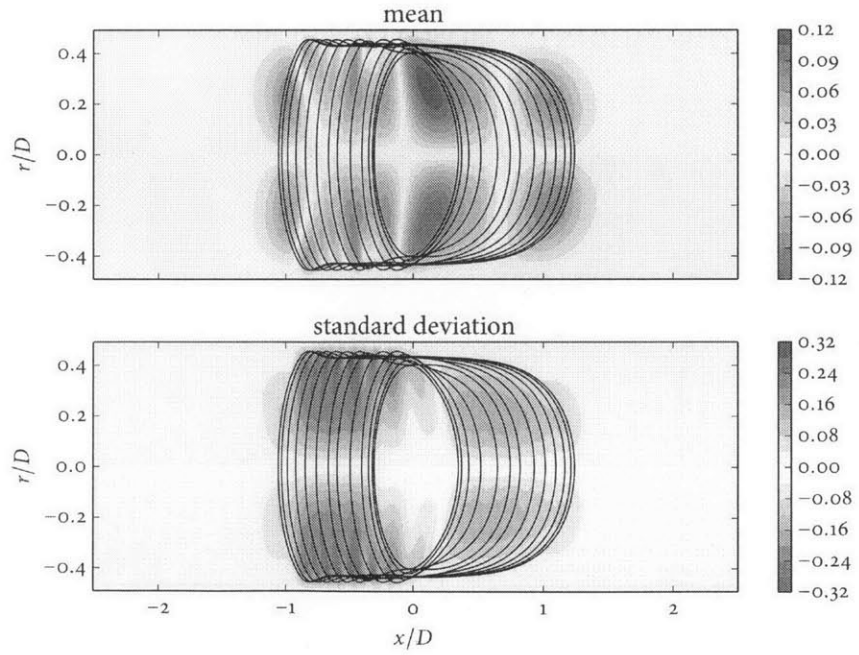


**(b)** $v(r, x; \xi)$

**Figure 4-34:** Mean and standard deviation of axial (a) and radial (b) components of velocity field for Ca = 0.050 and Re = 100.

THIS PAGE INTENTIONALLY LEFT BLANK

# Chapter 5

# Conclusions and Future Work

One of the main objectives of this work was to critically evaluate the generalized polynomial chaos formalism (in both its intrusive and non-intrusive forms) for uncertainty propagation in multiphase flow problems. In the course of this investigation, it was concluded that intrusive gPC methods, such as the stochastic Galerkin method, are unlikely to ever be successfully applied to computational multiphase fluid dynamics (CMFD) applications without significant advances in the theory. The gPC expansion is capable of achieving significant efficiency gains over Monte Carlo simulation by imposing certain smoothness restrictions on the random field/variable being analyzed. But for CMFD applications, these restrictions simply do not apply for many of the primitive flow quantities, such as the pressure field or density field. Consequently, gPC expansion is rendered ineffective for quantifying uncertainty in these quantities. Fortunately, the non-intrusive formulation (NISP) allows one to bypass these issues to some degree provided one considers only quantities that exhibit a smooth dependence on the input RVs. NISP is capable of approximating the probability distribution of such quantities using significantly fewer model evaluations (samples) than would be required of Monte Carlo simulation. The example problems discussed in Chapters 3 and 4 demonstrate that NISP can still be used to great effect for quantifying the uncertainty in quantities such as bubble velocity and pressure drop, while simultaneously demonstrating poor convergence when representing field quantities (pressure and velocity), especially in the vicinity of the liquid-vapor interface where these quantities are highly sensitive to the (uncertain) location of the interface. On the other hand, away from the interface the gPC performs satisfactorily.

Admittedly, however, the applications studied in this work were rather simple, which was ne-

cessitated by the limited computational resources available to this project. Moreover, CMFD is a challenging art, and there are many ways for simulations to go awry. Research codes, like *Gerris*, are not always robust, and it is often a non-trivial task to get even a single simulation corresponding to one particular input configuration to run successfully (i.e., without crashing) while also giving realistic results. For this study, a concious effort was therefore made to avoid highly-complex simulations for which the code would be unable to accommodate significant variations in the input parameters. A more interesting application of the gPC-UQ methods discussed herein might be the study of the Marangoni effect. In practice, the initial concentration of contaminants would likely be uncertain, resulting in uncertainty in the magnitude of Marangoni stresses. Although this phenomena occurs near the interface, and therefore one might anticipate the gPC expansion to perform poorly, the Marangoni effect will affect other, non-local quantities, such as those studied in this work: bubble velocity and pressure drop. Unfortunately, *Gerris* is currently unequipped with the necessary machinery to handle surface tension gradients, but being open source, there is nothing preventing its future implementation. This could prove an interesting and worthwhile future study.

Besides demonstrating that the gPC expansion, despite its limitations, could still be successfully applied to UQ problems in CMFD applications, there are a handful of other contributions that have come out of this work. We developed and validated a moving frame of reference approach in *Gerris* for the study of rising bubbles and slug flow. A numerical database was generated for terminal velocity, film thickness and pressure drop of Taylor bubbles in slug flow for nearly 150 combinations of capillary and Reynolds numbers for $Ca \in [0.001, 2]$ and $Re \in [0, 1000]$. These simulations were similar to those reported by Kreutzer et al. [73], who used finite element method (FEM) to simulate slug flow over a similar range of Re but for $Ca \leq 0.04$. Higher Ca cases, similar to those studied here, were simulated by Giavedoni and Saita [43, 44] using FEM, but they simulated the front and rear sections of the bubble separately. To our knowledge, the present work comprises the most extensive numerical study to-date of capillary slug flow using the VoF method. Finally, using the numerical database, a new correlation for the film thickness was proposed that reduces the data with an average relative error of 0.76% and standard deviation of 2.97%. The accuracy of the correlation is comparable to the correlation proposed by Han and Shikazono [49], but requires knowledge of only the average liquid velocity, $\bar{U}$, and not the bubble velocity, $U_b$. A related correlation for the bubble velocity was also presented that reduces the data with an average relative error of 0.15% and standard deviation of 0.81%.

# Appendix A

# Overview of Interfacial Resistance Models

Consider the interface configuration illustrated in Fig. A-1. For a static ($U = 0$) interface, the mass flux incident from the left is given by [*cf.* 17, §4.5]

$$j'_- = \sqrt{\frac{R^* T_v}{2\pi}}\, \rho_v, \tag{A.1}$$

where $T_v$ and $\rho_v$ denote, respectively, the temperature and density of the vapor phase, and $R^*$ is the ideal gas constant for the fluid of interest. Intuitively, we expect that if the interface is moving to the right (liquid is evaporating) with velocity $U$, then the actual incident mass flux should be smaller than that given by (A.1) since the speed of the vapor molecules relative to the moving interface will be be reduced. Specifically, we expect the true incident mass flux $j_-$ to be related to the static flux $j'_-$ by

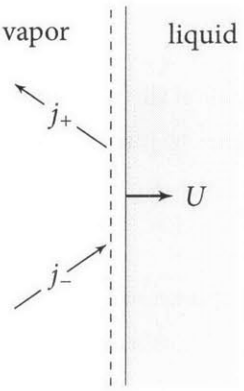


**Figure A-1:** Left- and right-incident mass flux, respectively $j_-$ and $j_+$, on an evaporating interface moving with velocity $U$.

$$j_- = \Gamma\, j'_-, \tag{A.2}$$

where $\Gamma$ is a non-equilibrium correction factor that accounts for interface motion. Schrage [115] derived and analytical expression for $\Gamma$ using arguments from kinetic theory, assuming the vapor

phase to be an ideal gas. For low Mach number flows, Schrage's result is given approximately as

$$\Gamma \approx 1 - \sqrt{\frac{\pi\gamma}{2}}\frac{U}{C}, \tag{A.3}$$

where $\gamma \equiv \frac{c_p}{c_v}$ is the adiabatic index and $C \equiv \sqrt{\gamma R^* T_v}$ is the sound speed of the vapor. One could proceed similarly to obtain an expression for the right-incident mass flux $j_+$. For this case, however, it turns out that the non-equilibrium effects are negligible so that no correction factor is needed. Carey [17] justifies this assumption by arguing that since the surface moves with the liquid, there is no relative motion between the surface and the vapor particles immediately adjacent to the interface. Consequently, we have

$$j_+ = \sqrt{\frac{R^* T_i}{2\pi}}\,\rho^e(T_i), \tag{A.4}$$

where $\rho^e(T_i)$ is the equilibrium vapor density corresponding to the interface temperature $T_i$ [99].

We are not interested in the total mass fluxes across the surface, as given above, but rather only that fraction of the mass flux that is due to a phase change process, such as evaporation or condensation. For instance, of the mass flux $j_-$ incident on the interface from the vapor side, only a fraction actually condenses while the remainder is merely "reflected" off the interface. Thus, we can define the condensation mass flux as

$$j_c \equiv \hat{\sigma}_c\, j_-,$$

where $\hat{\sigma}_c$ is called the *condensation coefficient*, and represents the fraction of the incident mass flux that contributes to phase change via condensation. Similarly, the evaporative mass flux is defined by

$$j_e \equiv \hat{\sigma}_e\, j_+,$$

where the *evaporation coefficient* $\hat{\sigma}_e$ accounts for the fact that only a fraction of the mass flux passing through the surface from the right is due to evaporation, the remainder being due to reflection. With these definitions, it is clear that the net mass flux due to phase change is simply

$$j = j_e - j_c = \hat{\sigma}_e\, j_+ - \hat{\sigma}_c\, j_-, \tag{A.5}$$

where we have adopted the convention that the net mass flux is positive for evaporation*. Substituting

*This is opposite the convention taken by Carey [17], but is more convenient for our purposes.

(A.2) and (A.4) into (A.5) and simplifying gives

$$j = \frac{1}{\sqrt{2\pi R^*}} \left( \hat{\sigma}_e \frac{P_{i,l}}{T_i^{1/2}} - \hat{\sigma}_c \Gamma \frac{P_v}{T_v^{1/2}} \right), \tag{A.6}$$

where $P_v = \rho_v R^* T_v$ is the partial pressure of the vapor and $P_{i,l} \equiv \rho^e(T_i) R^* T_i$ denotes an effective pressure that is 'defined' by the ideal gas law. Morris [89] refers to $P_{i,l}$ as the liquid-vapor coexistence pressure, i.e., the partial pressure of vapor required for the liquid to coexist with its vapor phase at temperature $T_i$ when the liquid pressure is $P_l$. If we neglect the non-equilibrium effects arising the motion of the interface by assuming $\Gamma = 1$, then (A.6) reduces to the **Hertz–Knudsen–Langmuir (HKL) Equation** [15]

$$j = \frac{1}{\sqrt{2\pi R^*}} \left( \hat{\sigma}_e \frac{P_{i,l}}{\sqrt{T_i}} - \hat{\sigma}_c \frac{P_v}{\sqrt{T_v}} \right). \tag{A.7}$$

Alternatively, substituting (A.3) into (A.6) gives

$$\begin{aligned} j &= \frac{1}{\sqrt{2\pi R^*}} \left( \hat{\sigma}_e \frac{P_{i,l}}{\sqrt{T_i}} - \hat{\sigma}_c \frac{P_v}{\sqrt{T_v}} \right) + \left( \frac{P_v}{C} \sqrt{\frac{\gamma}{R^* T_v}} \right) U \frac{\hat{\sigma}_c}{2} \\ &= \frac{1}{\sqrt{2\pi R^*}} \left( \hat{\sigma}_e \frac{P_{i,l}}{\sqrt{T_i}} - \hat{\sigma}_c \frac{P_v}{\sqrt{T_v}} \right) + \rho_v \frac{\hat{\sigma}_c}{2} U. \end{aligned}$$

When the interface motion is due solely to phase change, $j = \rho_v U$ and the above result reduces to the **Hertz–Knudsen–Schrage (HKS) Equation** [137]

$$j = \frac{1}{\sqrt{2\pi R^*}} \left( \frac{2}{2 - \hat{\sigma}_c} \right) \left( \hat{\sigma}_e \frac{P_{i,l}}{\sqrt{T_i}} - \hat{\sigma}_c \frac{P_v}{\sqrt{T_v}} \right). \tag{A.8}$$

Comparison of (A.7) and (A.8) reveals that the HKL equation underestimates the mass flux by as much as a factor of 2 when $\hat{\sigma}_c = 1$ as compared to the HKS equation. Physically, this is be the HKL equation (A.7) fails to account for the fact as that the interface is retreating due to evaporation, fewer vapor molecules are able to catch up, resulting in fewer condensation events.

At equilibrium, $j_+ = j_-$ and $j = 0$, and (A.5) implies that $\hat{\sigma}_e = \hat{\sigma}_c$. This is the usual justification for assuming that the evaporation and condensation coefficients are equal; see, e.g., Carey [17], who cautions that this assumption is suspect whenever phase change is occurring. Nevertheless, this assumption is common, if only for lack of better information. Letting $\hat{\sigma} \equiv \hat{\sigma}_e = \hat{\sigma}_c$ be the so-called

*accommodation coefficient*[†], (A.8) reduces to the **Kutcherov–Rikenglaz (KR) Equation**

$$j = \frac{1}{\sqrt{2\pi R^*}} \left( \frac{2\hat{\sigma}}{2 - \hat{\sigma}} \right) \left( \frac{P_{i,l}}{\sqrt{T_i}} - \frac{P_v}{\sqrt{T_v}} \right). \tag{A.9}$$

The distinction between (A.8) and (A.9) is merely a matter of convenience as the two are essentially equivalent. In the literature, both equations are variously referred to as either the HKS equation or the KR equation; for instance, Li et al. [84] use both names in reference to (A.8).

To use any of the aforementioned models, one must first determine the coexistence pressure $P_{i,l}$. This can be related to the saturation pressure corresponding to the interface temperature $T_i$ through the Kelvin equation

$$P_{i,l} = P_{sat}(T_i) \exp\left[ \frac{P_{i,l} - P_{sat}(T_i) - (P_v - P_l)}{\rho_l R^* T_i} \right]. \tag{A.10}$$

Furthermore, an expression relating $P_{sat}(T_i)$ to the vapor pressure $P_v = P_{sat}(T_v)$ is given by the Clausius-Clapeyron equation

$$P_{sat}(T_i) = P_v \exp\left[ \frac{h_{fg}}{R^*} \left( \frac{1}{T_v} - \frac{1}{T_i} \right) \right] \tag{A.11}$$

where $h_{fg}$ denotes the latent heat of evaporation. Wang et al. [136] use (A.10) and (A.11) together with (A.9) to compute the interfacial mass transfer. Alternatively, we can follow Morris [89] and linearize (A.10) about the vapor state $(T_v, P_v)$ to obtain

$$P_{i,l} \approx P_v + \frac{\rho_v h_{fg}}{T_v}(T_i - T_v) + \frac{\rho_v}{\rho_l}(P_l - P_v). \tag{A.12}$$

Substituting (A.12) into (A.9) yields the **Kelvin–Clapeyron Equation**

$$j = \frac{1}{\sqrt{2\pi R^* T_m}} \left( \frac{2\hat{\sigma}}{2 - \hat{\sigma}} \right) \frac{T_v}{T_i} \left[ \frac{\rho_v h_{fg}}{T_v}(T_i - T_v) + \frac{\rho_v}{\rho_l}(P_l - P_v) \right], \tag{A.13}$$

where $T_m = \frac{1}{2}(T_i + T_v)$. Wayner [139] derives (A.13) in a slightly modified form following earlier work by Potash and Wayner [102] and Wayner, Jr. et al. [138]. It is evident from (A.13) that the interfacial mass flux is driven by two sources: the temperature jump, $T_i - T_v$, and the pressure difference, $P_l - P_v$.

[†]This terminology is consistent with Carey [17] and Ajaev [5]. It should be pointed out, however, that others (e.g., DasGupta et al. [27]) refer to the quantity $C = \frac{2\hat{\sigma}}{2-\hat{\sigma}}$ as the accommodation coefficient.

Wayner [140] refers to these "forces" as the Clapeyron effect and the Kelvin effect, respectively, i.e.,

$$j = \underbrace{a(T_i - T_v)}_{\text{Clapeyron Effect}} + \underbrace{b(P_l - P_v)}_{\text{Kelvin Effect}}$$

with

$$a \equiv \frac{1}{\sqrt{2\pi R^* T_m}} \left( \frac{2\hat{\sigma}}{2 - \hat{\sigma}} \right) \frac{\rho_v h_{fg}}{T_i}$$

$$b \equiv \frac{1}{\sqrt{2\pi R^* T_m}} \left( \frac{2\hat{\sigma}}{2 - \hat{\sigma}} \right) \frac{\rho_v}{\rho_l} \frac{T_v}{T_i}.$$

DasGupta et al. [26–28] used (A.14) to model the heat transfer within evaporating extended menisci. Lay and Dhir [78] used (A.14) to model the heat transfer in vapor stems during nucleate boiling[‡]. A slightly simplified form of (A.14) has been used by Son et al. [118, 119], Stephan and Hammer [121], and Stephan and Busse [122], all of whom have assumed $T_m \approx T_v$ and $T_i \approx T_v$ in the expressions for $a$ and $b$. Finally, Kern and Stephan [66] extend this model to account for evaporation of binary mixtures. Despite the popularity of the linearized model (A.14), Wang et al. [136] found that for superheats greater than 5 K, (A.14) significantly underestimates the heat transfer coefficient compared to the full model obtained using Eqs. (A.9)-(A.11) unmodified.

For convencience, Fig. A-2 summarizes the various interfacial mass transport models and schematizes the relationships between each.

[‡]In the formulation given by Lay and Dhir [78], the prefactor $\frac{2\hat{\sigma}}{2-\hat{\sigma}}$ is replaced with a quantity $a_1$, which the authors refer to as the evaporation coefficient, noting that its value should be approximately unity. This is yet another example of the confusion of terminology that has persisted in the literature. Moreover, an evaporation coefficient (more precisely, accommodation coefficient as we have defined above) of unity would give $a_1 = 2$. This confusion is evidently resolved in later works by Dhir and collaborators [e.g., 118].

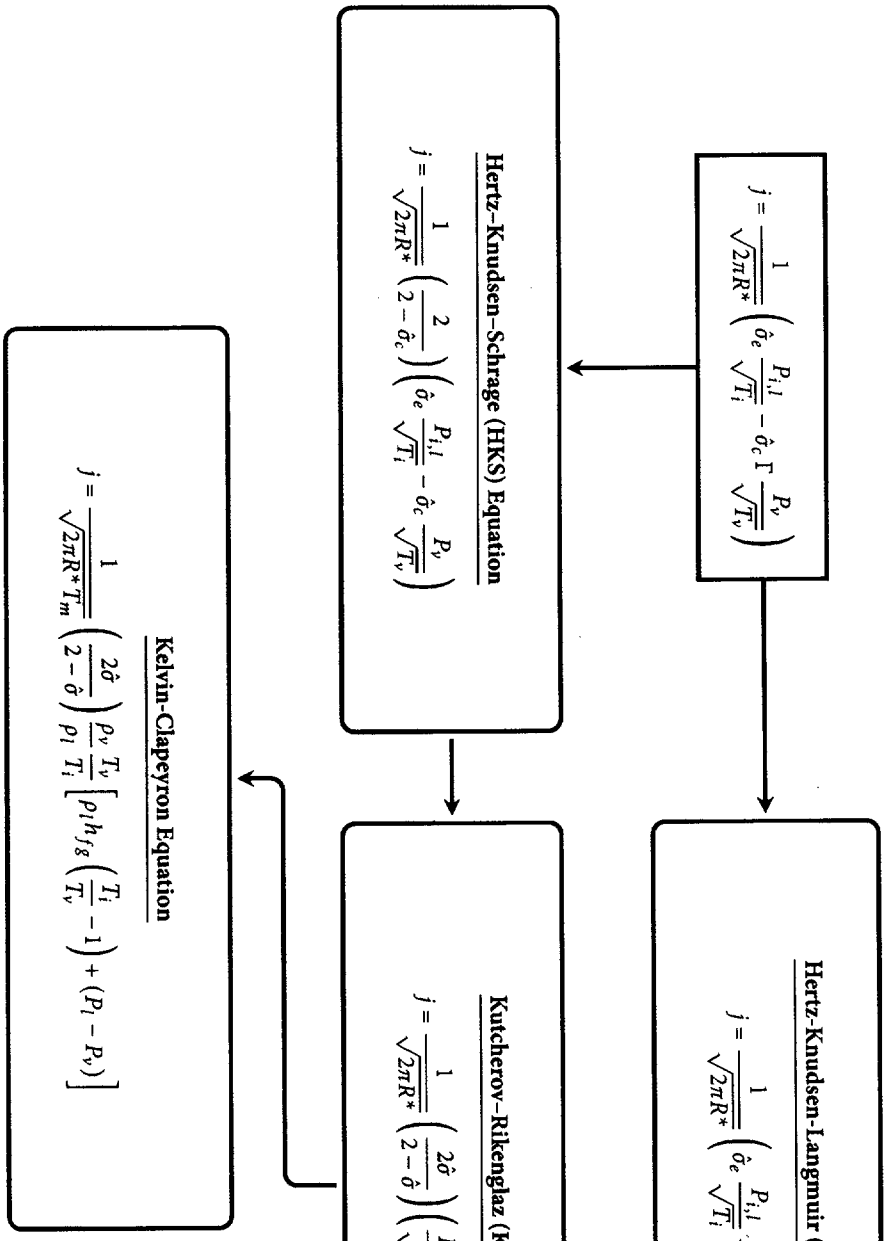


**Figure A-2:** Evolution of interfacial mass transfer models.

# Appendix B

# Derivation of the Asymptotic Film Solution

This appendix presents a detailed derivation of the asymptotic film solution (1.15) following the analysis given in [28]. Figure B-1 illustrates the anticipated solution when the following limiting behavior is imposed:

$$\begin{aligned} H &\to 1 \quad \text{and} \quad \phi \to 1 \quad \text{as} \quad X \to -\infty \\ H &\to \infty \quad \text{and} \quad \phi \to 0 \quad \text{as} \quad X \to +\infty \end{aligned} \tag{B.1}$$

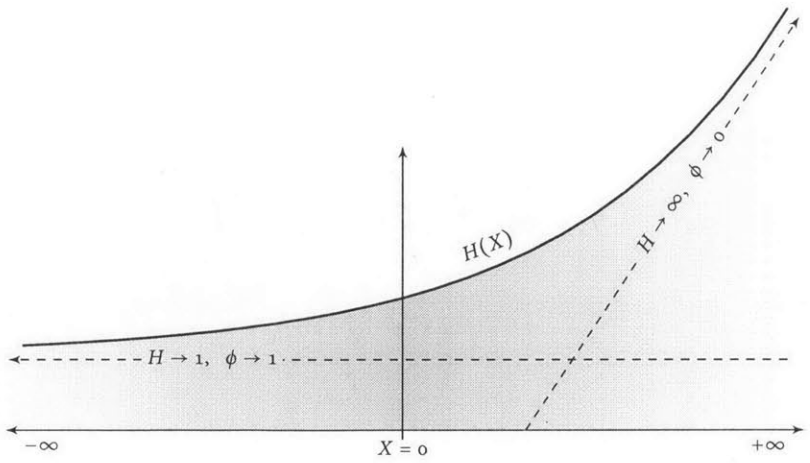


**Figure B-1:** Expected film profile according to the asymptotic conditions specified by (B.1).

Equation (1.12) can be equivalently written as,

$$-\frac{1}{3}\frac{\mathrm{d}}{\mathrm{d}X}\left(H^3\frac{\mathrm{d}\phi}{\mathrm{d}X}\right) = f\frac{1-\phi}{1+\beta H}. \tag{B.2a}$$

$$\phi = \frac{\mathrm{d}^2 H}{\mathrm{d}X^2} + \frac{1}{H^3}. \tag{B.2b}$$

Motivated by the limiting conditions as $X \to -\infty$, we write

$$H = 1 + H_0$$

$$\phi = 1 + \phi_0,$$

where $H_0$ and $\phi_0$ satisfy

$$\lim_{X\to-\infty} H_0 = \lim_{X\to-\infty} \phi_0 = 0.$$

We approximate

$$\frac{1}{H^3} = \frac{1}{(1+H_0)^3} \approx 1 - 3H_0,$$

and, from (B.2b),

$$1 + \phi_0 = \frac{\mathrm{d}^2 H_0}{\mathrm{d}X^2} + 1 - 3H_0 \quad \Longrightarrow \quad \phi_0 = \frac{\mathrm{d}^2 H_0}{\mathrm{d}X^2} - 3H_0. \tag{B.3}$$

Furthermore,

$$\frac{1}{1+\beta H} = \frac{1}{1+\beta+\beta H_0} = \frac{\left(\frac{1}{1+\beta}\right)}{1+\left(\frac{\beta}{1+\beta}\right)H_0} \approx \left(\frac{1}{1+\beta}\right)\left[1-\left(\frac{\beta}{1+\beta}\right)H_0\right],$$

so the right-hand side of (B.2a) can be written

$$f\frac{1-\phi}{1+\beta H} =\approx -\frac{f\phi_0}{1+\beta}\left[1-\left(\frac{\beta}{1+\beta}\right)H_0\right]. \tag{B.4}$$

The left-hand side of (B.2a) gives

$$
\begin{aligned}
-\frac{1}{3}\frac{\mathrm{d}}{\mathrm{d}X}\left(H^3\frac{\mathrm{d}\phi}{\mathrm{d}X}\right) &= -H^3\left[\frac{1}{3}\frac{\mathrm{d}^2\phi_0}{\mathrm{d}X^2}+\left(\frac{\mathrm{d}\phi_0}{\mathrm{d}X}\right)\left(\frac{1}{H}\frac{\mathrm{d}H}{\mathrm{d}X}\right)\right] \\
&= -H^3\left[\frac{1}{3}\frac{\mathrm{d}^2\phi_0}{\mathrm{d}X^2}+\left(\frac{\mathrm{d}\phi_0}{\mathrm{d}X}\right)\left(\frac{\mathrm{d}}{\mathrm{d}X}\ln\left(1+H_0\right)\right)\right] \\
&\approx -H^3\left[\frac{1}{3}\frac{\mathrm{d}^2\phi_0}{\mathrm{d}X^2}+\left(\frac{\mathrm{d}\phi_0}{\mathrm{d}X}\right)\left(\frac{\mathrm{d}H_0}{\mathrm{d}X}\right)\right] \\
&\approx -\frac{1}{3}H^3\frac{\mathrm{d}^2\phi_0}{\mathrm{d}X^2} \qquad \text{(B.5)}
\end{aligned}
$$

Combining (B.5) and (B.4):

$$
\begin{aligned}
\frac{1}{\phi_0}\frac{\mathrm{d}^2\phi_0}{\mathrm{d}X^2} &= \left(\frac{3f}{1+\beta}\right)\left[1-\frac{\beta}{1+\beta}H_0\right]\frac{1}{H^3} \\
&\approx \left(\frac{3f}{1+\beta}\right)\left[1-\frac{\beta}{1+\beta}H_0\right]\left(1-3H_0\right) \\
&= \left(\frac{3f}{1+\beta}\right)\left[1-\left(3+\frac{\beta}{1+\beta}\right)H_0+\frac{3\beta}{1+\beta}H_0^2\right] \\
\therefore\quad \frac{\mathrm{d}^2\phi_0}{\mathrm{d}X^2} &= \frac{3f}{1+\beta}\left[\phi_0-\left(3+\frac{\beta}{1+\beta}\right)H_0\phi_0+\frac{3\beta}{1+\beta}H_0^2\phi_0\right]
\end{aligned}
$$

Neglecting product terms such as $H_0\phi_0$, we have:

$$
\frac{\mathrm{d}^2\phi_0}{\mathrm{d}X^2}-3\gamma^2\phi_0=0, \quad \text{as} \quad X\to-\infty \qquad \text{(B.6)}
$$

where

$$
\gamma^2=\frac{f}{1+\beta}
$$

The general solution to (B.6) is given by

$$
\phi_0(X)\sim C_1\exp\left(\sqrt{3}\gamma X\right)+C_2\exp\left(-\sqrt{3}\gamma X\right) \quad \text{as} \quad X\to-\infty.
$$

Boundedness of $\phi_0$ as $X\to-\infty$ requires $C_2=0$. Substituting this result into (B.3) gives

$$
\frac{\mathrm{d}^2H_0}{\mathrm{d}X^2}-3H_0=C_1\exp\left(\sqrt{3}\gamma X\right),
$$

with homogenous and particular solutions given, respectively, by

$$\left.\begin{aligned} H_{o_h}(X) &\sim C_3 \exp\left(\sqrt{3}X\right) + C_4 \exp\left(-\sqrt{3}X\right) \\ H_{o_p}(X) &\sim \frac{C_1}{3(\gamma^2-1)} \exp\left(\sqrt{3}\gamma X\right) \end{aligned}\right\} \text{ as } X \to -\infty$$

As before, boundedness demands we take $C_4 = 0$. In summary,

$$\left.\begin{aligned} H(X) &\sim 1 + C_3 \exp\left(\sqrt{3}X\right) + \frac{C_1}{3(\gamma^2-1)} \exp\left(\sqrt{3}\gamma X\right) \\ \phi(X) &\sim 1 + C_1 \exp\left(\sqrt{3}\gamma X\right) \end{aligned}\right\} \text{ as } X \to -\infty$$

This result is found to be equivalent to (1.15) by writing $B_1 = \frac{C_1}{3(\gamma^2-1)}$ and $B_2 = C_3$.

# Appendix C

# Detailed Analysis of the Bretherton Problem

## C.1 Solution of the front meniscus

Consider the dynamic meniscus profile at the front of a bubble moving with velocity $U_b$ through a capillary of radius $R$, as illustrated in Fig. C-1. Let $h = h(x)$ denote the local film thickness, and let $h_0$ denote the thickness of the uniform film that is established at some distance sufficiently far behind the nose of the bubble. We assume $h \ll R$ so that the flow in the liquid film can be treated as 2D-planar flow in a Cartesian coordinate system. We assume further that the flow is steady and inertial effects are negligible (i.e., Stokes flow). Then the Stokes equations for this system can be written

$$\mu \frac{\mathrm{d}^2 u}{\mathrm{d}y^2} = \frac{\mathrm{d}p}{\mathrm{d}x}. \tag{C.1}$$

The boundary conditions on $u$ are given by

$$\begin{aligned} u &= -U_b \quad \text{at} \quad y = 0 \\ \mu \frac{\mathrm{d}u}{\mathrm{d}y} &= 0 \quad \text{at} \quad y = h \end{aligned} \tag{C.2}$$

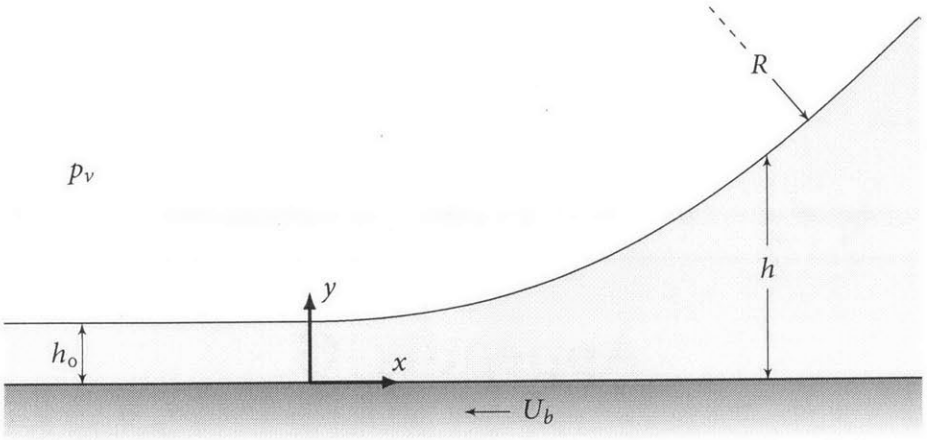


**Figure C-1:** Schematic of the dynamic meniscus region near the front of the bubble. In a frame of reference moving with the bubble, the wall appears to move to the left with velocity $U_b$.

From the Young–Laplace equation,

$$p(x) = p_v - \sigma\kappa(x) = p_v - \sigma\frac{h_{xx}}{(1+h_x^2)^{\frac{3}{2}}} \approx p_v - \sigma\frac{\mathrm{d}^2h}{\mathrm{d}x^2}. \tag{C.3}$$

The last approximation follows from the assumption that $h_x^2 \ll 1$ in the dynamic meniscus. Using a scaling argument, one can show that this is valid when $\mathrm{Ca}_b \ll 1$. Indeed,

$$\frac{\mathrm{d}^2h}{\mathrm{d}x^2} \sim \left(\frac{h_0}{\ell}\right)^2 \sim \frac{h_0}{R} \sim \mathrm{Ca}_b^{\frac{2}{3}}$$

where we have used the scaling results from Section 4.2.1, specifically, Eq. (4.11) substituting $h_0$ for $\delta$. Alternatively, one can simply proceed with the analysis assuming this approximation is valid, and then use the results to demonstrate self-consistency.

Substituting (C.3) into (C.1) gives

$$\mu\frac{\mathrm{d}^2u}{\mathrm{d}y^2} = -\sigma\frac{\mathrm{d}^3h}{\mathrm{d}x^3} \tag{C.4}$$

The solution of (C.4) subject to the boundary conditions in (C.2) is

$$u(y) = -U_b + \frac{\sigma}{2\mu}\frac{\mathrm{d}^3h}{\mathrm{d}x^3}(2hy - y^2)$$

The volumetric flow rate is

$$Q(x) = \int_0^h u(y)\mathrm{d}y = -U_b h + \frac{\sigma}{3\mu}\frac{\mathrm{d}^3 h}{\mathrm{d}x^3}h^3 = Q(-\infty) = -U_b h_0$$

where the last step follows from mass conservation. Thus, after rearranging, we obtain,

$$\frac{\mathrm{d}^3 h}{\mathrm{d}x^3} = (3\mathrm{Ca}_b)\frac{h - h_0}{h^3} \tag{C.5}$$

where $\mathrm{Ca}_b = \mu U_b/\sigma$ is the capillary number. Defining $H \equiv h/h_0$ and $X \equiv x/\ell$, with $\ell = h_0(3\mathrm{Ca})^{-\frac{1}{3}}$, Eq. (C.5) simplifies to

$$\frac{\mathrm{d}^3 H}{\mathrm{d}X^3} = \frac{H-1}{H^3} \tag{C.6}$$

Equation (C.6) was first derived in a slightly different context by Landau and Levich [76], and is consequently known as the *Landau–Levich equation* (see also, [82, 87]). Less frequently, it is also referred to as the *Bretherton equation* [19]. Appropriate "boundary" conditions for Eq. (C.6) are given by

$$\begin{aligned} H \to 1,\ H_X \to 0, \quad &\text{as} \quad X \to -\infty \\ H_{XX} \to \frac{h_0}{R}(3\mathrm{Ca}_b)^{-\frac{2}{3}}, \quad &\text{as} \quad X \to +\infty \end{aligned} \tag{C.7}$$

The last condition in (C.7) follows from the requirement that

$$\frac{\mathrm{d}^2 h}{\mathrm{d}x^2} \to \frac{1}{R},$$

for sufficiently large $x$, i.e., that the dynamic meniscus curvature and the static meniscus curvature match outside the transition region.

Owing to its nonlinear nature, no closed-form solutions to Eq. (C.6) are known to exist, and it must therefore be solved numerically [130]. This is slightly complicated by the fact that $H$ is defined on the entire real line, and we lack any true boundary conditions—only limiting conditions for $X \to \pm\infty$. Nevertheless, with some finesse, it is possible to obtain a numerical solution to Eq. (C.6), as demonstrated in the following sections.

### C.1.1 Asymptotic solution for $X \to -\infty$

We start by considering the limit as $X \to -\infty$, in which case the meniscus converges to a uniform film with thickness $H = 1$. For $X < 0$, with $|X|$ sufficiently large but finite, we expect the solution to have

the form

$$H(X) = 1 + \epsilon(X), \qquad X \to -\infty$$

where $\epsilon(X) \ll 1$ represents a small deviation from the uniform film. Substituting this into (C.6) gives

$$\frac{d^3\epsilon}{dX^3} = \frac{\epsilon}{(1+\epsilon)^3} \approx \epsilon \tag{C.8}$$

Supposing $\epsilon(X) = e^{\lambda X}$ gives $\lambda^3 = 1$, which admits the following three solutions (the cube-roots of unity):

$$\lambda_1 = 1, \quad \text{and} \quad \lambda_2 = \bar{\lambda}_3 = e^{2\pi i/3} = -\frac{1}{2} + i\frac{\sqrt{3}}{2},$$

where the overbar denotes complex conjugation. Thus, the general solution of Eq. (C.8) can be written

$$\epsilon(X) = ae^X + e^{-\frac{1}{2}X}\left(b\cos\left(\frac{\sqrt{3}}{2}X\right) + c\sin\left(\frac{\sqrt{3}}{2}X\right)\right).$$

The oscillatory terms are seen to grow unbounded as $X \to -\infty$, so we impose $b = c = 0$, leaving us with the following asymptotic solution:

$$H(X) = 1 + ae^X, \qquad X \to -\infty. \tag{C.9}$$

The integration constant, $a$, is an arbitrary, positive constant; a change in $a$ corresponds to a shift of the origin of our coordinate system, reflecting the fact that Eq. (C.6) is translation-invariant. Indeed, $\forall\ a > 0$, $\exists\ X_0 \in \mathbb{R}$ such that $a = e^{X_0}$ and $H(X) = 1 + e^{X+X_0}$, or equivalently, $H(X - X_0) = 1 + e^X$. Thus, by choosing $X_0$ to be large and negative (equivalently, choosing $a \ll 1$), we effectively place the origin ($X = 0$) at a point just outside the uniform film region. This allows us to use Eq. (C.9) as a starting point to numerically integrate (march) Eq. (C.6) outward from $X = 0$ to $X \to \infty$.

### C.1.2 Marching to $\infty$ and curvature matching

Given a value for the integration constant, $a$, in Eq. (C.9), say $a = 10^{-3}$, it is straightforward to march out a solution of Eq. (C.6) for $X \to +\infty$. To get things started, we evaluate $H$ and its first two derivatives

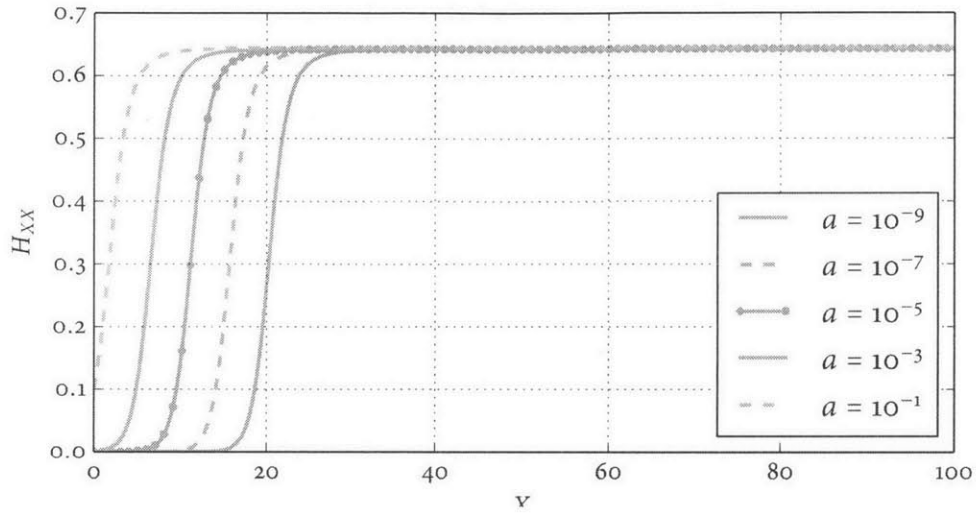


**Figure C-2:** Effect of varying $a$ in (C.10) on the asymptotic curvature of the solution to the Landau–Levich equation.

at $X = 0$ using the solution given by (C.9):

$$\begin{aligned} H(0) &= 1 + a \\ H'(0) &= a \\ H''(0) &= a \end{aligned} \tag{C.10}$$

With these "initial conditions," one can integrate (C.6) forward using, e.g., MATLAB®'s `ode45` or SciPy's `dopri5` integrators, until $H_{XX}$ approaches its asymptotic limit, possibly adjusting $a$ until $H_{XX}$ approaches the correct limiting value given in (C.7). In this case, however, adjusting $a$ turns out to be unnecessary; provided $a \lesssim 10^{-2}$, the solutions always yield the same limiting value, $H_{XX} \to 0.643$. This is seen in Fig. C-2, which illustrates the effect of varying $a$ over eight orders of magnitude. Bretherton's solution for the asymptotic film thickness follows immediately from the curvature matching condition in (C.7):

$$\lim_{X\to\infty} H_{XX} = 0.643 = \frac{h_0}{R}(3\mathrm{Ca}_b)^{-\frac{2}{3}} \iff \frac{h_0}{R} = 0.643\,(3\mathrm{Ca}_b)^{\frac{2}{3}}. \tag{C.11}$$

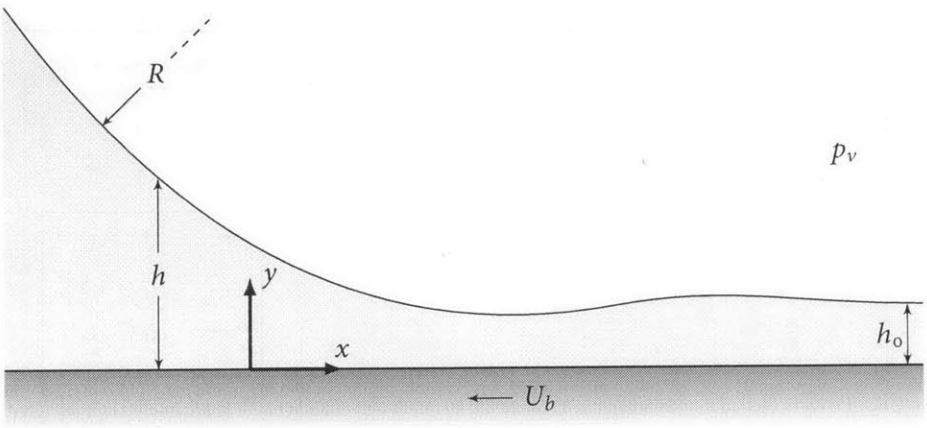


**Figure C-3:** Schematic of the dynamic meniscus region near the rear of the bubble.

## C.2 Solution of the rear meniscus

A similar analysis can be applied for the meniscus at the rear of the bubble, although in this case, the numerical solution turns out to be less straightforward. Figure C-3 illustrates the dynamic the meniscus in the vicinity of the bubble's rear. Besides the slight change in the interface shape (the reasons for which will soon be clear), the only difference between this configuration and that illustrated in Fig. C-1 seems to be that the $x$-coordinate is reversed; that is, the positive $x$-direction points towards the uniform film rather than the static meniscus. We could reverse the $x$-axis to be consistent with the previous case, but this would change the sign of the wall velocity boundary condition. Conveniently, these two changes counteract one another, and lead to the same governing ODE as before, namely the Landau–Levich equation (C.6). The fact remains, however, that now the asymptotic film solution is approached for $X \to +\infty$, and this has a dramatic effect on the character of the solutions.

As before, we begin by considering the asymptotic solution in the immediate vicinity of the uniform film in the limit $X \to +\infty$. We again seek a solution of the form $H(X) = 1 + \epsilon(X)$, and we are once again led to the general solution given by

$$\epsilon(X) = ae^X + e^{-\frac{1}{2}X}\left(b\cos\left(\frac{\sqrt{3}}{2}X\right) + c\sin\left(\frac{\sqrt{3}}{2}X\right)\right).$$

In this case, however, it is the *non*-oscillatory solution, $ae^X$, that grows without bound as $X \to +\infty$,

and we must therefore take $a = 0$, leaving

$$H(X) = 1 + be^{-\frac{1}{2}X}\cos\left(\frac{\sqrt{3}}{2}X\right) + ce^{-\frac{1}{2}X}\sin\left(\frac{\sqrt{3}}{2}X\right).$$

There are two implications to this. The first and more obvious being that the rear mensicus is non-monotonic, and exhibits a wavy nature, resulting in the film attaining a local minimum thickness near the rear of the bubble. Second, we now have two free parameters, $b$ and $c$, that we must contend with. One of these parameters can be attributed to the translation-invariance of Eq. (C.6) and can therefore be arbitrarily set to some small value. But that still leaves one free parameter, and it is for this reason that the numerical solution of the rear meniscus is somewhat more challenging than for the front meniscus. In this case, we must use a shooting method (or a comparable technique) to ensure that the limiting curvature $H_{XX}$ approaches the required value of 0.643 (as determined from the solution of the front meniscus) as $X \to -\infty$. Fortunately, this proves to be relatively easy to accomplish. Figure C-4 illustrates the computed solution for $H(X)$ and $H_{XX}(X)$ for both the front and rear menisci. The solution of the rear menisci was obtained by taking $b = 10^{-5}$, and using the Newton solver in SciPy's optimization module to solve for the unknown coefficient $c$ that gave the required curvature for $X \to -\infty$. For $b = 10^{-5}$, we computed $c = 1.75 \times 10^{-5}$.

Careful inspection of the computed solution illustrated in Fig. C-4 reveals that the minimum film thickness is given by $H_{\min} = 0.7176$, or

$$\frac{h_{\min}}{R} = 0.7176\frac{h_0}{R} = 0.461\,(3\mathrm{Ca}_b)^{\frac{2}{3}}.$$

For reference, Bretherton [13] reports the minimum film thickness to be $0.716h_0$, which is nearly identical to our computed value.

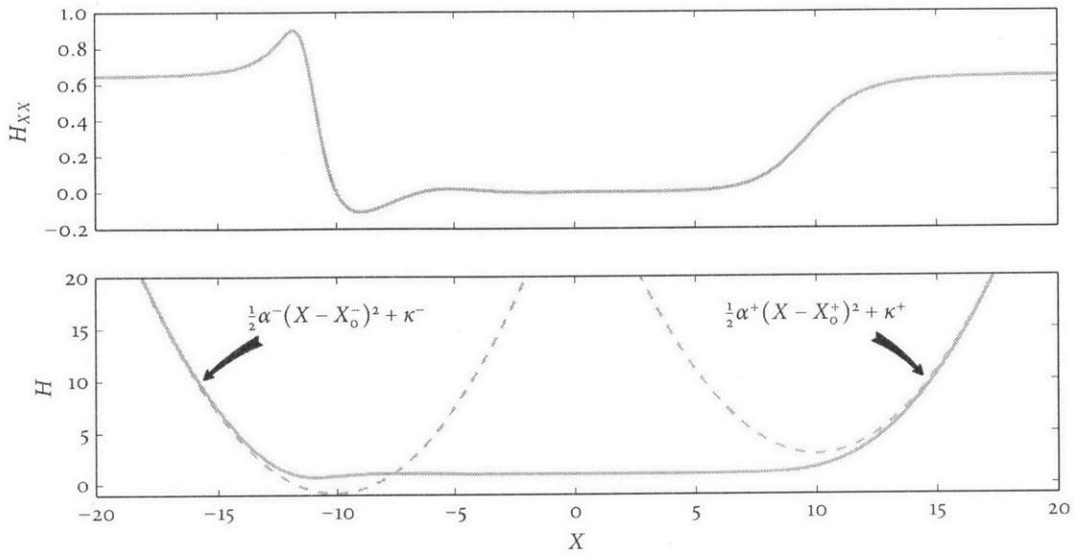


**Figure C-4:** Computed solutions for the interfacial curvature $H_{XX}$ (top) and dimensionless film thickness $H$ (bottom) for Bretherton's problem. The parabolae at either end of the bubble depict the imposed constant curvature matching condition. The coefficients were computed as $\alpha^+ = \alpha^- = 0.643$, $\kappa^+ = 2.895$, and $\kappa^- = -0.841$.

## C.3 Pressure drop across the bubble

The previous analysis can be similarly used to compute the capillary pressure drop across the length of the bubble. Consider the computed interface illustrated in Fig. C-4. The front and back menisci have been matched to parabolae described, respectively, by

$$H^+(X) = \frac{1}{2}\alpha^+(X - X_0^+)^2 + \kappa^+$$

$$H^-(X) = \frac{1}{2}\alpha^-(X - X_0^-)^2 + \kappa^-$$

where $\alpha^+ = \alpha^- = 0.643$, $\kappa^+ = 2.895$, and $\kappa^- = -0.841$. The vertices of these parabolae are located at $X_0^+ = 10$ and $X_0^- = -10$, but this is irrelevant; these values simply resulted from the way in which the front and rear solutions were spliced together. The values of $\kappa^+$ and $\kappa^-$ agree well with those reported by Chan and Demekhin [18], who give $\kappa^+ = 2.898$ and $\kappa^- = -0.8415$. By contrast, Bretherton himself gives $\kappa^+ = 2.79$ and $\kappa^- = -0.725$ [13]. The discrepancy is noted by Chang [19]. Now, consider the pressure difference between two points, say at $X = X_0^+ + 5$ and $X = X_0^- - 5$, located on the front and back interfaces, respectively (again, these coordinates can be chosen more-or-less arbitrarily, but they

should be chosen to be equidistant from the vertex of their respective parabolae). The pressures at these locations are given by

$$P_{\text{front}} = P(X_0^+ + 5) = P_v - \frac{2\sigma}{R_{\text{front}}}$$

$$P_{\text{back}} = P(X_0^- - 5) = P_v - \frac{2\sigma}{R_{\text{back}}}$$

where $R_{\text{front}}$ and $R_{\text{back}}$ are the local radii of the menisci, which we can express in terms of the local film thickness as

$$R_{\text{front}} = R - h_0 H^+(X_0^+ + 5) = R - h_0\left(\tfrac{1}{2}\alpha^+ 5^2 + \kappa^+\right)$$

$$R_{\text{back}} = R - h_0 H^-(X_0^- - 5) = R - h_0\left(\tfrac{1}{2}\alpha^- 5^2 + \kappa^-\right).$$

The capillary pressure drop across the bubble is thus found to be

$$\begin{aligned} P_{\text{back}} - P_{\text{front}} &= 2\sigma\left(\frac{1}{R - h_0\left(\frac{1}{2}\alpha^+ 5^2 + \kappa^+\right)} - \frac{1}{R - h_0\left(\frac{1}{2}\alpha^- 5^2 + \kappa^-\right)}\right) \\ &= \frac{2\sigma}{R}\left(\frac{1}{1 - \frac{h_0}{R}\left(\frac{1}{2}\alpha^+ 5^2 + \kappa^+\right)} - \frac{1}{1 - \frac{h_0}{R}\left(\frac{1}{2}\alpha^- 5^2 + \kappa^-\right)}\right) \\ &\approx \frac{2\sigma}{R}\left(1 + \frac{h_0}{R}\left(\tfrac{1}{2}\alpha^+ 5^2 + \kappa^+\right) - 1 - \frac{h_0}{R}\left(\tfrac{1}{2}\alpha^- 5^2 + \kappa^-\right)\right) \\ &= \frac{2\sigma}{R}(\kappa^+ - \kappa^-)\frac{h_0}{R}, \end{aligned}$$

where we have used the fact that $\alpha^+ = \alpha^-$ the simplify the last expression. Substituting our result from Eq. (C.11) gives

$$\frac{\Delta P}{\sigma/R} = 2(\kappa^+ - \kappa^-)\frac{h_0}{R} = 2(\kappa^+ - \kappa^-)0.643(3\text{Ca}_b)^{\frac{2}{3}} = 1.29(\kappa^+ - \kappa^-)(3\text{Ca}_b)^{\frac{2}{3}}.$$

Finally, using the computed values of $\kappa^+ = 2.895$ and $\kappa^- = -0.841$ gives

$$\Delta P = 4.82(3\text{Ca}_b)^{\frac{2}{3}}\frac{\sigma}{R} = 10.0\,\text{Ca}_b^{\frac{2}{3}}\frac{\sigma}{R} \tag{C.15}$$

Note that this result, which agrees with the expression given by Chang [19], is *not* the same result obtained by Bretherton, who gave

$$\Delta P = 4.52(3\mathrm{Ca}_b)^{\frac{2}{3}}\frac{\sigma}{R} = 9.40\,\mathrm{Ca}_b^{\frac{2}{3}}\frac{\sigma}{R}. \tag{C.16}$$

Note also that many authors [e.g., 2, 7, 9, 72, 73, 132] give Bretherton's expression for the pressure drop across the bubble as

$$\Delta P = 3.58(3\mathrm{Ca}_b)^{\frac{2}{3}}\frac{\sigma}{R} = 7.45\,\mathrm{Ca}_b^{\frac{2}{3}}\frac{\sigma}{R}. \tag{C.17}$$

This confusion seemingly originates from Bretherton's statement in the abstract of his article that Eq. (C.17) gives the pressure drop across a bubble. Yet, from the main text of his article (specifically, the first paragraph of pg. 172), it is clear that Eq. (C.17) accounts only for the pressure drop across the front meniscus; in the subsequent paragraph he gives the pressure drop across the rear meniscus, and lists the total pressure drop as Eq. (C.16).

# Bibliography


[1] H. S. Abarajith and V. K. Dhir. "A Numerical Study of the Effect of Contact Angle on the Dynamics of a Single Bubble During Pool Boiling." *ASME Int. Mechanical Engineering Congress and Exposition*. New Orleans, Louisiana: ASME, Nov. 2002, pp. 17–22.

[2] R. S. Abiev. Modeling of pressure losses for the slug flow of a gas–liquid mixture in mini- and microchannels. *Theoretical Foundations of Chemical Engineering* **45** (2) (2011), pp. 156–163.

[3] P. Abrahamsen. *A Review of Gaussian Random Fields and Correlation Functions*. Norsk Regnesentral/Norwegian Computing Center, 1997.

[4] B. M. Adams, W. J. Bohnoff, K. R. Dalbey, J. P. Eddy, J. P. Eldred, M. S. Gay, K. Haskell, P. D. Hough, and L. P. Swiler. *DAKOTA, A Multilevel Parallel Object-Oriented Framework for Design Optimization, Parameter Estimation, Uncertainty Quantification, and Sensitivity Analysis. Version 5.2 User's Manual*. Tech. rep. sand2010-2183. Sandia National Laboratories, 2011.

[5] V. S. Ajaev. *Interfacial Fluid Mechanics. A Mathematical Modeling Approach*. New York: Springer, 2012.

[6] B. K. Alpert. A class of bases in $L^2$ for the sparse representations of integral operators. *SIAM Journal on Mathematical Analysis* **24** (1) (Jan. 1993), pp. 246–262.

[7] P. Angeli and A. Gavriilidis. Hydrodynamics of Taylor flow in small channels: A Review. *Proceedings of the Institution of Mechanical Engineers, Part C: Journal of Mechanical Engineering Science* **222** (5) (2008), pp. 737–751.

[8] G. E. APOSTOLAKIS. The Concept of Probability in Safety Assessments of Technological Systems. *Science* **250** (1990), pp. 1359–1364.

[9] A. N. ASADOLAHI, R. GUPTA, S. S. Y. LEUNG, D. F. FLETCHER, and B. S. HAYNES. Validation of a CFD model of Taylor flow hydrodynamics and heat transfer. *Chemical Engineering Science* **69** (1) (2012), pp. 541–552.

[10] P. AUSSILLOUS and D. QUÉRÉ. Quick deposition of a fluid on the wall of a tube. *Physics of Fluids* **12** (10) (2000), pp. 2367–2371.

[11] G. K. BATCHELOR. *An Introduction to Fluid Dynamics*. Reissue of the 1967 edition. Cambridge University Press, 2000.

[12] D. BHAGA and M. E. WEBER. Bubbles in viscous liquids: shapes, wakes and velocities. *Journal of Fluid Mechanics* **105** (1981), pp. 61–85.

[13] F. P. BRETHERTON. The motion of long bubbles in tubes. *J. Fluid Mech* **10** (2) (1961), pp. 166–188.

[14] H.-J. BUNGARTZ and M. GRIEBEL. Sparse grids. *Acta Numerica* **13** (May 2004), pp. 147–269.

[15] H. K. CAMMENGA. "Evaporation Mechanisms of Liquids." *Current Topics in Materials Science*. Ed. by E. KALDIS. Vol. 5. North-Holland, 1980. Chap. 4.

[16] J. C. CANO-LOZANO, P. BOHORQUEZ, and C. MARTÍNEZ-BAZÁN. Wake instability of a fixed axisymmetric bubble of realistic shape. *International Journal of Multiphase Flow* **51** (2013), pp. 11–21.

[17] V. P. CAREY. *Liquid-Vapor Phase-Change Phenomena. An Introduction to the Thermophysics of Vaporization and CondensationProcesses in Heat Transfer Equipment*. 2nd ed. New York: Taylor & Francis Group, 2008.

[18] H.-C. CHAN and E. A. DEMEKHIN. Mechanism for drop formation on a coated vertical fibre. *Journal of Fluid Mechanics* **380** (1999), pp. 233–255.

[19] H.-C. CHANG. *Bubble/Drop Transport in Microchannels. MEMS: Introduction and Fundamentals*. CRC Press, 2006. Chap. 13, pp. 1–13.

[20] A. J. CHORIN and O. H. HALD. *Stochastic Tools in Mathematics And Science*. 2nd ed. Vol. 1. New York: Springer, 2009. 162 pp.

[21] D. M. CHRISTOPHER and Z. LU. Heat Transfer in the Microlayer Under a Bubble During Nucleate Boiling. *Tsinghua Science and Technology* **15** (2010), pp. 404–413.

[22] M. G. COOPER and A. J. P. LLOYD. The microlayer in nucleate pool boiling. *Int. J. Heat Mass Transfer* **12** (1969), pp. 895–913.

[23] B. G. COX. On driving a viscous fluid out of a tube. *J. Fluid Mech.* **14** (1962), pp. 81–96.

[24] B. G. COX. An experimental investigation of the streamlines in viscous fluid expelled from a tube. *J. Fluid Mech.* **20** (1964), pp. 193–200.

[25] Z. CUI, S. CHANG, and A. FANE. The use of gas bubbling to enhance membrane processes. *Journal of Membrane Science* **221** (1-2) (2003), pp. 1–35.

[26] S. DASGUPTA, I. Y. KIM, and P. C. WAYNER. Use of the Kelvin-Clapeyron Equation to Model an Evaporating Curved Microfilm. *J. Heat Transfer* **116** (1994), p. 1007.

[27] S. DASGUPTA, J. A. SCHONBERG, I. Y. KIM, and P. C. WAYNER. Use of the Augmented Young–Laplace Equation to Model Equilibrium and Evaporating Extended Menisci. *J. Colloid Interface Sci.* **157** (1993), pp. 332–342.

[28] S. DASGUPTA, J. A. SCHONBERG, and P. C. WAYNER. Investigation of an Evaporating Extended Meniscus Based on the Augmented Young-Laplace Equation. *J. Heat Transfer* **115** (1993).

[29] P.-G. DE GENNES. Wetting: Statics and Dynamics. *Reviews of Modern Physics* **57** (1985), pp. 827–863.

[30] P.-G. DE GENNES, F. BROCHARD-WYART, and D. QUÉRÉ. *Capillarity and Wetting Phenomena. Drops, Bubbles, Pearls, Waves.* Trans. by A. REISINGER. New York: Springer, 2004. 296 pp.

[31] B. V. DERJAGUIN. Modern State of the Investigation of Long-Range Surface Forces. *Langmuir* **3** (1987), pp. 601–606.

[32] V. K. DHIR. Numerical simulations of pool-boiling heat transfer. *AIChE Journal* **47** (2001), pp. 813–834.

[33] V. K. DHIR. "Simulation of Boiling—How far we have come." *ECI Int. Conference on Boiling Heat Transfer.* Florianópolis, Brazil, May 2009.

[34] R. K. EDVINSSON and S. IRANDOUST. Finite-Element Analysis of Taylor Flow. *AIChE Journal* **42** (7) (1996), pp. 1815–1823.

[35] J. FABRE. *Gas-liquid slug flow. Modelling and experimentation in two-phase flow.* Springer, 2003, pp. 117–156.

[36] F. FAIRBROTHER and A. E. STUBBS. The bubble-tube method of measurement. *J. Chem. Soc.* **1935** (1935), pp. 527–529.

[37] R. D. FALGOUT and U. M. YANG. "hypre: A library of high performance preconditioners." *Computational Science—ICCS 2002*. Springer, 2002, pp. 632–641.

[38] M. W. GEE, C. M. SIEFERT, J. J. HU, R. S. TUMINARO, and M. G. SALA. *ML 5.0 Smoothed Aggregation User's Guide*. Tech. rep. SAND2006-2649. Sandia National Laboratories, 2006.

[39] C. GERARDI, J. BUONGIORNO, L.-W. HU, and T. MCKRELL. Study of bubble growth in water pool boiling through synchronized, infrared thermometry and high-speed video. *Int. Journal of Heat and Mass Transfer* **53** (19-20) (Sept. 2010), pp. 4185–4192.

[40] M. GERRITSMA, J.-B. VAN DER STEEN, P. VOS, and G. KARNIADAKIS. Time-dependent generalized polynomial chaos. *Journal of Computational Physics* **229** (22) (2010), pp. 8333–8363.

[41] T. GERSTNER and M. GRIEBEL. Dimension-Adaptive Tensor-Product Quadrature. *Computing* **71** (2003), pp. 65–87.

[42] R. G. GHANEM and P. D. SPANOS. Spectral techniques for stochastic finite elements. English. *Archives of Computational Methods in Engineering* **4** (1 1997), pp. 63–100.

[43] M. D. GIAVEDONI and F. A. SAITA. The axisymmetric and plane cases of a gas phase steadily displacing a Newtonian liquid—A simultaneous solution of the governing equations. *Physics of Fluids* **9** (8) (1997), pp. 2420–2428.

[44] M. D. GIAVEDONI and F. A. SAITA. The rear meniscus of a long bubble steadily displacing a Newtonian liquid in a capillary tube. *Physics of Fluids* **11** (4) (1999), pp. 786–794.

[45] H. GOLDSMITH and S. MASON. The flow of suspensions through tubes. II. Single large bubbles. *Journal of Colloid Science* **18** (3) (1963), pp. 237–261.

[46] A. GUION, D. LANGEWISCH, and J. BUONGIORNO. "On the Liquid Microlayer Underneath a Vapor Bubble Growing at a Heated Wall." *International Conference on Multiphase Flow*. Submitted. Mar. 2013.

[47] A. GUNTHER, S. A. KHAN, M. THALMANN, F. TRACHSEL, and K. F. JENSEN. Transport and reaction in microscale segmented gas-liquid flow. *Lab Chip* **4** (4 2004), pp. 278–286.

[48] W. L. HABERMAN and R. M. SAYRE. *Motion of rigid and fluid spheres in stationary and moving liquids inside cylindrical tubes*. David Taylor Model Basin Report. Tech. rep. 1143. Department of the Navy, 1958.

[49] Y. HAN and N. SHIKAZONO. Measurement of the liquid film thickness in micro tube slug flow. *International Journal of Heat and Fluid Flow* **30** (5) (2009), pp. 842–853.

[50] K. HAYASHI, S. HOSODA, G. TRYGGVASON, and A. TOMIYAMA. Effects of shape oscillation on mass transfer from a Taylor bubble. *International Journal of Multiphase Flow* **58** (2014), pp. 236–245.

[51] M. HEIL. Finite Reynolds number effects in the Bretherton problem. *Physics of Fluids* **13** (9) (2001), pp. 2517–2521.

[52] J. C. HELTON, J. D. JOHNSON, and W. L. OBERKAMPF. An exploration of alternative approaches to the representation of uncertainty in model predictions. *Reliability Engineering & System Safety* **85** (1-3) (2004), pp. 39–71.

[53] J. C. HELTON, J. D. JOHNSON, C. J. SALLABERRY, and C. STORLIE. Survey of sampling-based methods for uncertainty and sensitivity analysis. *Reliability Engineering & System Safety* **91** (10-11) (2006), pp. 1175–1209.

[54] J. C. HELTON and W. L. OBERKAMPF. Alternative representations of epistemic uncertainty. *Reliability Engineering & System Safety* **85** (1-3) (2004). Alternative Representations of Epistemic Uncertainty, pp. 1–10.

[55] M. A. HEROUX. *AztecOO User Guide.* Tech. rep. SAND2004-3796. Sandia National Laboratories, 2004.

[56] M. A. HEROUX and J. M. WILLENBRING. *Trilinos Users Guide.* Tech. rep. SAND2003-2952. Sandia National Laboratories, 2003.

[57] M. A. HEROUX, J. M. WILLENBRING, and R. HEAPHY. *Trilinos Developers Guide.* Tech. rep. SAND2003-1898. Sandia National Laboratories, 2003.

[58] M. HEROUX, R. BARTLETT, V. H. R. HOEKSTRA, J. HU, T. KOLDA, R. LEHOUCQ, K. LONG, R. PAWLOWSKI, E. PHIPPS, A. SALINGER, H. THORNQUIST, R. TUMINARO, J. WILLENBRING, and A. WILLIAMS. *An Overview of Trilinos.* Tech. rep. SAND2003-2927. Sandia National Laboratories, 2003.

[59] HOLTZ. "Sparse Grid Quadratures in High Dimensions with Applications in Finance and Insurance." *Lecture Notes in Computational Science and Engineering.* Vol. 77. Berlin: Springer-Verlag, 2011, pp. 51–76.

[60] C. HORVATH, B. A. SOLOMON, and J.-M. ENGASSER. Measurement of Radial Transport in Slug Flow Using Enzyme Tubes. *Industrial & Engineering Chemistry Fundamentals* **12** (4) (1973), pp. 431–439.

[61] J. HUA and J. LOU. Numerical simulation of bubble rising in viscous liquid. *Journal of Computational Physics* **222** (2) (2007), pp. 769–795.

[62] J. HUA, J. F. STENE, and P. LIN. Numerical simulation of 3D bubbles rising in viscous liquids using a front tracking method. *Journal of Computational Physics* **227** (6) (2008), pp. 3358–3382.

[63] J. N. ISRAELACHVILI. *Intermolecular and Surface Forces.* 3rd ed. Academic Press, 2011.

[64] E. T. JAYNES. *Probability Theory. The Logic of Science.* Ed. by G. L. BRETTHORST. Cambridge University Press, 2003.

[65] Y. Y. JIANG, H. OSADA, M. INAGAKI, and N. HORINOUCHI. Dynamic modeling on bubble growth, detachment and heat transfer for hybrid-scheme computations of nucleate boiling. *International Journal of Heat and Mass Transfer* **56** (2013), pp. 640–652.

[66] J. KERN and P. C. STEPHAN. Theoretical Model for Nucleate Boiling Heat and Mass Transfer of Binary Mixtures. *J. Heat Transfer* **125** (6) (Dec. 2003), pp. 1106–1115.

[67] A. M. KHOKHLOV. Fully Threaded Tree Algorithms for Adaptive Refinement Fluid Dynamics Simulations. *J. Comput. Phys.* **143** (2) (1998), pp. 519–543.

[68] H. KIM and J. BUONGIORNO. Detection of liquid-vapor-solid triple contact line in two-phase heat transfer phenomena using high-speed infrared thermometry. *International Journal of Multiphase Flow* **37** (2) (2011), pp. 166–172.

[69] J. KIM. Review of nucleate pool boiling bubble heat transfer mechanisms. *Int. Journal of Multiphase Flow* **35** (12) (Dec. 2009), pp. 1067–1076.

[70] E. KLASEBOER, R. GUPTA, and R. MANICA. An extended Bretherton model for long Taylor bubbles at moderate capillary numbers. *Physics of Fluids* **26** (3), 032107 (2014).

[71] L. D. KOFFMAN and M. S. PLESSET. Experimental Observations of the Microlayer in Vapor Bubble Growth on a Heated Solid. *J. Heat Transfer* **105** (1983), pp. 625–632.

[72] M. T. KREUTZER, F. KAPTEIJN, J. A. MOULIJN, and J. J. HEISZWOLF. Multiphase monolith reactors: Chemical reaction engineering of segmented flow in microchannels. *Chemical Engineering Science* **60** (22) (2005), pp. 5895–5916.

[73] M. T. KREUTZER, F. KAPTEIJN, J. A. MOULIJN, C. R. KLEIJN, and J. J. HEISZWOLF. Inertial and Interfacial Effects on Pressure Drop of Taylor Flow in Capillaries. *AIChE Journal* **51** (9) (2005), pp. 2428–2440.

[74] C. KUNKELMANN and P. STEPHAN. "CFD Simulation of Boiling Flows Using the Volume-of-Fluid Method within OpenFOAM." *ECI Int. Conference on Boiling Heat Transfer.* Florianópolis, Brazil, May 2009.

[75] F. Y. KUO and I. H. SLOAN. Lifting the curse of dimensionality. *Notices of the AMS* **52** (11) (2005), pp. 1320–1329.

[76] L. LANDAU and V. G. LEVICH. Dragging of a liquid by a moving plate. *Acta Physicochim. URSS* **17** (1942), pp. 42–54.

[77] LAWRENCE LIVERMORE NATIONAL LABORATORY. *The PSUADE Uncertainty Quantification Project.* URL: https://computation.llnl.gov/casc/uncertainty_quantification/.

[78] J. H. LAY and V. K. DHIR. Shape of a Vapor Stem During Nucleate Boiling of Saturated Liquids. *J. Heat Transfer* **117** (1995), pp. 394–401.

[79] O. P. LE MAÎTRE and O. M. KNIO. *Spectral Methods for Uncertainty Quantification. With Applications to Computational Fluid Dynamics.* 1st ed. New York: Springer, 2010.

[80] O. P. LE MAÎTRE, O. M. KNIO, H. N. NAJM, and R. G. GHANEM. Uncertainty propagation using Wiener–Haar expansions. *Journal of Computational Physics* **197** (1) (June 2004), pp. 28–57.

[81] O. P. LE MAÎTRE, H. N. NAJM, R. G. GHANEM, and O. M. KNIO. Multi-resolution analysis of Wiener-type uncertainty propagation schemes. *Journal of Computational Physics* **197** (2) (2004), pp. 502–531.

[82] V. G. LEVICH. *Physiochemical Hydrodynamics.* Englewood Cliffs, NJ: Prentice–Hall, 1962.

[83] D. LI and V. K. DHIR. Numerical Study of Single Bubble Dynamics During Flow Boiling. *J. Heat Transfer* **129** (2007), pp. 864–876.

[84] Z. M. LI, X. F. PENG, and D. J. LEE. Interfacial mass transfer around a vapor bubble during nucleate boiling. *Heat and Mass Transfer* **41** (2004), pp. 5–11.

[85] M. MAGNINI, B. PULVIRENTI, and J. R. THOME. Numerical investigation of hydrodynamics and heat transfer of elongated bubbles during flow boiling in a microchannel. *International Journal of Heat and Mass Transfer* **59** (2013), pp. 451–471.

[86] M. MAGNINI, B. PULVIRENTI, and J. R. THOME. Numerical investigation of the influence of leading and sequential bubbles on slug flow boiling within a microchannel. *International Journal of Thermal Sciences* **71** (2013), pp. 36–52.

[87] M. MALEKI, M. REYSSAT, F. RESTAGNO, D. QUÉRÉ, and C. CLANET. Landau–Levich menisci. *Journal of Colloid and Interface Science* **354** (1) (2011), pp. 359–363.

[88] S. MOOSMAN and G. M. HOMSY. Evaporating menisci of wetting fluids. *J. Colloid Interface Sci.* **73** (1) (Jan. 1980), pp. 212–223.

[89] S. J. S. MORRIS. A phenomenological model for the contact region of an evaporating meniscus on a superheated slab. *J. Fluid Mech.* **411** (2000), pp. 59–89.

[90] S. J. S. MORRIS. Contact angles for evaporating liquids predicted and compared with existing experiments. *J. Fluid Mech.* **432** (2001), pp. 1–30.

[91] A. MUKHERJEE and V. K. DHIR. Study of Lateral Merger of Vapor Bubbles During Nucleate Pool Boiling. *J. Heat Transfer* **126** (2004), pp. 1023–1039.

[92] A. MUKHERJEE and S. G. KANDLIKAR. Numerical study of single bubbles with dynamic contact angle during nucleate pool boiling. *Int. Journal of Heat and Mass Transfer* **50** (1-2) (Jan. 2007), pp. 127–138.

[93] H. N. NAJM. Uncertainty Quantification and Polynomial Chaos Techniques in Computational Fluid Dynamics. *Annual Review of Fluid Mechanics* **41** (2009), pp. 35–52.

[94] H. N. NAJM. *Uncertainty Quantification in Fluid Flow.* T. ECHEKKI and E. MASTORAKOS. *Turbulent combustion modeling: Advances, new trends and perspectives.* Vol. 95. Springer, 2011. Chap. 16.

[95] F. NOBILE, R. TEMPONE, and C. WEBSTER. A Sparse Grid Stochastic Collocation Method for Partial Differential Equations with Random Input Data. *SIAM Journal on Numerical Analysis* **46** (5) (2008), pp. 2309–2345.

[96] W. L. OBERKAMPF and T. G. TRUCANO. *Verification and Validation in Computational Fluid Dynamics.* Sandia Report SAND2002-0529. Albuquerque, NM: Sandia National Laboratories, Mar. 2002.

[97] A. O'HAGAN and J. E. OAKLEY. Probability is perfect, but we can't elicit it perfectly. *Reliability Engineering & System Safety* **85** (1-3) (2004), pp. 239–248.

[98] T. O'HAGAN. Dicing with the unknown. *Significance* **1** (3) (2004), pp. 132–133.

[99] M. S. PLESSET and A. PROSPERETTI. Flow of vapour in a liquid enclosure. *J. Fluid Mech.* **78** (1976), pp. 433–444.

[100] S. POPINET. Gerris: a tree-based adaptive solver for the incompressible Euler equations in complex geometries. *J. Comput. Phys.* **190** (2) (2003), pp. 572–600.

[101] S. POPINET. An accurate adaptive solver for surface-tension-driven interfacial flows. *J. Comput. Phys.* **228** (16) (2009), pp. 5838–5866.

[102] M. POTASH and P. C. WAYNER. Evaporation from a Two-Dimensional Extended Meniscus. *Int. J. Heat Mass Transfer* **15** (1972), pp. 1851–1863.

[103] W. H. PRESS, S. A. TEUKOLSKY, W. VETTERLING, and B. P. FLANNERY. *Numerical Recipes. The Art of Scientific Computing.* 3rd ed. New York: Cambridge University Press, 2007.

[104] H. R. QUACH and V. S. AJAEV. *Numerical computation of local vapor-liquid interface shape and heat transfer near steady contact line on heated surface.* SMU Report. Available at: http://www.smu.edu/math/techreports/quach.pdf. 2005.

[105] C. E. RASMUSSEN and C. K. I. WILLIAMS. *Gaussian Processes for Machine Learning (Adaptive Computation andMachine Learning).* The MIT Press, 2005.

[106] J. RATULOWSKI and H.-C. CHANG. Transport of gas bubbles in capillaries. *Physics of Fluids A: Fluid Dynamics* **1** (10) (1989), pp. 1642–1655.

[107] J. RATULOWSKI and H.-C. CHANG. Marangoni effects of trace impurities on the motion of long gas bubbles in capillaries. *J. Fluid Mech.* **210** (1990), pp. 303–328.

[108] F. RENK, P. C. WAYNER, JR., and G. M. HOMSY. On the transition between a wetting film and a capillary meniscus. *J. Colloid Interface Sci.* **67** (3) (Dec. 1978), pp. 408–414.

[109] P. J. ROACHE. Quantification of Uncertainty in Computational Fluid Dynamics. *Annual Review of Fluid Mechanics* **29** (1) (1997), pp. 123–160.

[110] M. SALA, K. STANLEY, and M. HEROUX. "Amesos: A Set of General Interfaces to Sparse Direct Solver Libraries." *Proceedings of PARA'06 Conference.* Umea, Sweden, 2006.

[111] M. G. SALA. *Amesos 2.0 Reference Guide.* Tech. rep. SAND2004-4820. Sandia National Laboratories, 2004.

[112] M. SALA, K. S. STANLEY, and M. A. HEROUX. On the design of interfaces to sparse direct solvers. *ACM Transactions on Mathematical Software* **34** (2) (Mar. 2008), pp. 1–22.

[113] T. P. SAPSIS and P. F. J. LERMUSIAUX. Dynamically orthogonal field equations for continuous stochastic dynamical systems. *Physica D. Nonlinear Phenomena* **238** (23-24) (2009), pp. 2347–2360.

[114] J. A. SCHONBERG, S. DASGUPTA, and P. C. WAYNER. An augmented Young-Laplace model of an evaporating meniscus in a microchannel with high heat flux. *Experimental Thermal and Fluid Science* **10** (2) (1995), pp. 163–170.

[115] R. W. SCHRAGE. *A Theoretical Study of Interphase Mass Transfer.* New York: Columbia University Press, 1953.

[116] A. SHARMA. Equilibrium and Dynamics of Evaporating or Condensing Thin Fluid Domains: Thin Film Stability and Heterogeneous Nucleation. *Langmuir* **14** (1998), pp. 4915–4928.

[117] G. SON and V. K. DHIR. Three-dimensional simulation of saturated film boiling on a horizontal cylinder. *Int. Journal of Heat and Mass Transfer* **51** (5-6) (Mar. 2008), pp. 1156–1167.

[118] G. Son, V. K. Dhir, and N. Ramanujapu. Dynamics and Heat Transfer Associated With a Single Bubble During Nucleate Boiling on a Horizontal Surface. *J. Heat Transfer* **121** (1999), pp. 623–631.

[119] G. Son, N. Ramanujapu, and V. K. Dhir. Numerical Simulation of Bubble Merger Process on a Single Nucleation Site During Pool Nucleate Boiling. *J. Heat Transfer* **124** (1) (2002), pp. 51–62.

[120] V. M. Starov, M. G. Velarde, and C. J. Radke. *Wetting and Spreading Dynamics.* CRC Press, 2007.

[121] P. Stephan and J. Hammer. A new model for nucleate boiling heat transfer. *Heat and Mass Transfer* **30** (2) (1994), pp. 119–125.

[122] P. C. Stephan and C. A. Busse. Analysis of the Heat Transfer Coefficient of Grooved Heat Pipe Evaporator Walls. *Int. Journal of Heat and Mass Transfer* **35** (2) (Feb. 1992), pp. 383–391.

[123] M. Suo and P. Griffith. Two-phase flow in capillary tubes. *Journal of Basic Engineering* **86** (3) (1964), pp. 576–582.

[124] V. Talimi, Y. S. Muzychka, and S. Kocabiyik. A review on numerical studies of slug flow hydrodynamics and heat transfer in microtubes and microchannels. *International Journal of Multiphase Flow* **39** (2012), pp. 88–104.

[125] G. I. Taylor. Deposition of a viscous fluid on the wall of a tube. *J. Fluid Mech.* **10** (1961), pp. 161–165.

[126] T. C. Thulasidas, M. A. Abraham, and R. L. Cerro. Bubble-train flow in capillaries of circular and square cross section. *Chemical Engineering Science* **50** (2) (1995), pp. 183–199.

[127] T. C. Thulasidas, M. A. Abraham, and R. L. Cerro. Flow patterns in liquid slugs during bubble-train flow inside capillaries. *Chemical Engineering Science* **52** (17) (1997), pp. 2947–2962.

[128] J. G. Truong and P. C. Wayner. Effects of Capillary and van der Waals Dispersion Forces on the Equilibrium Profile of a Wetting Liquid: Theory and Experiment. *The Journal of Chemical Physics* **87** (1987), pp. 4180–4188.

[129] G. Tryggvason, R. Scardovelli, and S. Zaleski. *Direct Numerical Simulations of Gas-Liquid Multiphase Flows.* Cambridge University Press, 2011.

[130] E. O. Tuck and L. W. Schwartz. A Numerical and Asymptotic Study of Some Third-Order Ordinary Differential Equations Relevant to Draining and Coating Flows. *SIAM Rev.* **32** (1990), pp. 453–469.

[131] H. K. VERSTEEG and W. MALALASEKERA. *An Introduction to Computational Fluid Dynamics. The Finite Volume Method.* 2nd ed. Prentice Hall, 2007.

[132] E. WALSH, Y. MUZYCHKA, P. WALSH, V. EGAN, and J. PUNCH. Pressure drop in two phase slug/bubble flows in mini scale capillaries. *International Journal of Multiphase Flow* **35** (10) (2009), pp. 879–884.

[133] X. WAN and G. KARNIADAKIS. Beyond Wiener–Askey Expansions: Handling Arbitrary PDFs. *Journal of Scientific Computing* **27** (1 2006), pp. 455–464.

[134] X. WAN and G. E. KARNIADAKIS. An adaptive multi-element generalized polynomial chaos method for stochastic differential equations. *Journal of Computational Physics* **209** (2) (2005), pp. 617–642.

[135] X. WAN and G. E. KARNIADAKIS. Multi-Element Generalized Polynomial Chaos for Arbitrary Probability Measures. English. *SIAM Journal on Scientific Computing* **28** (3) (2006), pp. 901–928.

[136] H. WANG, S. V. GARIMELLA, and J. Y. MURTHY. Characteristics of an evaporating thin film in a microchannel. *Int. J. Heat Mass Transfer* **50** (2007), pp. 3933–3942.

[137] Z. WANG, M. CHEN, and Z. GUO. "A non-equilibrium molecular dynamics simulation of evaporation." *International Conference Passive and Low Energy Cooling for the Built Environment, Santorini, Greece.* Vol. 1. 2005, pp. 543–547.

[138] P. C. WAYNER, JR., Y. K. KAO, and L. V. LACROIX. The interline heat-transfer coefficient of an evaporating wetting film. *Int. Journal of Heat and Mass Transfer* **19** (5) (May 1976), pp. 487–492.

[139] P. C. WAYNER. The Effect of Interfacial Mass Transport on Flow in Thin Liquid Films. *Colloids and Surfaces* **52** (1991), pp. 71–84.

[140] P. C. WAYNER. Intermolecular forces in phase-change heat transfer: 1998 Kern Award review. *AIChE J.* **45** (1999), pp. 2055–2068.

[141] P. B. WHALLEY. *Boiling, Condensation, and Gas-Liquid Flow.* Oxford University Press, 1990.

[142] D. XIU. *Numerical Methods for Stochastic Computations. A Spectral Method Approach.* Princeton University Press, 2010. 152 pp.

[143] D. XIU and G. E. KARNIADAKIS. The Wiener–Askey Polynomial Chaos for Stochastic Differential Equations. English. *SIAM Journal on Scientific Computing* **24** (2) (2002), pp. 619–626.

[144] D. XIU and G. E. KARNIADAKIS. Modeling uncertainty in flow simulations via generalized polynomial chaos. *Journal of Computational Physics* **187** (1) (2003), pp. 137–167.

[145] D. XIU, D. LUCOR, C.-H. SU, and G. E. KARNIADAKIS. "Performance Evaluation of Generalized Polynomial Chaos." *Computational Science–ICCS 2003*. Ed. by P. SLOOT, D. ABRAMSON, A. BOGDANOV, Y. GORBACHEV, J. DONGARRA, and A. ZOMAYA. Vol. 2660. Springer Berlin, 2003, pp. 723–723.